

# **Bioinspired Organic-Inorganic Hybrid Functional Nanoscale Materials: Synthesis and Applications**

**Ph.D. Thesis**

*by*

**BHAGWATI SHARMA**



**DISCIPLINE OF CHEMISTRY  
INDIAN INSTITUTE OF TECHNOLOGY INDORE  
JANUARY, 2016**

# **Bioinspired Organic-Inorganic Hybrid Functional Nanoscale Materials: Synthesis and Applications**

**A THESIS**

*Submitted in partial fulfillment of the  
requirements for the award of degree  
of*

**DOCTOR OF PHILOSOPHY**

*by*

**BHAGWATI SHARMA**



**DISCIPLINE OF CHEMISTRY  
INDIAN INSTITUTE OF TECHNOLOGY INDORE  
JANUARY, 2016**



# INDIAN INSTITUTE OF TECHNOLOGY INDORE

## CANDIDATE'S DECLARATION

I hereby certify that the work which is being presented in the thesis entitled **Bioinspired Organic-Inorganic Hybrid Functional Nanoscale Materials: Synthesis and Applications** for the partial fulfillment of the requirements for the award of the degree of **DOCTOR OF PHILOSOPHY** and submitted in the **DISCIPLINE OF CHEMISTRY, INDIAN INSTITUTE OF TECHNOLOGY INDORE**, is an authentic record of my own work carried out during the time period from JANUARY, 2011 to DECEMBER, 2015 under the supervision of Dr. Tridib Kumar Sarma, Assistant Professor, Discipline of Chemistry, IIT Indore.

The matter presented in this thesis has not been submitted by me for the award of any other degree of this or any other institute.

Signature of the student with date  
(**BHAGWATI SHARMA**)

-----  
This is to certify that the above statement made by the candidate is correct to the best of my knowledge.

Signature of Thesis Supervisor with date  
(**Dr. TRIDIB KUMAR SARMA**)

-----  
**BHAGWATI SHARMA** has successfully given his Ph.D. Oral Examination held on  
.....

Signature of Thesis Supervisor  
Date:

Convener, DPGC  
Date:

Signature of PSPC Member #1  
Date:

Signature of PSPC Member #1  
Date:

Signature of External Examiner  
Date:

-----



# Acknowledgements

It is my great pleasure to express my deep sense of gratitude to my supervisor Dr. Tridib Kumar Sarma, for giving me the amazing opportunity to pursue research in the wonderful world of chemistry and believing in my research abilities. He gave me complete scientific freedom for working in the research areas of my choice. His constant guidance, support and motivation have been immensely helpful in the completion of this journey. His assurance and encouragement during the hard times when research plans did not work are gratefully acknowledged.

I am thankful to my PSPC members, Dr. Suman Mukhopadhyay and Dr. Vipul Singh for their valuable suggestions. Further, I am also grateful to Dr. Deepa Dey for her constant support, help and encouragement.

I wish to express my gratitude to Prof. Pradeep Mathur, Director, IIT Indore for his continuous support in every aspect.

I am also thankful to Dr. Biswarup Pathak and Mr. Arup Mahata for collaborative work and help in Density Functional Theory Studies.

I would also like to thank Dr. Satya S. Bulusu, Dr. Anjan Chakraborty, Dr. Sanjay Kumar Singh, Dr. Tushar Kanti Mukherjee, Dr. Sampak Samanta, Dr. Apurba Kumar Das, Dr. Shaikh M. Mobin, Dr. Rajneesh Misra and Dr. Chelvam Venkatesh for their guidance and help during various activities in the department.

I take this opportunity to extend my sincere thanks to my groupmates Dr. Tamalika Bhattacharya, Ms. Sonam Mandani, Mr. Biju Majumdar, Mr. Anurag Sharma, Mr. Siddharth Jain, Ms. Neha Thakur, Mr. Abhiram Panigrahi and Ms. Daisy Sarma for their selfless co-operation and help in making my work successful. I am also grateful to the youngest member of our group, Ms. Riniki Ragini Kaushik for her smiley support.

I wish to thank the technical staff from Sophisticated Instrumentation Center (SIC), IIT Indore, Ms. Sarita Batra, Mr. Kinny Pandey, Mr. Ghanshyam Bhavsar, Mr. Manish Kushwaha and Mr. Nitin Upadhyay for their patience and timely technical support

without which it would never have been possible to complete my work. I would also like to thank Mrs. Anjali Bandiwadekar, Mr. Gati Krushna Nayak, Mr. Rajesh Kumar, Mr. Lala Ram Ahirwar and other library staff and Mr. Manoj Pal, Mr. Nitin Bhate, and other technical and non-technical staff for their constant help, whenever required.

I am thankful to University Grants Commission (UGC), New Delhi for fellowship. Further, I would like to acknowledge SIC, IIT Indore for instrumentation facilities. Also I would like to thank SAIF, NEHU, Shillong, STIC, Cochin University, Department of Physics, Pune University and AMRC, IIT Mandi for TEM facility, SAIF, IIT Bombay for TEM and ICP-AES facilities and UGC-DAE Consortium for Scientific Research, Indore for Powder XRD and XPS facilities.

I would personally like to extend my sincere thanks to my friends, Dr. Bhausheeb K. Dhokale, Dr. N Rajendar, Dr.. Mahesh Chandra, Dr. Raina Thakur, Mr. Ajay Panwar Mr. Debashis Majee, Mr. Anupam Das, Mr. Anupal Gogoi, Mr. Joydeep K. Das, Mr. Lakhyajyoti Majumdar, Mr. Ashim Baishya, Mrs. Monsumi Gogoi, Ms. Nithi Phukan, Ms. Ashapurna Boro, Dr. Sabera Sultana, Mr. Somip Borphukan, Mr. Deepak Sharma, Mr. Debojit Hazarika and Mr. Sourab Sinha who were always there whenever required and never let me down during these Ph.D days.

Here it is specially to be mentioned that, it has been a wonderful experience to work with many friends during my Ph.D. who really helped me in many aspects. I would like to record my thanks to Dr. Dnyaneshwar, Dr. Indrajit, Dr. Archana, Dr. Pradeep, Dr. Prabhat, Shivendra, Anvita, Veenu, Manideepa, Maruthi, Thaksen, Anuradha, Surajit, Soumen, Mriganka, Rekha, Ramesh, Sagnik, Ajeet, Rohit, Deepika, Arpan, Roopali, Kavita, Indrani, Sagar, Ambikesh, Chandan, Soumitra, Kuber, Yuvraj, Novina, Nishu, Bidyut, Bishnu, Jonu, Ajay, Rahul and Gurpreet for their generous help and cooperation.

I also take this opportunity to express my love and gratitude to all my teachers from Fransalian High School, Jonai, Arya Vidyapith college, Guwahati and Gauhati University, Guwahati for their kind love and leading me to the right path.

Most importantly none of this would have been possible without the support of my family and I deeply express my love and gratitude to my lovable father Late Mr. Shankar Lal Sharma and mother Mrs. Tulsi Devi Sharma for their blessings, unconditional love and support, and my brothers Rajesh and Lalit and sister Suchita who have always inspired me to work hard. I am also thankful to my sister-in-law Kaushalya Sharma and brother-in-law Manoj Pandia for their affection and care. The youngest members of my family Ms. Disha, Ms. Rakshita, Ms. Aastha and Ms. Navika deserve special thanks for their smiley support.

There are many more who have directly or indirectly contributed in making this journey successful, I wish I could thank them all, but time and space compel me to stop here.

**BHAGWATI SHARMA**



***Dedicated to  
My Beloved Parents  
and Respected Teachers***



# Abstract

The interaction of biomolecules with inorganic metal ions results in the formation of nanoscale hybrid materials known as bio-inorganic hybrids. The use of biomolecules for the generation of hybrid functional materials is appealing because biomolecules not only offer rich functional group chemistry and have intrinsic self-assembling properties that can direct the final structure of the resulting material, but they also ensure an environmentally green and benign environment which can considerably reduce the energy consumption in manufacturing processes. In this thesis, two different classes of biological moieties have been exploited for the development of metal-organic hybrid materials: (i) enzymes as reducing as well as stabilizing agents for the synthesis of metallic nanoparticles with various compositions and (ii) nucleobases as low molecular weight hydrogelators for coordination polymer hydrogels through complexation with transition metal salts.

The thesis is divided into the following chapters: in Chapter 2, 3 and 4 the biomineralization capabilities of enzymes towards the formation of metallic nanoparticles, alloys and their composites with applications in catalysis have been demonstrated. In chapter 5, 6 and 7, the incredible capability of pure nucleobases to form coordination polymers with metal salts leading to hydrogels through self-assembly has been reported.

## 1. Introduction

A brief overview on the basic concepts and recent developments towards the generation of bio-inorganic hybrid nanosystems involving metal nanoparticles and coordination polymer hydrogels are reported in this chapter. This chapter tries to bring together the use of different classes of biomolecules employed in the development of hybrid materials such as metallic nanoparticles and coordination polymer hydrogels as well as coordination polymer particles. Finally, a brief summary of the research reported in this thesis and their relevance in the prospects of recent developments have been put forward.

## **2. Enzymes as bionanoreactors: Glucose oxidase for the synthesis of catalytic Au nanoparticles and Au nanoparticle-polyaniline nanocomposite**

In this chapter, the reducing ability of glucose oxidase, a flavoprotein has been exploited for the synthesis of Au nanoparticles under physiological conditions. The synthesized Au nanoparticles acted as effective catalysts towards the reduction of *p*-nitrophenol to *p*-aminophenol. Although the enzyme lost its natural activity after the synthesis of Au nanoparticles, the activity of the native enzyme could be made use of for the room temperature synthesis of Au nanoparticle-polyaniline nanocomposite.

## **3. Biogenic growth of alloys and core-shell nanostructures using urease as a nanoreactor at ambient conditions**

In this chapter, a commonly available enzyme urease was explored as a nanoreactor for the synthesis of monometallic as well as alloy nanoparticles. The natural activity of urease was partly inhibited after the synthesis of metallic nanoparticles due to conformational changes in its native structure, resulting in a significantly lower amount of ammonia generated in the process. However, even at this slightly basic pH, ZnO nanoparticles could be formed over the Au nanoparticles leading to the formation of Au-ZnO core-shell nanostructures at room temperature due to the “salting out” effect.

## **4. Catalytic activity of various pepsin reduced Au nanostructures towards reduction of nitroarenes and resazurin**

This chapter demonstrates the reducing and stabilizing ability of pepsin, a digestive protease for the size- and shape-controlled synthesis of Au nanostructures by simple variation in the pH of the reaction medium or concentration of the enzyme. Further, the correlation between the thickness of the surface stabilizing agent (pepsin) and the catalytic activity of the Au nanoparticle surface for the reduction reactions have been shown.

## **5. Ag(I) ion mediated self-assembly of nucleobases towards the generation of coordination polymer hydrogels**

In this chapter, metal binding ability of the pure nucleobases, adenine, cytosine, thymine and uracil leading to the formation of metallogels, upon the introduction of  $\text{Ag}^+$  ions under alkaline conditions have been reported. Under similar conditions, guanine resulted in the formation of a precipitate rather than a gel. Under the present conditions, the nucleobases cytosine, thymine and uracil resulted in the formation of Ag nanoparticles which were decorated along the fibers of the gel. Further, these Ag-nucleobase hydrogels could be used as an antimicrobial agent against both gram positive as well as gram negative bacteria.

## **6. $\text{Zn}^{2+}$ -nucleobase coordination polymer particles: Synthesis and photocatalytic activity**

The formation of metallogels upon the addition of  $\text{Zn}^{2+}$  ions to a basic solution of cytosine and guanine are reported in this chapter. Flower shaped coordination polymer microparticles were obtained by the addition of  $\text{Zn}^{2+}$  ions to a mixture of cytosine and guanine. All the three hybrid hydrogels have shown good activity as photocatalyst for the degradation of pollutant organic dyes.

## **7. Cd(II)-nucleobase coordination polymer hydrogels for the generation of CdS quantum dots**

In this chapter, the formation of strong self-standing hydrogels through the non-covalent interactions of nucleobases thymine and uracil with  $\text{Cd}^{2+}$  under basic medium have been reported. Further, the addition of a sulfide precursor to the nucleobase solutions followed by the addition of the  $\text{Cd}^{2+}$  afforded the formation of CdS quantum dots, decorated along the fibers of the hydrogels, with bright yellow fluorescence.

## **8. Relevance and scope**

This chapter summarizes the works described in this thesis. Further, the relevance and future prospects of the works have been discussed.



### List of Publications:

1. **Sharma B.**, Mandani S., Sarma T. K.\* (2015), Catalytic activity of various pepsin reduced Au nanostructures towards reduction of nitroarenes and resazurin, *J. Nanopart. Res.*, 17, 4 (DOI: 10.1007/s11051-014-2835-y).
2. **Sharma B.**, Mandani S., Sarma T. K.\* (2014), Enzymes as bionanoreactors: Glucose oxidase for the synthesis of catalytic Au nanoparticles and Au nanoparticle-polyaniline nanocomposite, *J. Mater. Chem. B*, 2, 4072-4079 (DOI: 10.1039/C4TB00218K).
3. **Sharma B.**, Mandani S., Sarma T. K.\* (2013), Biogenic growth of alloys and core-shell nanostructures using urease as a nanoreactor at ambient conditions, *Sci. Rep.*, 3, 2601 (DOI: 10.1038/srep02601).
4. Mandani S., **Sharma B.**, Dey D., Sarma T. K.\* (2015), Carbon nanodots as ligand exchange probes in Au@C-dot nanobeacons for fluorescent turn-on detection of biothiols, *Nanoscale*, 7, 1802-1808 (DOI: 10.1039/C4NR05424E).
5. Dey D.,\* Bhattacharya T., Majumdar B., Mandani S., **Sharma B.**, Sarma T. K.\* (2013), Carbon dot reduced Pd nanoparticles as active catalyst for carbon-carbon bond formation, *Dalton Trans.*, 42, 13821-13825 (DOI: 10.1039/C3DT51234G).
6. **Sharma B.**, Mahata A., Mandani S., Pathak B., Sarma T. K.\* Ag(I) Ion Mediated Self-Assembly of Nucleobases Towards the Generation of Coordination Polymer Hydrogels, *Communicated*.
7. **Sharma B.**, Mahata A., Mandani S., Pathak B., Sarma T. K.\* Zn<sup>2+</sup>-nucleobase coordination polymer particles: Synthesis and photocatalytic activity, *Communicated*.
8. **Sharma B.**, Mahata A., Mandani S., Pathak B., Sarma T. K.\* Synthesis of CdS quantum dots in cadmium based hydrogels generated using thymine and uracil as ligands, *Manuscript under preparation*.

### Conference Presentations:

1. **Sharma B.**, Mandani S., Sarma T. K.\* (2014), Enzymes as bionanoreactors for the synthesis of functional inorganic nanostructures, New advances and

horizons in Nanoscience and nanotechnology (NanoSci-2014), IASST, Guwahati, India (20-21 December, 2014); Presented poster.

2. **Sharma B.**, Mandani S., Sarma T. K.\* (2014), Green synthesis of Au nanoparticles using pepsin as a bionanoreactor and their application towards the reduction of resazurin to resorufin, International conference on nano science and technology (ICONSAT-2014), INST, Mohali, India (2-5 March, 2014); Presented poster.
3. **Sharma B.**, Mandani S., Sarma T. K.\* (2014), One pot green synthesis of catalytically active Au nanoparticles and Au nanoparticle-polyaniline nanocomposite using glucose oxidase as a bionanoreactor, International conference on advanced nanomaterials and nanotechnology (ICANN-2013), IIT Guwahati, Guwahati, India (1-3 December, 2013); Presented poster.
4. **Sharma B.**, Mandani S., Sarma T. K.\* (2012), Urease as a nanoreactor for the synthesis of metal@metal oxide core-shell nanostructures, International conference on nano science and technology (ICONSAT-2012), ARCI, Hyderabad, India (20-23 January, 2012); Presented poster.

# TABLE OF CONTENTS

<b>1. List of Figures</b>	<b>xxi</b>
<b>2. List of Schemes</b>	<b>xxxii</b>
<b>3. List of Tables</b>	<b>xxxiii</b>
<b>4. Acronyms</b>	<b>xxxv</b>
<b>5. Nomenclature</b>	<b>xxxvii</b>

## **Chapter 1: General Introduction and Background** **1-52**

1.1 Introduction	1
1.2 Hybrid organic-inorganic functional materials	2
1.2.1 Metallic nanoparticles	3
1.2.2 Coordination polymers	7
1.3 Biomolecules for the synthesis of inorganic nanoparticles and coordination polymers	9
1.3.1 Amino acids, peptides, nucleobases and nucleotides	11
1.3.2 Microbes	15
1.3.3 Enzymes	17
1.4 Gels	24
1.5 Organization of thesis	27
1.6 References	30

## **Chapter 2: Enzymes as Bionanoreactors: Glucose Oxidase for the Synthesis of Catalytic Au Nanoparticles and Au Nanoparticle-Polyaniline Nanocomposite** **53-80**

2.1 Introduction	53
2.2 Results and Discussions	55
2.2.1 Synthesis and characterization of Au nanoparticles	55
2.2.2 Effect of concentration of Au <sup>3+</sup> and GOx on the morphology of Au NPs	57

2.2.3. Catalytic activity of Au NPs	57
2.2.4 Activity of GOx after the synthesis of Au NPs	59
2.2.5 Conformational changes in the structure of GOx after the synthesis of Au NPs	61
2.2.6 Amino acids in GOx responsible for the reduction of Au <sup>3+</sup>	63
2.2.7 Synthesis and characterization of Au NP-polyaniline nanocomposite	65
2.3 Conclusions	70
2.4 Experimental Section	71
2.4.1. Materials	71
2.4.2 Instrumentation	71
2.4.3 Synthesis of Au nanoparticles	71
2.4.4 Catalytic activity of Au nanoparticles	72
2.4.5 Activity of native glucose oxidase and glucose oxidase after the synthesis of Au NPs (FOX method)	72
2.4.6 Circular dichroism studies	72
2.4.7 Fluorescence study	73
2.4.8 Modification of thiol groups in glucose oxidase using DTNB	73
2.4.9 Synthesis of Au NP-polyaniline nanocomposite	73
2.4.10 Cyclic voltametry studies	73
2.5 References	74

### **Chapter-3: Biogenic Growth of Alloys and Core-shell Nanostructures 81-116**

#### **Using Urease as a Nanoreactor at Ambient Conditions**

3.1 Introduction	81
3.2 Results and Discussions	83
3.2.1 Synthesis and characterization of metallic (Au, Ag and Pt) nanoparticles	83
3.2.2 Effect of phosphate buffer saline (PBS) on the morphology of nanoparticles	88

3.2.3 Synthesis and characterization of metallic alloy (Au-Ag, Ag-Pt and Au-Pt) nanoparticles	89
3.2.4 Activity of urease after the synthesis of nanoparticles	91
3.2.5 Conformational changes in urease after the synthesis of nanoparticles	93
3.2.6 Amino acid in urease responsible for reduction of metal salts	95
3.2.7 Mechanism of nanoparticle formation and subsequent loss in its activity	96
3.2.8 Synthesis and characterization of Au@ZnO core-shell nanostructures	97
3.2.9 Catalytic reduction of <i>p</i> -nitrophenol to 1,4- diaminobenzene	101
3.3 Conclusions	102
3.4 Experimental Section	103
3.4.1 Materials	103
3.4.2 Instrumentation	103
3.4.3 Synthesis of Au nanoparticles using K <sub>2</sub> CO <sub>3</sub>	104
3.4.4 Synthesis of Ag nanoparticles	104
3.4.5 Synthesis of Pt nanoparticles	104
3.4.6 Synthesis of alloy nanoparticles	104
3.4.7 Synthesis of Au@ZnO core-shell nanoparticles	104
3.4.8 XPS measurement	105
3.4.9 Conformational changes in urease after nanoparticle synthesis	105
3.4.9.1 Fluorescence studies	105
3.4.9.2 Circular dichroism studies	105
3.4.10. Activity study of urease	105
3.4.10.1 pH method	105
3.4.10.2 Bromocresol purple assay	106
3.4.11. Theoretical Calculation for the ratio of Au:Zn in Au@ZnO core-shell nanoparticles	106
3.5 References	108

**Chapter 4: Catalytic Activity of Various Pepsin Reduced Au Nanostructures Towards Reduction of Nitrophenols and Resazurin 117-148**

4.1 Introduction	117
4.2 Results and Discussions	119
4.2.1. Synthesis and characterization of Au nanostructures synthesized at pH 5.4 and 4.0	119
4.2.2 Activity of pepsin after synthesis of Au nanostructures	121
4.2.3 Conformational changes in the structure of pepsin after synthesis of Au nanostructures	122
4.2.4 Synthesis and characterization of red emitting Au nanoclusters	124
4.2.5 Effect of size of Au nanostructures on the reduction of <i>p</i> -nitrophenol	126
4.2.6 Effect of shape of Au nanostructures on the reduction of <i>p</i> -nitrophenol	127
4.2.7 Rate constants for the reduction of <i>p</i> -nitrophenol by different Au nanostructures and role of pepsin in the reduction reaction	129
4.2.8 Catalytic activity of different sized and shaped Au nanostructures towards reduction of resazurin to resorufin	130
4.2.9 Effect of surface stabilizing agent (pepsin) on the catalytic activity of Au nanostructures	133
4.2.10 Recyclability of the catalysts	136
4.3 Conclusions	136
4.4 Experimental Section	137
4.4.1 Materials	137
4.4.2 Instrumentation	138
4.4.3 Synthesis of Au nanoparticles at pH 5.4 and 4.0	138
4.4.4 Synthesis of Au nanoparticles at pH 5.4 for activity assay, fluorescence study and circular dichroism studies	138
4.4.5 Activity assay of pepsin after synthesis of Au nanoparticles	138
4.4.6 Synthesis of red emitting Au nanoclusters	139
4.4.7 Fluorescence study of pepsin before and after synthesis of Au	140

nanoparticles	
4.4.8 Circular dichroism studies	140
4.4.9 Catalytic reduction of <i>p</i> -nitrophenol to <i>p</i> -aminophenol	140
4.4.10 Catalytic reduction of resazurin to resorufin	140
4.5 References	141
<b>Chapter 5: Ag(I) Ion Mediated Self-Assembly of Nucleobases Towards</b>	<b>149-188</b>
<b>the Generation of Coordination Polymer Hydrogels</b>	
5.1 Introduction	149
5.2 Results and Discussions	151
5.2.1 Synthesis and characterization of Ag-adenine hydrogel	151
5.2.2 Synthesis and characterization of Ag-cytosine, Ag-thymine and Ag-uracil hydrogels	156
5.2.3 Interaction of AgNO <sub>3</sub> with guanine in alkaline conditions	161
5.2.4 Gel formation in a mixture of two or three nucleobases	162
5.2.5 Formation of Ag nanoparticles within the gels	165
5.2.6 Chemical response of the gels	166
5.2.7 Antimicrobial activity of the hydrogels	167
5.2.8 Interaction of Ag <sup>+</sup> ions with nucleobases under acidic conditions	168
5.2.9 Density functional theory (DFT) studies	170
5.3 Conclusions	176
5.4 Experimental Section	177
5.4.1 Materials	177
5.4.2 Instrumentation	177
5.4.3 Synthesis of Ag-nucleobase hydrogels in basic medium	177
5.4.4 Synthesis of Ag-guanine gel in acidic medium	178
5.4.5 Electron microscopy studies	178
5.4.6 Rheological studies	178
5.4.7 Study of response of gels towards various anions	178
5.4.8 Antimicrobial studies	179
5.4.9 DFT calculations	179

5.5 References	180
----------------	-----

**Chapter 6: Zn<sup>2+</sup>-Nucleobase Coordination Polymer Particles: Synthesis and Photocatalytic Activity** 189-208

6.1 Introduction	189
6.2 Results and Discussions	190
6.2.1 Synthesis and characterization of Zn-nucleobase hydrogels	190
6.2.2 Interaction of Zn <sup>2+</sup> ions with adenine, thymine or uracil	194
6.2.3 Interaction of Zn <sup>2+</sup> ions with a mixture of cytosine and guanine	195
6.2.4 Photocatalytic activity of the three zinc based materials	197
6.3 Conclusions	201
6.4 Experimental Section	202
6.4.1 Materials	202
6.4.2 Instrumentation	202
6.4.3 Synthesis of Zn-cytosine and Zn-guanine hydrogels	202
6.4.4 Electron microscopy studies	203
6.4.5 Rheological studies	203
6.4.6 Synthesis of Zinc-cytosine-guanine microflowers	203
6.4.7 Photocatalytic studies	203
6.5 References	204

**Chapter 7: Cd(II)-Nucleobase Coordination Polymer Hydrogels for the Generation of CdS Quantum Dots** 209-230

7.1 Introduction	209
7.2 Results and Discussions	211
7.2.1 Synthesis and characterization of Cd-nucleobase hydrogels	211
7.2.2 Interaction of Cd <sup>2+</sup> ions with adenine, guanine or cytosine	215
7.2.3 Gel formation in a mixture of thymine and uracil	217
7.2.4 Formation of CdS quantum dots within the gels	219
7.3 Conclusions	222
7.4 Experimental Section	223

7.4.1 Materials	223
7.4.2 Instrumentation	223
7.4.3 Synthesis of Cd-thymine and Cd-uracil hydrogels	223
7.4.4 Electron microscopy studies	224
7.4.5 Rheological studies	224
7.4.6 Formation of gel in the mixture of thymine and uracil	224
7.4.7 Synthesis of CdS quantum dots within the gel	224
7.5 References	225
<b>Chapter 8: Conclusions and Scope for Future Works</b>	<b>231-234</b>
8.1 Conclusions	231
8.2 Scope for future works	233



# LIST OF FIGURES

## Chapter-1: General Introduction and Background

- Figure 1.1** Unique optical properties of gold nanoparticles, showing a variation in color of the solution and hence the absorption maximum upon change in the size of the nanocrystals. 5
- Figure 1.2** Representation of different families of natural biomolecules present in living beings. 11
- Figure 1.3** TEM images of Au nanoplates and hexagons synthesized using aspartate as reducing agent and schematic illustration for the room temperature synthesis of various colored Au nanoclusters using cytidine/cytidine nucleotides. 13
- Figure 1.4** (a) and (b) FESEM and TEM image of of Cu-aspartate nanofibers, (c) and (d) SEM images of rod like coordination polymer particles obtained by the reaction of the tripeptide ValValGlu with Ca(II) and Cu(II) respectively, (e) FESEM image of hybrid adenine-HAuCl<sub>4</sub> microparticles formed through supramolecular interactions and (f) SEM image of 5'-AMP/Gd<sup>3+</sup> nanoparticles prepared in water by simple addition of Gd<sup>3+</sup> ions to a solution of AMP 15
- Figure 1.5** Time dependent UV-visible spectrum and TEM images of Au nanoparticles synthesized using *Fusarium Oxysporum*. 16
- Figure 1.6** Schematic illustration for the formation of ZnO using the activity of urease and TEM images, particle size distribution histogram and fluorescence spectrum of the formed ZnO. 20
- Figure 1.7** Illustration of a portion of bovine serum albumin undergoing structural changes upon exposure to heat/HAuCl<sub>4</sub> and SEM and TEM images of Au nanotriangles and hexagons synthesized using bovine serum albumin as reducing as well as stabilizing agent. 21
- Figure 1.8** Digital images, fluorescence spectra and TEM images of various Au nanoclusters synthesized using pepsin 23

**Figure 1.9** (a) Representation of an engineered protein based on the four-helix bundle heme protein cytochrome cb562, and (b) the porous structure resulted from its metal-directed assembly 24

## **Chapter-2: Enzymes as Bionanoreactors: Glucose Oxidase for the Synthesis of Catalytic Au Nanoparticles and Au Nanoparticle-Polyaniline Nanocomposite**

**Figure 2.1** Spectroscopic and microscopic characterization of Au nanoparticles synthesized using glucose oxidase as reducing and stabilizing agent 56

**Figure 2.2** TEM and HRTEM images of Au nanostructures synthesized at various concentrations of H<sub>2</sub>AuCl<sub>4</sub> and GOx 57

**Figure 2.3** Time dependent UV-visible spectra for the reduction of *p*-nitrophenol to *p*-aminophenol (a) in absence of catalyst and (b) in presence of Au NP-GOx composite as catalyst and (c) plot of natural log of absorbance at 400 nm versus time. 59

**Figure 2.4** (a) UV-visible spectrum of Au NP-GOx-PANI composite indicating the decrease in the activity of GOx after its involvement in the synthesis of Au nanoparticles, (b) Photograph and (c) UV-visible spectrum showing the inhibition of activity of GOx after its participation as a reducing agent in the synthesis of Au NPs. 60

**Figure 2.5** Circular dichroism, FTIR and fluorescence spectra suggesting conformational changes in the activity of GOx after its involvement in the synthesis of Au NPs 62

**Figure 2.6** Digital images, UV-visible spectrum and FTIR studies suggesting the probable involvement of thiol groups in GOx in the reduction of Au<sup>3+</sup> ions to Au NPs. 64

**Figure 2.7** (a) Time dependent UV-visible spectrum of Au NP-PANI composite, (b) UV-visible spectrum of Au NPs synthesized through the reduction of Au<sup>3+</sup> by H<sub>2</sub>O<sub>2</sub> generated by the oxidation of glucose by GOx. (c) Digital images showing the sequence of 68

reactions involved in the formation of Au NP- polyaniline composite by making use of the activity of glucose oxidase. (d) UV-visible spectrum of PANI alone synthesized using the activity of GOx and (e) FTIR spectrum of PANI alone (red line) and Au NP-PANI composite (blue line) synthesized using GOx.

- Figure 2.8** (a) Cyclic voltammogram of Au NP-PANI nanocomposite at a scan rate of 100 mV/s, (b) Powder XRD pattern of polyaniline alone (red line) and Au nanoparticle-polyaniline nanocomposite (blue line), (c) TEM image of Au NP-PANI nanocomposite and (d) EDS spectrum of Au NP-PANI nanocomposite. 69

### **Chapter-3: Biogenic Growth of Alloys and Core-shell Nanostructures Using Urease as a Nanoreactor at Ambient Conditions**

- Figure 3.1** Various spectroscopic and microscopic characterization of Au nanoparticles synthesized using urease as a reducing and stabilizing agent. 84
- Figure 3.2** Powder XRD and TEM characterization of Pt nanoparticles synthesized using urease 85
- Figure 3.3** Characterization of the Ag nanoparticles formed by urease using various spectroscopic and TEM techniques 86
- Figure 3.4** XPS spectrum of 3d electrons of Ag-Ag<sub>2</sub>O composite 87
- Figure 3.5** (a) UV-visible spectrum of Au NPs synthesized in K<sub>2</sub>CO<sub>3</sub> and PBS using urease and (b) TEM image of Au NPs synthesized in PBS showing agglomeration of nanoparticles 88
- Figure 3.6** Characterization of Au-Ag alloy nanoparticles employing UV-visible spectroscopy, Powder XRD, TEM and EDX techniques. 89
- Figure 3.7** UV-visible, Powder XRD and TEM characterization of Ag-Pt alloy nanoparticles synthesized using urease 90
- Figure 3.8** Characterization of Au-Pt alloy nanoparticles using UV-visible, Powder XRD and TEM analysis 91
- Figure 3.9** (a) pH change of the medium by native urease, Au nanoparticle- 92

urease composite (urease reduced Au nanoparticles), denatured urease and citrate capped Au nanoparticles with urease and (b) Comparison of the activity of native urease and urease after the synthesis of Au NPs using the dye bromocresol purple

- Figure 3.10** Fluorescence study, Circular dichroism study and FTIR studies suggesting conformational changes in the structure of urease after the synthesis of Au nanoparticles. 94
- Figure 3.11** Digital image, UV-visible spectrum and FTIR spectra, suggesting the involvement of thiol groups of urease in the reduction of metal salts to metal nanoparticles 96
- Figure 3.12** (a) Overall structure of the Jack bean urease monomer (b) stereo diagram of the active site architecture containing a binuclear nickel centre and mobile flap of urease. For clarity, only cys592 has been highlighted along with Ni ions and  $\text{PO}_4^{3-}$  residues present in the active site. 97
- Figure 3.13** UV-visible, Powder XRD and fluorescence emission spectrum of Au@ZnO core-shell nanostructures synthesized using urease. 98
- Figure 3.14** TEM and EDX characterization of Au@ZnO core shell nanostructures synthesized using urease 100
- Figure 3.15** (a) Scheme for the reduction of *p*-nitroaniline to 1,4-diamino benzene by urease reduced Au nanoparticles, (b), (c), (d) and (e) Time dependent UV-visible spectrum for the reduction of *p*-nitroaniline to 1,4-diamino benzene using Au nanoparticles, Au@ZnO core-shell nanostructures, in absence of any nanoparticle and ZnO nanoparticles respectively as catalyst. (f) plot of  $\ln A$  vs  $T$  for the reduction of *p*-nitroaniline to 1,4-diaminobenzene by  $\text{NaBH}_4$  in presence of urease reduced Au nanoparticles (blue) and Au@ZnO core-shell nanoparticles (red). 102

## Chapter-4: Catalytic Activity of Various Pepsin Reduced Au Nanostructures Towards Reduction of Nitroarenes and Resazurin

<b>Figure 4.1</b>	Digital images, UV-visible spectrum and Powder XRD spectrum of Au nanostructures synthesized at pH 5.4 and 4.0 using pepsin.	119
<b>Figure 4.2</b>	TEM and HRTEM images of Au nanostructures synthesized at pH 5.4 and 4.0 using pepsin as reducing and stabilizing agent.	120
<b>Figure 4.3</b>	UV-visible spectrum showing the action of native pepsin, citrate capped Au nanoparticle-pepsin composite, pepsin reduced Au NP-pepsin composite and denatured pepsin on hemoglobin.	122
<b>Figure 4.4</b>	Circular dichroism spectra, fluorescence spectra and FTIR spectra indicating conformational changes in the structure of pepsin after the synthesis of Au nanostructures.	123
<b>Figure 4.5</b>	Emission spectrum and TEM image of Au nanoclusters synthesized at pH 12.0 by pepsin.	125
<b>Figure 4.6</b>	Time dependent UV-visible spectrum for the reduction of <i>p</i> -nitrophenol to <i>p</i> -aminophenol using Au nanostructures synthesized by pepsin at pH 12.0, pH 5.4 and pH 4.0	128
<b>Figure 4.7</b>	(a) plot of $\ln A$ vs $T$ for the reduction of <i>p</i> -nitrophenol to <i>p</i> -aminophenol by $\text{NaBH}_4$ in absence of Au nanoparticles (black) and in presence of Au nanostructures synthesized at pH 4.0 (blue), pH 5.4 (red) and pH 12.0 (green). (b) Controlled experiment for the reduction of <i>p</i> -nitrophenol to <i>p</i> -aminophenol by $\text{NaBH}_4$ in presence of pepsin alone.	130
<b>Figure 4.8</b>	(a) Digital images of resazurin and resorufin, (b) Time dependent UV-visible spectrum for the reduction of resazurin to resorufin in absence Au nanostructures. (b), (c) and (d) Time dependent UV-visible spectrum for the reduction of resazurin to resorufin using Au nanostructures synthesized by pepsin at pH 5.4, pH 4.0 and pH 12.0 and plot of $\ln A$ vs $T$ for the reduction of resazurin to resorufin by $\text{NH}_2\text{OH}\cdot\text{HCl}$ in absence of Au nanostructures	132

(black) and in presence of Au nanostructures synthesized at pH 12.0 (green), pH 4.0 (blue) and pH 5.4 (red).

- Figure 4.9** Time dependent fluorescence spectrum for the reduction of resazurin to resorufin by  $\text{NH}_2\text{OH.HCl}$  catalyzed by pepsin reduced Au nanostructures of (a) pH 5.4, (b) pH 4.0 and (c) ultra small Au NCs synthesized at pH 12.0 133
- Figure 4.10** Time dependent UV-visible spectrum for the reduction of *p*-nitrophenol to *p*-aminophenol catalyzed by Au nanoparticles synthesized at pH 5.4 with pepsin concentration of (a) 2mg/mL, (b) 4 mg/mL and (c) 7.5mg/mL. (d) plot of  $\ln A$  vs  $T$  for the reduction of *p*-nitrophenol to *p*-aminophenol to resorufin by  $\text{NaBH}_4$  catalyzed by Au nanoparticles synthesized at pH 5.4 with pepsin concentration of 2mg/mL (black), 4 mg/mL (red) and 7.5mg/mL (blue). 134
- Figure 4.11** Time dependent UV-visible spectrum for the reduction of resazurin to resorufin catalyzed by Au nanoparticles synthesized at pH 5.4 with pepsin concentration of (a) 2mg/mL, (b) 4 mg/mL and (c) 7.5mg/mL. (d) plot of  $\ln A$  vs  $T$  for the reduction of resazurin to resorufin by  $\text{NH}_2\text{OH.HCl}$  catalyzed by Au nanoparticles synthesized at pH 5.4 with pepsin concentration of 2mg/mL (black), 4 mg/mL (blue) and 7.5mg/mL (red). 135
- Figure 4.12** Reusability of the Au nanostructures synthesized using pepsin for the conversion of *p*-nitrophenol to *p*-aminophenol and resazurin to resorufin in four successive cycles of reaction by various Au nanoparticle-pepsin composites. 136

## **Chapter-5: Ag(I) Ion Mediated Self-Assembly of Nucleobases Towards the Generation of Coordination Polymer Hydrogels**

- Figure 5.1** Electron microscopic characterization of Ag-adenine hydrogel. 153
- Figure 5.2** Powder X-ray diffraction spectrum and thermogravimetric plot of 154

	freeze dried Ag-adenine gel.	
<b>Figure 5.3</b>	Amplitude sweep and frequency sweep rheological investigation of the Ag-adenine hydrogel.	155
<b>Figure 5.4</b>	FTIR spectrum of pure adenine and Ag-adenine gel.	156
<b>Figure 5.5</b>	Electron microscopic images of Ag-cytosine, Ag-thymine and Ag-uracil hydrogels.	157
<b>Figure 5.6</b>	(a) Powder XRD pattern and (b) TGA plots of the freeze dried Ag-cytosine, Ag-thymine and Ag-uracil gels.	158
<b>Figure 5.7</b>	FTIR spectrum of (a) cytosine and Ag-cytosine, (b) thymine and Ag-thymine and (c) uracil and Ag-uracil.	159
<b>Figure 5.8</b>	Rheological investigation of Ag-cytosine, Ag-thymine and Ag-uracil hydrogels.	160
<b>Figure 5.9</b>	Digital image, FESEM images, powder XRD and FTIR spectrum of the Ag-guanine precipitate.	162
<b>Figure 5.10</b>	FESEM images of the hydrogels formed upon the addition of Ag <sup>+</sup> ions to a mixture of two or three nucleobases.	163
<b>Figure 5.11</b>	Rheological investigation of the hydrogels formed upon the addition of Ag <sup>+</sup> ions to a mixture of two or three nucleobases.	164
<b>Figure 5.12</b>	Digital image, solid state UV-visible spectra and TEM images of Ag nanoparticles formed within the Ag-cytosine, Ag-thymine and Ag-uracil hydrogels.	166
<b>Figure 5.13</b>	Antimicrobial activity of the four hydrogels against <i>E. Coli</i> and <i>Staphylococcus</i> .	168
<b>Figure 5.14</b>	FESEM images, rheological investigation, powder XRD spectrum and TGA plot of the Ag-guanine gel formed in acidic medium.	170
<b>Figure 5.15</b>	Optimized structure of silver-nucleobase monomeric unit in basic medium	172
<b>Figure 5.16</b>	Optimized structure of silver-nucleobase dimeric unit in basic medium.	173
<b>Figure 5.17</b>	Proposed structure of the complex formed upon the interaction of	174

Ag<sup>+</sup> ions to adenine under alkaline conditions.

**Figure 5.18** Optimized structure of silver-nucleobase monomeric unit in acidic medium. 175

**Figure 5.19** Optimized structure of silver-nucleobase dimeric unit in acidic medium. 176

## **Chapter-6: Zn<sup>2+</sup>-Nucleobase Coordination Polymer Particles: Synthesis and Photocatalytic Activity**

**Figure 6.1** Digital images, TEM and SEM images of Zn-C and Zn-G hydrogels. 191

**Figure 6.2** Dynamic strain sweep and frequency sweep rheological investigations of Zn-C and Zn-G hydrogels. 192

**Figure 6.3** Powder XRD and TGA plots of Zn-C and Zn-G gels. 193

**Figure 6.4** (a) FTIR spectrum of pure C and Zn-C and (b) FTIR spectrum of pure G and Zn-G 194

**Figure 6.5** Digital images and SEM images of the precipitate formed upon the interaction of Zn<sup>2+</sup> ions with adenine, thymine and uracil. 195

**Figure 6.6** SEM images, TEM image, Digital image, Powder XRD spectrum and TGA plot of Zn-C-G microflowers. 196

**Figure 6.7** Time dependent FESEM images for the growth of Zn-C-G microflowers. 197

**Figure 6.8** Solid state UV-visible spectrum for the calculation of the band gap of the three Zn based materials. 198

**Figure 6.9** Time dependent UV-visible studies for the degradation of methylene blue by UV lamp of wavelength 365 nm, using (a) Zn-cytosine, (b) Zn-G and (c) Zn-C-G as photocatalysts. (d) Plots of absorbance of the methylene blue solutions at different time intervals. 199

**Figure 6.10** Time dependent UV-visible studies for the degradation of methyl orange by UV lamp of wavelength 365 nm, using (a) Zn-cytosine, (b) Zn-G and (c) Zn-C-G as photocatalysts. (d) Plots of 200

absorbance of the methyl orange solutions at different time intervals.

## **Chapter-7: Cd(II)-Nucleobase Coordination Polymer Hydrogels for the Generation of CdS Quantum Dots**

- Figure 7.1** Digital images, TEM and SEM images of Cd-T and Cd-U hydrogels. 211
- Figure 7.2** (a) Powder XRD spectrum and (b) TGA plots of the freeze dried Cd-T and Cd-U gels. 213
- Figure 7.3** Dynamic strain sweep and frequency sweep rheological investigations of Cd-T and Cd-U hydrogels. 214
- Figure 7.4** (a) FTIR spectrum of pure T and Cd-T and (b) FTIR spectrum of pure U and Cd-U. 215
- Figure 7.5** Digital images of (a) Cd-A, (b) Cd-G precipitate and (c) Cd-U clear solution. 215
- Figure 7.6** FESEM images of precipitates obtained upon the addition of  $\text{Cd}(\text{NO}_3)_2$  to an alkaline solution of (a) adenine and (b) guanine. (c) FESEM image of the clear solution containing Cd-cytosine complex and (d) magnified SEM image of the rod like particles formed in the clear solution of Cd-cytosine. 216
- Figure 7.7** (a) and (b) FESEM images of the Cd-T-U hydrogel, (c) powder XRD spectrum and (d) TGA plot of the Cd-T-U hydrogel respectively; inset in (a); digital image of the Cd-T-U hydrogel. 217
- Figure 7.8** (a) Amplitude sweep experiment and (b) frequency sweep experiment at a constant strain of 1% for the Cd-T-U gel. 218
- Figure 7.9** Digital images of *in situ* formed CdS quantum dots in (a) Cd-T gel and (b) Cd-U gel, when observed under UV light of wavelength 365 nm. (c) Fluorescence emission spectrum of CdS quantum dots formed within the Cd-T and Cd-U gels ( $\lambda_{\text{ex}}=380$  nm). 219
- Figure 7.10** (a) and (b) TEM and HRTEM images of CdS nanoparticles 220

formed in the Cd-T gel respectively. (c) and (d) TEM and HRTEM images of CdS nanoparticles formed in the Cd-U gel respectively.

**Figure 7.11** Time dependent fluorescence emission spectrum of CdS 221 nanoparticles formed within (a) Cd-T gel and (b) Cd-U gel.

**Figure 7.12** Time dependent TEM studies for the growth of CdS 222 nanoparticles within Cd-T and Cd-U hydrogels

## LIST OF SCHEMES

### Chapter-1: General Introduction and Background

- Scheme 1.1** Scheme for the proposed signal generation mechanism by means of enzyme guided crystal growth. 4
- Scheme 1.2** Schematic representation of the assembly of coordination polymers showing 1D, 2D and 3D polymers. 8
- Scheme 1.3** Schematic illustration of the basic structure of a naturally occurring amino acid, a dipeptide and nucleobases as well as nucleotides. 12
- Scheme 1.4** Schematic illustration of the formation of red emitting Au nanoclusters using bovine serum albumin. 22

### Chapter-2: Enzymes as Bionanoreactors: Glucose Oxidase for the Synthesis of Catalytic Au Nanoparticles and Au Nanoparticle-Polyaniline Nanocomposite

- Scheme 2.1** Schematic representation of the use of glucose oxidase for the synthesis of Au NPs as well as Au NP-GOx nanocomposite. 55
- Scheme 2.2** Scheme for the reduction of *p*-nitrophenol to *p*-aminophenol by NaBH<sub>4</sub> with Au NPs synthesized using GOx acting as catalyst. 58
- Scheme 2.3** Scheme for the blocking of thiol groups in proteins by using DTNB. 63

### Chapter-3: Biogenic Growth of Alloys and Core-shell Nanostructures Using Urease as a Nanoreactor at Ambient Conditions

- Scheme 3.1** Schematic representation of the use of urease as a nanoreactor for the formation of metallic as well as core-shell nanostructures 82

### Chapter-4: Catalytic Activity of Various Pepsin Reduced Au Nanostructures Towards Reduction of Nitroarenes and Resazurin

- Scheme 4.1** Scheme for the reduction of weakly fluorescent resazurin to the highly fluorescent resorufin by NH<sub>2</sub>OH.HCl catalyzed by various 130

Au nanostructures synthesized using pepsin.

**Chapter-5: Ag(I) Ion Mediated Self-Assembly of Nucleobases Towards the Generation of Coordination Polymer Hydrogels**

**Scheme 5.1** Chemical structures of the five nucleobases found in DNA and RNA 150

**Scheme 5.2** Schematic illustration of the chemical response of the Ag-nucleobase gels towards different chemicals. 167

**Chapter-7: Cd(II)-Nucleobase Coordination Polymer Hydrogels for the Generation of CdS Quantum Dots**

**Scheme 7.1** Schematic for the generation of coordination polymer hydrogel using thymine and uracil as ligands and  $\text{Cd}(\text{NO}_3)_2$  as metal salt. 210

## LIST OF TABLES

### Chapter-5: Ag(I) Ion Mediated Self-Assembly of Nucleobases Towards the Generation of Coordination Polymer Hydrogels

<b>Table 5.1</b>	Table for the interaction of Ag <sup>+</sup> ions and adenine at various Ag <sup>+</sup> :adenine molar ratio.	152
<b>Table 5.2</b>	Binding energy of (1) silver with nucleobases (first two rows) with and without nitrate, (2) silver with nitrate (last two rows) when bound to nucleobases and binding energy of pure AgNO <sub>3</sub> .	171



## ACRONYMS

NPs	Nanoparticles
pH	The negative logarithm of hydronium-ion concentration ( $-\log_{10} [\text{H}_3\text{O}^+]$ )
UV-Vis	UV-Visible Spectroscopy
FTIR	Fourier Transform Infrared
XRD	X-ray diffraction
PXRD	Powder X-ray diffraction
TEM	Transmission Electron Microscope
HRTEM	High Resolution Transmission Electron Microscope
SEM	Scanning Electron Microscope
FESEM	Field Emission Scanning Electron Microscope
XPS	X-ray Photoelectron Spectroscopy
TGA	Thermogravimetric Analysis
NMR	Nuclear Magnetic Resonance
CD	Circular Dichroism
EDX	Energy Dispersive X-ray spectroscopy
GOx	Glucose Oxidase
Asp	Aspartic acid
Cys	Cysteine
GMP	Guanosine-5'-monophosphate
DNA	Deoxyribonucleic acid
RNA	Ribonucleic acid
FAD	Flavin adenine dinucleotide
PANI	Polyaniline
DMF	N, N'Dimethylformamide
MOFs	Metal-Organic Frameworks
CPPs	Coordination Polymer Particles
DFT	Density Functional Theory

$G'$	Storage Modulus
$G''$	Loss Modulus
A	Adenine
G	Guanine
C	Cytosine
T	Thymine
U	Uracil

## NOMENCLATURE

$\lambda$	Wavelength
$\varepsilon$	Extinction coefficient
$\alpha$	Alfa
$\beta$	Beta
$\gamma$	Gamma
$\pi$	Pi
$\Phi$	Fluorescence quantum yield
$\sigma$	Sigma
$\text{\AA}$	Angstrom
nm	Nanometer
$\mu\text{m}$	Micrometer
cm	Centimeter
$^{\circ}$	Degree
$^{\circ}\text{C}$	Degree Centigrade
mmol	Millimol
mL	Milliliter
$\mu\text{L}$	Microliter
a. u.	Arbitrary Unit
cps	Counts Per Second

# Chapter 1

## General Introduction and Background

### 1.1 Introduction

Nature offers an ideal platform for the generation of functional materials without imposing any limitations or design constraints through the plethora of biomolecules that can interact or couple with metals to generate a myriad of materials with diverse technological relevance. Nature itself uses the perfect match of metals and ligands with perfect geometries for the generation of molecules known as metallobiomolecules.<sup>[1]</sup> The omnipresence of metals in biosystems are critical for several important functions such as oxygen management (hemoglobin, myoglobin, hemocyanin etc), electron carriers (cytochromes, iron- sulphur proteins) or metal management (ferritin, transferrin, ceruloplasmin) etc.<sup>[1-4]</sup> The role of metals in these molecules has been described as structural or functional. In the former the metal ion helps to stabilize the structure of the metallobiomolecule, while in the latter it is involved in the reactivity of the bio-site. The interaction of metals with biomolecules is a complex yet interesting area of research, not only for understanding the various biological processes but also for the development of bioinspired strategies for important functional materials. The evolution of a metal in a living organism occurs by its interaction with the highly complex bio-ligand coordinating environment.<sup>[5]</sup> Since the bio-ligands possess electron donating coordination sites, they play an essential role in the transport, take up and storage of essential metals.<sup>[2,3]</sup> The importance of metal-biomolecule interactions can be understood from the fact that several important biological processes such as respiration, photosynthesis etc. require the interaction of metal ions with biological ligands. Specific interactions of metal ions with proteins play a very important role in the functioning of the protein. The binding of some metal ions increases the stability of proteins or protein domains. Some metal ions can regulate various cell processes being first, second or third messengers.<sup>[5,6]</sup> Metal ions are an integral part of many enzymes and are indispensable in many catalytic reactions.

## 1.2 Hybrid organic-inorganic functional materials

Functional materials are defined as any class of materials which possess particular native properties and functions of their own.<sup>[7]</sup> As the term suggests, organic-inorganic functional materials are hybrid materials, composed of an inorganic part as well as an organic part, with some functional value.<sup>[8]</sup> In the present day research, the term “functional” is often used in combination with newly synthesized materials to showcase their importance for various applications. Thus an organic-inorganic functional material may also be defined as a hybrid material which is being prepared from a “target motivated” approach by combining organic and inorganic building blocks such that all its properties are adjusted and optimized in a way to serve certain specific purposes.<sup>[7]</sup> The great versatility of organic-inorganic hybrids lies in the range of properties afforded by the combination of organic and inorganic constituents and in the multiple length scales - from atomic through molecular and mesoscopic to micro- and macroscopic - over which the chemical interactions and structure of the materials may be controlled.

The function of a hybrid material depends on several parameters. One and the most important among those parameters is the size and shape of the hybrid materials, as many hybrid functional materials such as semiconductor quantum dots or noble metal nanoparticles/nanoclusters (metals being the inorganic part and the capping agent being the organic part) display functional properties only when in a particular size range or morphology. The introduction of porosity into a hybrid coordination material such that its accessible surface area can be maximized is another way to enhance the function of an organic-inorganic hybrid material.<sup>[7,9]</sup> Indeed, the introduction of small pores into such materials gives rise to several important functions in it, which is otherwise absent.

Nanotechnology and biotechnology are two fields of importance which are merging.<sup>[10]</sup> While the former is mainly associated with the synthesis of materials in the nanometer dimension with variable size, shapes, chemical compositions and controlled dispersity, the latter exploits the extraordinary properties of biomolecules to solve significant medical, chemical and engineering problems. Biomolecules, ranging from simple molecules such as amino acids, peptides, nucleobases and nucleotides to complex entities such as proteins and enzymes possess several functional groups that

---

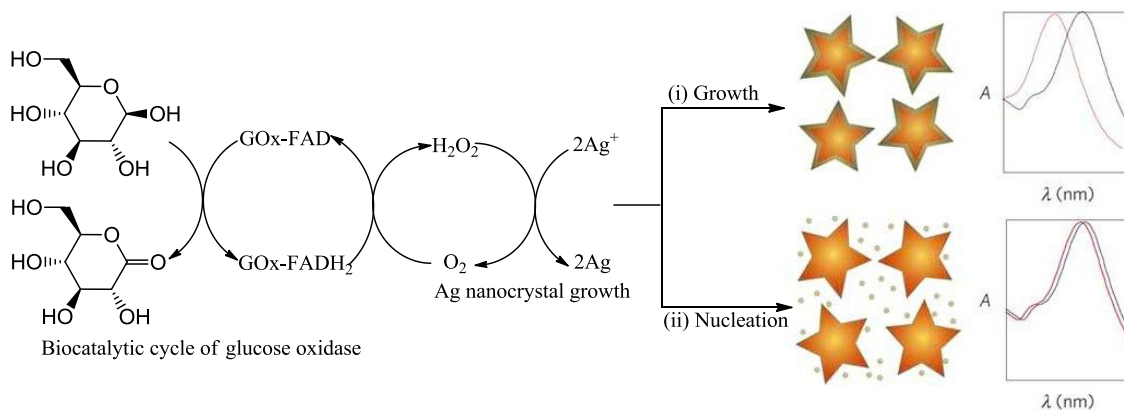
allow coordination with metal ions giving rise to metal- biomolecule hybrids that serve as functional materials for various applications. The present day nanotechnology focuses on the development of two classes of hybrid materials, the first being the inorganic nanoparticles (metallic and semiconductor nanoparticles), where the inorganic component is metal and the organic component is the capping agent/stabilizer and the second being the ordered nanoscale metal organic frameworks, better known as coordination polymer particles, where metal ions serve as inorganic component, while the ligands coordinating to the metals are organic in nature.

### **1.2.1 Metallic Nanoparticles**

A nanoparticle or a nanoscale material is any material which has at least one dimension less than 100 nm. The research on nanoparticles has gained tremendous attention because of their unexpected but valuable physico-chemical properties.<sup>[11,12]</sup> Such interesting properties stem from their nanometer dimension and are often tunable with size and shape. For instance, in semiconductors, the properties result from the further confinement of the electronic motion to a length scale that is comparable to or smaller than the length scale characterizing the electronic motion in bulk semiconducting material.<sup>[13]</sup>

Metal nanoparticles have inspired materials chemists as well as physicists due to their inherent but surprising optical, electronic, magnetic and catalytic properties with enormous potential in many fields of applications.<sup>[11,12,14-16]</sup> As their physicochemical properties are a result of particle size, shape and inter-particle distance,<sup>[17,18]</sup> the properties of NPs are distinctly dissimilar from those of bulk materials and from those of molecular compounds. Among the metallic nanoparticles, noble metal nanoparticles have attracted immense interest due to their optical properties. The miniaturization of noble metals into nanoscale materials results in a new and very strong absorption, arising from the collective oscillation of the electrons in the conduction band from one surface of the particle to the other. This oscillation has a frequency that absorbs the visible light and is called surface plasmon resonance.<sup>[19]</sup> Due to this phenomenon the nanoparticles of coinage metals (gold, silver and copper) exhibit distinct colors and hence have been used as sensors for heavy metals as well as biomolecules.<sup>[20-26]</sup> Such

colorimetric detection of analyte is based on the shift in the absorbance of the colloidal particles that can be modified through changes in the size and shape of the particles or in their local environment. For example, the specific activity of an enzyme on a substrate can result in the formation of aggregates of the particles, leading to a red shift in the absorption maximum or can even result in the dispersion of agglomerated particles, leading to a blue shift in the absorption maxima, thus forming the basis for the detection of such biomolecules. For example, a glucose oxidase plasmonic sensor was developed by the reduction of  $\text{Ag}^+$  ions using biocatalytically generated  $\text{H}_2\text{O}_2$  on preformed gold nanostars that act as plasmon sensors.<sup>[25]</sup> This method could be used for the sensing of glucose oxidase at lower concentrations (scheme 1.1).



**Scheme 1.1.** Scheme for the proposed signal generation mechanism by means of enzyme guided crystal growth. Glucose oxidase generates  $\text{H}_2\text{O}_2$  which reduces  $\text{Ag}^+$  ions to grow a thin layer of silver coating over the plasmonic Au nanostars; (i) at low concentrations of glucose oxidase the rate of nucleation is slow, which favors the growth of silver layer over the nanosensors, leading to a large blue shift in the LSPR of the plasmonic nanosensors; (ii) At higher concentrations of glucose oxidase the fast crystal growth induces the formation of Ag nanocrystals and hence lesser amount of Ag is deposited on the nanosensors, which results in a smaller variation of the LSPR of the nanosensors. [Adapted from reference 25].

When the concentration of the enzyme is low, the lower amount of generated  $\text{H}_2\text{O}_2$  dictates slow crystal growth conditions, leading to the formation of homogeneous layer of silver on the gold nanostars as seeding points, resulting in a blue shift of the localized surface plasmon resonance of the gold nanostars. On the other hand, at higher concentrations of glucose oxidase, the abundant reducing agent favors nucleation rather than epitaxial growth, resulting in the formation of free-standing silver nanocrystals. Thus, a lesser amount of silver is deposited on the nanosensors, leading to a

significantly lower shift in the plasmon resonance band compared to glucose oxidase at lower concentrations. In a similar work, the same group used Au nanoparticles that aggregated upon the functionalization by the tripeptide Fmoc-Gly-Phe-Cys-NH<sub>2</sub> for the sensing of the enzyme thermolysin.<sup>[26]</sup> The hydrolysis of the amide bond of the tripeptide was catalyzed by thermolysin and resulted in the dispersion of the Au nanoparticles, which could be seen visually.

The decrease in the size of the particles to the nanometer regime results in an increase in their surface area to volume ratio, accounting for several improved properties in the nanoparticles, including the catalytic activity as compared to the bulk materials.<sup>[12,14-16]</sup> The properties of the metallic nanoparticles are largely dependent on their size and shape.<sup>[19,27]</sup> The archetypal example is color tuning of the metallic nanoparticles and hence their absorption maximum upon simple variation of their size (figure 1.1).

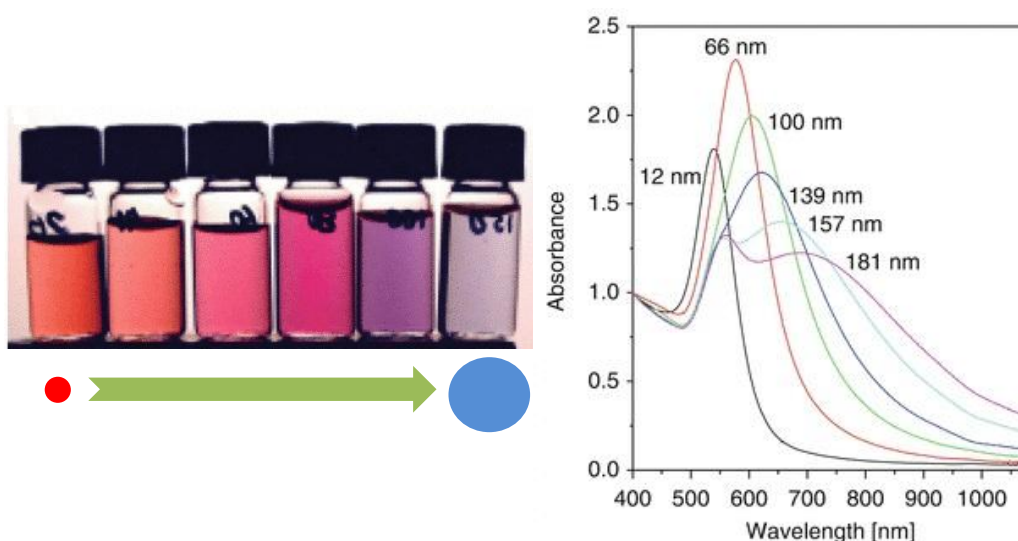


**Figure 1.1.** Unique optical properties of gold nanoparticles, showing a variation in color of the solution and hence the absorption maximum upon change in the size of the nanocrystals. As the size of the nanoparticles increases the color of the solution changes from red to blue and the absorption maximum shifts towards red region [Adapted from reference 27].

Again, in case of noble metal nanoparticles such as Au, Ag, Pt or Pd, the dependence of shape is particularly evident. For example, whereas highly symmetrical, spherical Au and Ag nanoparticles exhibit a single scattering peak, nanocrystals with anisotropic shapes such as rod, triangle, plates and cubes exhibit multiple scattering in

the visible region due to highly localized charge polarizations at the corners and edges.<sup>[28,29]</sup> Further, the chemical reactivity of the nanocrystals is also highly dependent on their surface morphology. The bounding facets of the nanocrystal, the number of step edges and kink sites, as well as the surface area to volume ratio can dictate unique surface chemistries.<sup>[28-31]</sup> Consequently, Pt and Pd nanocrystals exhibit shape and size dependent catalytic properties that may prove useful in achieving highly selective catalysis.<sup>[32]</sup> Therefore synthesis of metallic nanoparticles with controlled size and desired shape is highly appealing.

A wide variety of synthetic methods have been employed for the growth of nanoparticles, which can be divided into three main types:<sup>[15]</sup>

- (i) Grinding method,<sup>[15]</sup> which involves wet and dry grinding, reactive grinding etc.
- (ii) Gas phase methods<sup>[33]</sup> such as chemical vapor deposition, laser ablation deposition, sputtering techniques etc.
- (iii) Liquid phase syntheses,<sup>[34]</sup> which involves forced hydrolysis, hydrothermal synthesis, sol-gel process, microemulsion method etc.

Of the three synthetic methods, the liquid phase synthesis is the most widely used by the chemists, because the size of the particles and agglomeration behavior can be controlled using this method, which are difficult in the other two methods. The reactive surfaces can be saturated with functionalized organic molecules, surfactants, dendrimers or polymers as stabilizers immediately after nucleation, thus providing a precise control over the size of the nanoparticles formed.

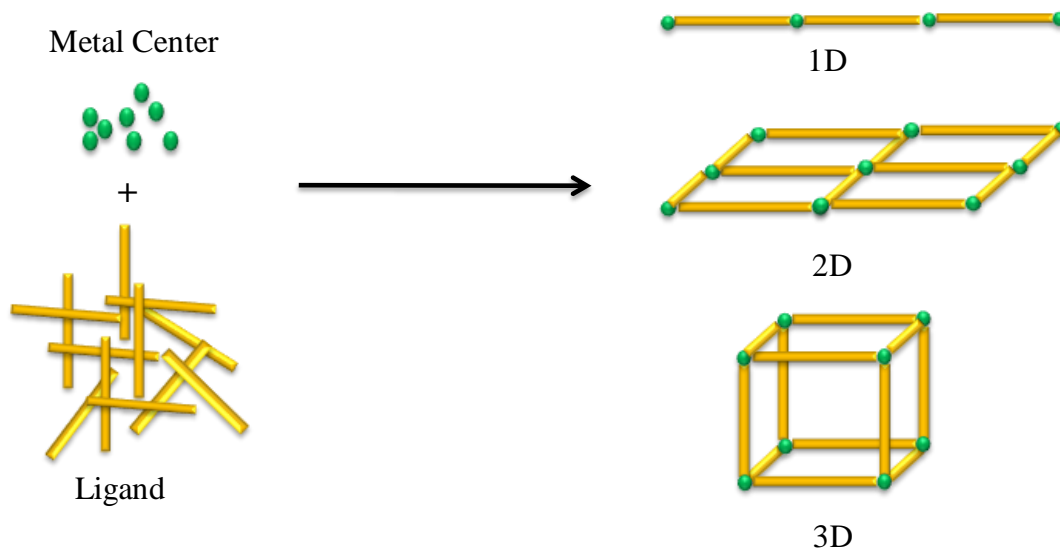
The procedures for the formation of shape controlled nanostructures are however limited.<sup>[19,35-39]</sup> Structures other than spheres form as a result of specific interaction of the capping agents with different growing faces of the particles.<sup>[19,38]</sup> Nevertheless, the use of a template provides a precise control over the final morphology of the nanostructures. Templates provide a constrained environment during the nanoparticle growth and thus shapes can be tuned according to the template.<sup>[38]</sup> Commonly used templates are porous alumina, polycarbonate membranes, carbon nanotubes and micelles.<sup>[40-43]</sup> However, the presence of templates does not produce 100% shape monodispersity; rather, a significant fraction of thermodynamically

favorable spheres are also formed.<sup>[38]</sup> In addition, soft templates such as micelles may not be stable at higher temperatures, and thus the template may not function. Therefore, engineering of monodispersed nanoparticles with precise and controlled size as well as morphology has been a hot topic of research.

Among various newly developed nanostructured materials, a new class of metallic nanoparticles called metal nanoclusters has attained tremendous research interest in the last few years because of their unique optical and photophysical properties as well as low toxicity and high biocompatibility.<sup>[44-52]</sup> Metal nanoclusters comprise of a few hundreds of metal atoms or less, and represent an intermediate state of matter between isolated molecules and large nanoparticles (nanoparticles with diameter  $> 2$  nm).<sup>[44,45]</sup> Since the size of the metal nanoclusters is comparable to the Fermi wavelength of electrons, hence the continuous density of states of the particles breaks into discrete energy levels. Consequently, several unique optical as well as electronic properties such as luminescence, magnetism, HOMO-LUMO transitions, quantized charging etc. arise.<sup>[45,46,48]</sup> These properties are clearly different from the larger metal nanoparticles having size in the range of 2-100 nm. Due to their facile synthesis, excellent stability and good biocompatibility, metal nanoclusters have been studied extensively in the recent years.

### **1.2.2 Coordination Polymers**

Coordination polymers may be defined as hybrid organic-inorganic compounds extended in one, two or three dimensions through coordination bonds<sup>[53-55]</sup> (scheme 1.2). In other words they are polymeric solids held by coordination bonds between metal centers and organic ligands forming infinite arrays. The final structure of a coordination polymer depends mainly on the nature and coordination geometry of the metal ions as well as the number of binding sites and the geometry of the organic ligands.<sup>[55]</sup> Further, the weak interactive forces such as  $\pi$ - $\pi$  stacking, hydrogen bonding or van der Waals interaction may also have a significant impact on the final geometry and structure of the coordination polymers.



**Scheme 1.2.** Schematic representation of the assembly of coordination polymers showing 1D, 2D and 3D polymers.

In the early 90's Prof. Robson and his co-workers first proposed that coordination polymers could be generated by simple connection of metal centers having tetrahedral or octahedral array of valences with organic linkers.<sup>[56]</sup> They proposed that following their approach, functional materials with fascinating properties such as catalysis, porosity etc. could be engineered. At that time, probably none had imagined that Prof. Robson had introduced a concept that would open a new world not only in the field of chemistry but also nanotechnology and materials science. Since the first work by Prof. Robson, thousands of new coordination polymers are synthesized due to their facile synthesis and applications.<sup>[57-59]</sup> Following the methodology developed by Robson and co-workers, it has been possible to engineer crystalline materials with empty spaces (porous materials), more commonly known as metal organic frameworks, which find use in a myriad of applications.

A new class of polymers, known as coordination polymer particles has emerged as a front runner in the group of coordination polymers during the last decade due to their broad range of potential applications such as catalysis, sensing, tissue engineering, data storage, electronics, medical diagnostics as well as drug delivery.<sup>[55,60-70]</sup> Coordination polymer particles (CPPs) having variety of shapes such as rods, tubes, belts, fibers, spheres and tapes can be generated by the simple self-assembly of metal

ions and/or organic ligands. A simple but careful selection of ligands and metal ions can lead to the formation of various shaped coordination polymer particles. Several studies have demonstrated that infinite coordination polymerization of metal ions through organic ligands, followed by precipitation can generate infinite coordination particles (ICPs) of various shapes having nanometer dimensions.<sup>[61,64,66]</sup>

Two classes of particles<sup>[55]</sup> can be generated by the method of infinite coordination polymerization: (i) crystalline particles and (ii) amorphous particles. The first class can be obtained by controlling the crystallization processes in the nanometer scale, which can be achieved by either increasing the rate of nucleation by solvothermal conditions, microwave irradiation, ultrasound, rapid precipitation etc. or by confining the crystallization using a template or an emulsion. On the other hand, the amorphous coordination polymer particles are generally obtained by using biomolecules as ligands because biomolecules are usually flexible molecules and are difficult to crystallize.

### **1.3 Biomolecules for the synthesis of inorganic nanoparticles and coordination polymers**

Both inorganic nanoparticles as well as coordination polymers have been widely studied, mainly due to their distinctive physico-chemical properties and wide range of applications. Although, these functional materials offer several advantages, one drawback which most of these materials suffer is their toxicity, which in principle is due to the synthetic procedure employed for their synthesis.<sup>[45,55]</sup> Most of the reported chemical synthetic routes employ the use of hazardous chemicals and organic solvents, which are not feasible from an environmental point of view and limit their applications in medicine and biology. So, materials scientists have been in pursuit of strategies alternative to the conventional chemical synthesis of hybrid functional materials, to exploit their potential for bio based applications.

Biomolecules provide an excellent strategy for the development of functional materials by providing green, environmentally benign conditions.<sup>[71]</sup> Biological systems can synthesize and assemble a range of inorganic nanomaterials such as amorphous silica (diatoms), magnetite (magnetotactic bacteria) and minerals such as calcite into functional superstructures.<sup>[72-77]</sup> Therefore, understanding the biochemical processes

---

that lead to the formation of nanoscale hybrid materials is potentially appealing as environmental friendly alternatives to chemical methods. The three main steps for the synthesis of functional nanostructured materials that should be evaluated from a green chemistry perspective are the choice of solvent medium used for the synthesis (water), choice of an environmentally benign reducing agent (for nanoparticles) and the choice of a non-toxic material for the stabilization of the nanoparticles.<sup>[78]</sup> In this regard, biomolecules, due to their own nanometer dimension serve as perfect nanoreactors that can facilitate the formation of metal nanostructures through a combination of concerted efforts involving the complex formation, metal ion reduction and protection of the nanocrystals formed against agglomeration. Biomolecules have been extensively used for the synthesis of functional nanoscale materials due to the following reasons:<sup>[45,55]</sup>

- (i) Simple biomolecules such as amino acids, peptides, nucleobases etc. are readily and naturally available at low cost and hence can be used to prepare bulk quantities of materials.
- (ii) Biomolecules, such as amino acids, peptides or nucleic acids, feature rich chemistries in their functional groups, such as amine, thiols, carboxyl, hydroxyl or phosphates and sugars, which can serve as efficient binding sites for metal ions and facilitate the multi directional growth of functional materials in a controlled manner.
- (iii) Biomolecules mediated synthesis of nanoparticles most often occurs in water medium at room or physiological temperatures, without the need for toxic reagents, and hence can lead to biologically compatible materials.
- (iv) Biomolecules can themselves function as both reducing as well as stabilizing agents for nanoparticles.
- (v) Many biomolecules have intrinsic self-assembling properties, which can be used to direct the final structure and properties of functional materials.

Thus, the use of biomolecules for the synthesis of nanoparticles can not only reduce the use of toxic reagents leading to an eco-friendly approach, but also protect them from the deleterious effect of metal toxicity. Further, the use of biomolecules as reducing as well as stabilizing agent for growth of inorganic nanoparticles combines and integrates the unique optical, electronic and catalytic properties of the nanoparticles with the

specific binding, catalytic and recognition properties of functionally active biomolecules in a single entity.<sup>[79]</sup> Nature has endowed us with thousands of biomolecules, whose basic units can be grouped under four main classes: amino acids, lipids, saccharides and nucleic acids<sup>[55]</sup> (figure 1.2). The works in this thesis are based on the use of enzymes (basic unit amino acids) as nanoreactors for the growth of functional metallic nanostructures and nucleobases as ligands for the development of nanoscale coordination polymer particles. The present chapter discusses the history and present work being carried out using these basic units as well as enzymes for the generation of functional inorganic nanostructures as well as coordination polymers.

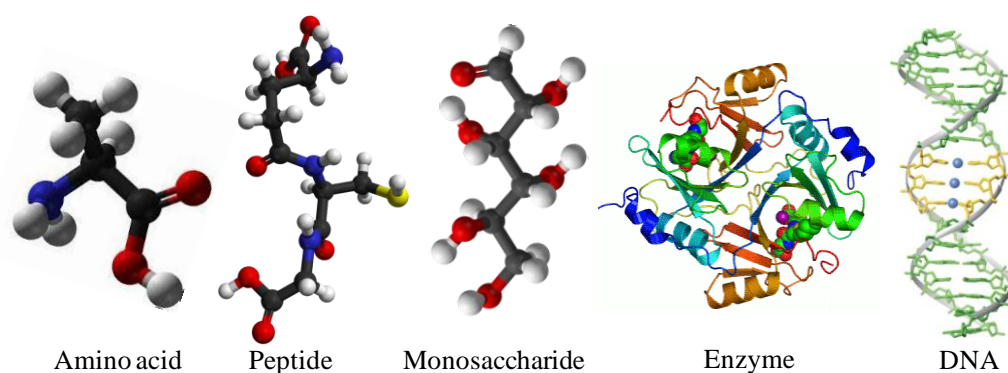
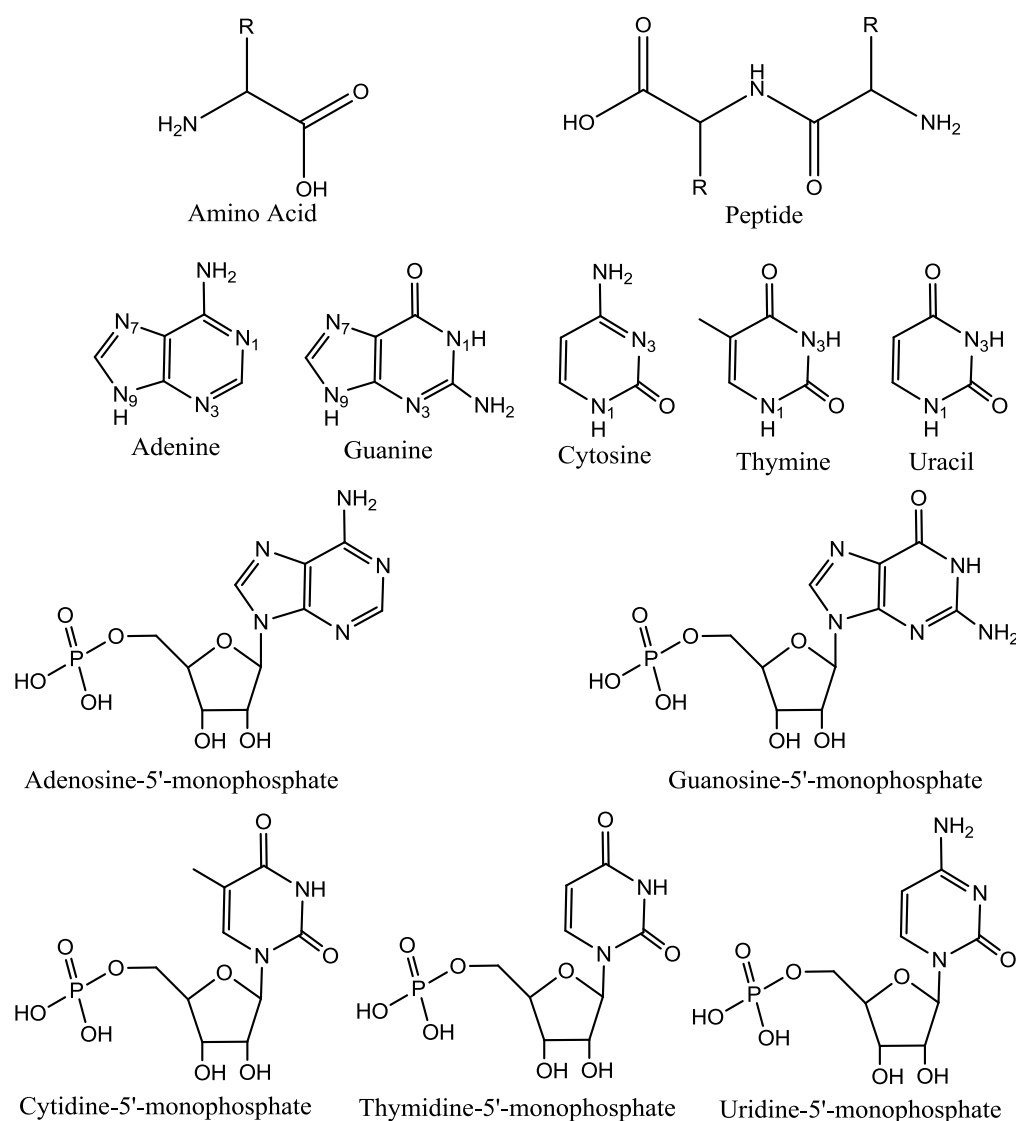


*Figure 1.2. Representation of different families of natural biomolecules present in living beings.*

### 1.3.1 Amino acids, peptides, nucleobases and nucleotides

Amino acids, peptides, nucleobases and nucleotides are considered as elemental molecules of life and are the basic units of almost every biomolecule found in the nature. Amino acids are molecules having a general formula  $\text{NH}_2\text{CHR}\text{COOH}$ . As the formula suggests, amino acids are composed of amine and carboxylic acid group, along with a side chain, which is specific to each amino acid. On the other hand, peptides are short oligomers of amino acids, linked by peptide bonds. The peptide bond is formed by the reaction between the carboxylic group of one amino acid and the amino group of another amino acid, leading to the formation of an amide group, with the loss of a water molecule. Nucleobases and nucleotides are components of the genetic material DNA and RNA. There are five nucleobases found in nucleic acids, namely, adenine, guanine, thymine, cytosine and uracil. The helical structure of the DNA and RNA is a result of the ability of these bases to form base pairs that directly stack upon one another.<sup>[71]</sup> Nucleotides, on the other hand are composed of a nitrogenous base, a pentose sugar and

at least one phosphate group. For the amino acids and peptides, the presence of amino and carboxylic groups, which have known reducing as well as excellent binding ability towards metal ions, makes them ideal nanoreactors for the growth and development of functional nanomaterials. On the other hand, the presence of several metal coordinating sites in the nucleobases and the added advantage of phosphate groups and a sugar moiety in nucleotides makes them attractive candidates for the fabrication of hybrid organic-inorganic nanomaterials such as metallic nanoparticles and coordination polymers.



**Scheme 1.3.** Schematic illustration of the basic structure of a naturally occurring amino acid, a dipeptide and nucleobases as well as nucleotides.

Several amino acids such as tyrosine, arginine, glutamic acid, cysteine, lysine etc. have been successfully employed as reducing as well as stabilizing agent for the growth of metallic nanoparticles.<sup>[80-86]</sup> Amino acids have been used not only for the synthesis of spherical nanoparticles, but also for the synthesis of nanostructures with shapes such as triangles, plates, ribbon and wires.<sup>[87,88]</sup> In 2004, Shao *et al.* reported that whereas lysine, arginine and tyrosine gave spherical Au nanoparticles, using aspartic acid as a reducing as well as stabilizing agent resulted in single crystalline nanoplates with thickness less than 30 nm.<sup>[87]</sup> They argued that the formation of triangular plates, when aspartic acid was used was a result of the specificity of aspartate for binding to facets other than {111}. Similarly, several peptides by virtue of the presence of functional groups such as amino, carboxylic acid, sulphhydryl etc. serve as excellent reducing and/stabilizing agents for the growth of inorganic nanostructures.<sup>[89-96]</sup> Further the nucleobases and nucleotides have also been used for the growth of several inorganic nanoparticles and nanoclusters.<sup>[97-102]</sup> For example, Jiang *et al.*<sup>[98]</sup> prepared Au nanoclusters with different emissions at different pHs or reaction times using the nucleoside/nucleotide cytidine, cytidine-5'-monophosphate or cytidine-5'-triphosphate at room temperature as template and citrate as the reducing agent (figure 1.3).

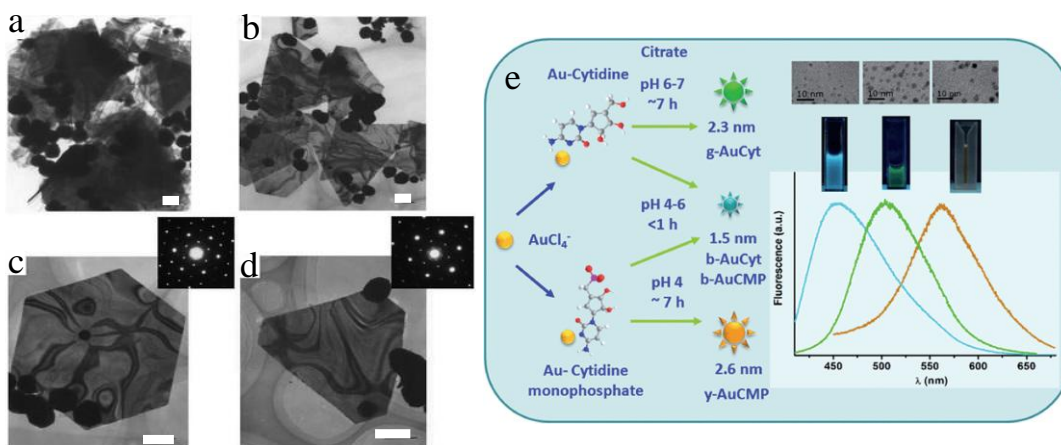


**Figure 1.3.** (a) and (b) TEM images (Scale bars 200 nm) of higher and slightly lower degree assembled nanoplates synthesized using aspartate. (c) and (d) TEM images (Scale bars 200 nm) of individual hexagons and truncated triangular nanoplates. The insets show the selected area electron diffraction patterns, and (e) Schematic illustration for the room temperature syntheses of various colored Au nanoclusters using cytidine/cytidine nucleotides.[Adapted from references 87 and 98].

Since, these biomolecules possess several metal binding sites, such as amino, carboxylate or different ring nitrogen and oxygen atoms, they have also been successfully used as ligands for the generation of coordination polymers. Several metal ions such as Cd(II), Pb(II), Ni(II), Zn(II), Cu(II), Co(II) have been used for the generation of coordination polymers using aspartic acid, glutamic acid, valine and isovaline and different peptides as ligands.<sup>[103-120]</sup> In an excellent work, Imaz *et al.* have used aspartic acid for the growth of chiral copper aspartate nanofibers.<sup>[108]</sup> They have shown that nanofibers with lengths several millimeters long (up to 1 cm) could be generated by simple addition of an aqueous solution of Cu(NO<sub>3</sub>)<sub>2</sub> to a solution of deprotonated aspartic acid (ethanol-water mixture). Further, nanofibers with shorter diameters in the form of hydrogel could be generated by a fast addition of the copper salt to an aqueous aspartate solution. According to them, the copper coordinates to the  $\alpha$ -carboxylate group of the amino acid, leading to the formation of Cu-aspartate coordination polymer nanofibers. Similarly, Manton *et al.* have used a tripeptide ValValGlu to construct submicron rod like coordination polymer particles by combining the tripeptide with Cu(II) and Ca(II) at room temperature and at 80 °C respectively.<sup>[120]</sup> Nucleobases and nucleotides in particular, have been used as excellent ligands for the generation of coordination polymers due to the versatility of bonding with metal ions they offer.<sup>[121-132]</sup> Wei *et al.* used adenine to construct adenine-Au hybrid spherical submicron particles at room temperature.<sup>[123]</sup> They observed that simple mixture of the precursor aqueous solutions of adenine and HAuCl<sub>4</sub> resulted in the spontaneous formation of the hybrid colloidal particles with a diameter ~300 nm. They suggested that the coordination interactions of Au (III) and the N atoms in adenine could produce particles with sizes 2-3 nm. These small particles could then evolve into submicrometer spherical particles via noncovalent interactions (i.e. aromatic  $\pi$ - $\pi$  stacking of adenine), and finally these submicrometer particles could be connected together through fusion of the fringes of every independent particle. Similarly, Kimizuka and co-workers synthesized functional fluorescent ~40 nm spherical amorphous coordination polymer particles that served as MRI contrast agents just by mixing the nucleotide adenosine-5'-monophosphate and lanthanide ions such as Gd<sup>3+</sup>, Tb<sup>3+</sup> etc.<sup>[128]</sup>

---

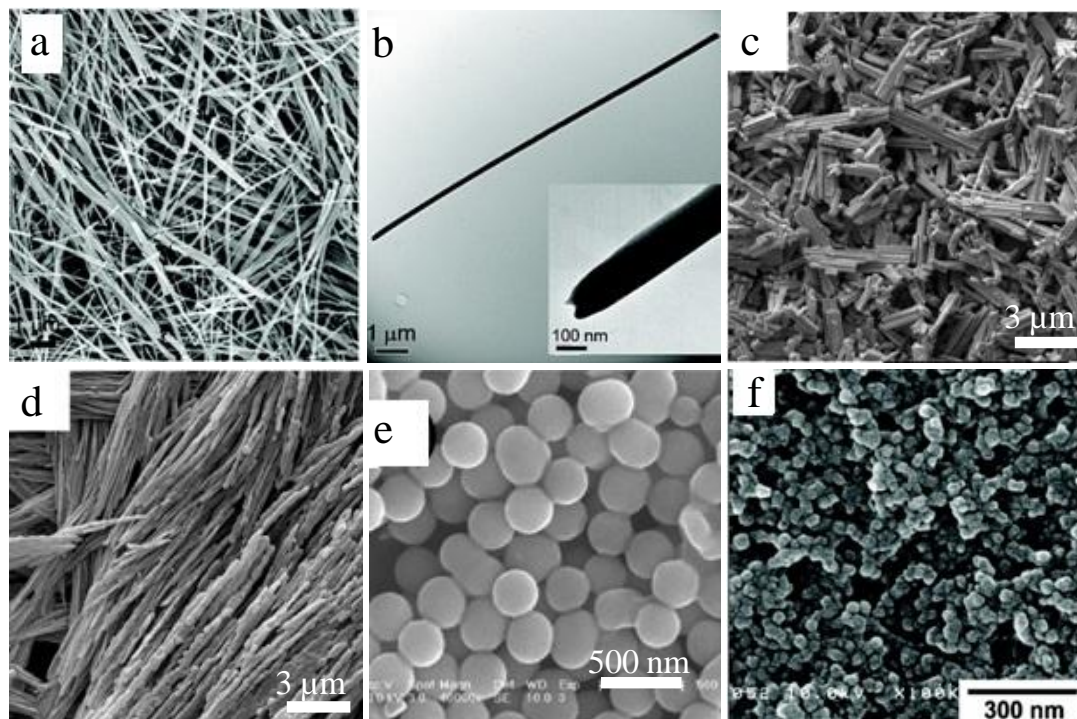


**Figure 1.4.** (a) and (b) FESEM and TEM image of Cu-aspartate nanofibers, (c) and (d) SEM images of rod like coordination polymer particles obtained by the reaction of the tripeptide ValValGlu with Ca(II) and Cu(II) respectively, (e) FESEM image of hybrid adenine-HAuCl<sub>4</sub> microparticles formed through supramolecular interactions and (f) SEM image of 5'-AMP/Gd<sup>3+</sup> nanoparticles prepared in water by simple addition of Gd<sup>3+</sup> ions to a solution of AMP. [Adapted from references 108, 120, 123 and 128].

### 1.3.2 Microbes

Microorganisms are often exposed to extreme environmental conditions, which forces them to develop a specific defense mechanism to suppress the stress induced by the extreme conditions. One such condition, which the microorganisms often encounter, is the toxicity of foreign metal ions or metals.<sup>[133]</sup> Microorganisms often reduce or completely eliminate the toxicity of metal ions by changing the redox state of the metal ions and/or precipitation of the metals intracellularly, which forms the basis of many important applications of microorganisms such as bioleaching, bioremediation, microbial corrosion, as well as the synthesis of nanoparticles.<sup>[133,134]</sup>

Different microorganisms ranging from bacteria, viruses, fungi, actinomycetes and yeasts have been used to synthesize several nanoparticles ranging from metallic and semiconductor to magnetic nanoparticles, either intracellularly or extracellularly.<sup>[134-153]</sup>

It has been demonstrated that placing the bacteria *Pseudomonas stutzeri* AG259 (isolated from a silver mine) in a concentrated aqueous solution of  $\text{AgNO}_3$ , resulted in the reduction of the Ag ions and formation of silver nanoparticles of well-defined size and distinct morphology such as equilateral triangles and hexagons of size 200 nm, within the periplasmic space of the bacteria.<sup>[136]</sup> Moving a step further, they have shown that biocomposites of nanocrystalline silver and the bacteria may be thermally treated to yield a carbonaceous material with interesting optical properties for potential application in functional thin film coatings.<sup>[137]</sup> In another report, Dameron *et al.* have used the yeasts, *Candida glabrata* and *Schizosaccharomyces pombe* for the growth of CdS quantum dots.<sup>[153]</sup> Sastry and co-workers have performed extensive studies on microorganism mediated growth of nanoparticles. They have shown that the fungus *Fusarium Oxysporum* can be successfully employed for the synthesis of several nanoparticles including gold, silica, titania, zirconia, magnetite, barium titanate as well as CdS nanoparticles under ambient conditions.<sup>[145-151]</sup> They speculated that the extracellular proteins secreted by the fungus provided a reducing, hydrolyzing as well as confining template for the synthesis of these nanoscale particles.<sup>[145-148]</sup>

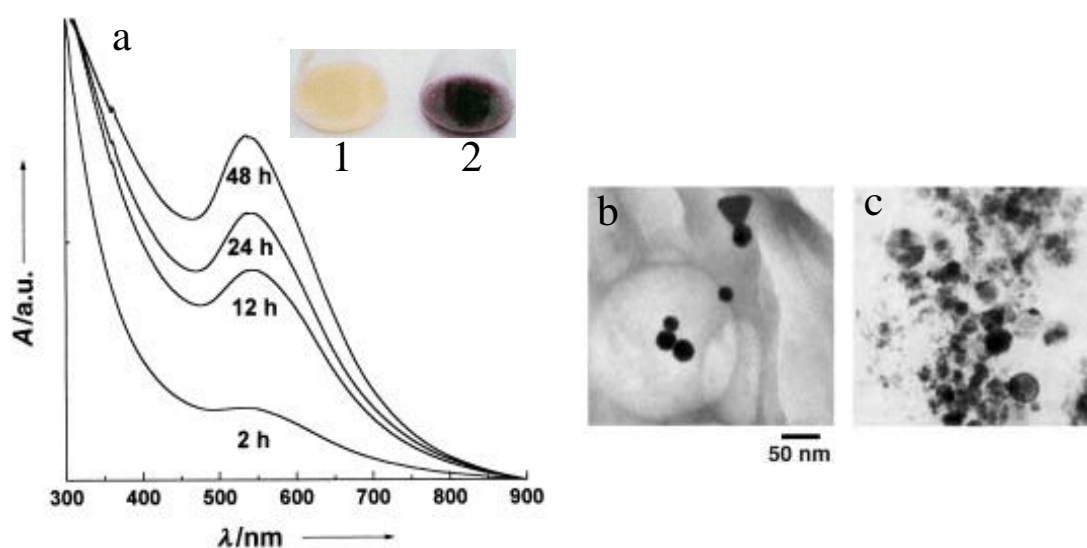


**Figure 1.5.** (a) Time dependent UV-visible spectrum for the growth of Au nanoparticles, using the fungi *Fusarium Oxysporum*; Inset Digital images of *Fusarium Oxysporum* (1) before and (2) after exposure to  $\text{AuCl}_4^-$  ions for 72 hours, (b) and (c) corresponding TEM images of the Au nanoparticles; scale bar 50 nm. [Adapted from reference 146].

Although the detailed and precise mechanism for the formation of nanoparticles using these microorganisms is not yet clear, it has been hypothesized that the formation of nanoparticles by such microorganisms occurs either intracellularly or extracellularly.<sup>[134]</sup> In the intracellular synthesis of nanoparticles, the cell wall of the microbes plays an important role. This method involves a special ion transport in the microbial cell, where electrostatic interaction between the positively charged metal ions and the negatively charged cell wall of the microorganisms occur. The enzymes present within the cell wall reduce the metal ions to nanoparticles and these nanoparticles get diffused off the cell wall.<sup>[134]</sup> The mechanism of extracellular synthesis of silver nanoparticles is generally considered to be nitrate reductase mediated.<sup>[134]</sup> For e.g. nitrate reductase, a NADH dependent enzyme, secreted by the fungus helps in the bioreduction of the metal ions and formation of nanoparticles. A similar mechanism was reported for the extracellular synthesis of gold nanoparticles using the bacteria *Rhodopseudomonas capsulate*.<sup>[138]</sup> The bacterium is known to secrete cofactor NADH, which transfers electrons to the gold ions to reduce them to gold nanoparticles.

### 1.3.3 Enzymes

Enzymes, an important class of biomolecules have been largely studied as catalyst for various complex reactions everywhere in life. They have become very attractive during the last few decades for their use in a wide range of industrial applications including biocatalysis, biosensors, biomedical applications, bioremediations as well as with the objective of reducing energy and raw material consumption and amounts of waste and toxic by-products formation.<sup>[10,154,155]</sup> Recently enzymes have been used in the field of nanotechnology, thanks to their nanometer dimensions and rich functional group chemistry. It has been suggested that since the enzymes would provide a defined number of initiation or reduction sites, the stabilization of metal nanoparticles by enzymes would enable their formation with controlled dimensions and contribute towards our understanding of biomimetic approaches for nanoparticle synthesis.<sup>[10]</sup>

Enzymes due to the presence of several functional groups such as hydroxyls, amines, thiols and carboxylic acid groups have been extensively used as

---

templates/stabilizers for the growth of inorganic nanoparticles.<sup>[79,156-162]</sup> The nanoparticle-enzyme studies have gained tremendous attention because the interaction of nanoparticles with enzymes can often modulate the natural activity of the latter, leading to enhancement, retention or loss in their activity.<sup>[163-170]</sup> For example, Deka *et al.* have shown that by varying the concentration of enzyme and keeping the concentration of citrate stabilized Au nanoparticles constant, the specific activity of  $\alpha$ -amylase could significantly be enhanced.<sup>[163]</sup> They speculated that the attachment of a group of proteins onto a single nanoparticle surface, with their active sites exposed to the medium might have led to the cooperative digestion of the same substrate molecule (starch), which might be the reason for the enhanced activity. Similarly, You *et al.* studied the catalytic behavior of  $\alpha$ -chymotrypsin adsorbed on amino acid functionalized gold clusters towards cationic, anionic and neutral substrates and found that enzyme-nanoparticle composite substrate specificity increased by three folds for cationic species but decreased by 95% for the anionic substrates compared to the free chymotrypsin.<sup>[164]</sup> In another study, Rangnekar *et al.* have reported that the surface functionalization of Au nanoparticles using  $\alpha$ -amylase (used as a reducing and stabilizing agent) led to the preserved activity of the enzyme in the composite for a considerably longer period of time.<sup>[165]</sup> They observed that the hydrolysis was almost complete in about 400 minutes and the rate of digestion of starch by the enzyme-nanoparticle composite was identical to that of free enzyme. Similar retention in enzymatic activity was observed by Brennan and colleagues<sup>[166]</sup> as well as Gole *et al.*<sup>[167]</sup> who researched lipase from *Thermomyces lanuginosus* and aspartic protease from *Aspergillus satoii* stabilized onto Au nanoparticles respectively. Again in some cases the electrostatic or covalent functionalization of enzymes onto Au nanoparticles has led to a loss in the catalytic activity of the enzyme. For instance, Sharma *et al.* showed that using glucose oxidase or urease for the synthesis of metal nanoparticles led to changes in the conformation of the proteins, resulting in a significant decrement in their catalytic activity.<sup>[169,170]</sup> Thus, understanding the mechanism of the nanoparticle induced alteration of the properties of biomolecules is not only central to taking full advantage of nanoscale materials but also important in knowing the implications of manufactured nanomaterials on human health and the environment.

Apart from being used as a stabilizer to prevent the agglomeration of nanoparticles, enzymes have also been used as nanoreactors for the synthesis of nanoparticles.<sup>[171-174]</sup> There are two methodology employed for the use of enzymes for the growth of nanoparticles. The first is the enzyme assisted synthesis in which the enzyme performs its natural activity on the substrate and produces a compound, capable of reduction of metal salts to their corresponding nanoparticles. The second methodology is based on the ability of enzymes to themselves act as a reducing as well as stabilizing agents due to the presence of large number of amino acid residues in the complex three dimensional structures of the enzymes.

Different oxidases generate compounds such as  $H_2O_2$  upon the biocatalyzed oxidation of the corresponding substrates merely in the presence of molecular oxygen, which have capability of reducing metal salts to their corresponding nanoparticles.<sup>[171,175,176]</sup> Willner and co-workers used the  $H_2O_2$  generated in a glucose oxidase stimulated pathway to reduce  $AuCl_4^-$  in the presence of Au NP seeds that acted as catalyst.<sup>[175]</sup> This method led to the successful development of an optical detection pathway for glucose oxidase activity and sensing of glucose. Similarly, they used the *p*-aminophenol generated by the hydrolysis of *p*-aminophenol phosphate using the enzyme alkaline phosphatase for the reduction of  $Ag^+$  on Au nanoparticle seeds to yield Ag nanowires.<sup>[176]</sup>

Enzyme stimulated pathway has been used not only for the generation of metallic nanoparticles, but also for metallic oxide nanoparticles.<sup>[177-180]</sup> Alkaline pH is the favorable condition for the growth of oxide nanoparticles, as the alkaline pH can catalyze the condensation and hydrolysis of the hydroxide intermediate to form the oxide nanostructures. A particular amidohydrolase whose activity has been used for the mineralization of several inorganic oxide nanostructures such as those of Zn, Ti and Fe is the nickel containing enzyme urease.<sup>[177-179]</sup> Urease is involved in the hydrolysis of urea to produce  $NH_3$  and  $CO_2$ . The production of ammonia in the biocatalyzed reaction makes conditions favorable for the growth of oxide nanoparticles. Matsui and co-workers<sup>[177]</sup> have used urease for the growth of semiconductor ZnO nanoshells at room temperature in water (figure 1.6). According to them, at alkaline pH, above the isoelectric point of urease (pI- 4.9), the protein has an overall negative charge and the

---

positively charged  $\text{Zn}^{2+}$  ions electrostatically interact with the protein and result in the formation of  $\text{Zn}(\text{OH})_2$  intermediate. The additional energy required for the dehydration of the hydroxide intermediate to the oxide product is provided due to the “salting out” effect. They hypothesized that the highly ordered and tightly bound layer of water molecules surrounding the protein was disturbed upon binding of  $\text{Zn}^{2+}$  ions to the protein, which resulted in an overall increase in entropy of the system. This increase in entropy was sufficient to convert the  $\text{Zn}(\text{OH})_2$  intermediate to ZnO nanoshells. Using the same methodology and the same enzyme, Kisailus and co-workers synthesized nanocrystalline  $\text{TiO}_2$  under environmentally benign conditions,<sup>[178]</sup> while Shi *et al.* successfully demonstrated the mineralization of magnetic  $\text{Fe}_3\text{O}_4$  nanoparticles.<sup>[179]</sup>

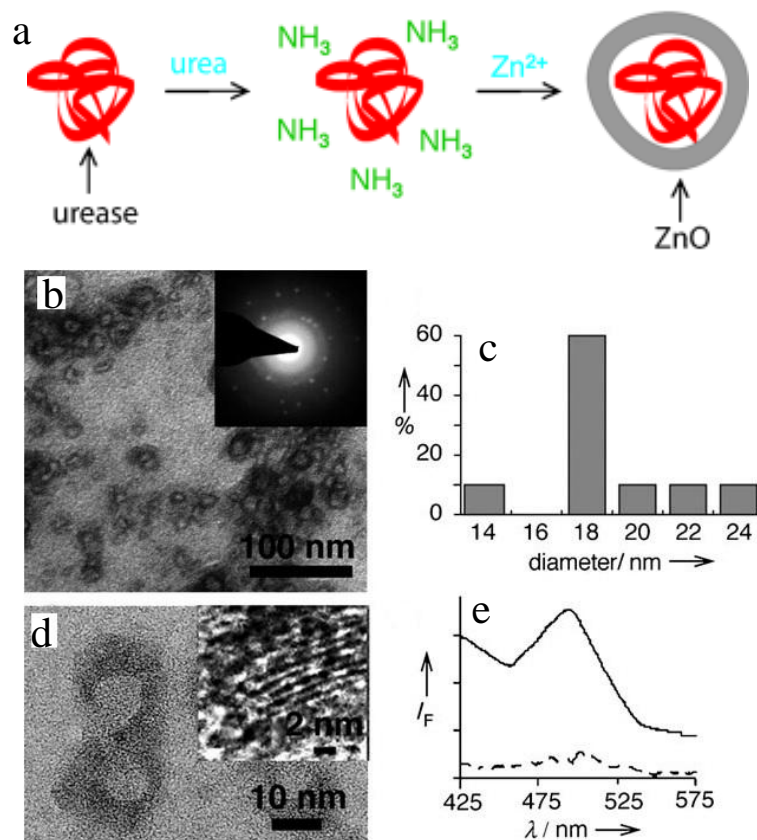


**Figure 1.6.** (a) Schematic for the synthesis of ZnO nanoshells using the enzyme urease, (b) TEM image of the ZnO nanoshells, (c) particle size distribution and (d) HRTEM image of enzyme–ZnO core–shell nanoparticles. Inset: HRTEM image of ZnO nanoshell. (e) Fluorescence spectra of ZnO nanoshell (solid line) and denatured enzyme particles in the presence of ammonia and Zn ions ( $\lambda_{\text{ex}}=390 \text{ nm}$ ). [Adapted from reference 177].

More recently, enzymes have been used in the field of nanotechnology due to their ability to function themselves as reducing as well as stabilizing agents utilizing covalent or usually non-specific routes of attachment.<sup>[165,181-194]</sup> The presence of large number of functional groups in the enzymes makes them attractive candidates for the precise growth and mineralization of nanostructures. Rangnekar *et al.* utilized the enzyme  $\alpha$ -amylase for the reduction as well as stabilization of Au nanoparticles at 37 °C, with the retention in enzymatic activity.<sup>[165]</sup> They investigated and concluded that the two exposed cysteine residues in the enzyme were responsible for the reduction and simultaneous stabilization of the nanoparticles. Similarly, the enzyme bovine serum albumin was used as a reducing as well as stabilizing agent for the growth of anisotropic Au nanoplates.<sup>[181,182]</sup> (figure 1.7)

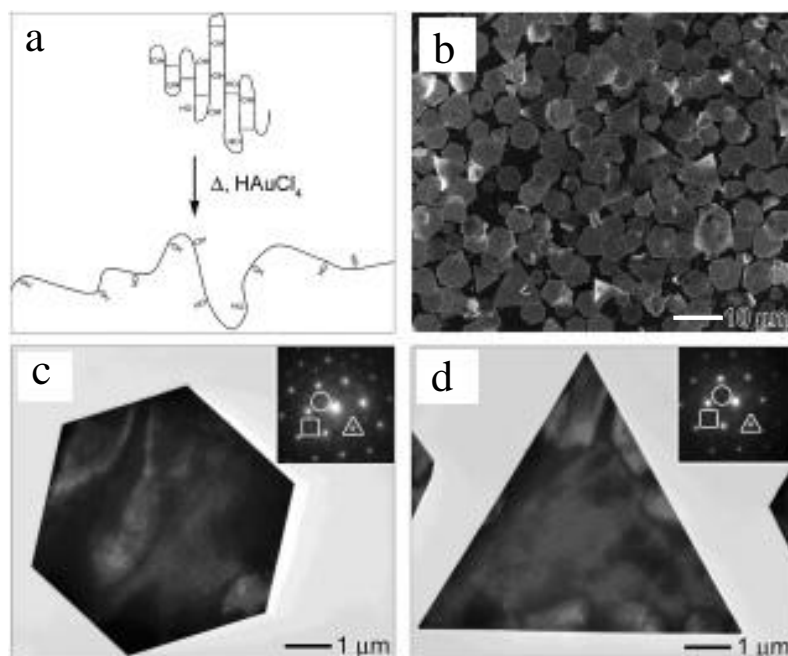
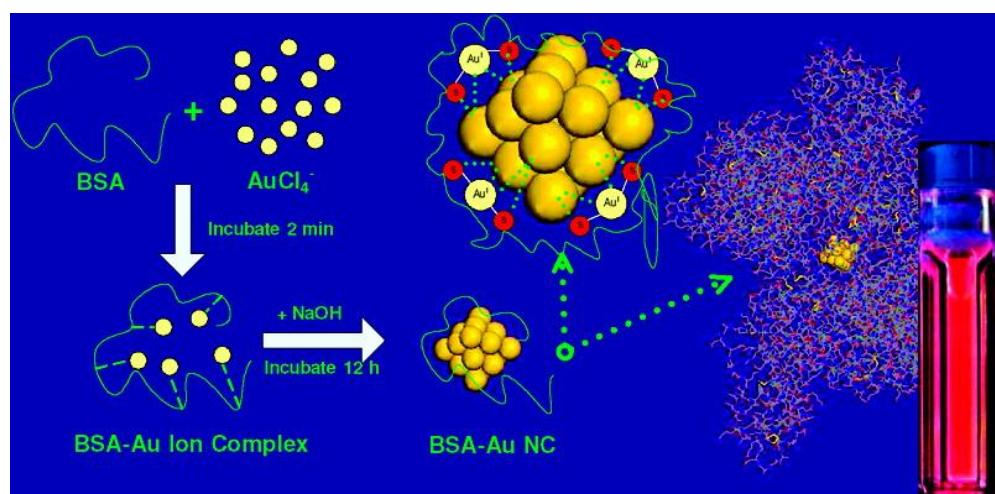


**Figure 1.7.** (a) Illustration of a portion of bovine serum albumin undergoing structural changes upon exposure to heat/ $\text{HAuCl}_4$ . (b) SEM image; Scale bar 10 $\mu\text{m}$ , (c) TEM image; Scale bar 1 $\mu\text{m}$  and (d) TEM image; Scale bar 1 $\mu\text{m}$  of hexagonal and triangular plates synthesized using bovine serum albumin as a reducing and stabilizing agent. [Adapted from reference 181].

According to them, the hydroxyl groups of the amino acids serine and threonine were involved in the reduction as well as stabilization of the nanostructures formed. In a similar study it was observed that the presence of several cysteine residues in the

enzyme urease, which could function as efficient reductant as well as stabilizer, resulted in the formation of metal as well as metallic alloy nanoparticles.<sup>[170]</sup> Further, it was observed that although the catalytic activity of the enzyme was diminished after the synthesis of metal nanoparticles, it was not completely denatured. Hence the partially inhibited catalytic functionality of the enzyme was utilized for the room temperature growth of Au@ZnO core-shell nanostructures.

Among several biomolecules, enzymes have been extensively used for the growth of metal nanoclusters because of the ease of preparation with enzymes.<sup>[186-194]</sup> Xie *et al.*<sup>[187]</sup> for the first time used the commercially available protein bovine serum albumin (BSA) for the growth of red fluorescent Au nanoclusters at physiological temperature of 37 °C with a quantum yield of 6% (scheme 1.4). The first step of the synthesis involved the sequestration and entrapment of Au ions by BSA. The second step was the reduction of Au ions to Au nanoclusters by increasing the pH of the medium to 12.0 at which aromatic amino acid residues such as tyrosine or tryptophan in the protein can reduce the Au ions. The Au nanoclusters formed showed red emission with the maxima at 640 nm, and consisted of 25 atoms of Au which was established by means of MALDI-TOF studies.



**Scheme 1.4.** Schematic illustration of the formation of red emitting Au nanoclusters using bovine serum albumin. [Adapted from reference 187].

In a similar study, Arakawa and co-workers used the enzyme pepsin for the pH dependent synthesis of Au nanoclusters with red, blue and green emissions.<sup>[188]</sup> It was

observed that mere change in pH led to the formation of Au nanoclusters of different sizes and hence different emissions (figure 1.8).

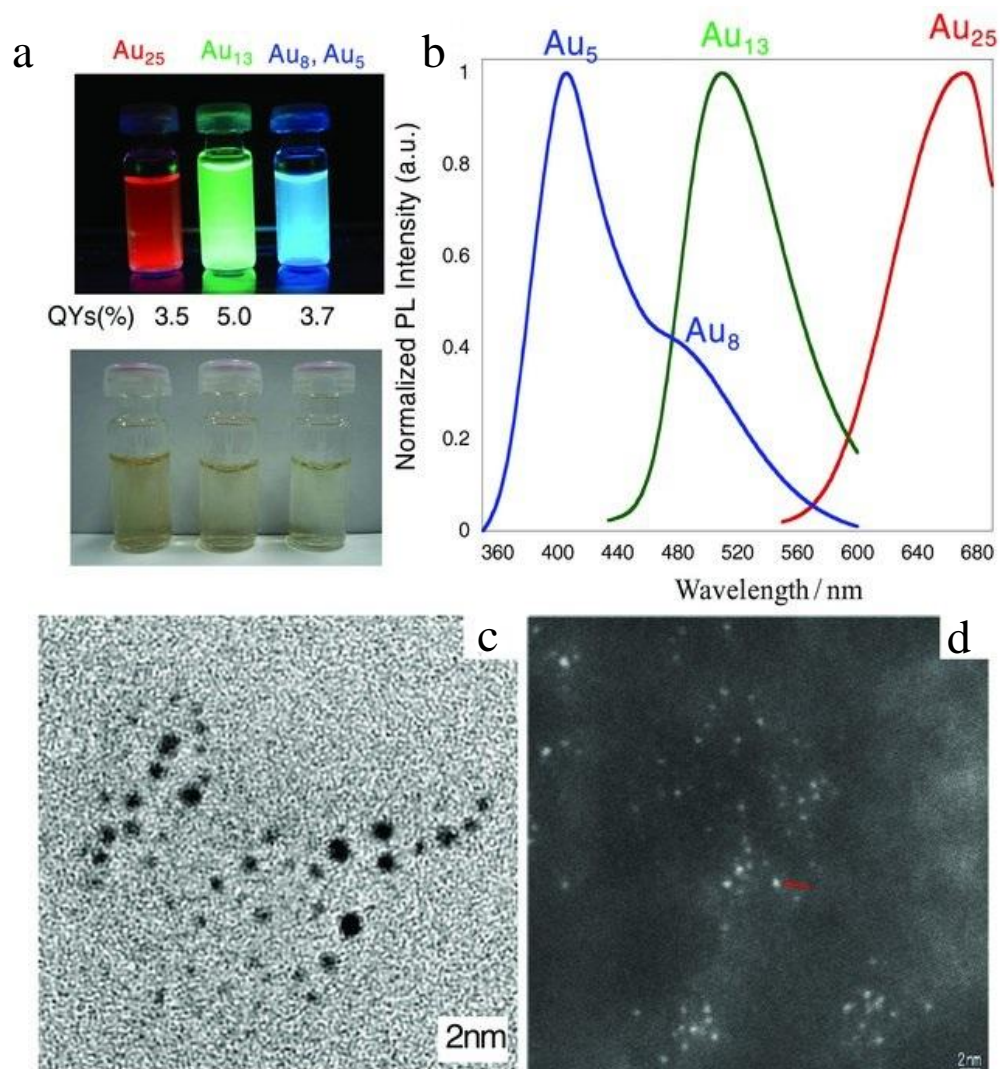


**Figure 1.8.** (a) Digital image of pepsin mediated Au nanoclusters showing red, green and blue emission under UV lamp (above) and visible light (below). Fluorescence spectra of aqueous solution of Au nanoclusters with red at pH 12, green at pH 1 and blue emission at pH 9, (c) TEM image; Scale bar 2 nm of red emitting  $Au_{25}$  nanoclusters and (d) HAADF-STEM image (scale bar 2 nm) of pepsin mediated  $Au_{13}$  nanoclusters. [Adapted from reference 188].

At pH 12.0, red emitting  $Au_{25}$  nanoclusters were formed, whereas at pH 9.0 and pH 1.0, blue ( $Au_5$  and  $Au_8$ ) and green emitting ( $Au_{13}$ ) nanoclusters were obtained respectively. They speculated that the red emitting nanoclusters at pH 12.0 were formed due to the reduction by tyrosine residues present in the enzyme, while the green

emitting nanoclusters at pH 1.0 were a result of the reduction of Au ions by the carboxylic acid groups in the enzyme. This study suggested that a control over the size of the nanoclusters using biological molecules, such as enzymes could be obtained by delicately controlling the reaction conditions. In addition, several other enzymes such as lysozyme, insulin, horseradish peroxidase and trypsin have been employed for the synthesis of luminescent metal nanoclusters.<sup>[189-194]</sup>

Although enzymes and proteins are composed of amino acid sequences, that possess several binding modes, not many coordination polymers with proteins as ligands are reported in the literature. The probable reason for this might be the complexity and flexibility of the protein structure and the difficulty in controlling the coordination of metal ions at the interfaces of the protein. Recently, Tezcan and co-workers have performed some studies illustrating the use of proteins as ligands for constructing metal organic frameworks.<sup>[195-199]</sup> Using the metal directed protein self assembly approach, they constructed the first porous protein-derived framework.<sup>[199]</sup> The framework consisted of two engineered proteins based on the four-helix bundle heme protein cytochrome cb562 connected through Ni(II) and Zn(II) ions.

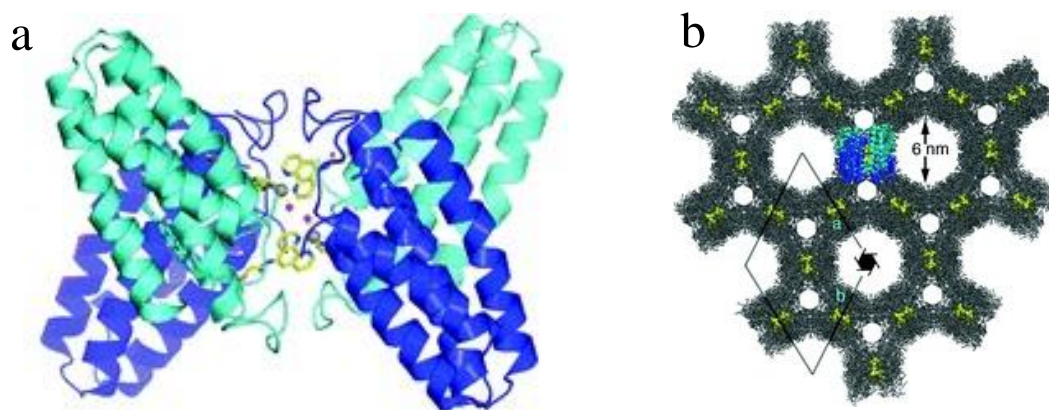


**Figure 1.9.** (a) Representation of an engineered protein based on the four-helix bundle heme protein cytochrome cb562, and (b) the porous structure resulted from its metal-directed assembly. [Adapted from reference 199].

## 1.4. Gels

Gels are viscoelastic solid-like materials comprised of an elastic cross-linked network and a solvent, which is the major component.<sup>[200-203]</sup> The solid-like appearance

of a gel is a result of the entrapment and adhesion of the liquid in the large surface area solid 3D matrix.<sup>[200]</sup> The formation of the solid matrix is a result of cross linking of the polymeric strands of molecules by physical or chemical forces. The cross linked network in the gel is capable of trapping several guest molecules including dyes, drugs and other biomolecules such as enzymes. The formation of a gel results from the self-association of the gelator molecules leading to the formation of long and thick fibrous aggregates that get entangled during the aggregation process to form a matrix that can trap the solvent principally by surface tension.<sup>[200]</sup> Such a process prevents the flow of solvent under gravity and the mass appears like a solid. If the solvent trapped is water, the term 'hydrogel' is used, whereas if the trapped solvent is an organic solvent (other than water), the term 'solvogel' or 'organogel' is used. The traditional method for the preparation of gels is to heat the gelator molecule in a particular solvent or mixture of solvents, until all the solid dissolves and a clear solution is obtained. Upon cooling, the gelator molecules undergo supramolecular assembly to form three-dimensional nano- or microstructures (such as fibers) that can immobilize solvent molecules and a stable gel is formed.<sup>[204]</sup> Ultrasonication is also employed for the generation of hydrogels in case of several low molecular weight gelators.<sup>[205,206]</sup>

For a long time, hydrogels from several biopolymers such as chitosan, agarose, gelatin, heparin etc have been used for biomedical applications as well as crystal growth of enzymes.<sup>[207]</sup> Synthetic polymeric hydrogels have been developed and commercially used for a variety of applications including superabsorbent materials, matrix chemistry and biology, media for storage and delivery of substances in biomedicine and as highly promising scaffolds to reconstitute artificial extra-cellular matrix environments.<sup>[208]</sup>

During the last twenty five years, molecules having a molecular mass less than 3000, known as low molecular mass organic gelators (LMOGs) have been intensely studied.<sup>[200,201]</sup> Peptides represent an important class of LMOGs and several peptides have been designed that act as gelators and have been used for several applications including drug delivery and tissue engineering.<sup>[209-212]</sup> The gelation in case of such molecules results from weak physical molecular interactions such as hydrogen bonding,  $\pi$ - $\pi$  stacking, van der waals forces, electrostatic interactions and London dispersion forces. Since the supramolecular networks formed are due to weak interactions, they

---

can easily be transformed into a sol by heating and are generally thermoresponsive. In most of the peptide hydrogels, auxiliary units for  $\pi$ - $\pi$  interactions are essential for the growth and stability of the hydrogels.

Recently, a new concept of multicomponent supramolecular gel has been introduced, where ions together with gelators based on metal coordinating ligands have been used in order to gain better control over structure, morphology, physical properties, and applications of such soft materials.<sup>[204,213]</sup> Although organic based gelators have been developed for more than two decades, it was not until the past decade that investigations on metal complexes as supramolecular gelators have gained enormous research interest. The reason for such an interest stems from the availability and diversity of metal-ligand coordination that could readily induce and control the self-assembly processes of the gel formation, thereby largely influencing their physical properties.<sup>[204]</sup> The metal-ligand coordination chemistry has been used to direct the assembly of small organic molecules for the generation of functional soft materials. Metal-ligand interactions have been used as a driving force to construct large-scale structure, mainly due to its diverse and unidirectional properties that allows the formation of controllable and extended structures. Taking into account the interesting value addition in physico-chemical properties extended by the metal components, several metallogels or coordination polymer gels with different organic ligands and metal ions have been developed.<sup>[204,213-217]</sup>

## 1.5. Organization of Thesis

The research on organic-inorganic hybrid functional materials have evolved manifold in the recent times, because of the wide variety of applications they are involved in. The aim of the works included in this thesis was to develop mild and greener synthetic procedures for the engineering of hybrid functional materials such as metallic nanoparticles and coordination polymer hydrogels using biomolecules as nucleating or coordinating sites. Enzymes, one of the most important functional biomolecules available in nature have been exploited as reducing as well as stabilizing agent for the growth of metallic nanoparticles. The activity of the resulting composite has been envisaged for the generation of functional materials such as alloys or nanoparticle-conducting polymer composites. A detailed mechanistic insight towards the growth of nanomaterials by enzymes has been carried out. Also, the coordinating capability of pure nucleobases has been exploited towards the formation of coordination polymer nanofibers resulting in hydrogels through extensive three dimensional network formations and water trapping that can be used for several applications including as antimicrobial agents and catalysts.

**Chapter 2** discusses the ability of the enzyme glucose oxidase for the synthesis of Au nanoparticles as well as Au nanoparticle-polyaniline nanocomposite. The synthesized Au nanoparticles acted as efficient catalysts for the reduction of *p*-nitrophenol to *p*-aminophenol. The natural activity of glucose oxidase, i.e. generation of gluconic acid and H<sub>2</sub>O<sub>2</sub> by the oxidation of glucose was lost after the formation of Au nanoparticles suggesting the denaturation of the enzyme. This was an obstacle towards the aim of synthesizing Au nanoparticle-polyaniline nanocomposite using glucose oxidase. Therefore, in an alternative strategy, the natural activity of the native enzyme was utilized and the biocatalytically generated H<sub>2</sub>O<sub>2</sub> was used as both reducing as well as oxidizing agent for the room temperature synthesis of the nanocomposite product material.

**Chapter 3** demonstrates the capability of the enzyme urease for the synthesis of not only monometallic nanoparticles (Au, Ag and Pt), but also its ability to synthesize metallic alloy nanoparticles at physiological conditions. Activity assay indicated that a

significant fraction of the enzymatic activity, i.e. the hydrolysis of urea into  $\text{CO}_2$  and  $\text{NH}_3$  was inhibited after the synthesis of metallic nanoparticles due to some conformational changes in the native structure of the enzyme. Alkaline pH is an advantage for the formation of oxide nanostructures such as ZnO at elevated temperatures through the formation of a  $\text{Zn}(\text{OH})_2$  intermediate. However, the amount of ammonia generated upon the hydrolysis of urea by the Au nanoparticle-urease composite was significantly low and increased the pH of the medium only to 7.7, but even at this pH ZnO nanoshells could be grown on the synthesized Au nanoparticles at room temperature. This was attributed to the “salting out” effect, according to which whenever a metal ion binds on the surface of a protein, the hydration layer surrounding the protein is disrupted and results in an increase in the entropy of the system. This increase in entropy of the system in the present case was enough to convert the formed  $\text{Zn}(\text{OH})_2$  at pH of 7.7 to ZnO, resulting in Au@ZnO core-shell nanoparticles.

**Chapter 4** demonstrates the effect of the thickness of the enzyme stabilizing layer on the metal nanostructures on their catalytic activity in addition to their size and shape. Pepsin, a digestive protease enzyme was used to synthesize Au nanostructures with various sizes and shapes. Simple tuning of the reaction pH and varying the concentration of the enzyme resulted in the formation of spherical, anisotropic (plates, triangles, rods) as well as red emitting ultrasmall Au nanoclusters. For the reduction of *p*-nitrophenol to *p*-aminophenol, ultrasmall fluorescent Au nanoclusters were the most efficient, followed by the spherical particles and anisotropic Au nanostructures. On the other hand for the reduction of resazurin, a relatively larger substrate, opposite trends for the catalytic activity were observed. This opposite trend could be attributed to the thickness of the enzyme layer on the Au nanostructures, since a relatively larger concentration of pepsin was used for the synthesis of Au nanoclusters.

**Chapter 5** explores the ability of pure nucleobases to self assemble into nanofibers resulting in the formation of self standing hydrogels upon their interaction with  $\text{Ag}^+$  ions. Computational studies have been performed to have an insight into the nature of bonding of the nucleobases with  $\text{Ag}^+$  ions. Further under the conditions of formation of hydrogels, the reducing ability of the three nucleobases cytosine, thymine and uracil for

the formation of Ag nanoparticles was established. The antimicrobial activity of these hydrogels was studied by challenging the gels against various microorganisms.

**Chapter 6** investigates the formation of hydrogels with fibrous morphology as a result of the coordination of cytosine and guanine with  $Zn^{2+}$  ions. Particles with beautiful flower like morphology could be observed upon the introduction of  $Zn^{2+}$  ions to a mixture of both cytosine and guanine. The photocatalytic activity of synthesized materials was realized by studying the degradation of methyl orange and methylene blue dyes.

**Chapter 7** shows the ability of the nucleobases thymine and uracil to self-assemble into fibrous aggregates, resulting in the formation of metallogels by the interaction with cadmium ions. Further the ability of these strong self assembling gels to function as nanoreactors for the growth of semiconducting CdS nanoparticles within the gel has been exploited. The CdS quantum dots aggregated to form larger particles with time that led to a decrease in the emission intensity of the quantum dots, together with a red shift in the emission maximum.

**Chapter 8** discusses the relevance of the works done by us as well as their scope for future applications.

## 1.6 References

1. Lippard S. J., Berg J. M. (1994), *Principles of bioinorganic chemistry*, University Science Books.
2. Fenton D. E. (1995), *Biocoordination chemistry*, Oxford Chemistry Primers, Oxford University Press.
3. Rehder D. (2014), *Bioinorganic chemistry*, Oxford University Press.
4. Cotton F. A., Wilkinson G., Gaus P. A. (1995), *Basic inorganic chemistry*, John Wiley & Sons.
5. Lobinski R., Potin –Gautier M. (1998), Metals and biomolecules -Bioinorganic analytical chemistry, *Analisis*, 26, 21-24 (DOI: 10.1051/analisis:199826060021).
6. Yamasaki S. *et al.* (2007), Zinc is a novel intracellular second messenger, *J. Cell Biol.*, 177, 637-645 (DOI: 10.1083/jcb.200702081).
7. Thomas A. (2010), Functional materials: From hard to soft porous frameworks, *Angew. Chem. Int. Ed.*, 49, 8328-8344 (DOI: 10.1002/anie.201000167).
8. Sanchez C., Belleville P., Popall M., Nicole L. (2011), Applications of advanced hybrid organic–inorganic nanomaterials: from laboratory to market, *Chem. Soc. Rev.*, 40, 696-753 (DOI: 10.1039/C0CS00136H).
9. Liu P. S., Liang K. M. (2001), Review functional materials of porous metals made by P/M, electroplating and some other techniques, *J. Mater. Sci.*, 36, 5059-5072 (DOI: 10.1023/A:1012483920628).
10. Scott D., Toney M., Muzikar M. (2008), Harnessing the mechanism of glutathione reductase for synthesis of active site bound metallic nanoparticles and electrical connection to electrodes, *J. Am. Chem. Soc.*, 130, 865-874 (DOI: 10.1021/ja074666g).
11. You H., Yang S., Ding B., Yang H. (2013), Synthesis of colloidal metal and metal alloy nanoparticles for electrochemical energy applications, *Chem. Soc. Rev.*, 42, 2880-2904 (DOI: 10.1039/C2CS35319A).
12. Daniel M. C., Astruc D. (2004), Gold nanoparticles: Assembly, supramolecular chemistry, quantum-size-related properties, and applications towards biology,

- 
- catalysis, and nanotechnology, *Chem. Rev.*, 104, 293-346 (DOI: 10.1021/cr030698).
13. Granitzer P., Rumpf K. (2014), *Nanostructured semiconductors: From basic research to applications*, Pan Stanford Publishing.
  14. Costi R., Saunders A. E., Banin U. (2010), Colloidal hybrid nanostructures: A new type of functional materials, *Angew. Chem. Int. Ed.*, 49, 4878-4897 (DOI: 10.1002/anie.200906010).
  15. Goesmann H., Feldmann C. (2010), Nanoparticulate functional materials, *Angew. Chem. Int. Ed.*, 49, 1362-1395 (DOI: 10.1002/anie.200903053).
  16. Talapin D. V., Lee, J. -S., Kovalenko M. V., Shevchenko, E. V. (2010), Prospects of colloidal nanocrystals for electronic and optoelectronic applications, *Chem. Rev.*, 110, 389-458 (DOI: 10.1021/cr900137k).
  17. Ghosh S. K., Pal T. (2007), Interparticle coupling effect on the surface plasmon resonance of gold nanoparticles: From theory to applications, *Chem. Rev.*, 107, 4797-4862 (DOI: 10.1021/cr0680282).
  18. Kelly K. L., Coronado E., Zhao L. L., Schatz G. C. (2003), The optical properties of metal nanoparticles: The influence of size, shape, and dielectric environment, *J. Phys. Chem. B*, 107, 668-677 (DOI: 10.1021/jp026731y).
  19. Burda C., Chen X., Narayanan R., El-Sayed M. A. (2005), Chemistry and properties of nanocrystals of different shapes, *Chem. Rev.*, 105, 1025-1102 (DOI: 10.1021/cr030063a S0009-2665(03)00063-3).
  20. Saha K., Agasti S. S., Kim C., Li X., Rotello V. M. (2012), Gold nanoparticles in chemical and biological sensing, *Chem. Rev.*, 112, 1739-2779 (DOI: 10.1021/cr2001178).
  21. Vilela D., González M. C., Escarpa A. (2012), Sensing colorimetric approaches based on gold and silver nanoparticles aggregation: Chemical creativity behind the assay. A review, *Anal. Chim. Acta*, 751, 24-43 (DOI: 10.1016/j.aca.2012.08.043).
  22. Lee J. S., Han M. S., Mirkin C. A. (2007), Colorimetric detection of mercuric ion (Hg<sup>2+</sup>) in aqueous media using DNA-functionalized gold nanoparticles, *Angew. Chem. Int. Ed.*, 46, 4093-4096 (DOI: 10.1002/anie.200700269).
-

23. Hung Y. -L., Hsiung T. -M., Chen Y. -Y., Huang Y. -F., Huang C. -C. (2010), Colorimetric detection of heavy metal ions using label-free gold nanoparticles and alkanethiols, *J. Phys. Chem. C*, 114, 16329-16334 (DOI: 10.1021/jp1061573).
24. Xie X., Lu W., Liu X. (2012), Improving colorimetric assays through protein enzyme-assisted gold nanoparticle amplification, *Acc. Chem. Res.*, 45, 1511-1520 (DOI: 10.1021/ar300044j).
25. Rodriguez-Lorenzo L., de la Rica R., Álvarez-Puebla R. A., Liz-Marzán L. M., Stevens M. M. (2012), Plasmonic nanosensors with inverse sensitivity by means of enzyme-guided crystal growth, *Nat. Mater.*, 11, 604-607 (DOI: DOI: 10.1038/NMAT3337).
26. Laromaine A., Koh L., Murugesan M., Ulijin R. V., Stevens M. M. (2007), Protease-triggered dispersion of nanoparticle assemblies, *J. Am. Chem. Soc.*, 129, 4156-4157 (DOI: 10.1021/ja0706504).
27. Chanana M., Mateo C., Salgueirino V., Correa-Duarte M. A. (2012), Synthesis of gold nanoparticles, *Encyclopedia of Nanotechnology*, 2621-2630 (DOI: 10.1007/978-90-481-9751-4\_52).
28. Tao A. R., Habas S., Yang P. (2008), Shape control of colloidal metal nanocrystals, *Small*, 4, 310-325 (DOI: 10.1002/sml.200701295).
29. Sau T. K., Rogach A. L., Jäckel F., Klar T. A., Feldmann J. (2010), Properties and applications of colloidal nonspherical noble metal nanoparticles, *Adv. Mater.*, 22, 1805-1825 (DOI: 10.1002/adma.200902557).
30. Zaera F. (2013), Shape-controlled nanostructures in heterogeneous catalysis, *ChemSusChem*, 6, 1797-1820 (DOI: 10.1002/cssc.201300398).
31. An K., Somorjai G. A. (2012), Size and shape control of metal nanoparticles for reaction selectivity in catalysis, *ChemCatChem*, 4, 1512-1524 (DOI: 10.1002/cctc.201200229).
32. Ahmadi T. S., Wang Z. L., Green T. C., Henglein A., El-Sayed M. A. (1996), Shape-controlled synthesis of colloidal platinum nanoparticles, *Science*, 272, 1924-1925 (DOI: 10.1126/science.272.5270.1924).

33. Gutsch A., Mühlenweg H., Krämer M. (2005), Tailor-made nanoparticles via gas-phase synthesis, *Small*, 1, 30-46 (DOI: DOI: 10.1002/smll.200400021).
34. Cushing B. L., Kolesnichenko V. L., O'Connor J. (2004), Recent advances in the liquid-phase syntheses of inorganic nanoparticles, *Chem. Rev.*, 104, 3893-3946 (DOI: 10.1021/cr030027b).
35. Sun Y., Xia Y. (2002), Shape-controlled synthesis of gold and silver nanoparticles, *Science*, 298, 2176-2179 (DOI: 10.1126/science.1077229).
36. Grzlczak M., Pérez-Juste J., Mulvaney P., Liz-Marzán L. M. (2008), *Chem. Soc. Rev.*, 37, 1783-1791 (DOI: 10.1039/B711490G).
37. Xia Y., Xiong Y., Lim B., Skrabalak S. E. (2009), Shape-controlled synthesis of metal nanocrystals: Simple chemistry meets complex physics? *Angew. Chem. Intd. Ed.*, 48, 60-103 (DOI: 10.1002/anie.200802248).
38. Jana N. R., Gearheart L., Murphy C. J. (2001), Seed-mediated growth approach for shape- controlled synthesis of spheroidal and rod-like gold nanoparticles using a surfactant template, *Adv. Mater.*, 13, 1389-1393 (DOI: 10.1002/1521-4095(200109)13:18<1389::AID-ADMA1389>3.0.CO;2-F).
39. Sau T. K., Murphy C. J. (2004), Room temperature, high-yield synthesis of multiple shapes of gold nanoparticles in aqueous solution, *J. Am. Chem. Soc.*, 126, 8648-8649 (DOI: 10.1021/ja047846d).
40. Martin B. R., Dermody D. J., Reiss B. D., Fang M., Lyon L. A., Natan M. J., Mallouk T. E. (1999), Orthogonal self-assembly on colloidal gold-platinum nanorods, *Adv. Mater.*, 11, 1021-1025 (DOI: 10.1002/(SICI)1521-4095(199908)11:12<1021::AID-ADMA1021>3.0.CO;2-S).
41. Cepak V. M., Martin C. R. (1998), Preparation and stability of template-synthesized metal nanorod sols in organic solvents, *J. Phys. Chem. B*, 102, 9985-9990 (DOI: 10.1021/jp982882).
42. Govindaraj A., Satishkumar B. C., Nath M., Rao C. N. R. (2000), Metal nanowires and intercalated metal layers in single-walled carbon nanotube bundles, *Chem. Mater.*, 12, 202-205 (DOI: 10.1021/cm990546o).

43. Qi L., Ma J., Cheng H., Zhao Z. (1997), Reverse micelle based formation of BaCO<sub>3</sub> nanowires, *J. Phys. Chem. B*, 101, 3460-3463 (DOI: 10.1021/jp970419k).
44. Lu Y., Chen W. (2012), Sub-nanometre sized metal clusters: From synthetic challenges to the unique property discoveries, *Chem. Soc. Rev.*, 31, 3594-3623 (DOI: 10.1039/C2CS15325D).
45. Goswami, N., Zheng K., Xie J. (2014), Bio-NCs – the marriage of ultrasmall metal nanoclusters with biomolecules, *Nanoscale*, 6, 13328-13347 (DOI: 10.1039/C4NR04561K).
46. Shang L., Dong S., Ulrich Nienhaus G. (2011), Ultra-small fluorescent metal nanoclusters: Synthesis and biological applications, *Nano Today*, 6, 401-418 (DOI: 10.1016/j.nantod.2011.06.004).
47. Luo Z., Zheng K., Xie J. (2014), Engineering ultra small water soluble gold and silver nanoclusters for biomedical applications, *Chem. Commun.*, 50, 5143-5155 (DOI: 10.1039/C3CC47512C).
48. Choi. S., Dickson R. M., Yu J. (2012), Developing luminescent silver nanodots for biological applications, *Chem. Soc. Rev.*, 41, 1867-1891 (DOI: 10.1039/C1CS15226B).
49. Li G., Jin R. (2013), Atomically precise gold nanoclusters as new model catalysts, *Acc. Chem. Res.*, 46, 1749-1758 (DOI: 10.1021/ar300213z).
50. Sun J., Jin Y. (2014), Fluorescent Au nanoclusters: Recent progress and sensing applications, *J. Mater. Chem. C*, 2, 8000-8011 (DOI: 10.1039/C4TC01489H).
51. Mathew A., Pradeep T. (2014), Noble metal clusters: Applications in energy, environment, and biology *Part. Part. Syst. Charact.*, 31, 1017-1053 (DOI: 10.1002/ppsc.201400033).
52. Sun H. –T., Sakka Y. (2014), Luminescent metal nanoclusters: Controlled synthesis and functional applications, *Sci. Technol. Adv. Mater.*, 15, 014205 (DOI: 10.1088/1468-6996/15/1/014205).
53. Kitagawa S., Kitaura R., Noro S. –I. (2004), Functional porous coordination polymers, *Angew. Chem. Int. Ed.*, 43, 2334-2375 (DOI: 10.1002/anie.200300610).

- 
54. Furukawa H., Cordova K. E., O’Keefe M., Yaghi O. M. (2013), The chemistry and applications of metal-organic frameworks, *Science*, 341, 123044 (DOI: 10.1126/science.1230444).
55. Imaz I., Rubio-Martínez M., An J., Solé-Font I., Rosi N. L., MasPOCH D. (2011), Metal–biomolecule frameworks (MBioFs), *Chem Commun.*, 47, 7287-7302 (DOI: 10.1039/c1cc11202c).
56. Hoskins B. F., Robson R. (1990), Design and construction of a new class of scaffolding-like materials comprising infinite polymeric frameworks of 3D-linked molecular rods. A reappraisal of the zinc cyanide and cadmium cyanide structures and the synthesis and structure of the diamond-related frameworks  $[N(CH_3)_4][CuIZnII(CN)_4]$  and  $CuI[4,4',4'',4''']$ -tetracyanotetraphenylmethane]BF<sub>4</sub>.x C<sub>6</sub>H<sub>5</sub>NO<sub>2</sub>, *J. Am. Chem. Soc.*, 112, 1546-1554 (DOI: 10.1021/ja00160a038).
57. Czaza A. U., Trukhan N., Müller U. (2009), Industrial applications of metal–organic frameworks, *Coord. Chem. Rev.*, 38, 1284-1293 (DOI: 10.1039/B804680H).
58. Kuppler R. J. *et al.* (2009), Potential applications of metal-organic frameworks, *Coord. Chem. Rev.*, 253, 3042-3066 (DOI: 10.1016/j.ccr.2009.05.019).
59. Liu J., Chen L., Cui H., Zhang J., Zhang L., Su C. –Y. (2014), Applications of metal–organic frameworks in heterogeneous supramolecular catalysis, *Chem. Soc. Rev.*, 43, 6011-6061 (DOI: 10.1039/C4CS00094C).
60. Hu X. G., Li X. L., Yang S. I. (2015), Novel photochromic infinite coordination polymer particles derived from a diarylethene photoswitch, *Chem. Commun.*, 51, 10636-10639 (DOI: 10.1039/C5CC02447A ).
61. Lin W., Rieter W. J., Taylor K. M. L. (2009), Modular synthesis of functional nanoscale coordination polymers, *Angew. Chem. Int. Ed.*, 48, 650-658 (DOI: 10.1002/anie.200803387).
62. Ma Y., Ni Y., Guo F., Xiang N. (2015), Flowerlike copper(II)-based coordination polymers particles: Rapid room-temperature fabrication, influencing factors, and transformation toward CuO microstructures with good

- 
- catalytic activity for the reduction of 4-nitrophenol, *Cryst. Growth Des.*, 15, 2243-2252 (DOI: 10.1021/acs.cgd.5b00003).
63. Novio F., Ruiz-Molina D., Lorenzo J. (2014), Amorphous coordination polymer particles for biomedicine, in *Bio- and bioinspired nanomaterials*, Wiley-VCH Verlag GmbH & Co. KGaA, Weinheim, Germany (DOI: 10.1002/9783527675821.ch05).
64. Spokoyny A. M., Kim D., Sumrein A., Mirkin C. A. (2009), Infinite coordination polymer nano- and microparticle structures, *Chem. Soc. Rev.*, 38, 1218-1227 (DOI: 10.1039/B807085G).
65. Oh M., Mirkin C. A. (2005), Chemically tailorable colloidal particles from infinite coordination polymers, *Nature*, 438, 651-654 (DOI: 10.1038/nature04191).
66. Carnaé A., Carbonell C., Imaz I., MasPOCH D. (2011), Nanoscale metal–organic materials, *Chem. Soc. Rev.*, 40, 291-305 (DOI: 10.1039/C0CS00042).
67. Jung S., Oh M. (2008), Monitoring shape transformation from nanowires to nanocubes and size-controlled formation of coordination polymer particles, *Angew. Chem. Int. Ed.*, 47, 2049-2051 (DOI: 10.1002/anie.200704209).
68. Sun X., Dong S., Wang E. (2005), Coordination-induced formation of submicrometer-scale, monodisperse, spherical colloids of organic–inorganic hybrid materials at room temperature, *J. Am. Chem. Soc.*, 127, 13102-13103 (DOI: 10.1021/ja0534809).
69. He C., Liu D., Lin W. (2015), Nanomedicine applications of hybrid nanomaterials built from metal–ligand coordination bonds: Nanoscale metal–organic frameworks and nanoscale coordination polymers, *Chem. Rev.*, 115, 11079-11108 (DOI: 10.1021/acs.chemrev.5b00125).
70. Imaz I., Rubio-Martínez M., Garcia-Fernández L., Garcia F., Ruiz-Molina D., Hernando J., Puentes V., MasPOCH D. (2010), Coordination polymer particles as potential drug delivery systems, *Chem. Commun.*, 46, 4737-4739 (DOI: 10.1039/C003084H).
-

- 
71. Berti L., Burley G. A. (2008), Nucleic acid and nucleotide-mediated synthesis of inorganic nanoparticles, *Nat. Nanotechnol.*, 3, 81-87 (DOI: 10.1038/nano.2007.460).
  72. Mann S., Archibald D. D., Didimus J. M., Douglas T., Heywood B. R., Meldrum F. C., Reeves N. J. (1993), Crystallization at inorganic-organic interfaces: Biominerals and biomimetic synthesis, *Science*, 261, 1286-1292 (DOI: 10.1126/science.261.5126.1286).
  73. Mann S. (1993), Molecular tectonics in biomineralization and biomimetic materials chemistry, *Nature*, 365, 499-505 (DOI: 10.1038/365499a0).
  74. Dickson D. P. E. (1999), Nanostructured magnetism in living systems, *J. Magn. Magn. Mater.*, 203, 46-49 (DOI: 10.1016/S0304-8853(99)00178-X).
  75. Sakaguchi T., Burgess J. G., Matsunaga T. (1993), Magnetite formation by sulfate-reducing bacterium, *Nature*, 365, 47-49 (DOI: 10.1038/365047a0).
  76. Tsipursky S. J., Buseck B. R. (1993), Structure of magnesian calcite from sea urchins, *Am. Mineral.*, 78, 775-781.
  77. Ma Y., Cohen S. R., Addadi L., Weiner S. (2008), Sea urchin tooth design: An “All-Calcite” polycrystalline reinforced fiber composite for grinding rocks, *Adv. Mater.*, 20, 1555-1559 (DOI: 10.1002/adma.200702842).
  78. Raveendran P., Fu J., Wallen S. J. (2003), Completely “green” synthesis and stabilization of metal nanoparticles, *J. Am. Chem. Soc.*, 125, 13940-13941 (DOI: 10.1021/ja029267j).
  79. Willner I., Willner B. (2010), Biomolecule-based nanomaterials and nanostructures, *Nano Lett.*, 10, 3805-3815 (DOI: 10.1021/nl102083).
  80. Bhargava S. K., Booth J. M., Agarwal S., Coloe P., Kar G. (2005), Gold nanoparticle formation during bromoaurate reduction by amino acids, *Langmuir*, 21, 5949-5956 (DOI: 10.1021/la050283e).
  81. Selvakannan PR., Mandal S., Phadtare S., Gole A., Parischa R., Adhyanthaya S. D., Sastry M. (2004), Water-dispersible tryptophan-protected gold nanoparticles prepared by the spontaneous reduction of aqueous chloroaurate ions by the amino acid, *J. Colloid Interface Sci.*, 269, 97-102 (DOI: 10.1016/S0021-9797(03)00616-7).
-

82. Si S., Mandal T. K. (2007), Tryptophan-based peptides to synthesize gold and silver nanoparticles: A mechanistic and kinetic study, *Chem. Eur. J.*, 13, 3160-3168 (DOI: 10.1002/chem.200601492).
83. Ma Z., Han H. (2008), One-step synthesis of cystine coated gold nanoparticles in aqueous solutions, *Colloids Surf. A*, 317, 229-233 (DOI:10.1016/j.colsurfa.2007.10.018).
84. Selvakannan PR., Mandal S., Phadtare S., Parischa R., Sastry M. (2003), Capping of gold nanoparticles by the amino acid lysine renders them water-dispersible, *Langmuir*, 19, 3545-3549 (DOI: 10.1021/la026906v).
85. Wang Z., Zhu H., Wang X., Yang F., Yang X. (2009), One-pot green synthesis of biocompatible arginine-stabilized magnetic nanoparticles, *Nanotechnology*, 20, 465606 (DOI: 10.1088/0957-4484/20/46/465606)
86. Wangoo N., Bhasin K. K., Mehta S. K., Suri C. R. (2008), Synthesis and capping of water-dispersed gold nanoparticles by an amino acid: Bioconjugation and binding studies, *J. Colloid Interface Sci.*, 323, 247-254 (DOI: 10.1016/j.jcis.2008.04.043).
87. Shao Y., Jin Y., Dong S. (2004), Synthesis of gold nanoplates by aspartate reduction of gold chloride, *Chem. Commun.*, 1104-1105 (DOI: 10.1039/B315732F)
88. Tan Y. N., Lee J. Y., Wang D. I. C. (2008), Aspartic acid synthesis of crystalline gold nanoplates, nanoribbons, and nanowires in aqueous solutions, *J. Phys. Chem. C*, 112, 5463-5470 (DOI: 10.1021/jp800501k).
89. Kracht S., Messerer M., Lang M., Eckhardt S., Lauz M., Grob ty B., Fromm K. M., Giese B. (2015), Electron transfer in peptides: On the formation of silver nanoparticles, *Angew. Chem. Int. Ed.*, 54, 2912-2916 (DOI: 10.1002/anie.201410618).
90. Slocik J. M., Stone M. O., Naik R. R. (2007), Synthesis of gold nanoparticles using multifunctional peptides, *Small*, 1, 1048-1052 (DOI: 10.1002/sml.200500172).

- 
91. Slocik J. M., Naik R. R. (2006), Biologically programmed synthesis of bimetallic nanostructures, *Adv. Mater.*, 18, 1988-1992 (DOI: 10.1002/adma.200600327).
  92. Tan Y. N., Lee J. Y., Wang D. I. C. (2010), Uncovering the design rules for peptide synthesis of metal nanoparticles, *J. Am. Chem. Soc.*, 132, 5677-5686 (DOI: 10.1021/ja907454f).
  93. Song C., Zhao G., Zhang P., Rosi N. L. (2010), Expeditious synthesis and assembly of sub-100 nm hollow spherical gold nanoparticle superstructures, *J. Am. Chem. Soc.*, 132, 14033-14035 (DOI: 10.1021/ja106833g).
  94. Dickerson M. B., Sandhage K. H., Naik R. R. (2008), Protein- and peptide-directed syntheses of inorganic materials, *Chem. Rev.*, 108, 4935-4978 (DOI: 10.1021/cr8002328).
  95. Naik R. R., Stringer S. J., Agarwal G., Jones S. E., Stone M. O. (2002), Biomimetic synthesis and patterning of silver nanoparticles, *Nat. Mater.*, 1, 169-172 (DOI: 10.1038/nmat758).
  96. Cheng C. -L., Zhang P., Rosi N. L. (2008), A new peptide-based method for the design and synthesis of nanoparticle superstructures: Construction of highly ordered gold nanoparticle double helices, *J. Am. Chem. Soc.*, 130, 13555-13557 (DOI: 10.1021/ja805683r).
  97. Wei H., Wang E. (2007), Submicrometre scale single-crystalline gold plates of nanometre thickness: synthesis through a nucleobase process and growth mechanism, *Nanotechnology*, 18, 295603 (DOI: 10.1088/0957-4484/18/29/295603).
  98. Jiang H., Zhang Y., Wang X. (2014), Single cytidine units-templated syntheses of multi-colored water soluble Au nanoclusters, *Nanoscale*, 6, 10355-10362 (DOI: 10.1039/C4NR02180K).
  99. Dash J., Patil A. J., Das R. N., Dowdall F. L., Mann S. (2011), Supramolecular hydrogels derived from silver ion-mediated self-assembly of 5'-guanosine monophosphate, *Soft Matter*, 7, 8120-8126 (DOI:10.1039/C1SM05839H).
  100. Hinds S., Taft B. J., Levina L., Sukhovatkin V., Dooley C. J., Roy M. D., MacNeil D. D., Sargent E. A., Kelley S. O. (2006), Nucleotide-directed growth

- of semiconductor nanocrystals, *J. Am. Chem. Soc.*, 128, 64-65 (DOI: 10.1021/ja057002+).
101. Zhao W., Gonzaga F., Li Y., Brook M. A. (2007), Highly stabilized nucleotide-capped small gold nanoparticles with tunable size, *Adv. Mater.*, 19, 1766-1771, (DOI: 10.1002/adma.200602449).
102. Kumar A., Kumar V. (2014), Biotemplated inorganic nanostructures: Supramolecular directed nanosystems of semiconductor(s)/metal(s) mediated by nucleic acids and their properties, *Chem. Rev.*, 114, 7044-7078 (DOI: 10.1021/cr4007285).
103. Anokhina E. V., Jacobsen A. J. (2004),  $[\text{Ni}_2\text{O}(\text{L-Asp})(\text{H}_2\text{O})_2]\cdot 4\text{H}_2\text{O}$ : A homochiral 1D helical chain hybrid compound with extended Ni–O–Ni bonding, *J. Am. Chem. Soc.*, 126, 3044-3045 (DOI: 10.1021/ja031836f).
104. Gasque L., Bernés S., Ferrari R., Barbarín C. R. de, Gutiérrez M. de J., Mendoza-Díaz G. (2000), Complexation of lead(II) by L-aspartate: Crystal structure of polymeric  $\text{Pb}(\text{aspH})(\text{NO}_3)$ , *Polyhedron*, 19, 649-653 (DOI: 10.1016/S0277-5387(00)00299-0).
105. Gasque L., Bernés S., Ferrari R., Mendoza-Díaz G. (2002), Cadmium complexation by aspartate. NMR studies and crystal structure of polymeric  $\text{Cd}(\text{AspH})\text{NO}_3$ , *Polyhedron*, 21, 935-941 (DOI: 10.1016/S0277-5387(02)00871-9).
106. Gould J. A., Jones J. T. A., Bacsá J., Khimiyak Y. Z., Rosseinsky M. J. (2010), A homochiral three-dimensional zinc aspartate framework that displays multiple coordination modes and geometries, *Chem. Commun.*, 46, 2793-2795 (DOI: 10.1039/B925066B)
107. Li M. X., Zhao H. J., Shao M., Miao Z. X., Liang S. W. (2007), Synthesis, characterization and crystal structures of two binary acid complexes based on L-glutamate and L-aspartate, *J. Coord. Chem.*, 60, 2549-2557 (DOI: 10.1080/00958970701283711).
108. Imaz I., Rubio-Martínez M., Saletta W. J., Amabilino D. B., MasPOCH D. (2009), Amino acid based metal–organic nanofibers, *J. Am. Chem. Soc.*, 131, 18222-18223 (DOI: 10.1021/ja908721t).

- 
109. Wu H., Tian C., Zhang Y., Yang C., Zhang S., Jiang Z. (2015), Stereoselective assembly of amino acid-based metal–biomolecule nanofibers, *Chem. Commun.*, 51, 6329-6332 (DOI: 10.1039/C5CC00446B).
110. Zhang Y., Saha M. K., Bernal I. (2003), [Cobalt(II)L-glutamate(H<sub>2</sub>O)·H<sub>2</sub>O]<sub>∞</sub>: A new 3D chiral metal–organic interlocking network with channels, *CrystEngComm*, 5, 34-37 (DOI: 10.1039/B210753H).
111. Chao L., Deng K., Tang Z., Jiang L. (2010), Twisted Metal-Amino Acid Nanobelts: Chirality Transcription from Molecules to Frameworks, *J. Am. Chem. Soc.*, 132, 8202-8209 (DOI: 10.1021/ja102827f).
112. Strasdeit H., Büsching I., Behrends S., Saak W., Barklage W. (2001), Syntheses and properties of zinc and calcium complexes of valinate and isovalinate: Metal  $\alpha$ -amino acidates as possible constituents of the early earth's chemical inventory, *Chem. Eur. J.*, 7, 1133-1142 (DOI: 10.1002/1521-3765(20010302)7:5<1133::AID-CHEM1133>3.0.CO;2-T).
113. Takayama T., Ohuchida S., Koike Y., Watanabe M., Hashizume D., Ohasi Y. (1996), Structural analysis of cadmium–glycylglycine complexes studied by X-ray diffraction and high resolution <sup>113</sup>Cd and <sup>13</sup>C solid state NMR, *Bull. Chem. Soc. Jpn.*, 69, 1579-1586 (DOI: 10.1246/bcsj.69.1579).
114. Ueda E., Yoshikawa Y., Kisshimoto N., Tadokoro M., Sakurai H., Kajiwara N., Kojima Y. (2004), New bioactive zinc(II) complexes with peptides and their derivatives: Synthesis, structure, and in vitro insulinomimetic activity, *Bull. Chem. Soc. Jpn.*, 77, 981-986 (DOI: 10.1246/bcsj.77.981).
115. Lee H. Y., Kampf J. W., Park K. S., Marsh N. G. (2008), Covalent metal–peptide framework compounds that extend in one and two dimensions, *Cryst. Growth Des.*, 8, 296-303 (DOI: 10.1021/cg700724h).
116. Rabone J., Yue Y. F., Chong S. Y., Stylianou K. C., Bacsá J., Bradshaw D., Darling G. R., Berry N. G., Khimyak Y. Z., Ganin A. Y., Wiper P., Claridge J. W., Rosseinsky M. J. (2010), An adaptable peptide-based porous material, *Science*, 329, 1053-1057 (DOI: 10.1126/science.1190672).
-

117. Yan X., Zhu P., Fei J., Li J. (2010), Self-assembly of peptide-inorganic hybrid spheres for adaptive encapsulation of guests, *Adv. Mater.*, 22, 1283-1287 (DOI: 10.1002/adma.200901889).
118. Peri D., Ciston J., Gándara F., Zhao Y., Yaghi O. M. (2013), Crystalline fibers of metal–peptide double ladders, *Inorg. Chem.*, 52, 13818-13820 (DOI: 10.1021/ic402435z).
119. Martí-Gastaldo C., Antypov D., Warren J. E., Briggs M. E., Chater P. A., Wiper P. V., Miller G. J., Khimyak Y. J., Darling G. R., Berry N. G., Rosseinsky M. J. (2014), Side-chain control of porosity closure in single- and multiple-peptide-based porous materials by cooperative folding, *Nat. Chem.*, 6, 343-351 (DOI: 10.1038/nchem.1871).
120. Manton A., Massüger L., Rabu P., Palivan C., McCusker L. B., Taubert A. (2008), Metal-peptide frameworks (MPFs): “Bioinspired” metal organic frameworks, *J. Am. Chem. Soc.*, 130, 2517-2526 (DOI: 10.1021/ja0762588).
121. Verma S., Mishra A. K., Kumar J. (2010), The many facets of adenine: Coordination, crystal patterns, and catalysis, *Acc. Chem. Res.*, 43, 79-91, (DOI: 10.1021/ar9001334).
122. Gillen K., Jensen R., Davidson N. (1964), Binding of silver ion by adenine and substituted adenines, *J. Am. Chem. Soc.*, 86, 2792-2796 (DOI: 10.1021/ja01068a008).
123. Wei H., Li B., Du Y., Dong S., Wang E. (2007), Nucleobase–metal hybrid materials: Preparation of submicrometer-scale, spherical colloidal particles of adenine–gold(III) via a supramolecular hierarchical self-assembly approach, *Chem. Mater.*, 19, 2987-2993 (DOI: 10.1021/cm070028a).
124. An J., Geib S. J., Rosi N. L. (2010), High and selective CO<sub>2</sub> uptake in a cobalt adeninate metal–organic framework exhibiting pyrimidine- and amino-decorated pores, *J. Am. Chem. Soc.*, 132, 38-39 (DOI: 10.1021/ja909169x).
125. An J., Geib S. J., Rosi N. L. (2009), Cation-triggered drug release from a porous zinc-adeninate metal–organic framework, *J. Am. Chem. Soc.*, 131, 8376-8377 (DOI: 10.1021/ja902972w).

- 
126. An J., Farha O. K., Hupp J. T., Pohl E., Yeh j. I., Rosi N. L. (2012), Metal-adeninate vertices for the construction of an exceptionally porous metal-organic framework, *Nat. Commun.*, 3, 604 (DOI: 10.1038/ncomms1618).
  127. Garcia-Teran J. P., Castillo O., Luque A., Garcia-Couceiro U., Roman P., Lezama L. (2004), An unusual 3D coordination polymer based on bridging interactions of the nucleobase adenine, *Inorg. Chem.*, 43, 4549-4551 (DOI: 10.1021/ic049512v).
  128. Nishiyabu R. *et al.* (2009), Nanoparticles of adaptive supramolecular networks self-assembled from nucleotides and lanthanide ions, *J. Am. Chem. Soc.*, 131, 2151-2158 (DOI: 10.1021/cm070028a).
  129. Purohit C. S., Mishra A. K., Verma S. (2007), Four-stranded coordination helices containing silver–adenine (purine) metallaquartets, *Inorg. Chem.*, 46, 8493-8495 (DOI: 10.1021/ic701465d).
  130. Purohit C. S., Verma S. (2007), Patterned deposition of a mixed-coordination adenine– silver helicate, containing a  $\pi$ -stacked metallacycle, on a graphite surface, *J. Am. Chem. Soc.*, 129, 3488-3489 (DOI: 10.1021/ja068892b).
  131. Pandey M. D., Mishra A. K., Chandrasekhar V., Verma S. (2010), Silver-guided excimer emission in an adenine–pyrene conjugate: Fluorescence lifetime and crystal studies, *Inorg. Chem.*, 49, 2020-2022 (DOI: 10.1021/ic9022008).
  132. Purohit C. S., Verma S. (2006), A luminescent silver–adenine metallamacrocyclic quartet, *J. Am. Chem. Soc.*, 128, 400-401 (DOI: 10.1021/ja056452z).
  133. Silver S. (1996), Bacterial resistances to toxic metal ions - a review, *Gene*, 179, 9-19 (DOI: 10.1016/S0378-1119(96)00323-X).
  134. Hulkoti N. I., Taranath T. C. (2014), Biosynthesis of nanoparticles using microbes—A review, *Colloids Surf. B*, 121, 474-483 (DOI: 10.1016/j.colsurfb.2014.05.027).
  135. Bharde A. A. *et al.* (2008), Bacteria-mediated precursor-dependent biosynthesis of superparamagnetic iron oxide and iron sulfide nanoparticles, *Langmuir*, 24, 5787-5794 (DOI: 10.1021/la704019p).
-

- 
136. Klaus T., Joerger R., Olsson E., Granqvist C. –G. (1999), Silver-based crystalline nanoparticles, microbially fabricated, *Proc. Natl. Acad. Sci. USA*, 13611-13614 (DOI: 10.1073/pnas.96.24.13611)
137. Joerger R., Klaus T., Granqvist C. –G. (2000), Biologically produced silver–carbon composite materials for optically functional thin-film coatings, *Adv. Mater.*, 12, 407-409 (DOI: 10.1002/(SICI)1521-4095(200003)12:6<407::AID-ADMA407>3.0.CO;2-O).
138. He S., Guo Z., Zhang Y., Zhang S., Wang J., Gu N. (2007), Biosynthesis of gold nanoparticles using the bacteria *Rhodopseudomonas capsulate*, *Mater. Lett.*, 61, 3984-3987 (DOI:10.1016/j.matlet.2007.01.018).
139. Slocik J. M., Naik R. R., Stone M. O., Wright D. W. (2005), Viral templates for gold nanoparticle synthesis, *J. Mater. Chem.*, 15, 749-753 (DOI: 10.1039/B413074J).
140. Shah S. N., Steinmetz N. F., Aljabali A. A. A., Lomonossoff G. P., Evans D. J. (2009), Environmentally benign synthesis of virus-templated, monodisperse, iron-platinum nanoparticles, *Dalton Trans.*, 8479-8480 (DOI: 10.1039/B906847C).
141. de la Escosura A., Nolte R. J. M., Cornelissen J. J. L. M. (2009), Viruses and protein cages as nanocontainers and nanoreactors, *J. Mater. Chem.*, 19, 2274-2278 (DOI: 10.1039/B815274H).
142. Gole A., Dash C., Soman C., Sainkar S. R., Rao M., Sastry M. (2001), On the preparation, characterization, and enzymatic activity of fungal protease–gold colloid bioconjugates, *Bioconjugate Chem.*, 12, 684-690 (DOI: 10.1021/bc0001241).
143. Mukherjee P. *et al.* (2001), Bioreduction of  $\text{AuCl}_4^-$  ions by the fungus *Verticillium sp.* and surface trapping of the gold nanoparticles formed, *Angew. Chem. Int. Ed.*, 40, 3585-3588 (DOI: 10.1002/1521-3773(20011001)40:19<3585::AID-ANIE3585>3.0.CO;2-K).
144. Mukherjee P. *et al.* (2001), Fungus-mediated synthesis of silver nanoparticles and their immobilization in the mycelial matrix: A novel biological approach to nanoparticle synthesis, *Nano Lett.*, 1, 515-519 (DOI: 10.1021/nl0155274).
-

- 
145. Bharde A., Rautaray D., Bansar V., Ahmad A., Sarkar I., Yusuf S. M., Sanyal M., Sastry M. (2006), Extracellular biosynthesis of magnetite using fungi, *Small*, 2, 135-141 (DOI: 10.1002/sml.200500180).
  146. Mukherjee P., Senapati S., Mandal D., Ahmad A., Khan M. I., Kumar R., Sastry M. (2002), Extracellular synthesis of gold nanoparticles by the fungus *Fusarium oxysporum* (2002), *ChemBioChem*, 3, 461-463 (DOI: 10.1002/1439-7633(20020503)3:5<461::AID-CBIC461>3.0.CO;2-X).
  147. Bansal V., Sanyal A., Rautaray D., Ahmad A., Sastry M. (2005), Bioleaching of sand by the fungus *Fusarium Oxysporum* as a means of producing extracellular silica nanoparticles, *Adv. Mater.*, 17, 889- 892 (DOI: 10.1002/adma.200401176).
  148. Ahmad A., Mukherjee P., Mandal D., Senapati S., Khan M. I., Kumar R., Sastry M. (2002), Enzyme mediated extracellular synthesis of CdS nanoparticles by the fungus, *Fusarium oxysporum*, *J. Am. Chem. Soc.*, 124, 12108-12109 (DOI: 10.1021/ja027296o).
  149. Bansal V., Rautaray D., Bharde A., Ahire K., Sanyal A., Ahmad A., Sastry M. (2005), Fungus-mediated biosynthesis of silica and titania particles, *J. Mater Chem.*, 15, 2583-2589 (DOI: 10.1039/B503008K).
  150. Bansal V., Rautaray D., Ahmad A., Sastry M. (2004), Biosynthesis of zirconia nanoparticles using the fungus *Fusarium oxysporum*, *J. Mater. Chem.*, 14, 3303-3305 (DOI: 10.1039/B407904C).
  151. Bansal V., Poddar P., Ahmad A., Sastry M. (2006), Room-temperature biosynthesis of ferroelectric barium titanate nanoparticles, *J. Am. Chem. Soc.*, 128, 11958-11963 (DOI: 10.1021/ja063011m).
  152. Ahmad A., Senapati S., Khan M. I., Kumar R., Sastry M. (2003), Extracellular biosynthesis of monodisperse gold nanoparticles by a novel extremophilic actinomycete, *Thermomonospora* sp. *Langmuir*, 19, 3550-3553 (DOI: 10.1021/la026772l).
  153. Dameron C. T., Reese R. N., Mehra R. K., Kortan A. R., Carroll P. J., Steigerwald M. L., Brus L. E., Winge D. R. (1989), Biosynthesis of cadmium

- sulphide quantum semiconductor crystallites, *Nature*, 338, 596-597 (DOI: 10.1038/338596a0)
154. Virkutyte J., Varma R. S. (2011), Green synthesis of metal nanoparticles: Biodegradable polymers and enzymes in stabilization and surface functionalization, *Chem. Sci.*, 2, 837-846 (DOI: 10.1039/C0SC00338G).
155. Rokhina E. V., Lens P., Virkutyte J. (2009), Low-frequency ultrasound in biotechnology: state of the art, *Trends Biotechnol.*, 27, 298-306 (DOI: 10.1016/j.tibtech.2009.02.001).
156. Meldrum F. C., Wade V. J., Nimmo D. L., Heywood B. R., Mann S. (1991), Synthesis of inorganic nanophase materials in supramolecular protein cages, *Nature*, 349, 684-687 (DOI: 10.1038/349684a0).
157. Uchida M. *et al.* (2007), Biological containers: Protein cages as multifunctional nanoplatfoms, *Adv. Mater.*, 19, 1025-1042 (DOI: 10.1002/adma.200601168).
158. Ghadiali J. E., Stevens M. M. (2008), Enzyme-responsive nanoparticle systems, *Adv. Mater.*, 20, 4359-4363 (DOI: 10.1002/adma.200703158).
159. Karam P., Xin Y., Jaber S. Halaoui L. I. (2008), Active Pt nanoparticles stabilized with glucose oxidase, *J. Phys. Chem. C*, 112, 13846-13850 (DOI: 10.1021/jp800779c).
160. Zayats M., Katz E., Baron R., Willner I. (2005), Reconstitution of apo-glucose dehydrogenase on pyrroloquinoline quinone-functionalized Au nanoparticles yields an electrically contacted biocatalyst, *J. Am. Chem. Soc.*, 127, 12400-12406 (DOI: 10.1021/ja052841h).
161. Lee S. J., Scotti N., Ravasio N., Chung I. S., Song H. (2013), Bovine serum albumin as an effective surface regulating biopolymer for morphology control of gold polyhedrons, *Cryst. Growth Des.*, 13, 4131-4137 (DOI: 10.1021/cg400949x).
162. Xiao Y., Patolsky F., Katz E., Hainfeld J. F., Willner I. (2003), "Plugging into enzymes": Nanowiring of redox enzymes by a gold nanoparticle, *Science*, 299, 1877-1881 (DOI: 10.1126/science.1080664).

163. Deka J., Paul A., Chattopadhyay A. (2012), Modulating enzymatic activity in the presence of gold nanoparticles, *RSC Adv.*, 2, 4736-4745 (DOI: 10.1039/C2RA20056B).
164. You C. C., Agasti S. S., De M., Knapp M. J., Rotello V. M. (2006), Modulation of the catalytic behavior of  $\alpha$ -chymotrypsin at monolayer-protected Nanoparticle surfaces, *J. Am. Chem. Soc.*, 128, 14612-14618 (DOI: 10.1021/ja064433z).
165. Rangnekar A., Sarma T. K., Singh A. K., Deka J., Ramesh A., Chattopadhyay A. (2007), Retention of enzymatic activity of  $\alpha$ -Amylase in the reductive synthesis of gold nanoparticles, *Langmuir*, 23, 5700-5706 (DOI: 10.1021/la062749e).
166. Brennan *et al.* (2006), Bionanoconjugation via click chemistry: The creation of functional hybrids of lipases and gold nanoparticles, *Bioconjugate Chem.*, 17, 1373-1375 (DOI: 10.1021/bc0601018).
167. Gole A., Dash C., Soman C., Sainkar S. R., Rao M., Sastry M. (2001), On the preparation, characterization, and enzymatic activity of fungal protease-gold colloid bioconjugates, *Bioconjugate Chem.*, 12, 684-690 (DOI: 10.1021/bc0001241).
168. Gole A., Dash C., Ramakrishnan V., Sainkar S. R., Mandale A. B., Rao M., Sastry M. (2001), Pepsin-gold colloid conjugates: preparation, characterization, and enzymatic activity, *Langmuir*, 17, 1674-1679 (DOI: 10.1021/la001164w).
169. Sharma B., Mandani S., Sarma T. K. (2014), Enzymes as bionanoreactors: Glucose oxidase for the synthesis of catalytic Au nanoparticles and Au nanoparticle-polyaniline nanocomposites, *J. Mater. Chem. B*, 2, 4072-4079 (DOI: 10.1039/C4TB00218K).
170. Sharma B., Mandani S., Sarma T. K. (2013), Biogenic growth of alloys and core-shell nanostructures using urease as a nanoreactor at ambient conditions, *Sci. Rep.*, 3, 2601, (DOI: 10.1038/srep02601).
171. Willner I., Baron R., Willner B. (2006), Growing metal nanoparticles by enzymes, *Adv. Mater.*, 18, 1109-1120 (DOI: 10.1002/adma.200501865).

172. Baumann V., Muhammad M. A. H., Blanch A. J., Dey P., Rodríguez-Fernández J. (2015), Biomolecules in metal and semiconductor nanoparticle growth, *Isr. J. Chem.*, (DOI: 10.1002/ijch.201500031).
173. Ding Y., Shi L., Wei H. (2014), Protein-directed approaches to functional nanomaterials: a case study of lysozyme, *J. Mater. Chem. B*, 2, 8268-8291 (DOI: 10.1039/C4TB01235F).
174. Pavlov V., Xiao Y., Willner I. (2005), *Nano Lett.*, Inhibition of the acetylcholine esterase-stimulated growth of Au nanoparticles: Nanotechnology-based sensing of nerve gases, 5, 649-653 (DOI: 10.1021/nl050054c).
175. Zayats M., Baron R., Popov I., Willner I. (2005), Biocatalytic growth of Au nanoparticles: From mechanistic aspects to biosensors design, *Nano Lett.* 5, 21-25 (DOI: 10.1021/nl048547p).
176. Bansar B., Weizmann Y., Cheglakov Z., Willner I. (2006), Synthesis of nanowires using dip-pen nanolithography and biocatalytic inks, *Adv. Mater.*, 18, 713-718 (DOI: 10.1002/adma.200502320).
177. de la Rica R., Matsui H. (2008), Urease as a nanoreactor for growing crystalline ZnO nanoshells at room temperature, *Angew. Chem. Int. Ed.*, 47, 5415-5417 (DOI: 10.1002/anie.200801181).
178. Johnson J. M., Sinsinger N., Sun C., Li D. Kisailus D. (2012), Urease-mediated room-temperature synthesis of nanocrystalline titanium dioxide, *J. Am. Chem. Soc.*, 134, 13974-13977. (DOI: 10.1021/ja306884e).
179. Shi H., Tan L., Du Q., Chen X., Li L., Liu T., Fu C., Liu H., Meng X. (2014), Green synthesis of Fe<sub>3</sub>O<sub>4</sub> nanoparticles with controlled morphologies using urease and their application in dye adsorption *Dalton Trans.*, 43, 12474-12479 (DOI: 10.1039/C4DT01161A).
180. Shenton W., Mann S., Colfen H., Bacher A. Fischer, M. (2001), Synthesis of nanophase iron oxide in lumazine synthase Capsids, *Angew. Chem. Int. Ed.*, 40, 442-445 (DOI: 10.1002/1521-3773(20010119)40:2<442::AID-ANIE442>3.0.CO;2-2).

- 
181. Au L., Lim B., Colletti P., Jun Y. -S., Xia Y. (2010), Synthesis of Gold microplates using bovine serum albumin as a reductant and a stabilizer, *Chem Asian J.*, 5, 123-129 (DOI: 10.1002/asia.200900468).
  182. Xie J., Lee J. Y., Wang D. I. C. (2007), Synthesis of single-crystalline gold nanoplates in aqueous solutions through biomineralization by serum albumin protein, *J. Phys. Chem. C*, 111,10226-10232 (DOI: 10.1021/jp0719715).
  183. Eby D. M., Schaeublin N. M., Farrington K. E., Hussain S. M., Johnsor G. R. (2009), Lysozyme catalyzes the formation of antimicrobial silver nanoparticles, *ACS Nano*, 3, 984-994 (DOI: 10.1021/nn900079e).
  184. Guli M., Lambert E. M., Li M., Mann S. (2010), Template-directed synthesis of nanoplasmonic arrays by intracrystalline metalization of cross-Linked lysozyme crystals, *Angew. Chem. Int. Ed.*, 49, 520-523 (DOI: 10.1002/anie.200905070).
  185. Wei H. *et al.* (2011), Time-dependent, protein-directed growth of gold nanoparticles within a single crystal of lysozyme, *Nat. Nanotechnol.*, 6, 93-97 (DOI:10.1038/nnano.2010.280).
  186. Xu Y., Sherwood J., Qin Y., Crowley D., Bonizzoni M., Bao Y. (2014), The role of protein characteristics in the formation and fluorescence of Au nanoclusters, *Nanoscale*, 6, 1515-1524 (DOI: 10.1039/C3NR06040C).
  187. Xie J., Zhang Y., Ying J. Y., (2009), Protein-Directed Synthesis of Highly Fluorescent Gold Nanoclusters, *J. Am. Chem. Soc.*, 131, 888-889 (DOI: 10.1021/ja806804u).
  188. Kawasaki H., Hamaguchi K., Osaka I., Arakawa R. (2011), pH-dependent synthesis of pepsin-mediated gold nanoclusters with blue, green and red fluorescent emission, *Adv. Funct. Mater.*, 21, 3508-3515 (DOI: 10.1002/adfm.201100886).
  189. Wen F., Dong Y, Feng L., Wang S., Zhang S., Zhang X. (2011), Horseradish peroxide functionalized fluorescent gold nanoclusters for hydrogen peroxide sensing, *Anal. Chem.*, 83, 1193-1196 (DOI: 10.1021/ac1031447).
  190. Baksi A., Xavier P. L., Chaudhari K., Goswami N., Pal S. K., Pradeep T. (2013), Protein-encapsulated gold cluster aggregates: The case of lysozyme, *Nanoscale*, 5, 2009-2016 (DOI: 10.1039/C2NR33180B).
-

- 
191. Liu C. –L. *et al.* (2011), Insulin-directed synthesis of fluorescent gold nanoclusters: Preservation of insulin bioactivity and versatility in cell imaging, *Angew. Chem. Int. Ed.*, 50, 7056-7060 (DOI: 10.1002/anie.201100299).
  192. Ghosh S., Anand U., Mukherjee S. (2014), Luminescent silver nanoclusters acting as a label-free photoswitch in metal ion sensing, *Anal. Chem.*, 86, 3188-3194 (DOI: 10.1021/ac500122v).
  193. Chen T. –H., Tseng W. –L. (2012), (Lysozyme Type VI)-stabilized Au<sub>8</sub> clusters: Synthesis mechanism and application for sensing of glutathione in a single drop of blood, *Small*, 8, 1912-1919 (DOI: 10.1002/smll.201102741).
  194. Kawasaki H., Yoshimura K., Hamaguchi K., Arakawa R. (2011), Trypsin-stabilized fluorescent gold nanocluster for sensitive and selective Hg<sup>2+</sup> detection, *Anal. Sci.*, 27, 591-596 (DOI: 10.2116/analsci.27.591).
  195. Salgado E. N., Radford R. J., Tezcan F. A. (2010), Metal-directed protein self-assembly, *Acc. Chem. Res.*, 43, 661-672 (DOI: 10.1021/ar900273t)
  196. Brodin J. D., Medina –Morales A., Ni T., Salgado E. N., Ambroggio X. L., Tezcan F. A. (2010), Evolution of metal selectivity in templated protein interfaces, *J. Am. Chem. Soc.*, 132, 8610-8617 (DOI: 10.1021/ja910844n).
  197. Radford R. J., Tezcan F. A. (2009), A superprotein triangle driven by nickel(II) coordination: Exploiting non-natural metal ligands in protein self-assembly, *J. Am. Chem. Soc.*, 131, 9136-9137 (DOI: 10.1021/ja9000695)
  198. Radford R. J., Nguyen P.C., Ditri T. B., Figueroa J. S., Tezcan F. A. (2010), Controlled protein dimerization through hybrid coordination motifs, *Inorg. Chem.*, 49, 4362-4369 (DOI: 10.1021/ic100534y).
  199. Radford R. J., Lawrenz M., Nguyen P. C., McCammon J. A., Tezcan F. A. (2011), Porous protein frameworks with unsaturated metal centers in sterically encumbered coordination sites, *Chem. Commun.*, 47, 313-315 (DOI: 10.1039/C0CC02168G).
  200. Sangeetha N. M., Maitra U. (2005), Supramolecular gels: Functions and uses, *Chem. Soc. Rev.*, 34, 821-836 (DOI: 10.1039/b417081b).
  201. Estroff L. A., Hamilton A. D. (2004), Water gelation by small organic molecules, *Chem. Rev.*, 104, 1201-1218 (DOI: 10.1021/cr0302049).
-

- 
202. Praveen V. K., Ranjith C., Bandini E., Ajayaghosh A., Armaroli N. (2014), Oligo(phenylenevinylene) hybrids and self-assemblies: Versatile materials for excitation energy transfer, *Chem. Soc. Rev.*, 43, 4222-4242 (DOI: 10.1039/C3CS60406C).
  203. Das D., Kar T., Das P. K. (2012), Gel-nanocomposites: Materials with promising applications, *Soft Matter*, 8, 2348-2365 (DOI: 10.1039/c1sm06639k).
  204. Tam A. Y. –Y., Yam W. –W. (2013), Recent advances in metallogels, *Chem. Soc. Rev.*, 42, 1540-1567 (DOI: 10.1039/C2CS35354G).
  205. Naota T., Koori H. (2005), Molecules that assemble by sound: An application to the instant gelation of stable organic fluids, *J. Am. Chem. Soc.*, 127, 9324-9325 (DOI: 10.1021/ja050809h).
  206. Berdilang D. *et al.* (2005), Unusual sculpting of dipeptide particles by ultrasound induces gelation, *J. Am. Chem. Soc.*, 130, 3313-3315 (DOI: 10.1021/ja711342y).
  207. Li Y., Rodrgues J., Tomás H. (2012), Injectable and biodegradable hydrogels: Gelation, biodegradation and biomedical applications, *Chem. Soc. Rev.*, 41, 2193-2221 (DOI: 10.1039/c1cs15203c).
  208. Eppel E. A., Barrio J. D., Loh X. J., Scherman O. A. (2012), Supramolecular polymeric hydrogels, *Chem. Soc. Rev.*, 41, 6195-6214 (DOI: 10.1039/c2cs35264h).
  209. Adams D. J., Topham P. D., (2010), Peptide conjugate hydrogelators, *Soft Matter*, 6, 3707-3721 (DOI: 10.1039/C000813C).
  210. Du X., Zhou J., Shi J., Xu B. (2015), Supramolecular hydrogelators and hydrogels: from soft matter to molecular biomaterials, *Chem. Rev.*, 115, 13165-13307 (DOI: 10.1021/acs.chemrev.5b00299).
  211. Ulijin R. V., Smith A. M. (2008), Designing peptide based nanomaterials, *Chem. Soc. Rev.*, 37, 664-675 (DOI: 10.1039/b609047h).
  212. Mitra R. N., Das D., Roy S., Das P. K. (2007), Structure and properties of low molecular weight amphiphilic peptide hydrogelators, *J. Phys. Chem. B*, 111, 14107-14113 (DOI: 10.1021/jp076495x).
-

213. Jung J. H., Lee J. H., Silverman J. R., John G. (2013), Coordination polymer gels with important environmental and biological applications, *Chem. Soc. Rev.*, 42, 924-936 (DOI: 10.1039/c2cs35407a).
214. Xing B., Choi M. -F., Xu B. (2002), Design of coordination polymer gels as stable catalytic systems, *Chem. Eur. J.*, 8, 5028-5032 (DOI: 10.1002/1521-3765(20021104)8:21<5028::AID-CHEM5028>3.0.CO;2-1).
215. Zhang J., Su C. -Y. (2013), Metal-organic gels: From discrete metallogelators to coordination polymers, *Coord. Chem. Rev.*, 257, 1373-1408 (DOI: 10.1016/j.ccr.2013.01.005).
216. Bhattacharjee S., Samanta S. K., Moitra P., Pramoda K., Kumar R., Bhattacharya S., Rao C. N. R. (2015), Nanocomposite made of an oligo(p-phenylenevinylene)-based trihybrid thixotropic metallo(organo) gel comprising nanoscale metal-organic particles, carbon nanohorns, and silver nanoparticles, *Chem. Eur. J.*, 21, 5467-5476 (DOI: 10.1002/chem.201405522).
217. Aiyappa H. B., Saha S., Wadge P., Banerjee R., Kurungot S. (2014), Fe(III) phytate metallogel as a prototype anhydrous, intermediate temperature proton conductor, *Chem. Sci.*, 6, 603-607 (DOI: 10.1039/c4sc02294g).

## Chapter 2

# Enzymes as Bionanoreactors: Glucose Oxidase for the Synthesis of Catalytic Au Nanoparticles and Au Nanoparticle-Polyaniline Nanocomposite

### 2.1 Introduction

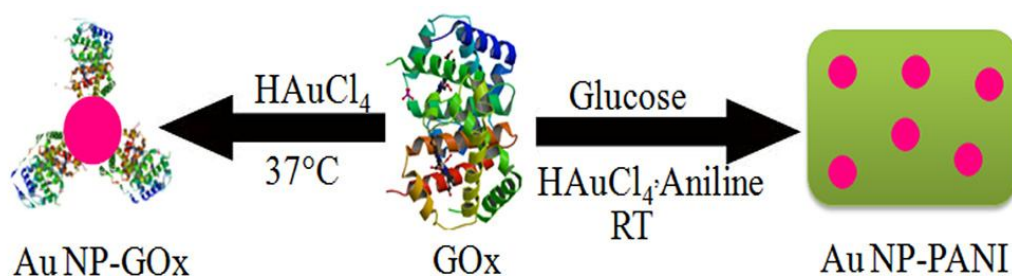
Inorganic nanoparticles are considered potential structural building blocks for new functional materials.<sup>[1-5]</sup> Since the properties of such functional materials largely depend on the size, shape and composition of the building blocks, therefore, exploration of facile and efficient methods for design and fabrication of such structures is critically important. Recently, the growth of inorganic nanoparticles directed by biomolecules has evolved as an area of intense research owing to the capability of biomolecules in the synthesis and directed assembly of inorganic nanostructures under environmentally benign conditions such as room temperature and in aqueous medium. Several microbes such as viruses,<sup>[6]</sup> fungi<sup>[7]</sup> etc. and a variety of biomolecules such as proteins, peptides and nucleic acids have been used as templates for the fabrication and functionalization of inorganic nanostructures.<sup>[8-14]</sup> Enzymes, another class of biomolecules, which are responsible for the interconversion of various reactions in the living world, have attracted tremendous interest in the development of nano-bio integrated materials. The spatially confined environment of the enzymes could be anticipated to facilitate the crystallization of inorganic materials with nanometer dimensions.<sup>[15-17]</sup> The natural activity of enzymes have been explored for the precise and dimensional growth of metal and metal oxide nanoparticles during an enzyme catalyzed reaction, where the product of the enzyme stimulated reaction governs the nucleation and growth of the nanoparticles.<sup>[15-22]</sup> Although, there have been quite a few reports exploring the enzymes as reducing as well as stabilizing agents themselves for the synthesis of metallic nanoparticles,<sup>[23-26]</sup> a clear detailed mechanistic investigation of reduction of metal salts by enzymes have not been performed. The use of enzymes as nanoreactors

for the synthesis of nanoparticles will not only offer a greener route by elimination of conventional drawbacks such as elevated temperatures and harsh chemical reagents, but will also provide a pathway for the development of nanoparticle incorporated functional materials with potential in diverse applications, taking advantage of the activity of the enzyme.

Polyaniline (PANI), as a conducting polymer is one of the most extensively studied because of its high environmental stability and tunability of opto-electrical properties.<sup>[27,28]</sup> PANI is an attractive material because on one hand it has optical, electronic and magnetic properties that could be tailored from metallic to insulator depending on its oxidation state and degree of protonation and on the other hand it shows property of flexibility and processability characteristic of conventional polymers.<sup>[29]</sup> Further, composite materials of PANI with metal nanoparticles are currently of great research interest as they combine the tunable opto-electronic properties of this low dimensional organic conductor with unique optical and catalytic properties of metallic nanoclusters. Therefore, there has been a great surge for synthetic methodologies involving single reagent for the generation of metallic nanoparticles as well as polymerization of aniline, thereby resulting in a composite.<sup>[30-34]</sup> The major concern of dispersibility as well as processability of PANI in common solvents could be overcome by controlling the size of the composite in the nanometer dimension. The use of bioreactors with spatially confined environment such as enzymes could provide an environmentally favourable pathway towards the controlled generation of biofunctionalized nanoparticle-PANI composites in water under mild conditions.

In this chapter, the capability of glucose oxidase (GOx), a flavoprotein towards the synthesis of Au NPs as well as Au NP- PANI nanocomposite has been reported. Glucose oxidase, a dimer of two identical monomer units with molecular mass of 160 kDa contains one flavin adenine dinucleotide (FAD) molecule, one free sulfhydryl group<sup>[35]</sup> and several other free amino acid residues per monomer, with known reduction capability for Au<sup>3+</sup> ions to form Au-NPs. The nanoparticles synthesized using GOx exhibited excellent catalytic activity towards the reduction of *p*-nitrophenol to *p*-aminophenol, with NaBH<sub>4</sub> acting as a reducing agent. Since GOx is a redox enzyme, involved in the breakdown of D-glucose to gluconic acid and H<sub>2</sub>O<sub>2</sub>, it was investigated

as reducing as well as stabilizing agent for the synthesis of Au NPs. The byproduct  $\text{H}_2\text{O}_2$  is well known to polymerize aniline into PANI.<sup>[30]</sup> So it was anticipated that after the synthesis of Au NPs, the enzyme activity might be capitalized to polymerize aniline, thereby resulting in Au NP-PANI nanocomposite. However, the enzyme activity was largely inhibited after it was involved in the reduction of  $\text{Au}^{3+}$  to form Au NPs. Therefore, in an alternative strategy, the Au NP-PANI composite was synthesized with controlled dimension in a glucose oxidase stimulated pathway, where the  $\text{H}_2\text{O}_2$  generated during the oxidation of glucose was used as both reducing as well as oxidizing agent.<sup>[30]</sup> It was interesting to note that the PANI as well as Au NP-PANI nanocomposite synthesized using GOx were well dispersed in water and stable without any signs of precipitation.



**Scheme 2.1.** Schematic representation of the use of glucose oxidase for the synthesis of Au NPs as well as Au NP-PANI nanocomposite.

## 2.2 Results and Discussion

### 2.2.1 Synthesis and characterization of Au nanoparticles

The reducing capability of GOx was realized by the incubation of the enzyme (3 ml of 0.7 mg/ml) with  $\text{HAuCl}_4$  (final concentration of  $6 \times 10^{-4}$  M) in phosphate buffer saline (PBS) at pH 7.0 and  $37^\circ\text{C}$ . The simple incubation resulted in a colour change from light yellow to pink after 36 hours (Figure 2.1a), which colorimetrically indicated the formation of Au NPs. The synthesized Au NPs were characterized using several spectroscopic techniques as well as electron microscopy. The nanoparticles exhibited their characteristic surface plasmon resonance (SPR) band at 533 nm (Figure 2.1a). The powder X-ray diffraction spectrum consisted of peaks at  $2\theta$  values of 38.2, 44.4, 64.6 and 77.7 degrees corresponding to (111), (200), (220) and (311) facets of the fcc structure of Au (Figure 2.1b). The TEM image (Figure 2.1c) showed nearly spherical

particles, and from the particle size histogram it was observed that the diameter of the nanoparticles varied from 3-18 nm and the average particle size was calculated to be  $7.5 \pm 3.0$  nm (figure 2.1d). The average crystallite size of 11.5 nm as calculated from the Scherrer equation was in good agreement with the TEM results. Selected area electron diffraction pattern (inset; Figure 2.1c) of the Au nanoparticles further confirmed their crystallinity and was in good accordance with the powder XRD results. The average particle size of Au NPs (as calculated from TEM images) correlated well with the optical properties of the nanoparticles as predicted by theoretical calculations (figure 2.1e) and previous experimental reports.<sup>[36,37]</sup> The HRTEM image of Au NPs as shown in figure 2.1f indicated the presence of planes with lattice spacing 0.23 nm due to the (111) plane of Au.

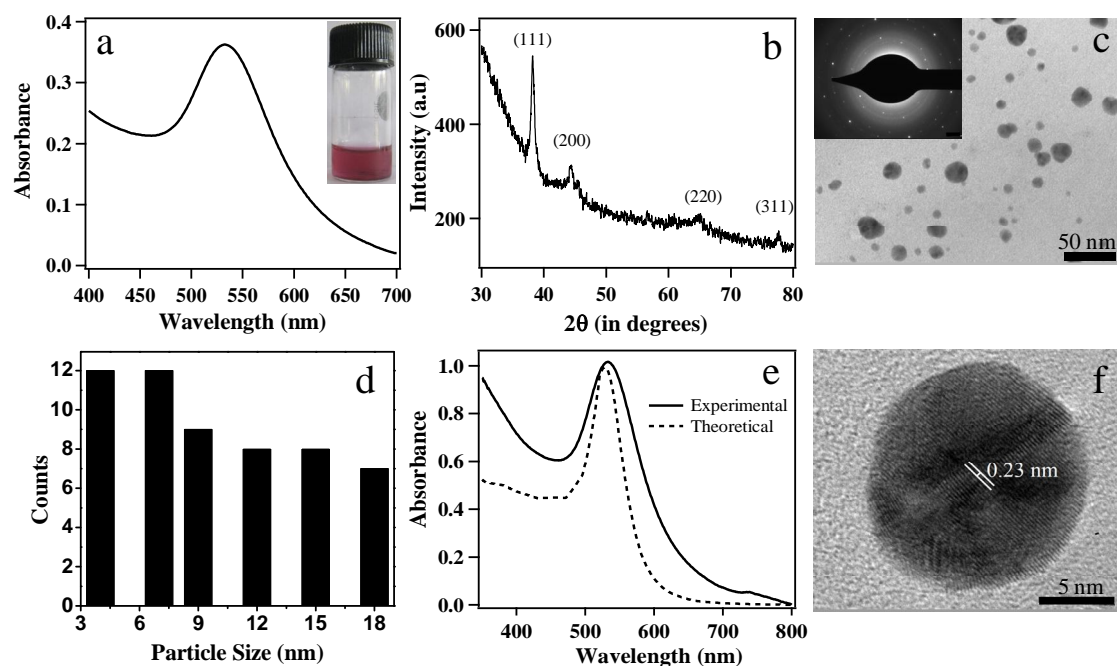


**Figure 2.1.** (a) UV-visible spectrum and digital image (inset) of the synthesized Au NPs, (b) Powder XRD spectrum of the Au NPs showing characteristic Bragg reflection, (c) TEM image and SAED pattern (inset) of the Au NPs, (d) Particle size distribution histogram of the Au NPs, (e) UV-visible spectrum of the Au NPs showing perfect match of the experimental absorption spectrum (solid line) with calculated absorption spectrum (dashed line) as calculated using Mieplot v4304 software for Au nanoparticles with average diameter 9.9 nm and (f) HRTEM image of the Au NPs showing lattice spacing of 0.23 nm corresponding to (111) plane of Au.

## 2.2.2 Effect of concentration of $\text{Au}^{3+}$ and GOx on the morphology of Au NPs

It is well known that the concentration of metal ions, reductant or the stabilizer plays a crucial role in controlling the final size and morphology of the metal nanoparticles.<sup>[38-40]</sup> So, in order to evaluate the effect of the concentrations of  $\text{HAuCl}_4$  and GOx on the morphology and size of Au nanoparticles, different set of reactions by varying the concentration of  $\text{Au}^{3+}$  ions and GOx were performed. Drastic changes in the morphology and size of nanoparticles together with agglomeration of the nanoparticles was observed upon varying the concentrations of enzyme or  $\text{Au}^{3+}$  ions.

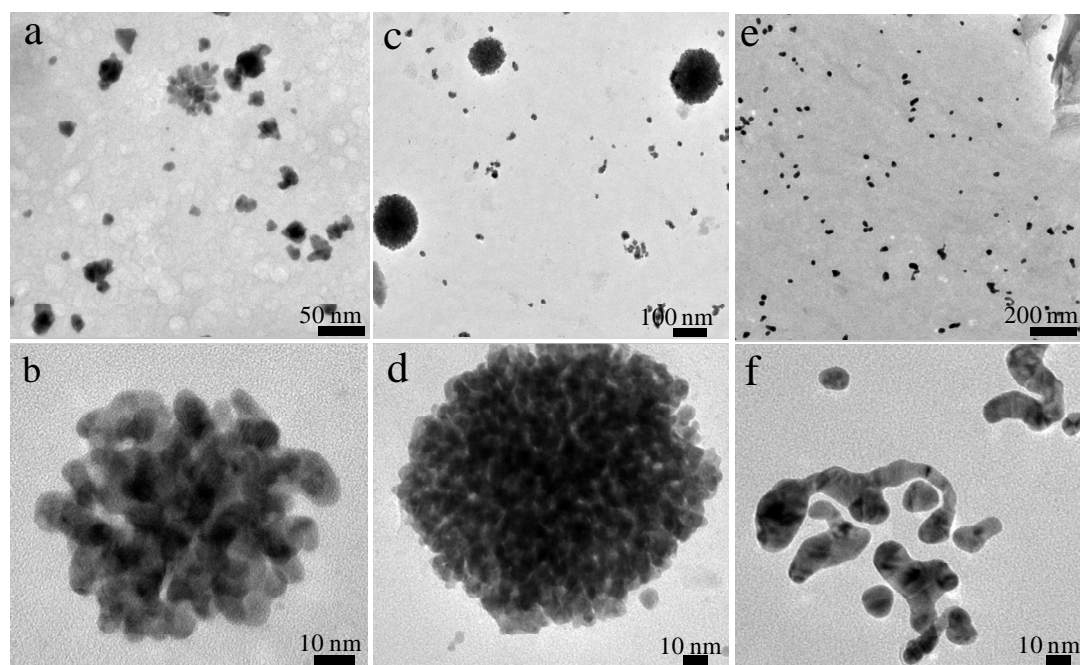


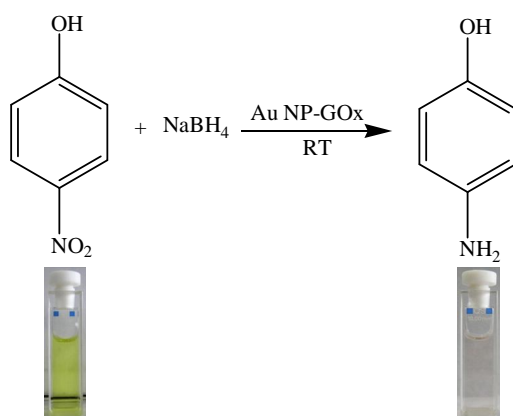
**Figure 2.2.** (a) TEM image and (b) HRTEM image of Au nanostructures synthesized using glucose oxidase with an enzyme concentration of 1.75 mg/ml and  $\text{HAuCl}_4$  concentration  $6 \times 10^{-4}$  M. (c) TEM image and (d) HRTEM image of Au nanostructures synthesized using glucose oxidase with an enzyme concentration of 0.7 mg/ml and  $\text{HAuCl}_4$  concentration  $1.5 \times 10^{-3}$  M. (e) TEM image and (f) HRTEM image of Au nanostructures synthesized with a glucose oxidase concentration of 0.7 mg/ml and  $\text{HAuCl}_4$  concentration  $3 \times 10^{-3}$  M.

It was observed that when the concentration of the enzyme was increased by 2.5 times (1.75 mg/ml), keeping the concentration of  $\text{HAuCl}_4$  constant (i.e.  $6 \times 10^{-4}$  M), the Au nanoparticles agglomerated to form flower like structure (Figure 2.2a and b). When

the concentration of enzyme was kept constant (0.7 mg/ml) and the concentration of  $\text{HAuCl}_4$  was increased to 2.5 times (final concentration  $1.5 \times 10^{-4}$  M) and 5 times (final concentration  $3 \times 10^{-4}$  M), it was observed that the particles agglomerated to give a flower like morphology (Figure 2.2c and d) and worm like morphology (Figure 2.2e and f) respectively.

### 2.2.3 Catalytic activity of the Au NPs

Metallic NPs deposited on various support systems such as polymers,<sup>[41,42]</sup> peptides,<sup>[43,44]</sup> inorganic oxides<sup>[45]</sup> etc. have shown tremendous applicability as heterogeneous catalysts. In order to realize the catalytic potential of Au NPs on an enzyme support, the reduction of *p*-nitrophenol in water using  $\text{NaBH}_4$  as the reducing agent was carried out. The reduction of *p*-nitrophenol by  $\text{NaBH}_4$  was chosen as a model reaction because the progress of the reaction can easily be monitored using UV-visible spectroscopy.<sup>[46]</sup> The addition of  $\text{NaBH}_4$  to a *p*-nitrophenol solution resulted in the change in color of the solution from light yellow to intense yellow due to the formation of *p*-nitrophenolate ion.



**Scheme 2.2.** Scheme for the reduction of *p*-nitrophenol to *p*-aminophenol by  $\text{NaBH}_4$  with Au NPs synthesized using GOx acting as catalyst. Below are the digital images of *p*-nitrophenolate ions (yellow) and *p*-aminophenol (colourless).

In absence of Au NPs the reduction leading to the formation of *p*-aminophenol did not occur at all even after 4 days. This was evident through the control experiments, which showed only a single peak at 400 nm in the UV-visible spectrum (figure 2.3a) as attributed to the *p*-nitrophenolate ion. However, with the addition of Au NP-GOx

composite, the yellow colour of the solution slowly faded away, as confirmed visually. UV-visible studies showed a gradual decrease in the intensity of the peak at 400 nm and formation of a new peak at 300 nm (Figure 2.3b), indicative of the gradual conversion of *p*-nitrophenolate ion to *p*-aminophenol. The Au NP-GOx composite was found to act as a highly effective catalyst as evidenced by the reduction of 0.12 mM *p*-nitrophenol in just 15 minutes, when 25  $\mu$ l of the Au nanoparticle-GOx composite was used as catalyst ( $\sim 0.005$  mmol). Controlled experiment with solution of *p*-nitrophenol containing GOx without Au NPs was also performed to ascertain that it was the Au NPs rather than GOx which acted as a catalyst. It was confirmed from the controlled experiment that GOx alone was incapable of catalyzing the reduction, as the color of the solution remained unaltered even after a week. Since for the reduction a large excess of  $\text{NaBH}_4$  was used, it was reasonable to consider its concentration to be constant throughout the reaction and the kinetics of the reaction could be evaluated with respect to the rate of *p*-nitrophenol consumption. A linear relationship between  $\ln$  (absorbance) and time (figure 2.3c) was indicative of pseudo first order kinetics. The apparent rate constant,  $k$  as calculated from the plot of  $\ln A$  versus time was found to be  $4.2 \times 10^{-3} \text{ s}^{-1}$ .

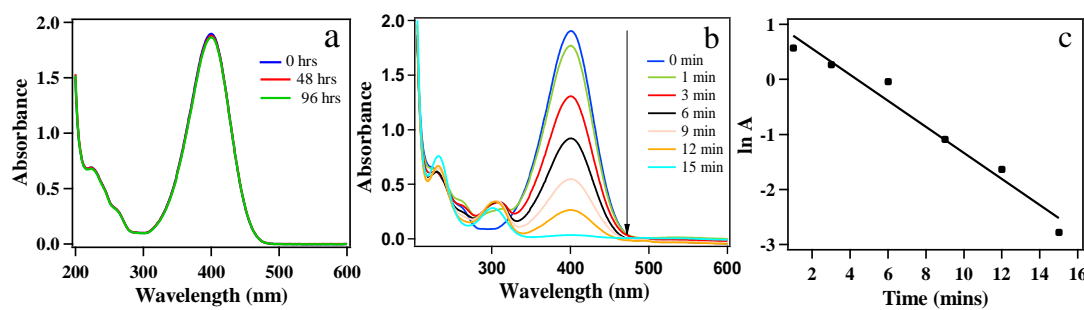


**Figure 2.3.** (a) UV-visible spectrum for the reduction of *p*-nitrophenol by  $\text{NaBH}_4$  in the absence of GOx reduced Au nanoparticles, (b) Time dependent UV-Visible spectra for the catalytic reduction of *p*-nitrophenol by  $\text{NaBH}_4$  in the presence of Au NPs synthesized using GOx. (c) plot of natural log of absorbance at 400 nm versus time.

#### 2.2.4 Activity of GOx after the synthesis of Au NPs

To elucidate the activity of the enzyme post the reduction of  $\text{Au}^{3+}$  to Au NPs, the synthesis of PANI using the Au NP-enzyme composite was attempted. For this, glucose was added to the Au NP-GOx solution followed by addition of aniline in HCl

(pH of the final solution was 2.0). In case of active GOx, glucose should have been converted to gluconic acid and H<sub>2</sub>O<sub>2</sub>, and the H<sub>2</sub>O<sub>2</sub> formed should have acted as an oxidant for the polymerization of aniline leading to the formation of green emeraldine salt form of PANI. However, there was only a slight change in the colour of the solution and the typical green colour of emeraldine salt form was not observed. The UV-visible spectrum showed a small peak at 738 nm along with a much intense peak at 536 nm corresponding to Au NPs (Figure 2.4a). This indicated that H<sub>2</sub>O<sub>2</sub> generation by GOx in this case was extremely low. From this experiment it was concluded that the enzymatic activity of GOx was largely inhibited after their participation as a reducing agent for the synthesis of Au NPs.

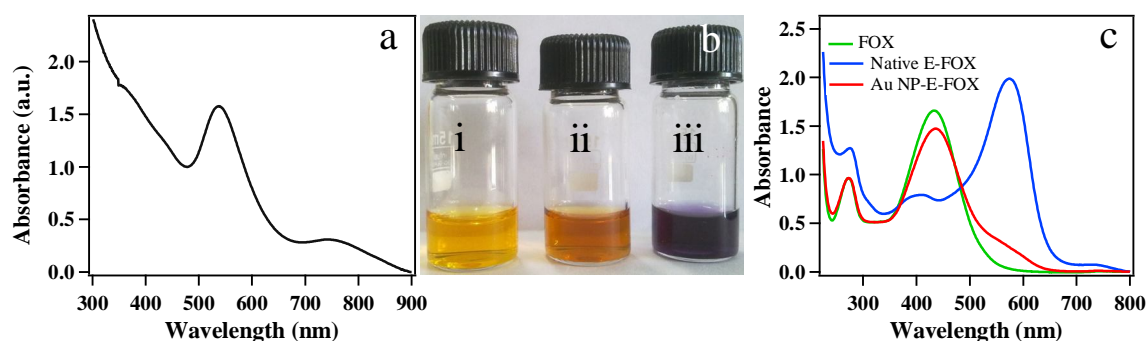


**Figure 2.4.** (a) UV-visible spectrum of Au NP-GOx-PANI composite indicating the decrease in the activity of GOx after its involvement in the synthesis of Au nanoparticles, (b) Photograph showing the reaction of native GOx and the Au NP- GOx composite with FOX reagent after addition of glucose, indicating the inhibition of activity of Au NP-GOx composite. (i) Blank FOX reagent, (ii) Au NP- GOx- FOX after addition of glucose and (iii) Native GOx- FOX after addition of glucose. (c) UV-visible spectrum showing the inhibition of activity of GOx after its participation as a reducing agent in the synthesis of Au NPs.

The decrease in the activity of the enzyme was further confirmed by the spectrophotometric assay known as FOX method.<sup>[47]</sup> The method is based on the oxidation of ferrous ions to ferric ions by hydrogen peroxide and simultaneous purple colored complex formation of the ferric ions with xylenol orange. It was observed that after incubation of solutions of FOX reagent with Au NP-GOx composite and native GOx for an appropriate duration of time, the color of the solution changed from yellow to brown and purple respectively (figure 2.4b). Also, from the UV-visible spectrum (figure 2.4c) it was seen that in case of Au NP-GOx composite, the peak at 435 nm due

to the FOX reagent slightly decreased in intensity. However, in case of native GOx the peak at 435 nm almost disappeared and a new peak due to the purple complex formed by the complexation of ferric ions with xylenol orange at 575 nm was observed. The results clearly indicated that a large fraction of the enzymatic activity of GOx was inhibited.

### **2.2.5 Conformational changes in the structure of GOx after the synthesis of Au NPs**

The decrease in the activity of the enzyme is attributed to the conformational change that the enzyme had undergone during the synthesis of Au NPs. Circular dichroism (CD) is a major tool for studies related to the conformational changes in a protein. Secondary and tertiary structural changes in the enzyme can be followed by observing the changes in the CD signals at particular wavelengths.<sup>[48]</sup> So, CD was used to probe the changes in the conformation of glucose oxidase after the synthesis of Au NPs. The native enzyme exhibited characteristic minima at around 208 nm and 222 nm in the far UV region (figure 2.5a), a strong band in the near UV region at 274 nm and another CD band due to flavin adenine dinucleotide (FAD) in the visible region at 375 nm (figure 2.5b). However in case of GOx after the synthesis of Au NPs, the CD band at 222 nm decreased in intensity and the minima at 208 nm was shifted to 206 nm together with a decrease in the intensity. The results signify a decrease in the  $\alpha$ -helical content of the enzyme which is an indication of changes in its secondary structure. In the near UV region, the intense CD band at 274 nm that arises due to the asymmetric environment of the aromatic amino acid residues disappeared completely suggesting the perturbation in the tertiary structure of the enzyme.<sup>[47]</sup> Also it was found that the band at 375 nm drastically decreased in intensity and was shifted to 333 nm. The change in environment around the FAD during the synthesis of Au NPs may probably be the reason for such a shift and decrease in intensity.<sup>[49]</sup>

In order to ascertain that the variations observed in CD spectrum of GOx after the synthesis of Au NPs were due to the conformational changes taking place during its involvement in the reduction of  $\text{Au}^{3+}$  to  $\text{Au}^0$  and not merely due to the presence or adsorption of the enzyme onto Au nanoparticles, CD investigation of GOx adsorbed on

Au NPs synthesized by citrate method was performed. The Au NPs synthesized using trisodium citrate as a reducing agent were incubated with GOx for 12 hours to allow its adsorption on the surface of nanoparticles. As observed from the CD spectra in the UV and visible region, there were no appreciable changes in the characteristic bands, signifying that the secondary and tertiary structure of GOx were intact after getting adsorbed on Au NPs. This was further confirmed by the polymerization of aniline in presence of glucose, where the green Au NP-PANI composite was formed.

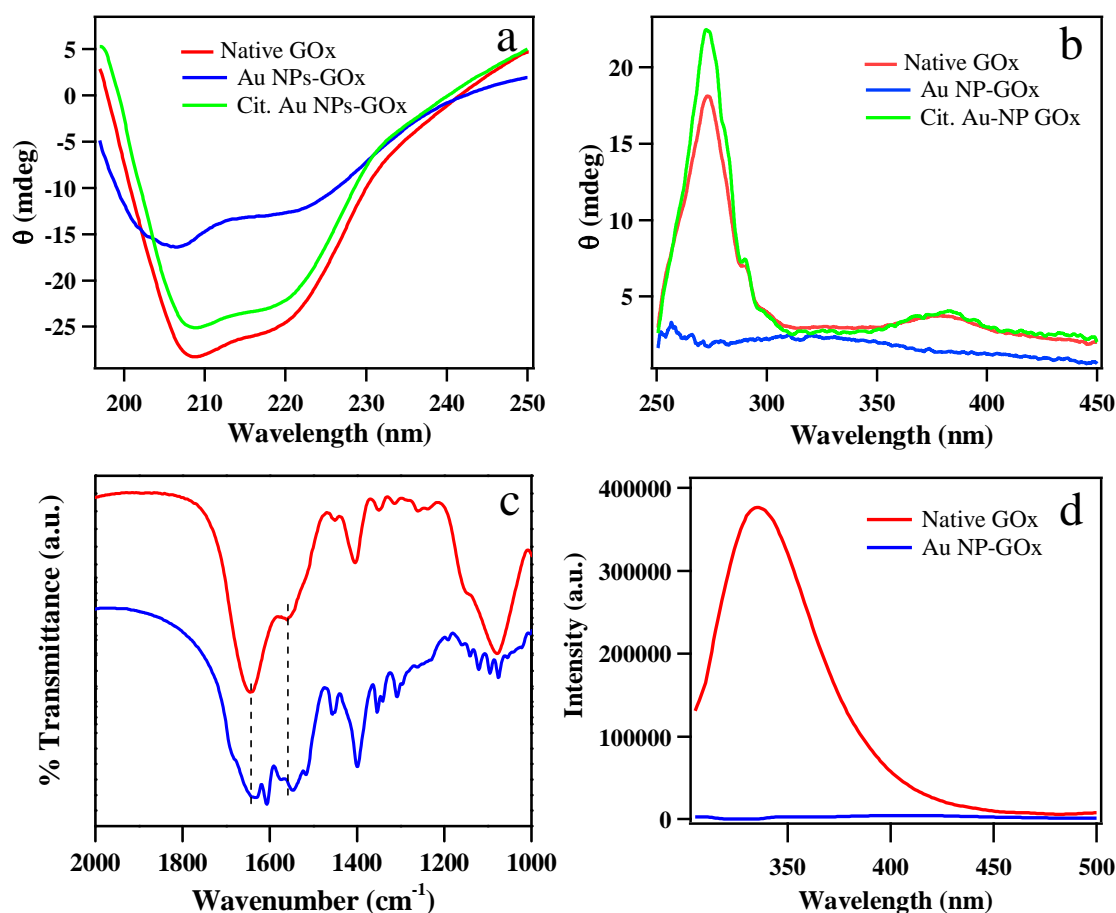


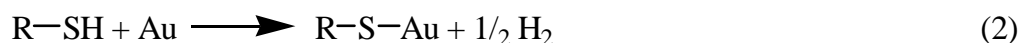
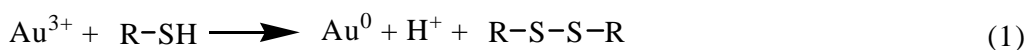
**Figure 2.5.** Circular dichroism spectra of native GOx and Au NP-GOx composite in (a) far UV region and (b) near UV and visible region. (c) FTIR spectrum of native GOx (red line) and Au NP-GOx composite (blue line). Dashed lines indicate the shift in the amide I and amide II bands in native GOx and the Au NP-GOx composite. (d) Emission spectra of GOx and the Au NP-GOx composite ( $\lambda_{ex} = 295$  nm).

The conformational changes in the enzyme structure were further confirmed using FTIR spectroscopy. FTIR spectrum in the region of 1700-1600  $\text{cm}^{-1}$  and 1600-1500  $\text{cm}^{-1}$  known as amide I and amide II region respectively yielded useful



To justify the assumption, the sulfhydryl groups in GOx were modified using 5,5'-dithiobis(2-nitrobenzoic acid) (DTNB).<sup>[51]</sup> Thiols react with DTNB, cleaving the disulfide bond in DTNB to give 2-nitro-5-thiobenzoate (TNB<sup>-</sup>) anion, which ionizes in water to give the TNB<sup>2-</sup> dianion, which is yellow in color and absorbs at 412 nm. The addition of HAuCl<sub>4</sub> to the DTNB modified enzyme did not result in the formation of Au NPs, as evidenced visually and from UV-visible studies (figures 2.6a and b), which showed the absence of SPR band of Au NPs. Further, FTIR studies showed the absence of a weak band at 2630 cm<sup>-1</sup> attributed to the S-H stretching<sup>[52]</sup> in the Au NP-GOx composite (figure 2.6c), confirming the oxidation of the free sulfhydryl group during Au NP synthesis. In case of heat denatured GOx, the incubation of HAuCl<sub>4</sub> led to the formation of Au NPs in an approximately similar duration as that of the native enzyme, clearly depicting the fact that it is not the native three dimensional structure of GOx but the functional groups present in it which are essential for the Au NP synthesis.

The reducing ability of the enzyme, presumably because of free thiols present in the cysteine residues function as follows during the synthesis of Au nanoparticles:



The free thiols provide electrons to Au<sup>3+</sup> for reduction and themselves get converted to disulfides.

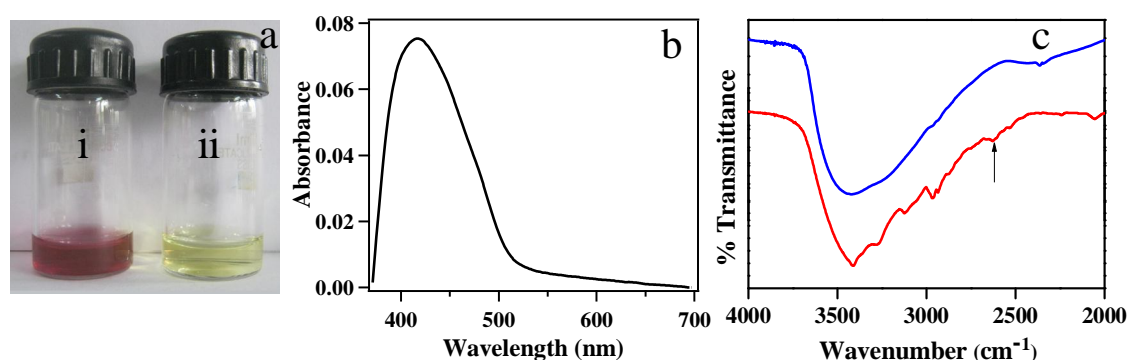


**Figure 2.6.** (a) Digital image showing reaction of GOx with HAuCl<sub>4</sub> in PBS (i) unmodified GOx and (ii) after modification using DTNB, (b) UV- vis spectrum of DTNB modified GOx after incubation with Au<sup>3+</sup> for 60 hours, showing the absence of SPR band of Au NPs. (c) FTIR spectrum of native GOx (red line) and Au-NP-GOx composite (blue line). Arrow in red line indicates the S-H stretching which is absent in blue line.

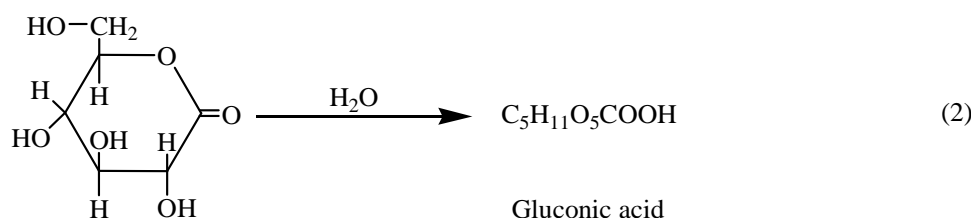
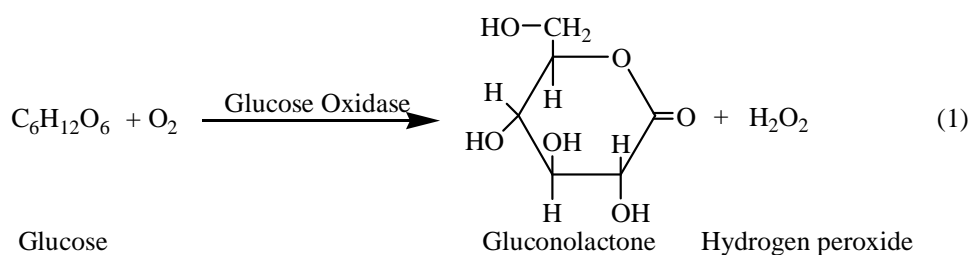
As the free cysteine group is located away from the FAD active site or glycosylation site, it was expected that modification of the cysteine groups will not have any impact on the catalytic activity of the enzyme after they participated in the reduction of the metal salt.<sup>[25]</sup> However, in case of GOx, large inhibition of enzymatic activity after their involvement in Au NP synthesis was observed. As observed from the CD experiments, there was a drastic conformational change in the FAD active site after the reduction process and subsequent adsorption on the nanoparticle surface. Hence, there is a possibility of involvement of other amino acids in the active site or FAD itself in the stabilization of nanoparticles. From the CD spectrum, it was observed that the band at 274 nm in case of native GOx was absent after the synthesis of Au NPs. As the band signifies the asymmetric environment of the aromatic amino acid residues, its absence suggested the possibility of the involvement of amino acids such as tryptophan, tyrosine and phenylalanine in the reduction/stabilization process. Also from the fluorescence studies, it was observed that the emission due to tryptophan residues was completely quenched, suggesting the probable loss or modification of the tryptophan residues. Previous report<sup>[49]</sup> have shown that in case of native enzyme, the emission intensity originating due to tryptophan residues in GOx is significantly lower due to Forster resonance energy transfer from the tryptophan residues to FAD. However, in case of heat denatured enzyme, the emission peak corresponding to tryptophan enhances significantly as FAD is dissociated from GOx in this case. However, in our case the fluorescence due to the tryptophan residues was completely quenched after the synthesis of Au NPs, suggesting their possible involvement in the reduction or capping of the nanoparticles. Nevertheless, a clear understanding of the mechanism for the biogenic reduction of metal salt by GOx remains unclear and needs further investigations.

### **2.2.7 Synthesis and characterization of Au NP-polyaniline nanocomposite**

Due to conformational changes in the native structure of the GOx during the formation of Au NPs, the enzyme lost a large fraction of its catalytic activity towards the oxidation of glucose forming gluconic acid and H<sub>2</sub>O<sub>2</sub>. The Au-GOx composite thus

formed was incapable of complete polymerization of aniline leading to the formation of Au NP-PANI composite. Therefore it became imperative for us to look for an alternative strategy for the biocatalytic synthesis of Au NP-PANI composite using GOx as the template.

The reduction of oxygen, resulting in the formation of hydrogen peroxide can be achieved via enzymatic route using the enzyme glucose oxidase. The enzyme glucose oxidase catalyzes the oxidation of glucose to gluconic acid and hydrogen peroxide according to the following reactions:



It is well known that  $\text{H}_2\text{O}_2$  has both oxidation and reduction properties.<sup>[30]</sup> Hence  $\text{H}_2\text{O}_2$  generated through the oxidation of glucose by GOx could be used for the reduction of  $\text{HAuCl}_4$  to form Au NPs followed by oxidative polymerization of aniline in a one-pot synthesis leading to Au NP-PANI composite material with nanometer dimensions.

The time dependent formation of Au NP-PANI nanocomposite was followed by UV-visible spectroscopy and the results are shown in figure 2.7a.  $\text{H}_2\text{O}_2$  generated by the catalytic oxidation of glucose by GOx was able to reduce  $\text{HAuCl}_4$  to form Au NPs that showed purple color and exhibited SPR band at 562 nm (figure 2.7b). However upon the addition of HCl, the colour of the solution changed to pink within 30 minutes and the SPR band blue shifted to 537 nm. It is known that nanoparticles are very sensitive to the dielectric constant of the surrounding environment and a slight change in the medium can result in a marked variation in the position and intensity of the SPR

band.<sup>[53,54]</sup> In the present case, the change of dielectric constant upon change of pH from 7.0 to 2.0 probably caused the SPR band of Au NPs to shift from 562 nm to 537 nm. When aniline was added, the intensity of the SPR band of Au NPs at 537 nm first increased but began to decrease as the aniline started to polymerize. With time, the colour of the solution became light green to dark green (figure 2.7c) suggesting the formation of the conductive emeraldine salt form of PANI, with the continuous growth of two new peaks at 360 nm and 735 nm in the UV-visible spectra. The decrease in the intensity of the Au SPR band at 537 nm could be attributed to the PANI coating on the Au NPs. It was observed that the SPR band of Au NPs, though decreased in intensity with time, but was clearly evident in the UV-visible spectrum even after complete polymerization of aniline. Previously, it was reported that the plasmon resonance band of Au NPs disappeared while they were exposed to positively charged anilinium ions, hence optical characteristics of Au NPs could not be observed in the Au NP-PANI composite.<sup>[30,31]</sup> In our case, the Au NPs formed as a result of the reduction of  $\text{HAuCl}_4$  by  $\text{H}_2\text{O}_2$  were stabilized by the enzyme. Thus the enzyme layer on the nanoparticle surface prevented the direct interaction of Au NPs with the positively charged anilinium ions. As a result of this, the SPR band of the Au NPs was evident in the composite. For comparison, PANI nanoparticles by the same synthetic pathway, but in absence of Au NPs were synthesized. In this case, the longitudinal band of PANI was observed at 755 nm, a 20 nm shift towards the longer wavelength as compared to Au NP-PANI composite (figure 2.7d). The shift might be due to the formation of PANI of a molecular weight different from that of the composite or it might also be a signature of the level of proton doping in the PANI synthesized in the absence of Au NPs.<sup>[31]</sup>

The FTIR spectrum of the Au NP-PANI nanocomposite (Figure 2.7e) showed peaks at 1495 and 1570  $\text{cm}^{-1}$  which are characteristic of the benzenoid and quinoid ring deformations respectively. The broad peak at 3400  $\text{cm}^{-1}$  is assigned to N-H stretching. This spectrum was quite similar to the spectrum of PANI synthesized by the same procedure but in the absence of Au NPs, which suggested that there was little structural difference between the PANI alone and PANI in the Au NP-PANI composite. In both the cases, the benzenoid band at 1495  $\text{cm}^{-1}$  was more intense than the quinoid band.

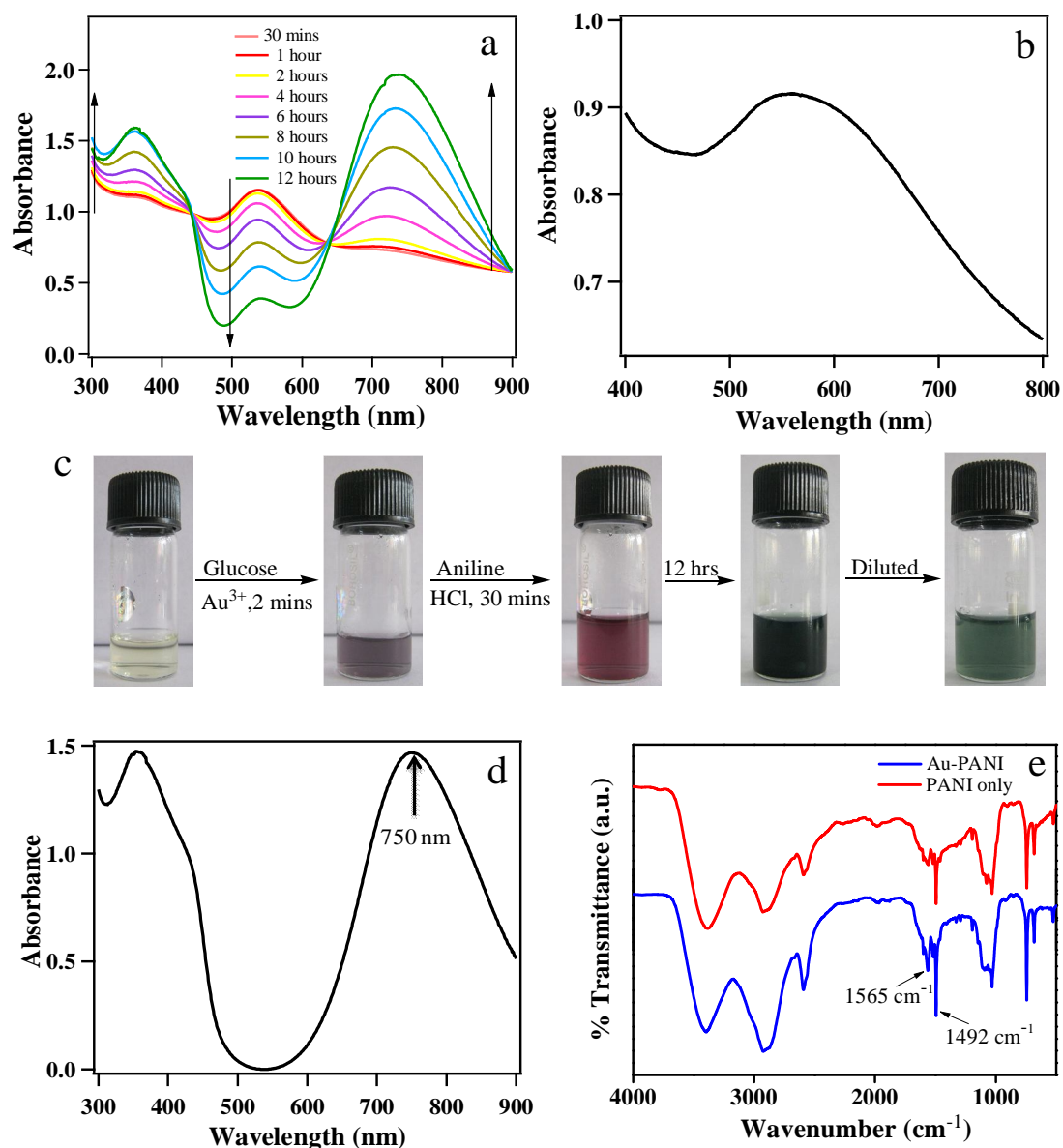


**Figure 2.7.** (a) Time dependent UV-visible spectrum of Au NP-PANI composite, (b) UV-visible spectrum of Au NPs synthesized through the reduction of Au<sup>3+</sup> by H<sub>2</sub>O<sub>2</sub> generated by the oxidation of glucose by GOx. (c) Digital images showing the sequence of reactions involved in the formation of Au NP-polyaniline composite by making use of the activity of glucose oxidase. (d) UV-visible spectrum of PANI alone synthesized using the activity of GOx and (e) FTIR spectrum of PANI alone (red line) and Au NP-PANI composite (blue line) synthesized using GOx.

The electrochemical nature of the PANI in the Au NP-PANI nanocomposite was evaluated by cyclic voltammetry (figure 2.8a). Generally two sets of redox peaks are observed in case of PANI. However in our case the Au NP-PANI composite showed

only one set of redox peak at  $E_{1/2} = 0.45$  V. The absence of the second redox process may be attributed to the exceptional resistance of PANI to oxidation to pernigraniline state, as has been reported earlier.<sup>[55]</sup>

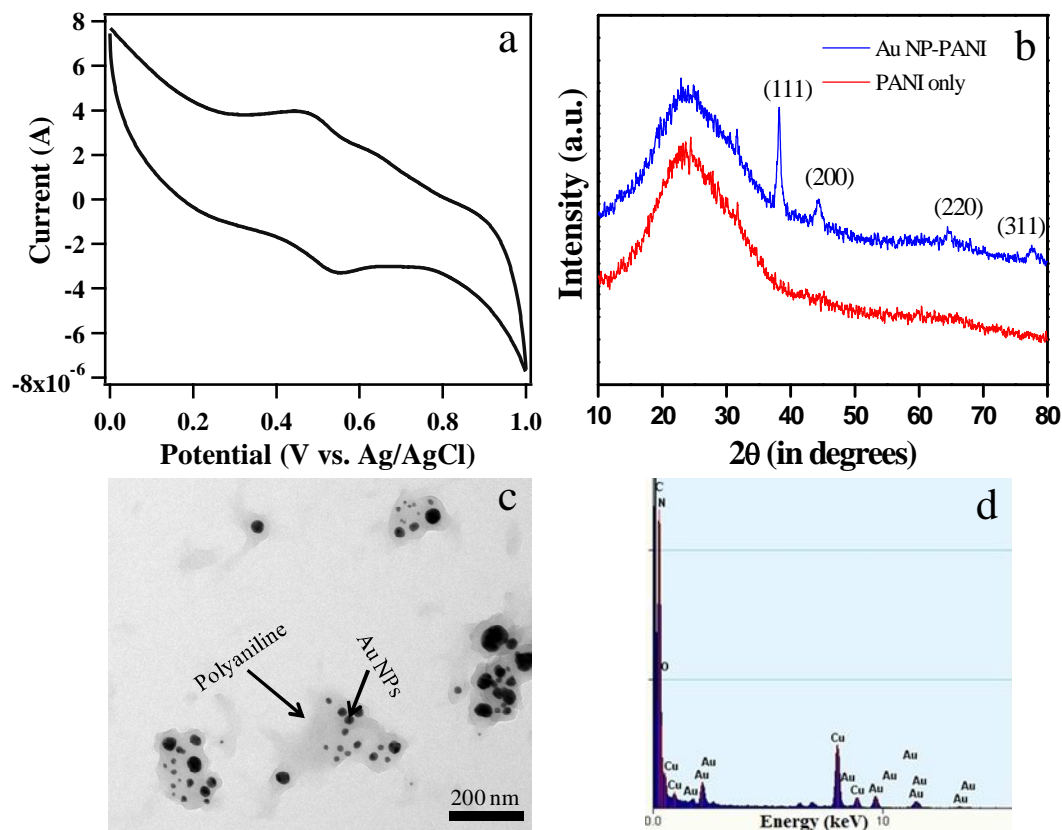


**Figure 2.8.** (a) Cyclic voltammogram of Au NP-PANI nanocomposite at a scan rate of 100 mV/s, (b) Powder XRD pattern of polyaniline alone (red line) and Au nanoparticle-polyaniline nanocomposite (blue line), (c) TEM image of Au NP-PANI nanocomposite and (d) EDS spectrum of Au NP-PANI nanocomposite.

The incorporation of Au NPs in the PANI moiety was established using powder XRD and transmission electron microscopy. The powder XRD spectrum (figure 2.8b) in case of PANI alone consisted of only a broad peak at  $2\theta$  value of  $23.8^\circ$  indicating that low level of crystalline phase in the polymer had been formed.<sup>[31]</sup> However in case of the Au NP-PANI composite, in addition to the broad peak at  $24^\circ$ , peaks at  $2\theta$  values of  $38.2$ ,  $44.5$ ,  $64.7$  and  $77.6$  degrees corresponding to (111), (200), (222), and (311) planes of Au were observed, confirming the presence of Au nanoparticles along with the polymer. The transmission electron microscopy image (figure 2.8c) of the Au NP-PANI

composite revealed that the Au NPs were mostly in the form of a cluster of particles surrounded by a layer of PANI. The clusters were well separated from each other and the average size of each cluster was around 100 nm. The Au NP-PANI composite appeared to have a core-shell morphology where the cluster of the particles formed the core and the surrounding PANI layer formed the shell. The Au NPs and PANI in the Au NP-PANI composite were clearly distinguishable from each other where the Au NPs formed the dark core and the PANI layer was observed as light gray shell. The average size of the Au nanoparticles in the clusters was calculated to be  $14.1 \pm 6.4$  nm. The corresponding EDS spectrum (figure 2.8d) showed the presence of carbon, nitrogen and Au confirming the presence of Au NPs in the PANI matrix.

### 2.3 Conclusions

In conclusion, a simple and green method for the synthesis of Au NPs using a redox enzyme, glucose oxidase as both reducing as well as stabilizing agent have been developed. The synthesized Au nanoparticles showed excellent catalytic activity towards the reduction of *p*-nitrophenol to *p*-aminophenol. The use of enzymes for the synthesis of metal nanoparticles is important not only towards the development of biogenic pathway devoid of harsh reaction conditions, but also because it may provide an insight into the mechanism of nanoparticle formation in higher ordered organisms such as fungi, bacteria, viruses etc. With an enhanced role of opto-electronic properties of Au nanoparticles and their interaction with biomolecules such as enzymes in nanobiotechnology, fundamental understanding regarding the factors which lead to the property changes in either one or both of them are crucial in development of functional materials for applications such as ultrasensitive optical and electrochemical nanosensors.<sup>[56-58]</sup> Further the catalytic activity of glucose oxidase was exploited towards the formation of Au NP-polyaniline nanocomposite. With the tremendous potential of nanoparticle incorporated conducting polymer composite materials in various applications, development of this biogenic route using enzymes as templates under ambient conditions will offer a green alternative towards the formation of nanocomposite materials.

## 2.4 Experimental Section

### 2.4.1 Materials

Glucose oxidase from *Aspergillus niger*, hydrogen tetrachloroaurate and 5,5'-dithiobis(2-nitrobenzoic acid) (DTNB), were purchased from Sigma-Aldrich. Sorbitol and xylenol orange were purchased from SRL chemicals, India. Sodium dihydrogen phosphate monohydrate, di- Sodium hydrogen phosphate, glucose, ferrous ammonium sulfate and hydrochloric acid were purchased from Merck, India. Aniline was purchased from Merck, India and was distilled under vacuum prior to use. All the reagents were of analytical grade and were used without any further purification. Milli Q water was used throughout the experiments.

### 2.4.2 Instrumentation

UV- visible spectra were recorded on a Varian Cary 100 Bio spectrophotometer. Powder X-ray diffraction spectra (XRD) were recorded on a Bruker D8 Advance diffractometer with Cu K $\alpha$  source (wavelength of X- rays was 0.154 nm). The samples for XRD were prepared by drop casting the sample solutions on glass slides and drying them at room temperature. FTIR spectra were recorded in KBr pellet using Bruker Tensor 27 instrument. The transmission electron microscopy (TEM) images were recorded on Technai G<sup>2</sup> 20 Ultra-Twin microscope. The samples for TEM were prepared by drop casting the sample solutions on carbon coated copper grid followed by room temperature drying. Circular Dichroism (CD) experiments were performed using a JASCO J-815 spectropolarimeter. Fluorescence measurement was performed on a fluoromax-4p fluorometer from Horiba (Model: FM-100). Cyclic voltammetry was carried out on a CHI620D electrochemical analyzer.

### 2.4.3 Synthesis of Au nanoparticles

Au nanoparticles were synthesized in Phosphate buffer of strength 10 mM and pH 7.0. Briefly, HAuCl<sub>4</sub> solution with a final concentration of  $6 \times 10^{-4}$  M was added to 3 ml of 0.7 mg/ml glucose oxidase solution in phosphate buffer and the reaction was incubated at 37 °C for 36 hours with mild stirring, when the color of the solution changed from light yellow to pink.

#### **2.4.4 Catalytic activity of Au nanoparticles**

The catalytic activity of the Au NP-enzyme composite was tested by carrying out the reduction of *p*-nitrophenol to *p*-aminophenol using NaBH<sub>4</sub> as the reducing agent. To a standard quartz cell of 1 cm pathlength, 2.5 ml of 0.12 mM *p*-nitrophenol, 1 mg NaBH<sub>4</sub> and 0.025 ml of as prepared Au nanoparticles was added and the UV-visible spectra were recorded every 2 minutes in the range of 200-600 nm.

#### **2.4.5 Activity study of native glucose oxidase and glucose oxidase after the synthesis of Au NPs (FOX method)**

The activity of the native enzyme and the enzyme after the synthesis of Au NPs was tested spectrophotometrically following a reported procedure<sup>[47]</sup> using the FOX method. The method is based on the oxidation of ferrous ions to ferric ions by hydrogen peroxide and simultaneous purple colored complex formation of the ferric ions with xylenol orange. Briefly, solutions of native enzyme and Au NP-GOx composite with enzyme concentration of 0.3 mg/ml were prepared. To both these solutions 0.84 mg of glucose was added and allowed to stand for 3 minutes. Finally 35 µl of the above solutions were added to 4 ml of FOX reagent taken in two separate vials and the mixture was incubated at room temperature for 40 minutes before recording the UV-visible spectrum.

#### **2.4.6 Circular dichroism studies**

Circular Dichroism (CD) measurements were performed at 25 °C on a JASCO J-815 spectropolarimeter. All the spectra were recorded with a data pitch of 0.1 nm. The scanning speed was set to 20 nm/min with band width of 1nm. For the far UV region (190-250 nm), spectra were recorded with an enzyme concentration of 0.7 mg/ml using a quartz cell of 1mm pathlength (Starna Scientific Ltd. Hainault, UK). For the near UV and visible region (250-450 nm) an enzyme concentration of 1.85 mg/ml was used and the measurements were performed in a 1cm pathlength cell (Hellma Analytics). Each spectrum is the result of average of three consecutive scans.

### **2.4.7 Fluorescence study**

The fluorescence study of the native enzyme and Au NP-enzyme composite was performed using an excitation wavelength of 295 nm. The enzyme concentration used for the fluorescence measurements was 0.3 mg/ml.

### **2.4.8 Modification of thiol groups in glucose oxidase using DTNB**

The Thiol groups of glucose oxidase were modified using DTNB in PBS buffer of strength 10 mM and pH 8.0, following Ellmann's procedure.<sup>[51]</sup> Briefly, 1.75 mg of glucose oxidase was dissolved in 2 ml of phosphate buffer. To this solution 0.5 mL of 1 mM DTNB was added. After a few minutes, the color of the enzyme solution changed from almost colorless to yellow, indicating the modification of thiol groups.

### **2.4.9 Synthesis of Au NP-polyaniline nanocomposite**

Au nanoparticle-polyaniline nanocomposite was synthesized employing the activity of glucose oxidase. To 3.2 ml of 1.25 mg/ml enzyme solution in PBS of pH 7.0, 70 mg of glucose was added under mild stirring. After 2 minutes 50  $\mu$ l of 0.03 M HAuCl<sub>4</sub> was added that resulted in the formation of Au nanoparticles within 3 minutes. To this solution, 100  $\mu$ l of distilled aniline in 2.5 ml of 1 M HCl was added drop wise and the reaction mixture was stirred at room temperature for 16 hours, resulting in a dark green coloured solution.

### **2.4.10 Cyclic voltammetry studies**

Cyclic voltammetry study was performed on a CHI620D electrochemical analyzer in 0.75 M HCl solution at a scan rate of 100 mV/s by using Pt as a working electrode, Pt wire as the counter electrode and Ag/AgCl as the reference electrode.

---

## 2.5 References

1. Daniel M. C., Astruc D. (2004), Gold nanoparticles: Assembly, supramolecular chemistry, quantum-size-related properties, and applications towards biology, catalysis, and nanotechnology, *Chem. Rev.*, 104, 293- 346 (DOI: 10.1021/cr030698).
2. Goesmann H., Feldmann C. (2010), Nanoparticulate functional materials, *Angew. Chem. Int. Ed.*, 49, 1362-1395 (DOI: 10.1002/anie.200903053).
3. Costi R., Saunders A. E., Banin U. (2010), Colloidal hybrid nanostructures: A new type of functional materials, *Angew. Chem. Int. Ed.*, 49, 4878-4897 (DOI: 10.1002/anie.200906010).
4. Talapin D. V., Lee J. -S., Kovalenko M. V., Shevchenko E. V. (2010), Prospects of colloidal nanocrystals for electronic and optoelectronic applications, *Chem. Rev.*, 110, 389-458 (DOI: 10.1021/cr900137k).
5. Stark W. J. (2011), Nanoparticles in biological systems. *Angew. Chem. Int. Ed.*, 50, 1242-1258 (DOI: 10.1002/anie.200906684).
6. Slocik J. M., Naik R. R., Stone M. O., Wright D. W. (2005), Viral templates for gold nanoparticle synthesis, *J. Mater. Chem.*, 15, 749-753 (DOI: 10.1039/B413074J).
7. Ahmad A., Mukherjee P., Mandal D., Senapati S., Khan M. I., Kumar R., Sastry M. (2002), Enzyme mediated extracellular synthesis of CdS nanoparticles by the fungus, *Fusarium oxysporum*, *J. Am. Chem. Soc.*, 124, 12108-12109 (DOI: 10.1021/ja027296o).
8. Berti L., Burley G. A. (2008), Nucleic acid and nucleotide-mediated synthesis of inorganic nanoparticles, *Nat. Nanotechnol.*, 3, 81-87 (DOI:10.1038/nnano.2007.460).
9. Ma N., Sargent E. H., Kelley S. O. (2009), One-step DNA-programmed growth of luminescent and biofunctionalized nanocrystals, *Nat. Nanotechnol.*, 4, 121-125 (DOI:10.1038/nnano.2008.373).
10. Wei H., Wang Z., Zhang J., House S., Gao Y. G., Yang L., Robinson H., Tan L. H., Xing H., Hou C., Robertson I. M., Zhuo J. M., Lu Y. (2011), Time-

- dependent, protein-directed growth of gold nanoparticles within a single crystal of lysozyme, *Nat. Nanotechnol.*, 6, 93-97 (DOI:10.1038/nnano.2010.280).
11. Niemeyer C. M. (2001), Nanoparticles, proteins, and nucleic acids: Biotechnology meets materials science, *Angew. Chem. Int. Ed.*, 40, 4128-4158 (DOI: 10.1002/1521-3773(20011119)40:22<4128::AID-ANIE4128>3.0.CO;2-S).
  12. Gugliotti L. A., Feldheim D. L., Eaton B. E. (2004), RNA-mediated metal-metal bond formation in the synthesis of hexagonal palladium nanoparticles, *Science*, 304, 850-852 (DOI: 10.1126/science.1095678).
  13. Rodriguez-Lorenzo L., de la Rica R., Alvarez-Puebla A., Liz-Marzan L. M., Stevens M. M. (2012), Plasmonic nanosensors with inverse sensitivity by means of enzyme-guided crystal growth, *Nat. Mater.*, 11, 604-607 (DOI:10.1038/nmat3337).
  14. Dickerson M. B., Sandhage K. H., Naik R. R. (2008), Protein- and peptide-directed syntheses of inorganic materials, *Chem. Rev.*, 108, 4935-4978 (DOI: 10.1021/cr8002328).
  15. Shenton W., Mann S., Colfen H., Bacher A. Fischer M. (2001), Synthesis of nanophase iron oxide in lumazine synthase Capsids, *Angew. Chem. Int. Ed.*, 40, 442-445 (DOI: 10.1002/1521-3773(20010119)40:2<442::AID-ANIE442>3.0.CO;2-2).
  16. de la Rica R., Matsui, H. (2008), Urease as a nanoreactor for growing crystalline ZnO nanoshells at room temperature, *Angew. Chem. Int. Ed.*, 47, 5415-5417 (DOI: 10.1002/anie.200801181).
  17. Johnson J. M., Sinsinger N., Sun C., Li D. Kisailus D. (2012), Urease-mediated room-temperature synthesis of nanocrystalline titanium dioxide, *J. Am. Chem. Soc.*, 134, 13974-13977 (DOI: 10.1021/ja306884e).
  18. Willner I., Baron R., Willner B. (2006), Growing metal nanoparticles by enzymes, *Adv. Mater.*, 18, 1109-1120 (DOI: 10.1002/adma.200501865).
  19. Virkutyte J., Varma R. S. (2011), Green synthesis of metal nanoparticles: Biodegradable polymers and enzymes in stabilization and surface functionalization, *Chem. Sci.*, 2, 837-846 (DOI: 10.1039/C0SC00338G).

20. Scott D., Toney M., Muzikar M. (2008), Harnessing the mechanism of glutathione reductase for synthesis of active site bound metallic nanoparticles and electrical connection to electrodes, *J. Am. Chem. Soc.*, 130, 865-874 (DOI: 10.1021/ja074660g).
21. Xiao Y., Patolsky F., Katz E., Hainfeld J. F., Willner I. (2003), "Plugging into enzymes": Nanowiring of redox enzymes by a gold nanoparticle, *Science*, 299, 1877-1881 (DOI: 10.1126/science.1080664).
22. Bansar B., Weizmann Y., Cheglakov Z., Willner I. (2006), Synthesis of nanowires using dip-pen nanolithography and biocatalytic inks, *Adv. Mater.*, 18, 713-718 (DOI: 10.1002/adma.200502320).
23. Rangnekar A., Sarma T. K., Singh A. K., Deka J., Ramesh A., Chattopadhyay A. (2007), Retention of enzymatic activity of  $\alpha$ -Amylase in the reductive synthesis of gold nanoparticles, *Langmuir*, 23, 5700-5706 (DOI: 10.1021/la062749e).
24. Au L., Lim B., Colletti P., Jun Y. -S., Xia Y. (2010), Synthesis of Gold microplates using bovine serum albumin as a reductant and a stabilizer, *Chem Asian J.*, 5, 123-129 (DOI: 10.1002/asia.200900468).
25. Lee S. J., Scotti N., Ravasio N., Chung I. S., Song H. (2013), Bovine serum albumin as an effective surface regulating biopolymer for morphology control of gold polyhedrons, *Cryst. Growth Des.*, 13, 4131-4137 (DOI: 10.1021/cg400949x).
26. Zhang P., Yang X. X., Wang Y., Zhao N. W., Xiong Z. H., Huang C. Z. (2014), Rapid synthesis of highly luminescent and stable Au<sub>20</sub> nanoclusters for active tumor-targeted imaging *in vitro* and *in vivo*, *Nanoscale*, 6, 2261-2269 (DOI: 10.1039/C3NR05269A).
27. Gustafsson G., Cao Y., Treacy G. M., Klavetter F., Colaneri N., Heeger A. J. (1992), Flexible light emitting diodes made from soluble conducting polymers, *Nature*, 357, 477-479 (DOI:10.1038/357477a0).
28. Xia H., Wang Q. (2002), Ultrasonic irradiation: A novel approach to prepare conductive polyaniline/nanocrystalline titanium oxide composites. *Chem. Mater.*, 14, 2158-2165 (DOI: 10.1021/cm0109591).

- 
29. Zhao M., Wu X., Cai C. (2009), Polyaniline nanofibers: Synthesis, characterization and application to direct electron transfer of glucose oxidase, *J. Phys. Chem. C*, 113, 4987-4996 (DOI: 10.1021/jp807621y).
  30. Sarma T. K., Chowdhury D., Paul A., Chattopadhyay A. (2002), Synthesis of Au nanoparticle–conductive polyaniline composite using H<sub>2</sub>O<sub>2</sub> as oxidising as well as reducing agent, *Chem. Commun.*, 1048-1049 (DOI: 10.1039/B201014C).
  31. Sarma T. K., Chattopadhyay A. (2004), One pot synthesis of nanoparticles of aqueous colloidal polyaniline and its Au-nanoparticle composite from monomer vapour, *J. Phys. Chem. A*, 108, 7837-7842 (DOI: 10.1021/jp049348x)
  32. Sih B. C., Wolf M. O. (2005), Metal nanoparticle-conjugated polymer nanocomposites, *Chem. Commun.*, 3375-3384 (DOI: 10.1039/B501448D).
  33. Wang Y., Liu Z., Han B., Sun Z., Huang Y., Yang G. (2005), Facile synthesis of polyaniline nanofibres using chloroaurate acid as the oxidant, *Langmuir*, 21, 833-836 (DOI: 10.1021/la047442z)
  34. Pillalamarri S. K., Blum F. D., Tokuhiko A. T., Bertino M. F. (2005), One-pot synthesis of polyaniline-metal nanocomposites, *Chem. Mater.*, 17, 5941-5944 (DOI: 10.1021/cm050827y).
  35. Tsuge H., Natsuaki O., Ohashi K. (1975), Purification, properties and molecular features of glucose oxidase from *Aspergillus Niger*, *J. Biochem.*, 78, 835-843
  36. Haiss W., Thanh T. K. N., Aveyard J., Fernig D. G. (2007), Determination of size and concentration of gold nanoparticles from UV-Vis spectra, *Anal. Chem.* 79, 4215-4221 (DOI: 10.1021/ac0702084).
  37. Das S. K., Dickinson C., Lafir F., Brougham D. F., Marsilo E. (2012), Synthesis, characterization and catalytic activity of gold nanoparticles biosynthesized with *Rhizopus Oryzae* protein extract, *Green Chem.*, 14, 1322-1334 (DOI: 10.1039/C2GC16676C).
  38. Tang X. –L., Jiang P., Ge G. –L., Tsuji M., Xie S. –S., Guo Y. –J. (2008), Poly (N-vinyl-2-pyrrolidone) (PVP) – capped dendritic gold nanoparticles by a one step hydrothermal route and their high SERS effect, *Langmuir*, 24, 1763-1768 (DOI: 10.1021/la703495s).
-

39. Lee Y. W., Kim N. H., Lee K. Y., Kuon K., Kim M., Han S. W. (2008), Synthesis and Characterization of Flower-Shaped Porous Au–Pd Alloy Nanoparticles, *J. Phys. Chem. C*, 112, 6717-6722 (DOI: 10.1021/jp710933d).
40. Tao A. R., Habas S., Yang P. (2008), Shape Control of Colloidal Metal Nanocrystals, *Small*, 4, 310-325 (DOI: 10.1002/smll.200701295).
41. Tsunoyama H., Sakurai H., Ichikuni N., Negishi Y., Tsutuda T. (2004), Colloidal gold nanoparticles as catalyst for carbon-carbon bond formation: Application to aerobic homocoupling of phenylboronic acid in water, *Langmuir*, 20, 11293-11296 (DOI: 10.1021/la0478189).
42. Liang Q., Liu J., Wei Y., Zhao Z., Maclachlan M. J. (2013), Palladium nanoparticles supported on a triptycene-based microporous polymer: Highly active catalysts for CO oxidation, *Chem. Commun.*, 49, 8928-8930 (DOI: 10.1039/C3CC44500C)
43. Zaramella D., Scrimin P., Prins L. J. (2012), Self-assembly of catalytic multivalent peptide-nanoparticle complex, *J. Am. Chem. Soc.*, 134, 8396-8399 (DOI: 10.1021/ja302754h).
44. Coppage R., Slocik J. M., Dakhel H. R., Bedford N. M., Heinz H., Naik R. R., Knecht M. R. (2013), Exploiting localized surface binding effects to enhance the catalytic reactivity of peptide-capped nanoparticles, *J. Am. Chem. Soc.*, 135, 11048-11054 (DOI: 10.1021/ja402215t).
45. Zheng N., Stucky G. D. (2006), A general synthetic strategy for oxide-supported metal nanoparticle catalysts, *J. Am. Chem. Soc.*, 128, 14278-14280 (DOI: 10.1021/ja0659929).
46. Aditya T., Pal A., Pal T. (2015), Nitroarene reduction: A trusted model reaction to test nanoparticle catalysts, *Chem. Commun.*, 51, 9410-9431 (DOI: 10.1039/C5CC01131K).
47. Rhee S. G., Chang T. S., Jeong W. Kang D. (2010), Methods for detection and measurement of hydrogen peroxide inside and outside of cells, *Mol. Cells*, 29, 539-549 (DOI:10.1007/s10059-010-0082-3).
48. Cruz J. C., Pfromm P. H., Tomich M. J., Rezac M. E. (2010), Conformational changes and catalytic competency of hydrolases adsorbing on fumed silica

- nanoparticles: II. Secondary structure, *Colloids Surf. B*, 81, 1-10 (DOI:10.1016/j.colsurfb.2010.06.005).
49. Gouda M. D., Singh S. A., Rao A. G. A., Thakur M. S., Karanth N. G. (2003), Thermal inactivation of glucose oxidase: Mechanism and stabilization using additives, *J. Biol. Chem.*, 278, 24324-24333 (DOI:10.1074/jbc.M208711200).
50. Ma Z., Han H. (2008), One-step synthesis of cystine coated gold nanoparticles in aqueous solutions, *Colloids Surf. A*, 317, 229-233 (DOI:10.1016/j.colsurfa.2007.10.018).
51. Ellman G. L. (1959), Tissue sulfhydryl groups, *Arch. Biochem. Biophys.*, 82, 70-77 (DOI:10.1016/0003-9861(59)90090-6).
52. Colombo M., Mazzucchelli S., Colico V., Avvakuvoka S., Pandolfi L., Corsi F., Porta F., Prospero D. (2012), Protein-assisted one pot synthesis and biofunctionalization of spherical gold nanoparticles for selective targeting of cancer cells, *Angew. Chem. Int. Ed.*, 51, 9272-9275 (DOI: 10.1002/anie.201204699).
53. Mirkin C. A. (2000), Programming the assembly of two- and three dimensional architectures with DNA and nanoscale inorganic building blocks, *Inorg. Chem.*, 39, 2258-2272 (DOI: 10.1021/ic991123r).
54. Shin H. J., Huang I. W., Huang Y. N., Kim D., Han S. H., Lee J. S., Cho G. (2003), Comparative investigation of energy relaxation dynamics of gold nanoparticles and gold-polypyrrole encapsulated nanoparticles, *J. Phys. Chem. B*, 107, 4699-4704 (DOI: 10.1021/jp022055o).
55. Liu W., Kumar J. Tripathy S., Senecal K. J., Samuelson L. (1999), Enzymatically synthesized conducting polyaniline, *J. Am. Chem. Soc.*, 121, 71-78 (DOI: 10.1021/ja982270b)
56. Zayats M., Baron R., Popov I., Willner I. (2005), Biocatalytic growth of Au nanoparticles: From mechanistic aspects to biosensors design, *Nano Lett.*, 5, 21-25 (DOI: 10.1021/nl048547p).
57. Xu X., Han M. S., Mirkin C. A. (2007), A gold nanoparticle based real time colorimetric screening method for endonuclease activity and inhibition, *Angew. Chem. Int. Ed.*, 46, 3468-3470 (DOI: 10.1002/anie.200605249).

58. Xie X., Xu W., Liu X. (2012), Improving colorimetric assays through protein enzyme-assisted gold nanoparticle amplification, *Acc. Chem. Res.*, 45, 1511-1520 (DOI: 10.1021/ar300044j).

## Chapter 3

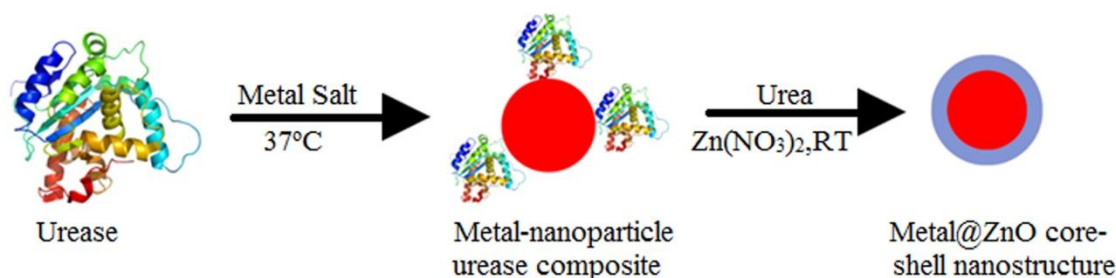
# Biogenic Growth of Alloys and Core-shell Nanostructures Using Urease as a Nanoreactor at Ambient conditions

### 3.1 Introduction

The assembly of nanoscale objects is considered to be a fundamental step in the development of new functional materials.<sup>[1-3]</sup> Since, structural precision is a must for the optimization of the properties and function of these materials, there is a continuous surge in research on self-assembled molecular systems such as molecular and polymeric micelles,<sup>[4]</sup> porous materials<sup>[5]</sup> etc. as templates for the directional growth of nano-dimensional systems. The precise nucleation and growth of nanomaterials is governed by the spatially confined environment and presence of nucleation sites in such systems. Biomolecule templated growth of nanostructured materials<sup>[6,7]</sup> has evolved as a magnificent strategy in the recent years because of their various and distinctive molecular structures, specificities, functionalities and versatility in recognition and assembly. Also the use of biomaterials for the synthesis of functional materials can significantly reduce the energy consumption in manufacturing processes. Among several biomolecules, enzymes, a key ingredient of the living world, have been subject of particular attention in nanoparticle-biomolecule interaction studies, where nanoparticles function as enzyme responsive systems. The chemical or electrostatic attachment of enzymes to the nanomaterials surface has resulted in the modulation of the natural activity of the enzyme leading to the enhancement, retention or inhibition of catalytic activity of the enzyme<sup>[8-14]</sup> that inspired the design of enzyme biosensors. On the other hand, the spatially confined environment of enzymes could be anticipated to facilitate the crystallization of inorganic materials with nanometer precisions. There have been several reports of enzyme stimulated synthesis of metallic and metal oxide nanoparticles, where the product of an enzyme catalyzed reaction facilitates the

formation of nanoparticles.<sup>[15-21]</sup> For instance, *E-coli* Glutathione Reductase catalyzes the NADPH-dependent reduction of  $\text{HAuCl}_4$ , leading to the formation of Au nanoparticles at its active site.<sup>[20]</sup> Although, enzymes have been used as nanoreactors for the growth of inorganic nanoclusters at elevated pH,<sup>[22-25]</sup> but the ability of enzymes as reducing as well as stabilizing agents for the growth of metal nanoparticles at physiological conditions has not been fully exploited and only a handful of reports are available.<sup>[26,27]</sup> Understanding the mechanism of the reduction capability of enzymes is not only critical to take full advantage of the nanoscale materials but also in studies related to structural alteration of enzymes that has profound influence on its kinetics.

In the previous chapter the ability of glucose oxidase to function as an efficient nanoreactor towards the formation of Au nanoparticles has been reported.<sup>[27]</sup> Following the previous work, we wanted to move a step further and see if enzymes could be envisaged as nanoreactors for the mineralization of metallic nanoparticles other than those of gold as well as higher order nanostructures such as alloys and core-shells. In this chapter, it has been demonstrated that the enzyme urease can be used as a reducing and stabilizing agent not only for the synthesis of metallic nanoparticles (Au, Ag and Pt) but also for the development of alloy nanoparticles (Au-Ag, Au-Pt and Ag-Pt). Further the activity of the enzyme was utilized for the room temperature growth of Au@ZnO core-shell nanostructures. Significantly, this is achieved in water under physiological conditions, thus expanding the current paradigm for biogenic nanoparticle synthesis with precisely controlled size and composition.



**Scheme 3.1** schematic representation of the use of urease as a nanoreactor for the formation of metallic as well as core-shell nanostructures. Step 1: Synthesis of metallic nanoparticles using urease both as reducing as well as stabilizing agent. Step 2: hydrolysis of urea by the nanoparticle-enzyme composite led to the increase in pH around the enzyme due to production of ammonia that catalyzed the growth of ZnO shells around the metal nanoparticle-enzyme composite.

## 3.2 Results and Discussion

### 3.2.1 Synthesis and characterization of metallic (Au, Pt, Ag) nanoparticles

The synthesis of Au nanoparticles was achieved by simple incubation of the urease solution (2mg/mL) with  $\text{HAuCl}_4$  ( $5.5 \times 10^{-4}$  M) in presence of  $\text{K}_2\text{CO}_3$  in water at optimal pH of 7.4 and  $37^\circ\text{C}$ . The result of the incubation was the formation of a stable red sol, signifying the formation of Au nanoparticles (figure 3.1a; inset). Confirmation about the formation of Au nanoparticles was obtained from UV-visible, powder X-ray diffraction and transmission electron microscopy studies. The UV-visible spectrum exhibited the characteristic surface plasmon resonance band for Au nanoparticles at 522 nm (figure 3.1a) and the powder X-ray diffraction spectrum consisted of peaks at  $2\theta$  values of 38.2, 44.4, 64.6 and 77.7 degrees, corresponding to the respective Bragg planes for face centered cubic gold (figure 3.1b). The transmission electron microscopy image (figure 3.1c) revealed the formation of spherical nanoparticles and the average diameter of the nanoparticles as calculated from the particle size histogram was  $8.9 \pm 1.6$  nm (figure 3.1d), which was consistent with the sizes of nanoparticles synthesized using biosynthetic routes involving natural reducing agents. For example, Slocik *et al.* have reported the synthesis of Au nanoparticles with an average diameter of  $8.3 \pm 2.6$  nm using (HRE)- Sub E virus.<sup>[28]</sup> The average particle sizes of Au nanoparticles (as calculated from TEM images) correlated well with the optical properties of the nanoparticles as predicted by theoretical calculations (figure 3.1e) and earlier experimental reports.<sup>[29,30]</sup> The high resolution transmission electron microscopy image (figure 3.1f) revealed a lattice spacing of 0.19 nm corresponding to the (200) face of Au. Scherrer equation was further employed to calculate the crystallite size from the powder XRD spectrum. The average crystal size of the Au nanoparticles was calculated to be 11.5 nm, which was slightly higher than the average particle size as measured from TEM studies ( $8.9 \pm 1.6$  nm). This discrepancy could be attributed to the fact that the calculation of size from XRD is just an approximation and is limited by the size of the particles, with no measurable signals being obtained in case of particles with sizes less than 5 nm.<sup>[31]</sup> Hence the average particle size measured from the XRD spectrum is essentially from the signals obtained from the particles with larger diameter and does

not represent all the nanoparticles synthesized, resulting in a size larger than those obtained from TEM measurements.

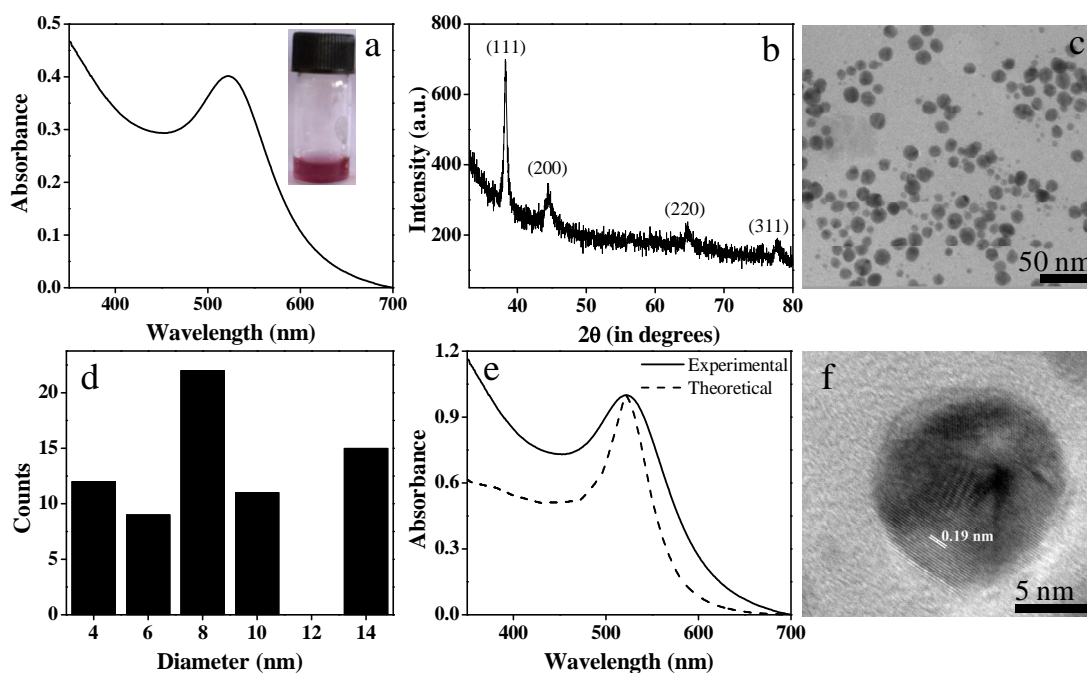


**Figure 3.1.** (a) UV-visible spectrum; Inset: digital image, (b) Powder XRD spectrum, (c) TEM image and (d) Particle size distribution histogram of Au NPs synthesized using urease. (e) UV-visible spectrum of the Au NPs showing perfect match of the experimental absorption spectrum (solid line) with calculated absorption spectrum (dashed line) as calculated using Mieplot v4304 software for Au nanoparticles with average diameter 8.9 nm and (f) HRTEM image of the Au NPs showing lattice spacing of 0.19 nm corresponding to (200) plane of Au.

Following a similar methodology Pt and Ag nanoparticles using urease as a reducing as well as stabilizing agent were synthesized. The incubation of  $K_2PtCl_4$  with jack bean urease led to a distinct color change of the solution from colorless to black indicating the formation of Pt nanoparticles. The formation of the Pt nanoparticles was further ascertained from powder X-ray diffraction and electron microscopy studies. The powder XRD pattern comprised of peaks due to the (111), (200) and (220) planes of metallic Pt (figure 3.2a). The TEM image showed the formation of small spherical nanoparticles having a mean size of  $2.8 \pm 0.8$  nm (figure 3.2b and c). The HRTEM image showed lattice fringes with a separation of 0.226 nm due to the (111) plane of metallic Pt (figure 3.2d).

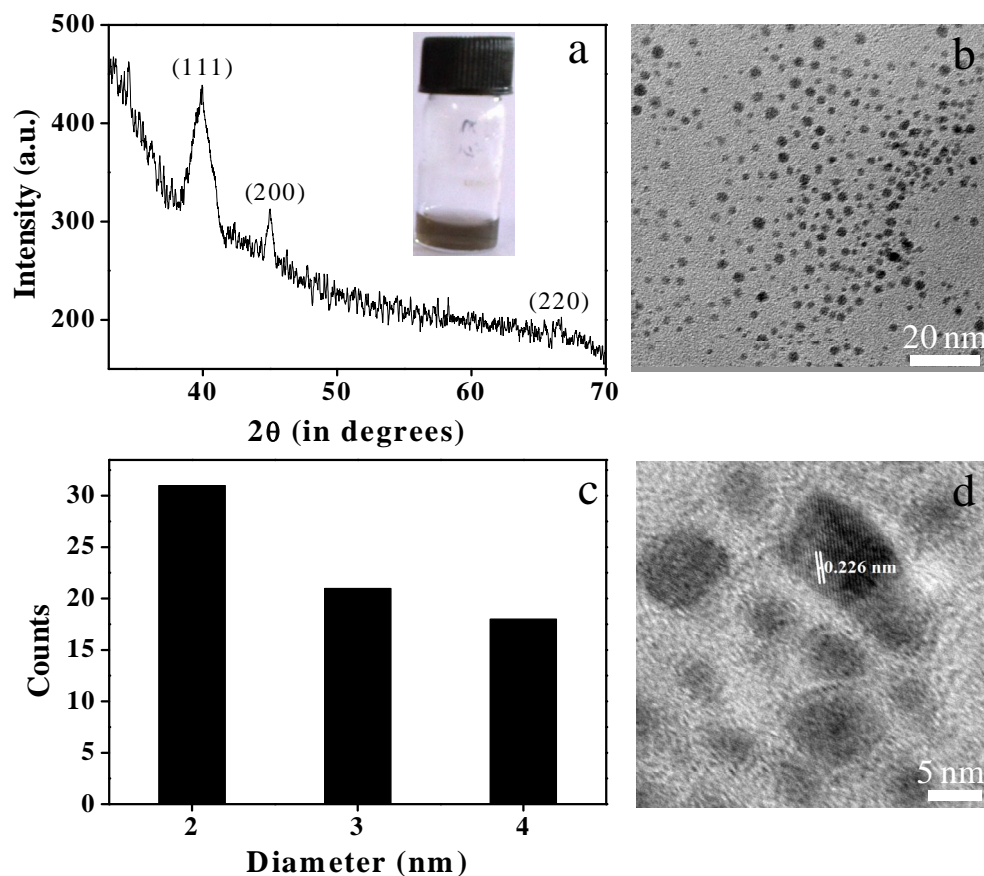


**Figure 3.2.** (a) Powder XRD spectrum; Inset Digital image, (b) TEM image, (c) Particle size distribution and (d) HRTEM image of Pt nanoparticles synthesized using urease as a reducing as well as stabilizing agent.

Similarly, a change in color of the solution from colorless to yellow upon incubation of  $\text{AgNO}_3$  with urease was indicative of the formation of Ag nanoparticles. The UV-visible spectrum showed the SPR band of the nanoparticles at 412 nm (figure 3.3a). In the powder XRD spectrum (figure 3.3b), in addition to the peak at  $2\theta$  value of 38.2 degrees, corresponding to the (111) plane of silver, intense peaks at  $2\theta$  values of 27.9 and 32.3 degrees were observed. According to previous literature reports these peaks corresponded to (110) and (111) reflections of  $\text{Ag}_2\text{O}$  respectively,<sup>[32,33]</sup> which indicated that the Ag nanoparticles formed, were actually Ag- $\text{Ag}_2\text{O}$  composite. The size and morphology of the composite was evaluated using transmission electron microscopy, which revealed the formation of spherical particles having an average size of  $4.1 \pm 1.2$  nm (figure 3.3c and d). It was observed that in case of the Ag- $\text{Ag}_2\text{O}$  composite nanoparticles, the experimental plasmon resonance band did not match well

with theoretical estimations and the experimental plasmon resonance band was red shifted as compared to the theoretical result (figure 3.3e). Although, a detailed theoretical calculation could not be performed, it is believed that the presence of a thin  $\text{Ag}_2\text{O}$  layer on Ag nanoparticle surface played an important role, as the oxide layer has reduced conductivity as well as complex refractive index relative to the metallic core.<sup>[34]</sup> The HRTEM image of the composite nanoparticle showed a lattice spacing of 0.23 nm due to the (111) plane of silver and a careful observation of the HRTEM image indicated the formation of a light grey shell of  $\text{Ag}_2\text{O}$  over the Ag core (figure 3.3f).

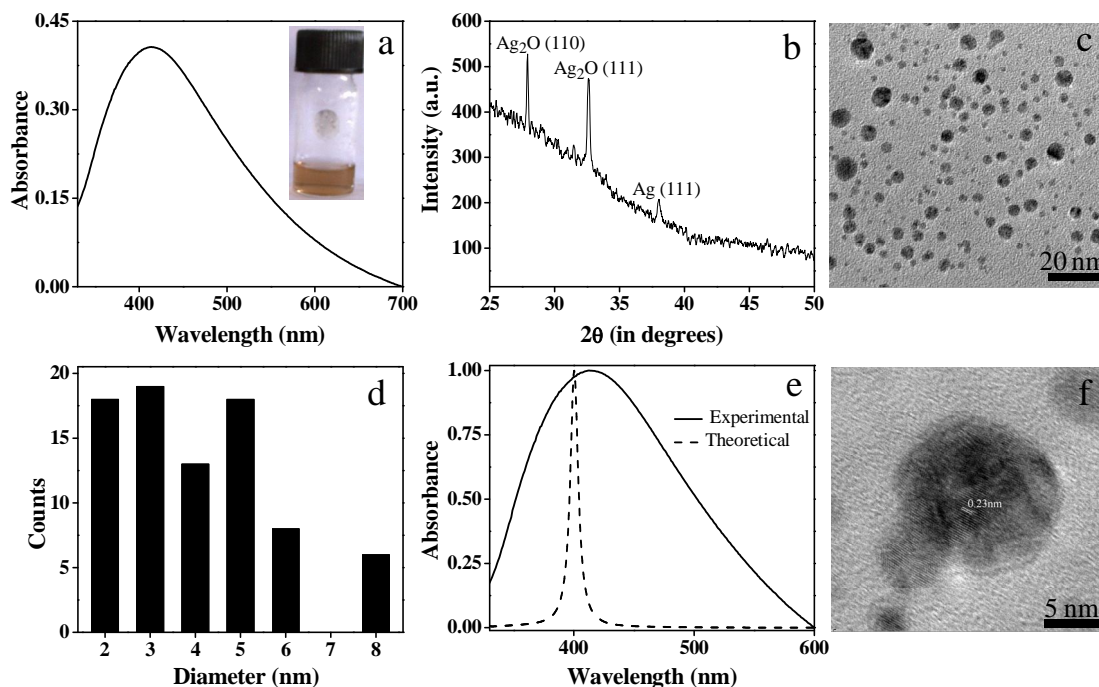


**Figure 3.3.** (a) UV-visible spectrum; Inset: digital image, (b) Powder XRD spectrum, (c) TEM image and (d) Particle size distribution histogram of Ag- $\text{Ag}_2\text{O}$  NPs synthesized using urease. (e) UV-visible absorption spectrum of Ag- $\text{Ag}_2\text{O}$  composite nanoparticles. Experimental absorption spectrum (Solid line) and calculated absorption spectrum (Dashed line) as calculated using Mieplot v4304 software for Ag nanoparticles with average diameter 4.1 nm and (f) HRTEM image of the Ag- $\text{Ag}_2\text{O}$  NPs showing lattice spacing of 0.23 nm corresponding to (111) plane of Ag.

The formation of  $\text{Ag}_2\text{O}$  over Ag nanoparticles was ascertained by X-ray photoelectron spectroscopy (figure 3.4). The core level XPS analysis of the Ag nanoparticles revealed the formation of a minor amount of  $\text{Ag}_2\text{O}$ , along with the Ag nanoparticles, as evidenced from the spectrum of the  $3d_{5/2}$  and  $3d_{3/2}$  electrons. Two

peaks at binding energies of 367.6 and 368.0 eV corresponding to  $3d_{5/2}$  photoelectrons of  $\text{Ag}_2\text{O}$  and Ag respectively were observed. In addition the spectrum also showed peaks at 373.6 and 374.0 eV, characteristic of  $3d_{3/2}$  photoelectrons of  $\text{Ag}_2\text{O}$  and Ag respectively.<sup>[35,36]</sup> Thus from the XPS analysis it was confirmed that in addition to Ag nanoparticles as major component, a minor amount of  $\text{Ag}_2\text{O}$  was also formed. Quantitatively, Ag- $\text{Ag}_2\text{O}$  nanocomposite consisted of 19.42% of  $\text{Ag}_2\text{O}$  and 80.58% of Ag. The  $\text{Ag}_2\text{O}$  layer is on the surface of the Ag nanoparticles, giving rise to a core-shell like morphology. The thickness of the  $\text{Ag}_2\text{O}$  layer on the Ag nanoparticles was in good agreement with previous literature report.<sup>[37]</sup>

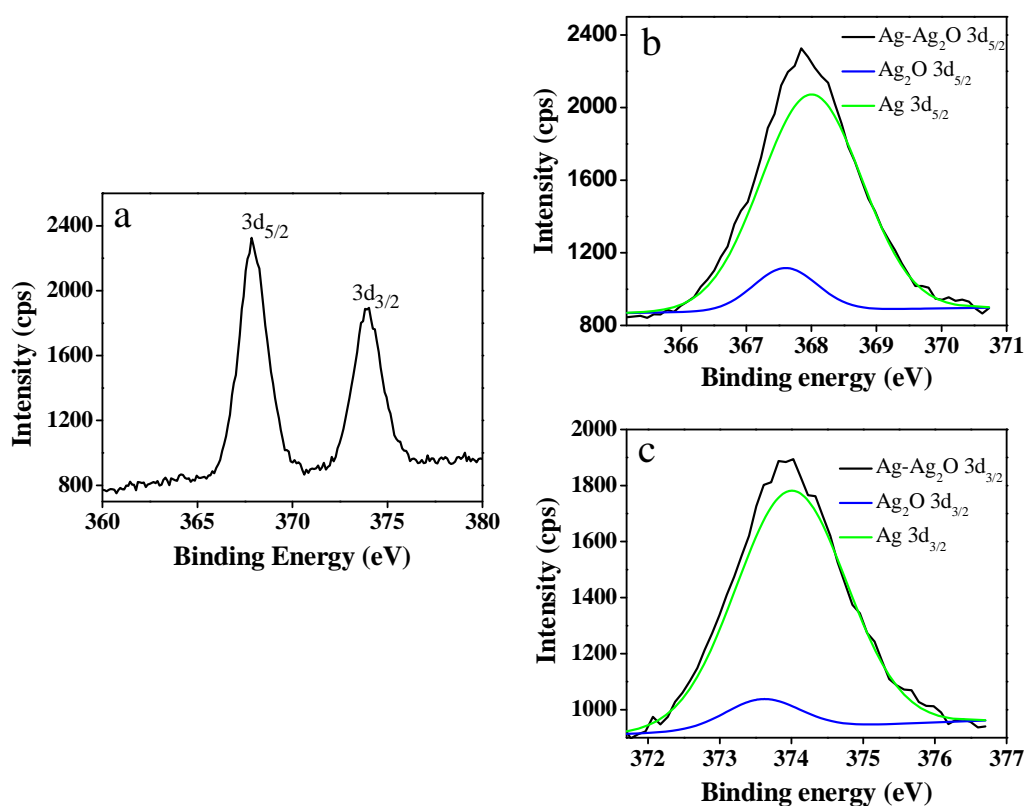


**Figure 3.4.** (a) XPS spectrum of 3d electrons of Ag- $\text{Ag}_2\text{O}$  composite nanoparticles. (b) XPS spectrum for Ag  $3d_{5/2}$  photoelectrons and (c), XPS spectrum for Ag  $3d_{3/2}$  photoelectrons showing the presence of both Ag and  $\text{Ag}_2\text{O}$ .

It is important to mention here that the sizes of Ag and Pt nanoparticles synthesized using urease were also in good accordance with the sizes of the nanoparticles synthesized using biosynthetic routes involving natural reducing agents. For instance, spherical Ag nanoparticles of average diameter 5.3 nm using natural

hydrocolloid gum kondagogu<sup>[38]</sup> and Pt nanoparticles having average size of 2.2 nm using natural wood<sup>[39]</sup> have been reported.

### 3.2.2 Effect of phosphate buffer saline (PBS) on the morphology of nanoparticles

It is well known that the size and morphology of nanoparticles depends on the ionic strength of the reaction medium.<sup>[40,41]</sup> So, in order to probe the effect of ionic strength on the size and shape of nanoparticles, Au nanoparticles were synthesized in PBS buffer without the use of  $K_2CO_3$ . It was interesting to note that the growth kinetics of the nanoparticles and the position of the plasmon resonance band depended very much on the reaction conditions. It was observed that when  $K_2CO_3$  was used, the nanoparticles were formed within 6 hours, while using PBS of pH 7.4 instead of  $K_2CO_3$  required 48 hours for nanoparticle formation. The UV-visible spectrum of the Au nanoparticles in PBS exhibited the SPR band at 537 nm, a 15 nm red shift compared to those synthesized in presence of  $K_2CO_3$  (figure 3.5a). The UV-visible results indicated an increase in the size of the particles, which was confirmed from TEM studies. The TEM images of Au nanoparticles in PBS showed substantial agglomeration (figure 3.5b), justifying the red shift in the plasmon resonance peak compared to those synthesized in presence of  $K_2CO_3$ . The increased ionic strength of the medium might have led to the agglomeration of the Au nanoparticles synthesized in PBS as previously reported.<sup>[42]</sup>

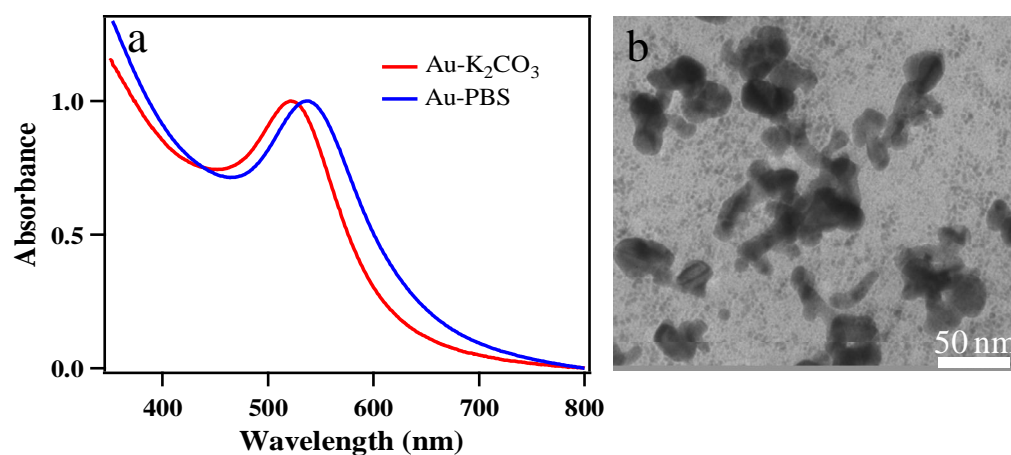


**Figure 3.5.** (a) UV-visible spectrum of Au NPs synthesized in  $K_2CO_3$  and PBS using urease and (b) TEM image of Au NPs synthesized in PBS showing agglomeration of nanoparticles.

### 3.2.3 Synthesis and characterization of metallic alloy (Au-Ag, Ag-Pt, Au-Pt) nanoparticles

After the successful synthesis of metallic nanoparticles using urease, the possibility of synthesizing metallic alloy nanoparticles using urease as a reducing agent was explored. The incubation of the enzyme with two metal salts such as  $\text{HAuCl}_4$  and  $\text{AgNO}_3$  led to the formation of AuAg alloy nanoparticles in water at ambient temperature. When 1:1 molar ratio of  $\text{HAuCl}_4$  and  $\text{AgNO}_3$  was added in the reaction medium, the resulting nanoparticles showed a plasmon resonance peak at 476 nm, which was in between that of pure Au and Ag nanoparticles, depicting the formation of  $\text{Au}_{0.5}\text{Ag}_{0.5}$  nanoparticles<sup>[43]</sup> (figure 3.6a).

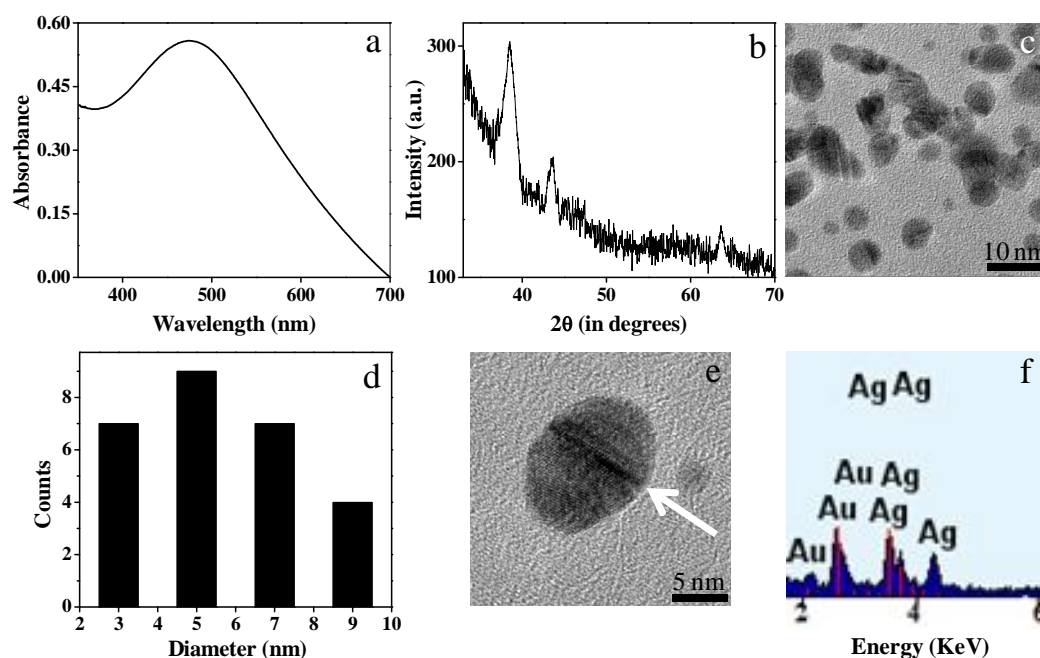


**Figure 3.6.** (a) UV-visible spectrum, (b) powder XRD spectrum, (c) TEM image, (d) particle size distribution, (e) HRTEM image; Arrow signifies the twin faults in the alloy and (f) EDS spectrum of Au-Ag alloy nanoparticles synthesized using urease.

The powder XRD spectrum confirmed the crystalline nature of the alloy nanoparticles (figure 3.6b). The average diameter of the nanoparticles as calculated from the TEM images was  $5.6 \pm 2.0$  nm (figure 3.6c and d). The HRTEM image (figure 3.6e) showed twins and stacking faults in most of the particles, probably due to high internal strain energy existing in these particles.<sup>[44]</sup> Energy dispersive X-ray (EDX)

analysis confirmed the presence of both Au and Ag in the alloy nanoparticles (figure 3.6f).

The synthetic methodology was successfully extended towards the development of other metallic alloy nanoparticles such as AgPt and AuPt alloy nanoparticles. The incubation of 1:1 molar ratio of  $\text{AgNO}_3$  and  $\text{K}_2\text{PtCl}_4$  resulted in the formation of AgPt alloy nanoparticles. The UV-visible spectrum showed a band at 378 nm, confirming the formation of AgPt alloy nanoparticles (figure 3.7a). The crystalline nature of the particles was confirmed from the powder XRD studies (figure 3.7b). The TEM and HRTEM images showed the formation of nearly spherical particles and the average size of the particles as calculated from the particle size distribution histogram was  $3.6 \pm 1.8$  nm (figure 3.7c, d and e).

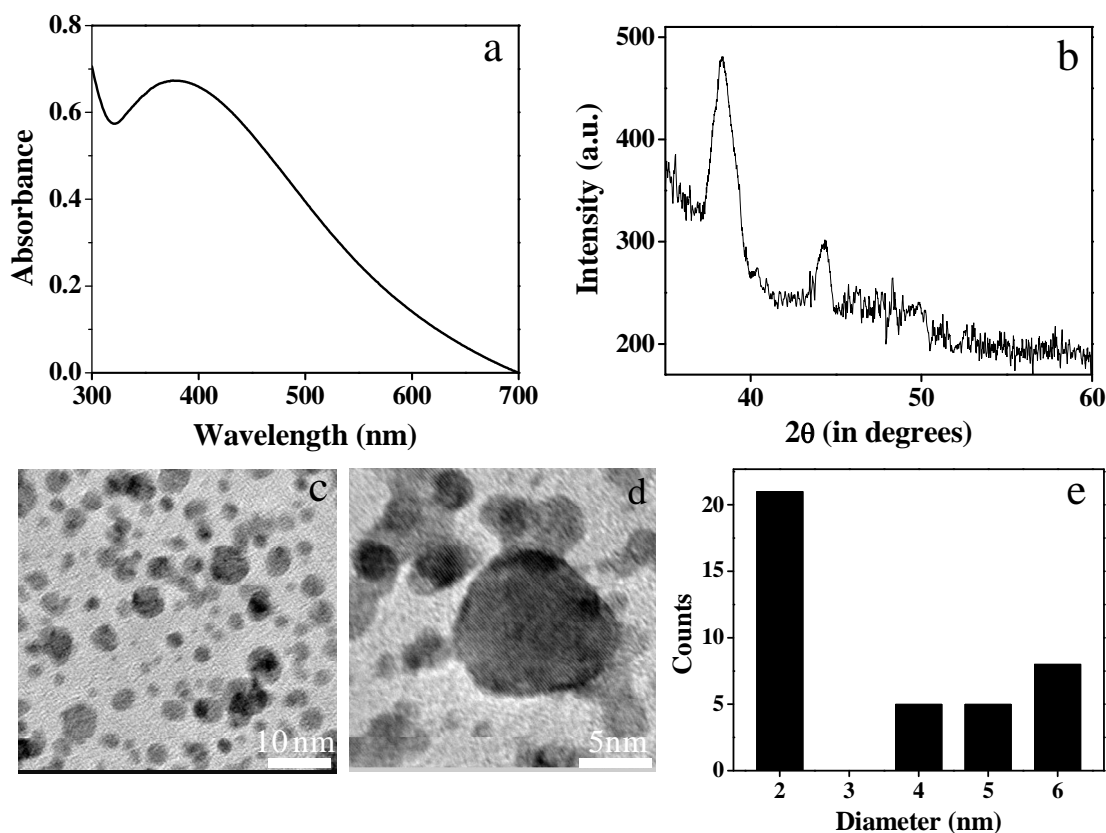


**Figure 3.7.** (a) UV-visible spectrum, (b) Powder XRD spectrum, (c) TEM image, (d) HRTEM image and (e) Particle size distribution histogram of Ag-Pt alloy nanoparticles synthesized using urease.

In a similar manner Au-Pt alloy nanoparticles were synthesized. The UV-visible spectrum exhibited a band at 476 nm, indicating the formation of AuPt alloy

nanoparticles (figure 3.8a). The PXRD spectrum of the nanoparticles confirmed their crystallinity (figure 3.8b) and the TEM images and the particle size distribution revealed the formation of nanoparticles with mean size  $3.9 \pm 2.0$  nm (figure 3.8a, b and c).

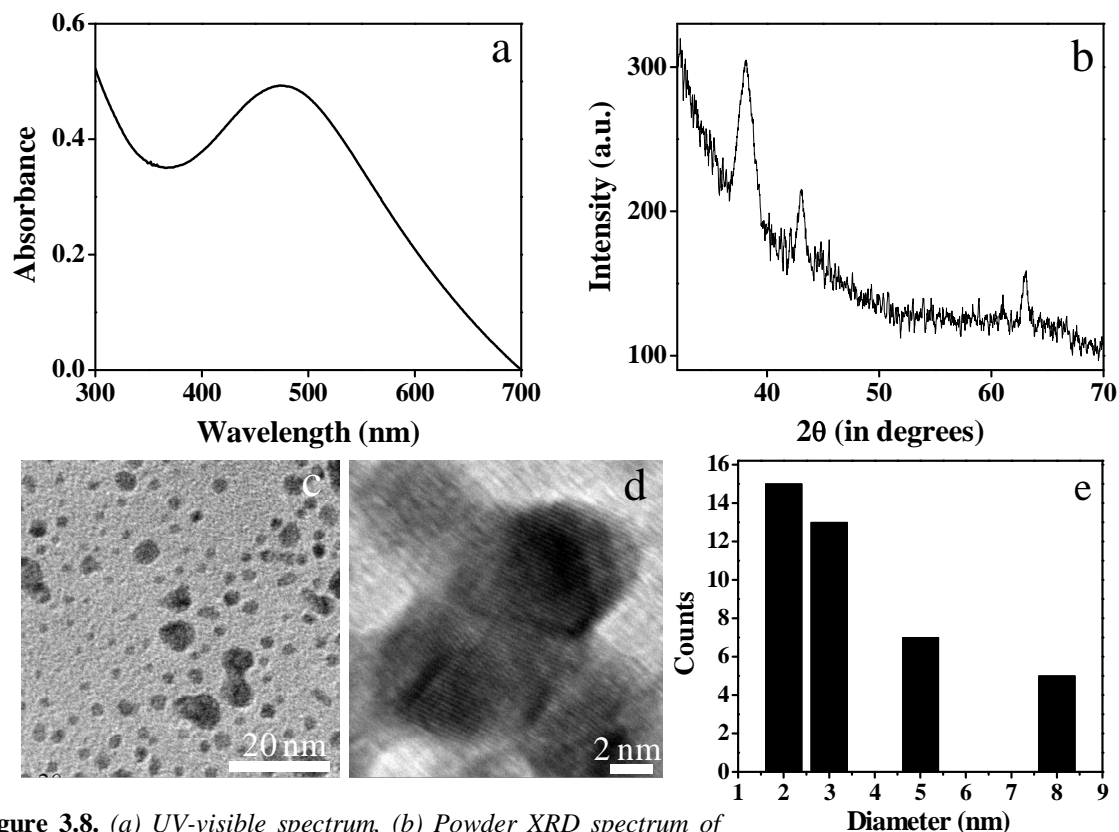
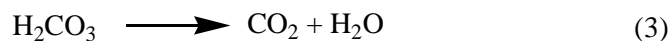


**Figure 3.8.** (a) UV-visible spectrum, (b) Powder XRD spectrum of the Au-Pt alloy nanoparticles synthesized using urease as reducing as well as stabilizing agent, (c) TEM image, (d) HRTEM image and (e) Particle size distribution histogram of Au-Pt alloy nanoparticles synthesized using urease.

### 3.2.4 Activity of urease after the synthesis of nanoparticles

The decomposition of urea, resulting in an increase in the pH of the system due to generation of ammonia can be achieved using enzymatic route. The enzyme urease decomposes urea into ammonia and carbon dioxide in aqueous solutions according to the following reactions:



It has been well studied that the conjugation of nanoparticles with enzyme often leads to alteration of its activity.<sup>[13]</sup> In case of urease, the increased pH of the medium is a good indicator for the measurement of enzyme activity, primarily, due to the liberation of ammonia by the hydrolysis of urea by urease. Ammonia molecules react with water to form ammonium hydroxide that subsequently dissociates to form hydroxide ions resulting in the net increase in the solution pH. As shown in figure 3.9a, the decomposition of urea by the native urease led to a pH increase of the medium from 6.9 to 9.0 whereas the Au nanoparticle-urease composite (as synthesized by the reduction of the metal salt with urease) could increase the pH from 6.8 to 7.7, thus indicating a decrease in the enzyme activity.

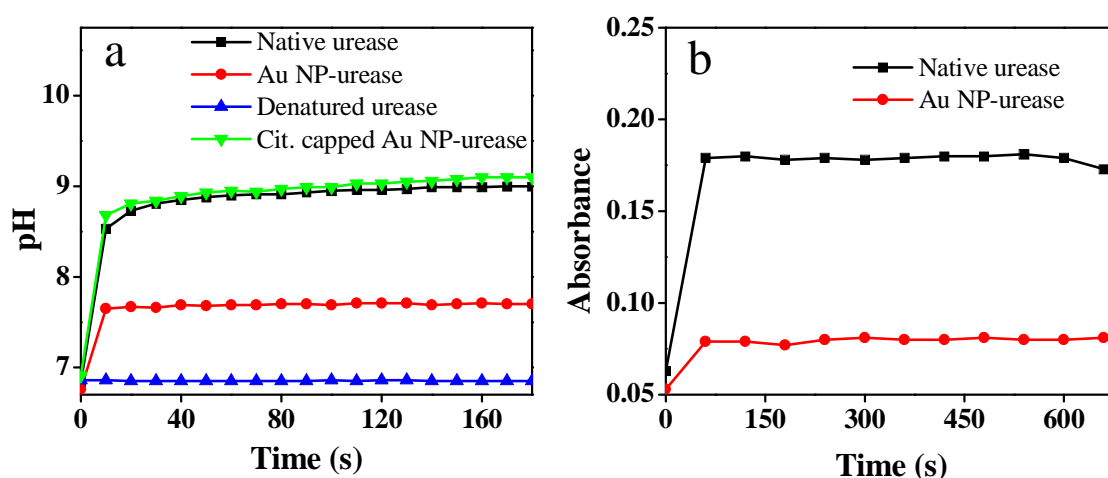


**Figure 3.9.** (a) pH change of the medium by native urease, Au nanoparticle-urease composite (urease reduced Au nanoparticles), denatured urease and citrate capped Au nanoparticles with urease and (b) Comparison of the activity of native urease and urease after the synthesis of Au NPs using the dye bromocresol purple

These results were further confirmed using a colorimetric assay,<sup>[45]</sup> where the solution pH increase was monitored by a pH sensitive dye, bromocresol purple (figure 3.9b). The increase in pH of the reaction medium led to an increase in the absorbance value at 588 nm. It was observed that while in case of native urease the absorbance at 588 nm increased from 0.06 to 0.18, the Au NP-urease composite could increase the absorbance from 0.05 to 0.08 only. Notably, denatured urease (enzyme heated at 90 °C for 30 minutes in water) could not increase the pH of the medium. For understanding the role of Au nanoparticles in modulating enzymatic activity of urease, citrate

stabilized Au nanoparticles were functionalized with urease and the activity of the enzyme was monitored by the pH change of the medium while decomposing urea. The pH of the medium increased from 6.9 to 9.1, clearly indicating that mere functionalization of Au nanoparticles separately synthesized had no distinct impact on the enzyme activity. However, during the process of reducing the metal salt to form Au nanoparticles, urease had some loss of activity, although it was not completely denatured.

### **3.2.5 Conformational changes in urease after the synthesis of nanoparticles**

The activity of urease was largely inhibited after its participation in the reduction and/stabilization of the formed nanoparticles. The decrease in the activity of urease could be attributed to the conformational changes and chemical modifications in urease during the synthesis of metal nanoparticles.

The conformational studies were performed by fluorescence spectroscopy using 1-anilino-8-naphthalene sulfonate (ANS) as an extrinsic probe, as reported earlier for protein studies.<sup>[46]</sup> ANS is highly fluorescent in hydrophobic environment such as interior of an enzyme, but has very low quantum yield in water. Upon unfolding, the intensity will decrease as ANS will be released from the hydrophobic interior of the enzyme into the surrounding medium. Predictably, as shown in figure 3.10a, the emission intensity of ANS at around 490 nm was quenched and blue-shifted to around 470 nm, when urease was involved in the formation of Au nanoparticles. The quenching of ANS emission might be due to two factors: (i) unfolding of urease during reduction and subsequent binding to the Au nanoparticle surface (ii) energy transfer from the ANS donor to the Au nanoparticle acceptor as the emission wavelength of ANS matches with the surface plasmon resonance band of Au nanoparticles. In order to confirm this, controlled experiment in which urease solution was incubated with ANS and citrate capped Au nanoparticles (maintaining the  $\text{HAuCl}_4$  concentration same as used in the urease reduction) was performed. The fluorescence results (figure 3.10b) showed that the emission intensity of ANS was indeed quenched by the Au nanoparticles with a change in line-shape signifying the energy transfer.<sup>[46]</sup> However the

quenching was not as much as observed for the urease reduced Au nanoparticles, suggesting that both energy transfer as well as partial unfolding of urease contributed to the emission quenching of ANS.

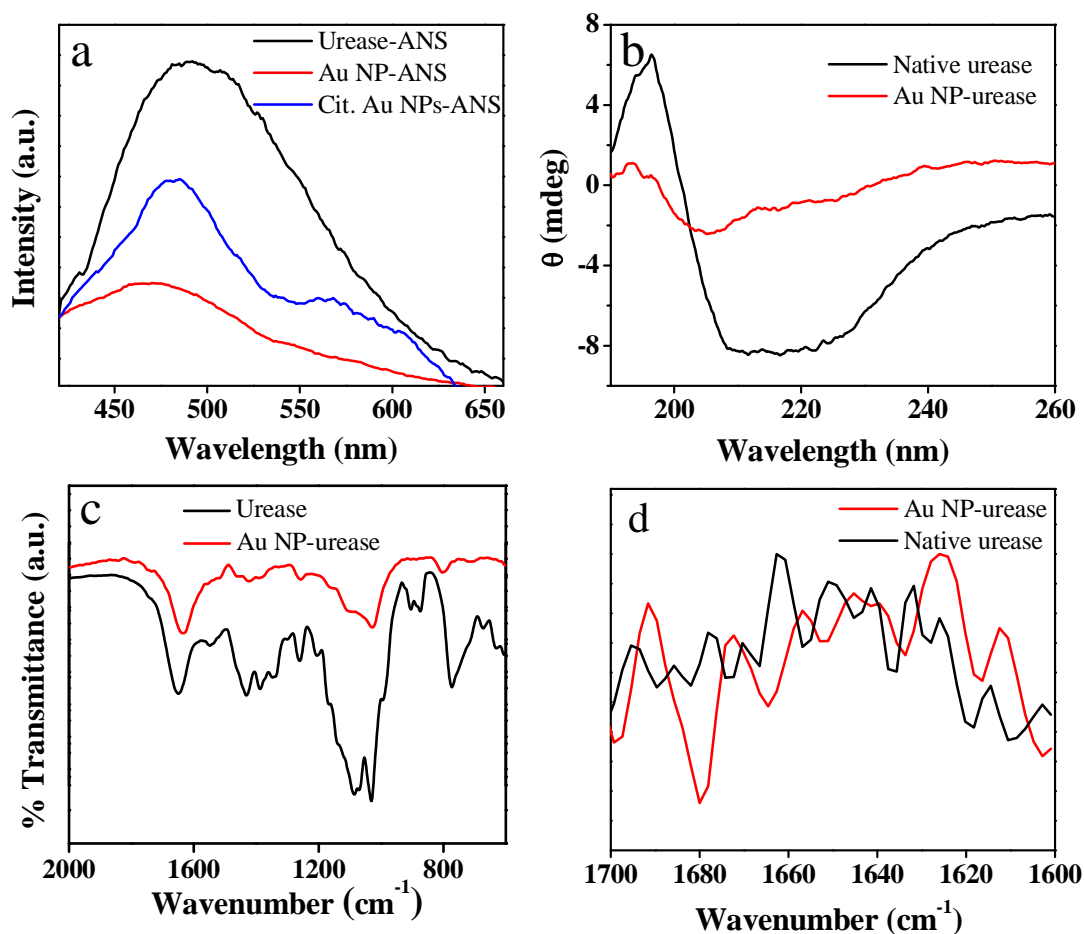


**Figure 3.10.** (a) Emission spectra of ANS in native urease, Citrate capped Au nanoparticles-urease composite and Au nanoparticle-urease composite (urease reduced Au nanoparticles) depicting the conformational modifications in enzyme structure ( $\lambda_{\text{ex}}=370$  nm). (b) Near UV Circular dichroism spectrum of native urease and Au nanoparticle urease composite in water, (c) FTIR spectrum showing the amide I and amide II region of native urease and Au NPs- urease composite and (d) Second derivative of the amide I region of native urease and Au NPs- urease composite.

To get a further insight into the conformational change of the enzyme, Circular Dichroism (CD) and FTIR studies were performed. The CD spectrum of native urease and Au NP-urease is shown in figure 3.10b. The decrease in the  $\alpha$ -helical content of a protein, which indicates the unfolding of the protein, can easily be monitored by tracking the loss in CD signal at 222 nm.<sup>[47]</sup> As shown in figure 3.10b, the CD signal at

222 nm in case of Au NP- urease composite showed a large decrease in intensity compared to that for the native urease, which is a clear indication of the enzyme being unfolded when it was involved in nanoparticle synthesis. This was further evidenced from the FTIR spectra (figure 3.10c), where the characteristic amide I band in native urease shifted from  $1650\text{ cm}^{-1}$  to  $1635\text{ cm}^{-1}$  in Au nanoparticle-urease composite signifying substantial perturbation in the enzyme structure.<sup>[48]</sup> The second derivative of the amide I band of urease showed peaks at  $1656$ ,  $1644$  and  $1636\text{ cm}^{-1}$  corresponding to  $\alpha$ - helix, disordered and  $\beta$ - sheet respectively, whereas in case of the enzyme reduced Au nanoparticles, these peaks were shifted to  $1652$ ,  $1641$  and  $1634\text{ cm}^{-1}$ , with a decrease in intensity<sup>[47,49]</sup> (figure 3.10d). Thus from fluorescence, CD and FTIR studies, it was clearly evident that there was a significant change in the structure of urease leading to partial inhibition of the enzyme activity.

### 3.2.6 Amino acid in urease responsible for reduction

Enzymes have a great structural complexity, as they are composed of several amino acid residues. The arrangement of these constituent amino acids into helices or sheets accounts for their structures with specific functionalities. Thus understanding the mechanism towards the growth of nanoparticles and subsequent structural and functional changes in enzymes is engrossing. It is established that cysteine has reducing as well as stabilizing capability for the generation of metal nanoparticles owing to high affinity of thiols for metals.<sup>[50]</sup> In enzymes also, cysteines have been postulated to be preferred sites for metal seeding and nanoparticle conjugation. Thus it was assumed that the free and exposed cysteine groups in an enzyme could act as a reducing agent for the synthesis of metal nanoparticles. To support the assumption, the free cysteine groups in urease were modified by reaction with 5,5'- dithiobis(2-nitrobenzoic acid) (DTNB) in non-denaturing conditions.<sup>[51]</sup> The addition of  $\text{HAuCl}_4$  to the DTNB modified urease, did not result in the formation of Au nanoparticles (figure 3.11a and b), clearly suggesting the involvement of cysteine in the formation of nanoparticles. The modification of the cysteine groups in urease was also evidenced by using FTIR, while observing the disappearance of a weak band at  $2660\text{ cm}^{-1}$  in the Au nanoparticle-urease composite, attributed to the S-H stretching mode in urease cysteine (figure 3.11c).<sup>[52]</sup>

Interestingly, in case of heat-denatured urease, faster growth of Au nanoparticles compared to the native enzyme was observed, clearly indicating that it is not essential for the enzyme to retain its native structure for being used as a reducing agent.

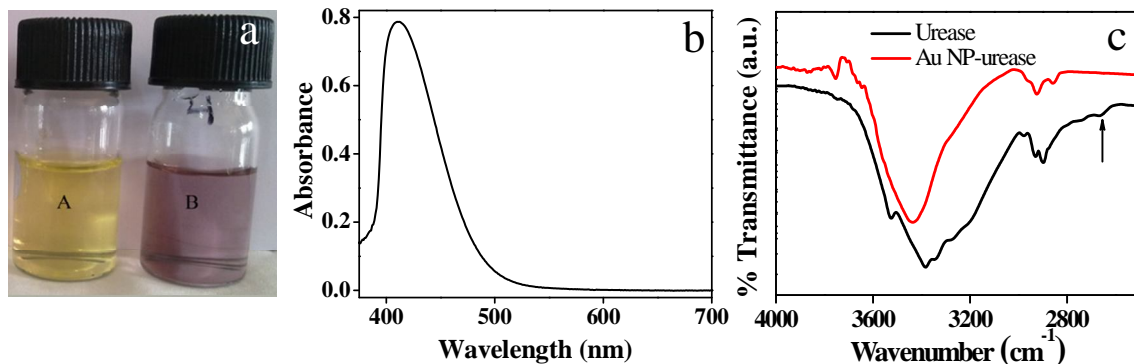


**Figure 3.11.** (a) Digital images showing reaction of urease with  $\text{HAuCl}_4$  in PBS (A) after blocking the thiol groups by DTNB and (B) unmodified urease. (b) UV-visible spectrum of DTNB treated urease after incubation with  $\text{HAuCl}_4$  for 48 hours, showing the absence of SPR band of Au nanoparticles. (c) FTIR spectra of native urease (black line) and Au NP- urease composite (red line). (Arrow in black line shows the peak at  $2660\text{ cm}^{-1}$  due to S-H stretching which is absent in the red line).

### 3.2.7 Mechanism of nanoparticle formation by urease and subsequent loss in its activity

In the synthesis of metallic nanoparticles, the involvement of urease in the reduction of the metal salts and subsequent binding to the nanoparticle surface led to conformational changes in the enzyme. The result was the partial inhibition of urease activity due to which hydrolysis of urea by the nanoparticle-urease conjugate led to pH enhancement only to a slightly basic 7.7, whereas in case of native urease the solution pH increased to 9.0. To have an insight into the mechanism of synthesis of nanoparticles by urease and the loss in the activity of the enzyme, the reported crystal structure of the Jack Bean Urease was examined. Jack Bean Urease was the first enzyme to be crystallized and the first example of a nickel metalloenzyme.<sup>[53]</sup> Spectroscopic, crystallographic and theoretical studies<sup>[54-57]</sup> have illustrated not only the molecular architecture and amino acid sequences in urease, but also the mechanism of enzymatic activity. Urease consists of 27-35 cysteine residues, which are divided into two groups, the inessential ones and essential ones.<sup>[57]</sup> It has been suggested that the

essential cysteine residues serve as acid catalysts in the mechanism of action of urease.<sup>[58]</sup> According to earlier reports, of the 27-35 cysteine residues present in JBU, only 3 of them (Cys59, Cys207 and Cys592) are the exposed ones and chemical modification of these groups impairs its activity<sup>[55]</sup> (protein data bank entry 3LA4). Out of these, Cys592 is located on the mobile flap adjacent to the active site (figure 3.12b) and plays a critical role in catalysis.<sup>[54]</sup> In the present study, it was hypothesized that the involvement of Cys592 in the formation of metallic nanoparticles followed by formation of disulfide bonds resulted in the structural changes in the mobile flap. As the mobile flap is involved in the regulation of access to the active site containing the nickel centre, the structural modification of the Cys592 and subsequent attachment to the metal nanostructures through the Metal-S bond greatly influenced the flap losing its mobility, leading to an inhibition in the activity of the enzyme. In case of denatured urease, five other buried cysteine residues per subunit become exposed and more reactive,<sup>[59]</sup> accounting for the faster growth of metallic nanoparticles by denatured urease.

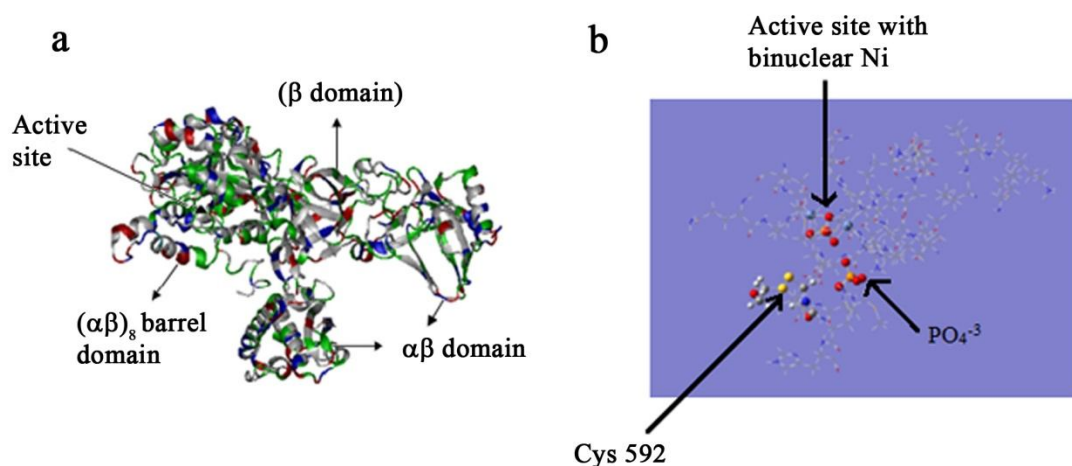


**Figure 3.12.** (a) Overall structure of the Jack bean urease monomer (b) stereo diagram of the active site architecture containing a binuclear nickel centre and mobile flap of urease. For clarity, only cys592 has been highlighted along with Ni ions and PO<sub>4</sub><sup>3-</sup> residues present in the active site.

### 3.2.8 Synthesis and characterization of Au@ZnO core-shell nanostructures

The primary activity of urease is the decomposition of urea, resulting in the liberation of ammonia with a net increase in the solution pH, making the environment

suitable for the growth of metal oxide nanoparticles. Hence, the possibility of the production of a semiconductor material such as ZnO as a shell around the Au nanoparticle-enzyme composite taking advantage of the catalytic ability of urease was explored. Under laboratory conditions addition of ammonia into a reaction medium containing metal salts resulted in the synthesis of metal oxide nanoparticles through condensation of the hydrolyzed product.<sup>[60]</sup> In the present method, although the urease activity was partially inhibited during nanoparticle synthesis, the hydrolysis of urea by Au nanoparticle-urease composite led to a homogeneous increase of the solution pH to 7.7 that has been exploited to synthesize ZnO nanoparticles.

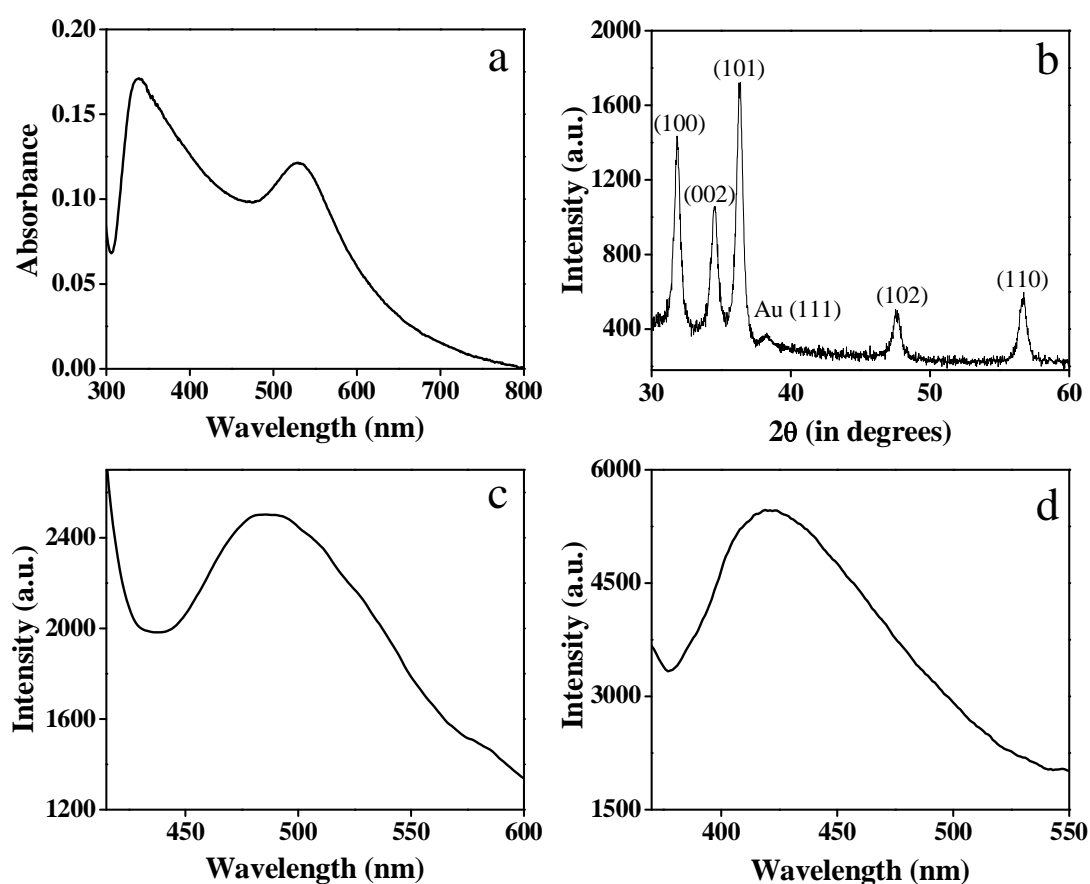


**Figure 3.13.** (a) UV- visible spectrum and (b) Powder X-ray diffraction spectrum of Au@ZnO core-shell nanostructures synthesized using urease. (c) and (d) Fluorescence emission spectrum of Au@ZnO core-shell nanostructures at an excitation wavelength of 390 nm and 340 nm respectively.

When Au nanoparticle-urease composite was incubated with urea and zinc nitrate hexahydrate in water at room temperature, ZnO nanoshells were formed over the

Au nanoparticles. The formation of the ZnO shell over the Au nanoparticles was established using several spectroscopic techniques as well as electron microscopy studies. The UV- visible spectrum of the Au@ZnO core-shell nanoparticles showed two distinct bands centred at 340 nm and 530 nm, characteristic of Au@ZnO core shell nanoparticles (figure 3.13a).<sup>[61]</sup> The intensity of the band at 530 nm decreased significantly and was red shifted by 8 nm compared to pure Au nanoparticles synthesized using urease, indicating the coating of the Au nanoparticles by a shell of ZnO. The X-ray diffraction pattern (figure 3.13b) of the Au-ZnO core-shell nanoparticles suggested nanocrystalline structure of the ZnO nanoshells with wurtzite structure (JCPDS card no. 0-3-0888). Along with the characteristic peaks of ZnO, one small reflection at  $38.2^\circ$ , characteristic of (111) plane of Au was observed. Scherrer analyses of the (101) and (102) reflections were used to calculate the crystal diameters of ZnO and showed an average size of 11.3 nm. The ZnO shell on the Au nanoparticles was further characterized by fluorescence spectroscopy. The ZnO nanoshells showed their characteristic emissions at 421 nm ( $\lambda_{\text{ex}}= 340$  nm) and 490 nm ( $\lambda_{\text{ex}}= 390$  nm) (figure 3.13c and d), originating from the oxygen defects present in the crystal.

Transmission electron microscopy studies were performed to study the size and morphology of the Au-ZnO core-shell nanoparticles. The TEM image and the particle size distribution histogram indicated that ZnO shells with an average thickness of  $2.1 \pm 0.4$  nm were formed around the Au nanoparticles (figure 3.14a and c), consistent with the overall diameter of Au-ZnO core-shell particles as measured by Scherrer analysis. The ZnO nanoshells showed high crystallinity as evidenced from the selected area electron diffraction pattern. The HRTEM image (figure 3.14b) clearly revealed the electron-dense core of Au surrounded by lesser dense shell of ZnO. EDX analysis of the sample further confirmed the presence of both Au and Zn in the composite material (figure 3.14d). Elemental analysis of the Au-ZnO nanoparticles, as acquired by inductively coupled plasma-atomic emission spectrometry (ICP-AES) measurements were used to calculate the ratio of Au and Zn in the core-shell nanocomposite. The results showed Au: Zn molar ratio of 55: 45, which was in close agreement with the theoretical calculations based on Au@ZnO core-shell morphology (details in experimental section).

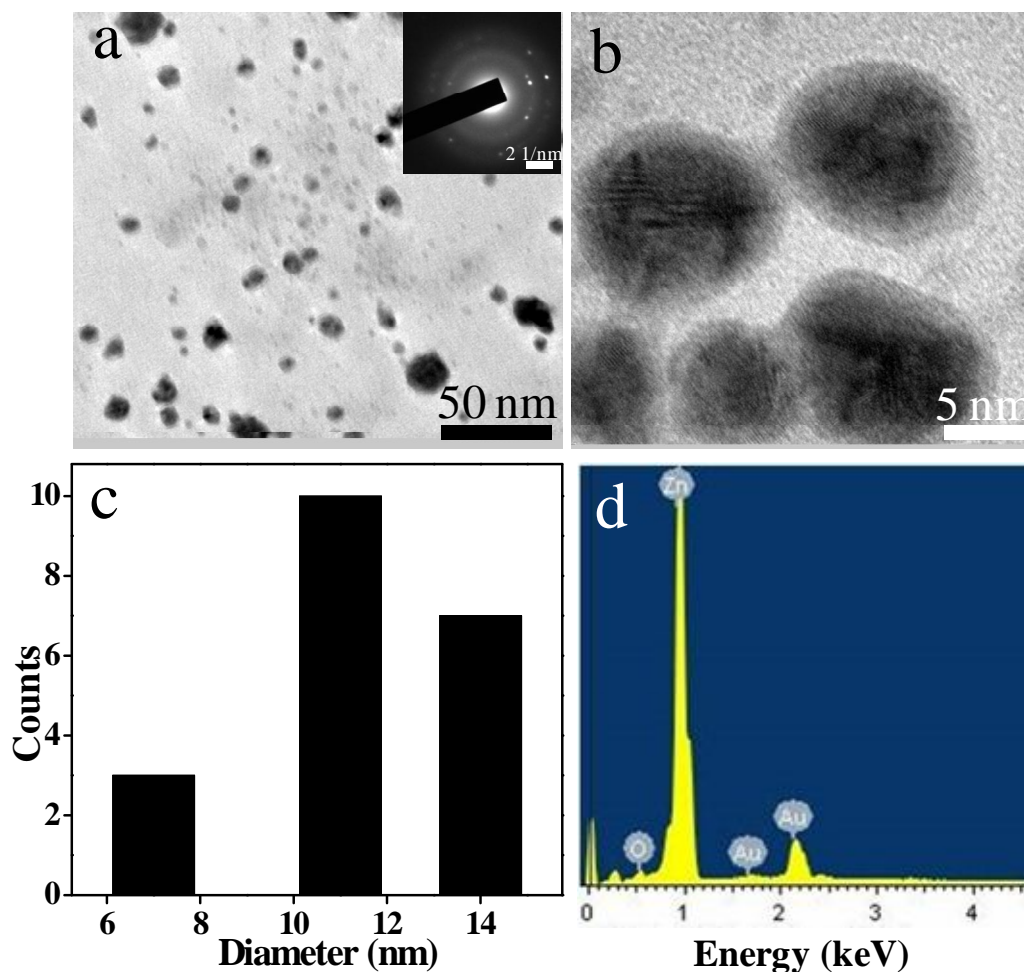


**Figure 3.14.** (a) TEM image; inset: SAED pattern, (b) HRTEM image, (c) Particle size distribution of Au@ZnO core-shell nanoparticles and (d) EDX spectrum of Au@ZnO core-shell nanostructures synthesized utilizing the activity of urease showing the presence of both Au and Zn.

Although the conformational changes in the enzyme structure did not have any impact on the metallic nanoparticle synthesis, they had a definitive role in the formation of ZnO nanostructures. It is noteworthy to mention that Au-denatured urease composite (Au nanoparticles reduced by heat-denatured urease) could not form the ZnO nanoshells, as the inherent characteristics of ZnO were not evidenced by XRD and fluorescence experiments. In case of native urease,  $\text{Zn}^{2+}$  binds on the negatively charged enzyme surface through electrostatic interaction at around pH 9. Previous reports have suggested the formation of zinc hydroxide intermediate under the basic conditions and further dehydration of these intermediates yield ZnO on the enzyme surface propelled by the "salting out" effect.<sup>[62,63]</sup> In the present case, the decomposition of urea by Au

nanoparticle-urease composite led to an increase of solution pH to 7.7. Even at this near neutral conditions, the entropy enhancement due to the disruption of the hydration layer around urease (because of  $\text{Zn}^{2+}$  binding to the enzyme surface) was enough to convert  $\text{Zn}(\text{OH})_2$  to ZnO nanoshells.

### 3.2.9 Catalytic reduction of *p*-nitroaniline to 1,4-diamino benzene

In order to have further evidence of Au-ZnO composite material with core-shell morphology, the reduction of *p*-nitroaniline with  $\text{NaBH}_4$  using Au-urease and Au@ZnO-urease as catalysts was performed. It is well known that Au nanoparticles can be used as an efficient heterogeneous catalyst for the reduction of *p*-nitroaniline to 1,4-diaminobenzene in presence of  $\text{NaBH}_4$ ,<sup>[64,65]</sup> whereas ZnO nanoparticles are not known to catalyze to the same reaction. So, in order to confirm the ZnO shell on the Au nanoparticles, the reduction of *p*-nitroaniline by  $\text{NaBH}_4$  with both Au nanoparticles and Au@ZnO core shell nanoparticles as catalyst was studied. It was found that in case of Au nanoparticles, the reduction was completed within 25 minutes, as evidenced by the decrease in the intensity of the peak at 380 nm and formation of a new peaks at 303 nm and 240 nm (figure 3.15b), characteristic of 1,4-diaminobenzene. However with the Au@ZnO core shell nanoparticles as catalyst, it was found that the reaction did not proceed substantially even after 10 hours, as evidenced by the absence of the peaks at 303 nm and 240 nm, but the peak at 380 nm decreased by 52% in intensity after 10 hours (figure 3.15c). For comparison, controlled experiments were performed with blank (without any nanoparticles) and ZnO-urease composite nanoparticles as catalyst. ZnO-urease nanoparticles were synthesized at pH 9.1 in water, originated from the production of ammonia due to breakdown of urea by urease. It was found that in case of blank the intensity of the peak at 380 nm decreased by 39% after 10 hours (figure 3.15d) and with ZnO-urease nanoparticles as catalysts the intensity decreased by 40% after 10 hours (figure 3.15e). A plot of logarithm of absorbance ( $\ln A$ ) for *p*-nitroaniline at 380 nm showed a linear decrease with time, confirming the reduction of *p*-nitroaniline with Au nanoparticles as catalyst, whereas in case of Au@ZnO core shell nanoparticles as catalyst, the plot of  $\ln A$  versus time (figure 3.15f) showed that the reaction proceeded very slowly, which further confirmed that the Au nanoparticles were

indeed coated with ZnO layer. Thus, from the catalytic experiments the formation of ZnO shell on Au nanoparticles could be confirmed further.

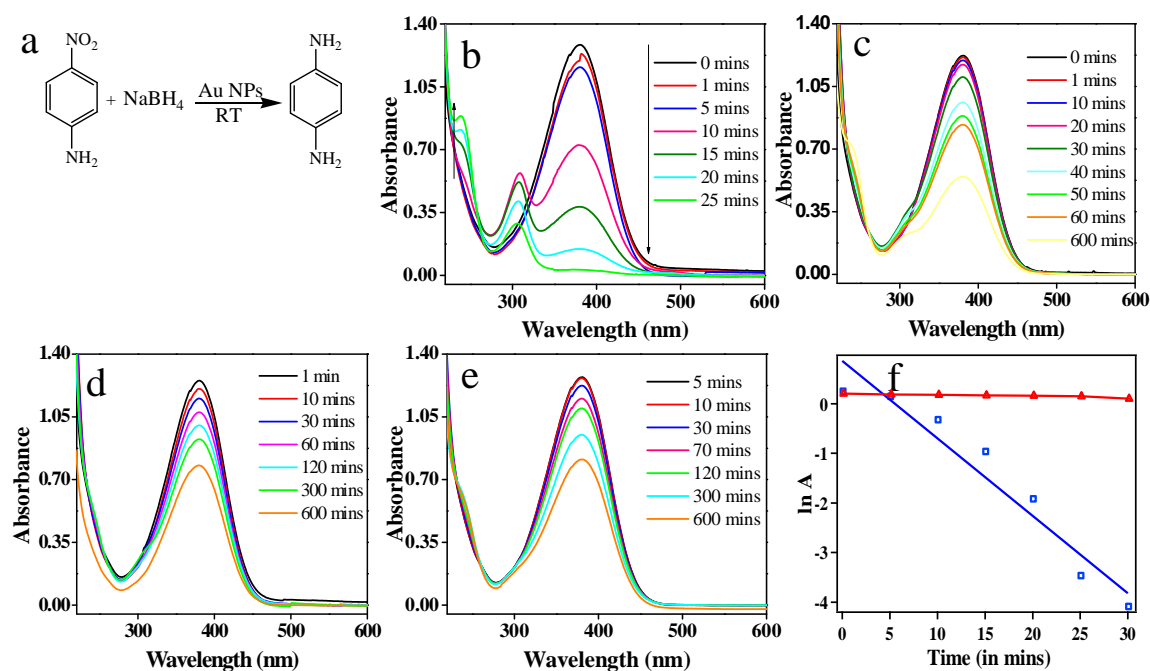


**Figure 3.15.** (a) Scheme for the reduction of *p*-nitroaniline to 1,4-diamino benzene by urease reduced Au nanoparticles. (b) Time dependent UV-visible spectra for the reduction of *p*-nitroaniline to 1,4-diamino benzene by urease reduced Au nanoparticles acting as catalyst. (c) Time dependent UV-visible spectra for the reduction of *p*-nitroaniline to 1,4-diamino benzene by Au@ZnO core-shell nanoparticles as catalyst. Time dependent UV-visible spectra for the reduction of *p*-nitroaniline to 1,4-diamino benzene catalyzed (d) in absence of any nanoparticles and (e) by ZnO nanoparticles synthesized using urease and (f) plot of  $\ln A$  vs  $T$  for the reduction of *p*-nitroaniline to 1,4-diaminobenzene by  $\text{NaBH}_4$  in presence of urease reduced Au nanoparticles (blue) and Au@ZnO core-shell nanoparticles (red).

### 3.3 Conclusions

In summary, the use of urease as an effective biomolecular reactor towards the growth of metallic nanoparticles, metallic alloys and metal-metal oxide core-shell nanostructures under ambient conditions has been demonstrated. The exposed cysteine residues in the enzyme were found to be responsible for the generation of metal and metallic alloy nanoparticles. Due to modification of the essential cysteine residues, there were conformational changes in the enzyme structure leading to partial inhibition of its activity during the nanoparticle synthesis, Although the activity was largely

inhibited, it could still be employed for the synthesis of metal-ZnO core-shell nanoparticles. The use of urease as a nanoreactor demonstrates the practicability of biomolecules such as enzymes, as an alternative to the current environmentally harsh and energy-exhaustive methods for material synthesis. Further these studies will give a mechanistic intimation towards the capability of microorganisms such as fungus, bacteria and viruses in synthesizing nanoparticles.<sup>[66-68,7]</sup> The proposed methodology can be extended easily towards the generation of a range of alloys and core-shell nanostructures involving metal and metal oxides. Further the immobilization and growth of these nanoparticle-enzyme composites on various substrates will afford opportunities for the development of technologically relevant systems.

### **3.4 Experimental Section**

#### **3.4.1 Materials**

Hydrogen tetrachloroaurate ( $\text{HAuCl}_4$ ), Silver nitrate ( $\text{AgNO}_3$ ), Potassium tetrachloroplatinate ( $\text{K}_2\text{PtCl}_4$ ), Jack Bean urease, Urea, Zinc nitrate hexahydrate, 5,5'-dithiobis(2-nitrobenzoic acid) (DTNB), and 8-Anilino-1-naphthalenesulfonic acid (ANS) were purchased from Sigma- Aldrich. Sodium dihydrogen phosphate monohydrate, di- Sodium hydrogen phosphate, Sodium nitrate and Bromocresol purple were purchased from Merck, India. Potassium carbonate was purchased from Rankem, India. *p*-nitroaniline and sodium borohydride were purchased from S.D Fine chemicals, India. All the chemicals were used as received without any further purification. Milli Q water was used throughout the experiments.

#### **3.4.2 Instrumentation**

A Varian Cary 100 Bio spectrophotometer was used for UV-visible measurements. Emission spectra were recorded on a fluoromax-4p fluorometer from Horiba (Model: FM-100). Powder X- ray diffraction patterns were recorded on a Bruker D8 Advance diffractometer with Cu  $K\alpha$  source (wavelength of X- rays was 0.154 nm). Transmission electron microscopy (TEM) images were recorded using a Philips CM 200 microscope and High resolution transmission electron microscope images were recorded using a JEOL JEM-2100 microscope at an operating voltage of 200kv. FTIR

spectra were recorded in KBr pellet using a Bruker Tensor 27 instrument. Circular Dichroism (CD) studies were performed using a JASCO J-815 spectropolarimeter. ICP-AES measurements were performed using instrument from M/s. Spectro, Germany (Model: Arcos). XPS spectra were recorded using an ESCA instrument: VSW of UK make.

### **3.4.3 Synthesis of Au nanoparticles using K<sub>2</sub>CO<sub>3</sub>**

In a typical synthesis of Au nanoparticles, 2.5 mL of 2mg/mL enzyme solution, 2.5 mg K<sub>2</sub>CO<sub>3</sub> and 50 μL of 0.03 M HAuCl<sub>4</sub> were taken in a vial and the reaction mixture was heated at 37 °C with mild stirring for 6 hours.

### **3.4.4 Synthesis of Ag nanoparticles**

For the synthesis of Ag nanoparticles 25 μL of 0.03 M AgNO<sub>3</sub> solution was added to 2.2 mL of 2mg/mL enzyme solution, containing 0.95 mg of K<sub>2</sub>CO<sub>3</sub>, and the resulting mixture was stirred at 37 °C for 6 hours.

### **3.4.5 Synthesis of Pt nanoparticles**

Pt nanoparticles were synthesized by the reaction of 2.5 mL of 2mg/mL urease solution with 75 μL of 0.02 M K<sub>2</sub>PtCl<sub>4</sub> in presence of 2 mg K<sub>2</sub>CO<sub>3</sub> and heated at 37 °C for 36 hours.

### **3.4.6 Synthesis of alloy nanoparticles**

The synthesis of all the alloy nanoparticles was carried out in 2.2 mL of 2mg/mL enzyme solution containing 2.5 mg of K<sub>2</sub>CO<sub>3</sub>. For all the three alloy nanoparticles (Au-Ag, Ag-Pt and Au-Pt), metal salts were added such that their individual concentration in the final solution was  $2.7 \times 10^{-4}$  M, and the resulting solution was stirred at 37 °C for 24 hours.

### **3.4.7 Synthesis of Au@ZnO core-shell nanoparticles**

The Au nanoparticle-urease composites (by reduction of HAuCl<sub>4</sub> with urease) were centrifuged and washed with water several times to remove any free enzyme unbound to the Au nanoparticle surface. The obtained pellet was re-dispersed in 0.1 M NaNO<sub>3</sub>. To 2mL of the Au nanoparticle-urease composite solution, was added 10 mg of

urea and 50  $\mu\text{L}$  of 0.02 M  $\text{Zn}(\text{NO}_3)_2 \cdot 6\text{H}_2\text{O}$  and the reaction mixture was stirred at room temperature for 12 hrs.

### **3.4.8 XPS Measurement**

The XPS measurements were performed using an ESCA instrument: VSW of UK make with an Al  $\text{K}\alpha$  source, at a resolution of 1eV. The sample was measured in thin film mode and the sample was prepared by drop casting the nanoparticle solution on a glass slide.

### **3.4.9 Conformational changes in urease after nanoparticle synthesis.**

#### **3.4.9.1 Fluorescence studies**

The conformational changes in urease after the synthesis of nanoparticles were studied using an extrinsic fluorophore, 8-Anilino-1-naphthalenesulfonic acid. For this purpose, ANS with a final concentration of 20  $\mu\text{M}$  was added to each of native urease solution, Au NP- urease solution and citrate capped Au nanoparticles- urease, and fluorescence spectra were recorded at excitation wavelength of 370 nm, after incubating the solutions in dark for 4 hours.

#### **3.4.9.2 Circular dichroism studies**

The CD studies were performed at 25  $^\circ\text{C}$  on a Jasco-815 spectrometer. Spectra were recorded between 260 and 190 nm with a data pitch of 0.1 nm. The scanning speed was set to 20 nm/ min with band width of 1nm. The path length was 1 mm quartz cell (Starna Scientific Ltd. Hainault, UK). An enzyme concentration of 1mg/mL was used throughout the experiments. Each spectrum is the result of average of three consecutive scans.

### **3.4.10 Activity study of urease**

#### **3.4.10.1 pH method**

The activity of urease can easily be monitored by noting the rise in pH upon addition of urea. So to test the activity of urease after the formation of Au NPs, 50 mg of urea was added to 10 mL of both native urease (1mg/mL) and urease-Au NP solution, and the increase in pH with time was recorded.

### 3.4.10.2 Bromocresol purple assay

The activity was also confirmed spectroscopically using the bromocresol purple assay, following a reported procedure.<sup>2</sup> Briefly, two test solutions were taken, one containing Native enzyme, 0.015 mM bromocresol purple and 0.2 mM EDTA. In the second solution the native enzyme was replaced by Au NP- enzyme composite, and the pH was adjusted to 5.8. Then urea was added to the solutions and absorbance at 588 nm was recorded at various time intervals.

### 3.4.11 Theoretical calculation of ratio of Au: Zn in Au@ZnO core-shell nanoparticles.

The average diameter of Au nanoparticles,  $d = 8.9$  nm

Hence, the radius of the Au nanoparticles,  $r = 4.45$  nm =  $4.45 \times 10^{-7}$  cm

$\therefore$  Volume occupied by Au nanoparticles,  $V = 4/3\pi r^3 = 3.69 \times 10^{-19}$  cc

Density of Au,  $\rho = 19.3$  g/cc

$\therefore$  Mass of Au,  $M = V \times \rho = 7.122 \times 10^{-18}$

$\therefore$  No. of moles of Au =  $7.122 \times 10^{-18} / 197$   
 $= 3.62 \times 10^{-20}$  moles

The average diameter of Au@ZnO core shell nanoparticles = 11 nm.

Hence the radius of the Au@ZnO core shell nanoparticles = 5.5 nm

$\therefore$  Volume occupied by the ZnO shell,  $V = 4/3\pi r_{\text{Au@ZnO}}^3 - 4/3\pi r_{\text{Au}}^3$   
 $= (6.95 - 3.68) \times 10^{-19}$  cc  
 $= 3.27 \times 10^{-19}$  cc

Density of Zn,  $\rho = 5.61$  g/cc

$\therefore$  Mass of Zn,  $M = V \times \rho = 1.834 \times 10^{-18}$  g

$$\therefore \text{No. of moles of Zn} = 1.834 \times 10^{-18} / 65.38$$

$$= 2.808 \times 10^{-20} \text{ moles}$$

$$\therefore \% \text{ of Au in the core shell composite} = \frac{3.62 \times 10^{-20}}{(3.62 + 2.808) \times 10^{-20}} \times 100$$

$$= 56.32 \%$$

$$\text{And, \% of Zn in the core shell composite} = \frac{2.808 \times 10^{-20}}{(3.62 + 2.808) \times 10^{-20}} \times 100$$

$$= 43.68 \%$$

### 3.5. References

1. Daniel M. C., Astruc D. (2004), Gold nanoparticles: Assembly, supramolecular chemistry, quantum-size-related properties, and applications towards biology, catalysis, and nanotechnology, *Chem. Rev.*, 104, 293- 346 (DOI: 10.1021/cr030698).
2. Costi R., Saunders A. E., Banin U. (2010), Colloidal hybrid nanostructures: A new type of functional materials, *Angew. Chem. Int. Ed.* 49, 4878-4897 (DOI: 10.1002/anie.200906010).
3. Goesmann H., Feldmann C. (2010), Nanoparticulate functional materials, *Angew. Chem. Int. Ed.*, 49, 1362-1395 (DOI: 10.1002/anie.200903053).
4. Khullar P., Singh V., Mahal A., Kaur H., Singh V., Banipal T. S., Kaur G., Bakshi M. S. (2011), Tuning the shape and size of gold nanoparticles with triblock polymer micelle structure transitions and environments, *J. Phys. Chem. C*, 115, 10442-10454 (DOI: 10.1021/jp201712a).
5. Fischer A., Muller J. O., Antonietti M., Thomas A. (2008), Synthesis of ternary metal nitride nanoparticles using mesoporous carbon nitride as reactive template, *ACS Nano*, 2, 2489-2496 (DOI: 10.1021/nn800503a).
6. Berti L., Burley G. A. (2008), Nucleic acid and nucleotide-mediated synthesis of inorganic nanoparticles, *Nat. Nanotechnol.*, 3, 81-87 (DOI:10.1038/nnano.2007.460).
7. Escosura A. de la, Nolte R. J. M., Cornelissen, J. J. L. M. (2009), Viruses and protein cages as nanocontainers and nanoreactors, *J. Mater. Chem.*, 19, 2274-2278 (DOI: 10.1039/B815274H).
8. Ghadiali J. E., Stevens M. M. (2008), Enzyme-responsive nanoparticle systems, *Adv. Mater.*, 20, 4359-4363 (DOI: 10.1002/adma.200703158).
9. Wang Z., Levy R., Fernig D. G., Brust, M. (2006), Kinase-catalyzed modification of gold nanoparticles: A new approach to colorimetric kinase activity screening, *J. Am. Chem. Soc.*, 128, 2214-2215 (DOI: 10.1021/ja058135y).

10. Choi Y., Ho N. H., Tung C. H. (2007), Sensing phosphatase activity by using gold nanoparticles, *Angew. Chem. Int. Ed.*, 46, 707-709 (DOI: 10.1002/anie.200603735).
11. Rodriguez-Lorenzo L., de la Rica R., Alvarez-Puebla A., Liz-Marzan L. M., Stevens M. M. (2012), Plasmonic nanosensors with inverse sensitivity by means of enzyme-guided crystal growth, *Nat. Mater.*, 11, 604-607 (DOI:10.1038/nmat3337).
12. You C. C., Agasti S. S., De M., Knapp M. J., Rotello V. M. (2006), Modulation of the catalytic behavior of  $\alpha$ -chymotrypsin at monolayer-protected nanoparticle surfaces, *J. Am. Chem. Soc.*, 128, 14612-14618 (DOI: 10.1021/ja064433z).
13. Deka J., Paul A., Chattopadhyay A. (2012), Modulating enzymatic activity in the presence of gold nanoparticles, *RSC Adv.*, 2, 4736-4745 (DOI: 10.1039/C2RA20056B).
14. Zhao F., Li H., Jiang Y., Wang X., Mu X. (2014), Co-immobilization of multi-enzyme on control-reduced graphene oxide by non-covalent bonds: An artificial biocatalytic system for the one-pot production of gluconic acid from starch, *Green Chem.*, 16, 2558-2565 (DOI: 10.1039/C3GC42545B).
15. Shenton W., Mann S., Colfen H., Bacher A. Fischer M. (2001), Synthesis of nanophase iron oxide in lumazine synthase Capsids, *Angew. Chem. Int. Ed.*, 40, 442-445 (DOI: 10.1002/1521-3773(20010119)40:2<442::AID-ANIE442>3.0.CO;2-2).
16. de la Rica R., Matsui H. (2008), Urease as a nanoreactor for growing crystalline ZnO nanoshells at room temperature, *Angew. Chem. Int. Ed.*, 47, 5415-5417 (DOI: 10.1002/anie.200801181).
17. Johnson J. M., Sinsinger N., Sun C., Li D., Kisailus D. (2012), Urease-mediated room-temperature synthesis of nanocrystalline titanium dioxide, *J. Am. Chem. Soc.*, 134, 13974-13977. (DOI: 10.1021/ja306884e).
18. Willner I., Baron R., Willner B. (2006), Growing metal nanoparticles by enzymes, *Adv. Mater.*, 18, 1109-1120 (DOI: 10.1002/adma.200501865).

19. Virkutyte J., Varma R. S. (2011), Green synthesis of metal nanoparticles: Biodegradable polymers and enzymes in stabilization and surface functionalization, *Chem. Sci.*, 2, 837-846 (DOI: 10.1039/C0SC00338G).
20. Scott D., Toney M., Muzikar M. (2008), Harnessing the mechanism of glutathione reductase for synthesis of active site bound metallic nanoparticles and electrical connection to electrodes, *J. Am. Chem. Soc.*, 130, 865-874 (DOI: 10.1021/ja074660g).
21. Xiao Y., Patolsky F., Katz E., Hainfeld J. F., Willner I. (2003), "Plugging into enzymes": Nanowiring of redox enzymes by a gold nanoparticle, *Science*, 299, 1877-1881 (DOI: 10.1126/science.1080664).
22. Xie J., Zhang Y., Ying J. Y. (2009), Protein-directed synthesis of highly fluorescent gold nanoclusters, *J. Am. Chem. Soc.*, 131, 888-889 (DOI: 10.1021/ja806804u).
23. Xu Y., Sherwood J., Qin Y., Crowley D., Bonizzoni M., Bao Y. (2014), The role of protein characteristics in the formation and fluorescence of Au nanoclusters, *Nanoscale*, 6, 1515-1524 (DOI: 10.1039/C3NR06040C).
24. Goswami N., Zheng K., Xie J. (2014), Bio-NCs – the marriage of ultrasmall metal nanoclusters with biomolecules, *Nanoscale*, 6, 13328-13347 (DOI: 10.1039/C4NR04561K).
25. Wen F., Dong Y, Feng L., Wang S., Zhang S., Zhang X. (2011), Horseradish peroxidase functionalized fluorescent gold nanoclusters for hydrogen peroxide sensing, *Anal. Chem.*, 83, 1193-1196 (DOI: 10.1021/ac1031447).
26. Rangnekar A., Sarma T. K., Singh A. K., Deka J., Ramesh A., Chattopadhyay A. (2007), Retention of enzymatic activity of  $\alpha$ -Amylase in the reductive synthesis of gold nanoparticles, *Langmuir*, 23, 5700-5706 (DOI: 10.1021/la062749e).
27. Sharma B., Mandani S., Sarma T. K. (2014), Enzymes as bionanoreactors: Glucose oxidase for the synthesis of catalytic Au nanoparticles and Au nanoparticle–polyaniline nanocomposites, *J. Mater. Chem. B*, 2, 4072-4079 (DOI: 10.1039/C4TB00218K).

- 
28. Slocik J. M., Naik R. R., Stone M. O., Wright D. W. (2005), Viral templates for gold nanoparticle synthesis, *J. Mater. Chem.*, 15, 749-753 (DOI: 10.1039/B413074J).
  29. Link S., El-Sayed M. A. (1999), Size and temperature dependence of the plasmon absorption of colloidal gold nanoparticles, *J. Phys. Chem. B*, 103, 4212-4217 (DOI: 10.1021/jp984796o).
  30. Haiss W., Thanh T. K. N., Aveyard J., Fernig D. G. (2007), Determination of size and concentration of gold nanoparticles from UV-Vis spectra, *Anal. Chem.* 79, 4215-4221 (DOI: 10.1021/ac0702084).
  31. Wojcieszak R., Genet M. J., Eloy P., Ruiz P. Gaigneaux E. M. (2010) Determination of the size of supported Pd nanoparticles by X-ray photoelectron spectroscopy. Comparison with X-ray diffraction, transmission electron microscopy, and H<sub>2</sub> chemisorption methods, *J. Phys. Chem. C*, 114, 16677-16684 (DOI: 10.1021/jp106956w).
  32. Janardhanan R., Karuppaiah M., Hebalkar N., Rao T. N. (2009), Synthesis and surface chemistry of nano silver particles, *Polyhedron*, 28, 2522-2530 (DOI: 10.1016/j.poly.2009.05.038).
  33. Dhoondhia Z. H., Chakraborty H. (2012) Lactobacillus mediated synthesis of silver oxide nanoparticles *Nanomater. Nanotechnol.*, 2, (DOI: 10.5772/55741).
  34. Pettersson L. L. A., Snyder P. G. (1995), Preparation and characterization of oxidized silver thin films, *Thin Solid Films*, 270, 69-72 (DOI:10.1016/0040-6090(96)80069-1).
  35. Tjeng L. H., Meinders M. B. J., Van Elp J., Ghijsen J., Sawatzky G. A. (1990), Electronic structure of Ag<sub>2</sub>O, *Phys. Rev. B*, 41, 3190-3199 (DOI: 10.1103/PhysRevB.41.3190).
  36. Xiao F., Liu H. G., Lee Y- III. (2008), Formation and characterization of two dimensional arrays of silver oxide nanoparticles under langmuir monolayers of n- Hexadecyl dihydrogen phosphate, *Bull. Korean. Chem. Soc.*, 29, 2368-2372 (DOI: 10.5012/bkcs.2008.29.12.2368).
  37. Mohan S., Jose G. (2007) Stability of core-shell nanoparticles formed in a dielectric medium, *Appl. Phys. Lett.*, 91, 253107 (DOI: 10.1063/1.2822895).

38. Vinod V. T. P., Saravanan P., Sreedhar B., Devi D. K., Sashidhar R. B. (2011), A facile synthesis and characterization of Ag, Au and Pt nanoparticles using a natural hydrocolloid gum kondagogu (*Cochlospermum gossypium*), *Colloids Surf. B*, 83, 291-298 (DOI: 10.1016/j.colsurfb.2010.11.035).
39. Lin X., Wu M., Wu D., Kuga S., Endo T., Huang Y. (2011), Platinum nanoparticles using wood nanomaterials: Eco-friendly synthesis, shape control and catalytic activity for *p*-nitrophenol reduction, *Green Chem.* **13**, 283-287 (DOI: 10.1039/C0GC00513D).
40. El Badawy A. M., Luxton T. P., Silva R. G., Scheckel G. K., Suidan M. T., Tolaymat T. M. (2010), Impact of environmental conditions (pH, Ionic Strength, and Electrolyte Type) on the surface charge and aggregation of silver nanoparticles suspensions, *Environ. Sci. Technol.*, 44, 1260-1266 (DOI: 10.1021/es902240k).
41. Sylvestre J. -P., Poulin S., Kabashin A. V., Sacher E., Meunier M., Luong J. H. T. (2004), Surface chemistry of gold nanoparticles produced by laser ablation in aqueous media, *J. Phys. Chem. B*, 108, 16864–16869. (DOI: 10.1021/jp047134+).
42. Du S., Kendall K., Panteha T., Mehrabadi Y., Gupta G., Newton J. (2012), Aggregation and adhesion of gold nanoparticles in phosphate buffered saline, *J. Nanopart. Res.*, 14, 758 (DOI 10.1007/s11051-012-0758-z).
43. Burda C., Chen X. B., Narayanan R., El-Sayed, M. A. (2005), Chemistry and properties of nanocrystals of different shapes. *Chem. Rev.*, 105, 1025-1102 (DOI: 10.1021/cr030063a).
44. Rao C. N. R., Matte H. S. S. R., Voggu R., Govindaraj A. (2012), Recent progress in the synthesis of inorganic nanoparticles, *Dalton Trans.*, 41, 5089-5120 (DOI: 10.1039/C2DT12266A)
45. Lvov Y., Antipov A. A., Mamedov A., Moehwald H., Sukhorukov G. B. (2001), Urease encapsulation in nanoorganized microshells, *Nano Lett.* 1, 125-128 (DOI: 10.1021/nl0100015).
46. Lystvet S. M., Volden S., Halskau O., Glomm W. R. (2011), Immobilization onto gold nanoparticles alters  $\alpha$ -lactalbumin interaction with pure and

- mixed phospholipid monolayers, *Soft Matter*, 7, 11501-11509 (DOI: 10.1039/C1SM06337E).
47. Cruz J. C., Pfromm P. H., Tomich J. M., Rezac M. E. (2010), Conformational changes and catalytic competency of hydrolases adsorbing on fumed silica nanoparticles: II. Secondary structure, *Colloids Surf. B*, 81, 1-10 (DOI:10.1016/j.colsurfb.2010.06.005).
48. Kumar C. V., Chaudhari A. (2001), Chemical chaperones: Influence of carboxylate orientation in the refolding of glucose oxidase, *Microporous and Mesoporous Materials*, 47, 407-410 (DOI: 10.1016/S1387-1811(01)00313-4).
49. Jiang X., Jiang J., Jin J., Wang E., Dong S. (2005), Effect of colloidal gold size on the conformational changes of adsorbed cytochrome c: Probing by circular dichroism, UV-visible, and infrared spectroscopy, *Biomacromolecules*, 6, 46- 53 (DOI: 10.1021/bm0497441).
50. Ma Z., Han H. (2008), One-step synthesis of cystine coated gold nanoparticles in aqueous solutions, *Colloids Surf. A*, 317, 229-233 (DOI:10.1016/j.colsurfa.2007.10.018).
51. Ellman G. L. (1959), Tissue sulfhydryl groups, *Arch. Biochem. Biophys.*, 82, 70-77 (DOI:10.1016/0003-9861(59)90090-6).
52. Colombo M., Mazzucchelli S., Colico V., Avvakuvoka S., Pandolfi L., Corsi F., Porta F., Prospero D. (2012), Protein-assisted one pot synthesis and biofunctionalization of spherical gold nanoparticles for selective targeting of cancer cells, *Angew. Chem. Int. Ed.*, 51, 9272-9275 (DOI: 10.1002/anie.201204699).
53. Sumner J. B. (1926), The isolation and crystallization of the enzyme urease, *J. Biol. Chem.*, 69, 435-441.
54. Roberts B. P., Miller B. R. III, Roitberg A. E., Merz K. M. Jr. (2012), Wide-open flaps are key to urease activity, *J. Am. Chem. Soc.*, 134, 9934-9937 (DOI: 10.1021/ja3043239).
55. Balasubramanian A., Ponnuraj K. (2010), Crystal structure of the first plant urease from jack bean: 83 years of journey from its first crystal to molecular structure, *J. Mol. Biol.*, 400, 274-283 (DOI: 10.1016/j.jmb.2010.05.009).

56. Krajewska B., Zaborska W. (2007) Jack bean urease: The effect of active-site binding inhibitors on the reactivity of enzyme thiol groups, *Bioorg. Chem.*, 35, 355-365 (DOI: 10.1016/j.bioorg.2007.02.002).
57. Takishima K., Suga T., Mamiya G. (1988), The structure of jack bean urease: The complete amino acid sequence, limited proteolysis and reactive cysteine residues, *Eur. J. Biochem.*, 175, 151-165 (DOI: 10.1111/j.1432-1033.1988.tb14177.x).
58. Dixon N. E., Riddles P. W., Gazzola C., Blakeley R. L., Zerner B. (1980), Jack bean urease (EC 3.5.1.5). V. On the mechanism of action of urease on urea, formamide, acetamide, N-methylurea, and related compounds, *Can. J. Biochem.*, 58, 1335-1344 (DOI: 10.1139/o80-181).
59. Jabri E., Karplus P. A. (1996), Structures of the *Klebsiella aerogenes* urease apoenzyme and two active-site mutants, *Biochemistry*, 35, 10616-10626 (DOI: 10.1021/bi960424z).
60. Kisailus D., Schwenzer B., Gomm J., Weaver J. C., Morse D. E. (2006), Kinetically controlled catalytic formation of Zinc oxide thin films at low temperature, *J. Am. Chem. Soc.*, 128, 10276-10280 (DOI: 10.1021/ja062434l).
61. Haldar K. K., Sen T., Patra A. (2008), Au@ZnO Core-shell nanoparticles are efficient energy acceptors with organic dye donors, *J. Phys. Chem. C*, 112, 11650-11656 (DOI: 10.1021/jp8031308).
62. Garczarek F. Gerwert K. (2006), Functional waters in intraprotein proton transfer monitored by FTIR difference spectroscopy, *Nature*, 439, 109-112 (DOI: 10.1038/nature04231).
63. Makarov V., Pettitt M., Feig M. (2002), Solvation and hydration of proteins and nucleic acids: A theoretical view of simulation and experiment, *Acc. Chem. Res.*, 35, 376-384 (DOI: 10.1021/ar0100273).
64. Aditya T., Pal A., Pal T. (2015), Nitroarene reduction: A trusted model reaction to test nanoparticle catalysts, *Chem. Commun.*, 51, 9410-9431 (DOI: 10.1039/C5CC01131K).

65. Yao Y., Xue M., Chi X., Ma Y., He J., Abliz Z., Huang F. (2012), A new water-soluble pillar[5]arene: Synthesis and application in the preparation of gold nanoparticles, *Chem. Commun.*, 48, 6505-6507 (DOI: 10.1039/C2CC31962D).
66. Mukherjee P. *et al.* (2001), Bioreduction of  $\text{AuCl}_4^-$  ions by the fungus *Verticillium sp.* and the surface trapping of the gold nanoparticles formed, *Angew. Chem. Int. Ed.*, 40, 3585-3588 (DOI: 10.1002/1521-3773(20011001)40:19<3585::AID-ANIE3585>3.0.CO;2-K).
67. Bharade A. A. *et al.* (2008), Bacteria-mediated precursor-dependent biosynthesis of superparamagnetic iron oxide and iron sulfide nanoparticles, *Langmuir*, 24, 5787-5794 (DOI: 10.1021/la704019p).
68. Mann S. (1993), Molecular tectonics in biomineralization and biomimetic materials chemistry, *Nature*, 365, 499-505 (DOI: 10.1038/365499a0).



## Chapter 4

# Catalytic Activity of Various Pepsin Reduced Au Nanostructures Towards Reduction of Nitroarenes and Resazurin

### 4.1 Introduction

Metallic nanoparticles have gained immense research interest due to their distinctive physico-chemical properties, which differ considerably from their bulk counterparts.<sup>[1,2]</sup> Catalysis is one of the most important areas where nanoparticles have made exceptional performance. Due to their large surface area to volume ratio, metallic nanoparticles can function as effective heterogeneous catalysts towards a myriad of organic reactions. Specially, Au nanoparticles have shown tremendous functionality as heterogeneous catalyst towards various organic transformations such as oxidation, reduction, C-C coupling reactions etc.<sup>[3-17]</sup> For effective catalysis and to prevent their agglomeration, nanoparticles are embedded in solid supports such as metal oxides,<sup>[18,19]</sup> metal-organic frameworks,<sup>[20,21]</sup> carbonaceous materials<sup>[22-24]</sup> etc. On the other hand, development of Au nanoparticle systems without any solid support has gained interest due to their simplicity of preparation, processability and tunability of size and shape. The catalytic activity of these unsupported systems depend largely on the nature and binding ability of the ligands and availability of preferential crystallographic planes.<sup>[14]</sup> Therefore there are open issues in this area regarding the intrinsic catalytic activity of size and shape controlled Au nanoparticle systems and the effect of stabilizing agents in influencing the activities inherent to Au nanoparticles besides avoiding particle aggregation.

As has already been discussed in the previous chapters, the biogenic synthetic routes for the generation of Au nanoparticles have gained interest because of the demand for environmentally acceptable synthetic conditions and eco-friendly reducing and capping agents (green chemistry). Since the enzymes provide a precise and

confined microenvironment, they can function as effective nanoreactors for the growth of nanoparticles.<sup>[25-34]</sup> The presence of a large number of amino acids with known reducing capability has propelled research activities in using enzymes as promising reducing and capping agent where the inorganic phase morphology is highly controlled by their specific physicochemical interactions with the biomolecular template. Also the coupling of the reducing ability of the enzymes with their specific catalytic activities has led to the development of higher order nanostructures such as alloys and core-shell composite materials.<sup>[26,27]</sup> Further, the attachment of an enzyme on the nanoparticle surface brings about changes in its three dimensional arrangement which might have a significant impact on the natural activity of the enzyme.<sup>[25-27,35]</sup> Therefore studies regarding the fate of the enzymes after their participation as reducing as well as stabilizing agent during the synthesis of nanostructures are highly desirable. Although there are several recent reports on enzyme stimulated synthesis of Au nanoparticles leading to the formation of Au nanoparticle-enzyme composites under mild conditions<sup>[32,33]</sup> there has been no report regarding the catalytic performance of the Au nanostructures stabilized by enzymes.

In this chapter, the catalytic activity of different size and shaped Au nanoparticles, synthesized using single biomolecule, pepsin under pH controlled conditions, towards reduction of nitroarenes and resazurin have been demonstrated. Pepsin, an aspartic protease consists of 327 amino acid residues with a molecular weight of 34,644 Da. Pepsin is a unique enzyme in the sense that it contains 30 aspartic acid and 13 glutamic acid residues, together with a rich content of aromatic amino acid residues.<sup>[36]</sup> The simple tuning of the pH of the reaction medium led to a distinct change in the size and morphology of the nanostructures. The catalytic ability of the various size and shaped nanostructures on the reaction rate were studied by carrying out the reduction of *p*-nitrophenol to *p*-aminophenol and resazurin to resorufin with NaBH<sub>4</sub> and NH<sub>2</sub>OH.HCl acting as the reducing agents respectively. The results indicated that in addition to the size and shape of the nanoparticles, the thickness of the stabilizing agent on the nanoparticle surface played a vital role in deciding the catalytic efficiency of the nanoparticles.

## 4.2 Results and Discussion

### 4.2.1 Synthesis and characterization of Au nanostructures at pH 5.4 and 4.0

The synthesis of different size and shaped Au nanostructures was achieved at different pH of the reaction medium by a slight modification of a synthetic method as reported by Kawasaki et al.<sup>[30]</sup> A simple room temperature stirring of the pepsin solution (1.0 mg/mL) with  $\text{HAuCl}_4$  ( $1.2 \times 10^{-3}$  M) in PBS buffer (100 mM) at pH value of 5.4 and 4.0 resulted in a change in color of the solution from colorless to dark pink and blue respectively (figure 4.1a) indicating the formation of Au nanostructures. The Au nanoparticles synthesized at pH 5.4 exhibited their characteristic surface plasmon resonance band at 529 nm, whereas the Au nanoparticles synthesized at pH 4.0 showed a shoulder at 700 nm in addition to their plasmon resonance band at 550 nm (figure 4.1b), indicating the formation of non-spherical particles. The crystalline nature of the Au nanostructures was ascertained using powder X-ray diffraction. The powder XRD spectrum (figure 4.1c) of the Au nanoparticles synthesized at both pH values of 5.4 and 4.0 exhibited the characteristic Bragg's peaks at  $2\theta$  values of  $38.2^\circ$ ,  $44.5^\circ$ ,  $64.6^\circ$  and  $77.7^\circ$  respectively corresponding to the (111), (200), (220) and (311) planes of the face centered cubic structure of Au.

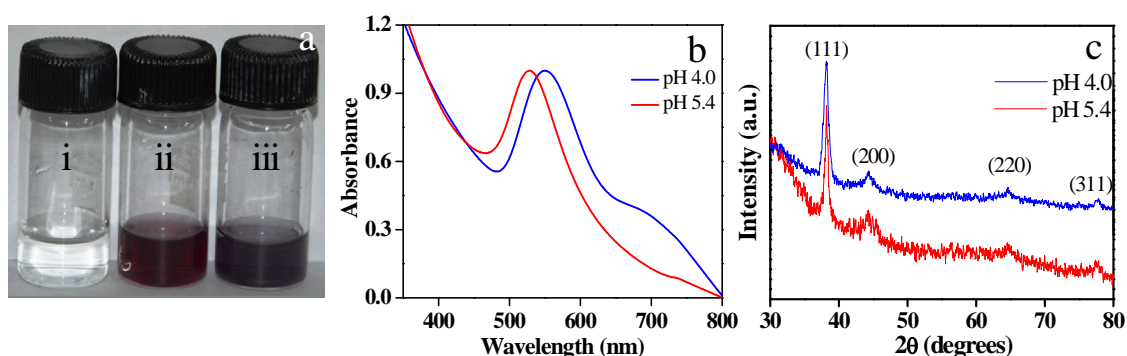


**Figure 4.1.** (a) Digital images of (i) native pepsin solution, (ii) Au nanoparticles synthesized using pepsin at pH 5.4, (iii) Au nanostructures synthesized at pH 4.0 using pepsin as a reducing as well as a stabilizing agent. (b) UV-visible spectrum of Au nanostructures synthesized at pH 5.4 and 4.0. (c) Powder XRD spectrum of Au nanostructures, showing the characteristic Bragg's reflection synthesized at pH 5.4 and 4.0 using pepsin as a stabilizing and reducing agent.

The size and morphology of the synthesized Au nanostructures was studied using transmission electron microscope. The TEM images of the nanoparticles synthesized at pH 5.4 revealed the formation of spherical Au nanoparticles (figure 4.2a). The high resolution transmission electron microscopy image showed a lattice spacing of 0.23 nm corresponding to the (111) plane of Au (figure 4.2b). The average particle size as calculated from the size distribution histogram for the nanoparticles synthesized at pH 5.4 was  $7.9 \pm 2.0$  nm (figure 4.2c). On the other hand, TEM images of the Au nanoparticles synthesized at pH 4.0 showed a mixture of anisotropic structures such as plates, triangles, rods and hexagons (figure 4.2d and e). The size of the particles varied between 30-200 nm. The HRTEM image of Au nanostructures synthesized at pH value of 4.0 showed lattice planes with a separation of 0.24 nm which again corresponded to the (111) facet of Au (figure 4.2f).

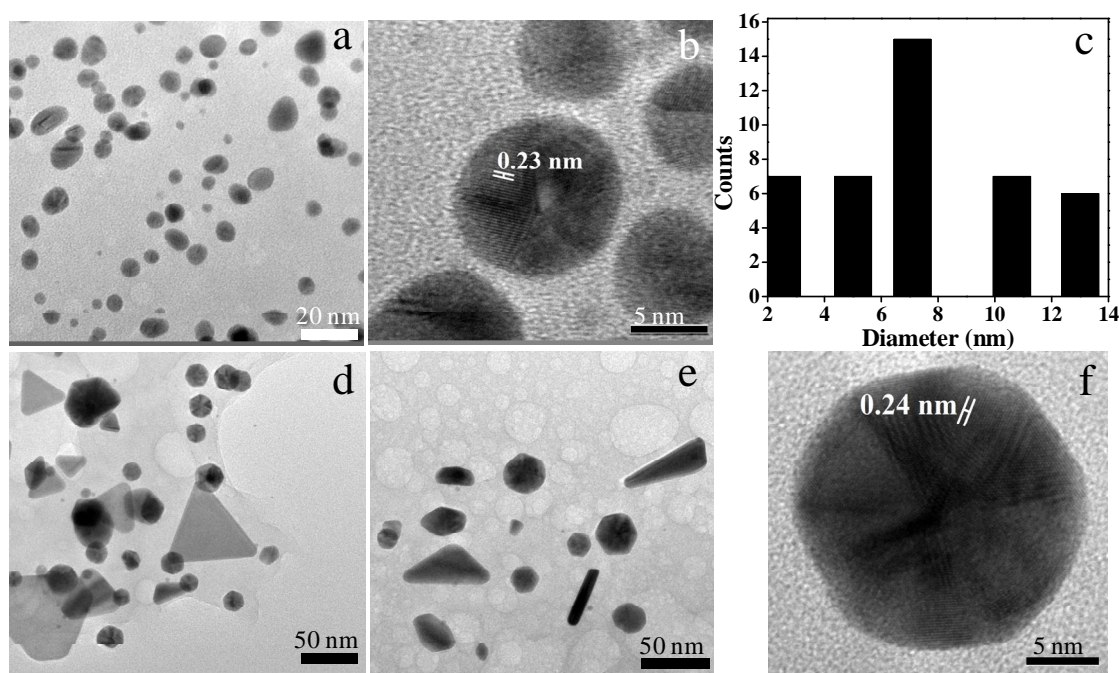
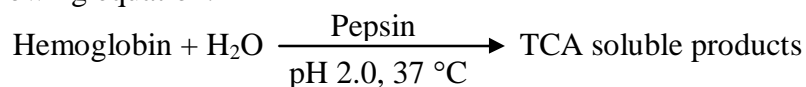


**Figure 4.2.** (a) TEM image, (b) HRTEM image and (c) particle size distribution histogram of Au nanoparticles synthesized at pH 5.4 using pepsin. (d) and (e) TEM images of anisotropic Au nanostructures synthesized at pH 4.0 using pepsin as a reducing as well as stabilizing agent and (f) HRTEM image of anisotropic Au nanostructures synthesized at pH 4.0 using pepsin as a reducing as well as stabilizing agent, showing a lattice separation of 0.24 nm corresponding to the (111) plane of face centered cubic Au.

### 4.2.2 Activity of pepsin after synthesis of Au nanostructures

Enzymes feature rich chemistries in their functional groups such as amine, thiol, carboxyl and hydroxyl due to the presence of variety of amino acids in it. Such functional groups could serve as efficient binding sites for metal ions and could facilitate the multidirectional growth of inorganic nanostructures in a controlled manner.<sup>[37]</sup> Therefore it is reasonable to speculate that the involvement of enzymes via such functional groups for the reduction of metal salts to their corresponding nanoparticles would lead to modulation of the natural activity of enzyme. Further, it has also been well studied that simple conjugation of enzymes on solid surfaces such as those of nanoparticles leads to amendment in their activity.<sup>[26,35]</sup> In the present case, pepsin participated as a reducing as well as surface stabilizing agent for the nanoparticles under acidic conditions. Therefore it was imperative for us to study the activity of pepsin after the Au nanoparticle synthesis. The activity was studied following a standard assay based on the action of pepsin on hemoglobin.<sup>[38]</sup> At acidic pH, pepsin breaks hemoglobin into trichloroacetic acid soluble products according to the following equation:



The formation of the products can easily be monitored by observing the increase in the absorbance value at 280 nm. It was found that in case of the native enzyme, the absorbance reading at 280 nm was 1.23 as compared to 0.21 for the blank, indicating extensive digestion of hemoglobin by pepsin, whereas with the Au NP-pepsin composite, the absorbance reading was only 0.29, signifying a substantial loss in the enzyme activity (figure 4.3). In order to confirm that the loss in the activity of pepsin is only due to the participation of the enzyme in the reduction of  $\text{Au}^{3+}$  to  $\text{Au}^0$  and not merely due to the presence or adsorption on Au nanoparticles, pepsin was incubated with citrate capped Au nanoparticles for 24 hours and then the activity assay was performed. The digestion of hemoglobin with citrate capped Au NP-pepsin composite led to an absorbance reading of 1.13 at 280 nm, suggesting that mere presence of Au nanoparticles added from outside did not affect the activity of the enzyme, and the loss in the activity of the enzyme was due to its participation in the reduction of  $\text{HAuCl}_4$  to

form Au nanoparticles. Also the activity of the denatured enzyme (denatured by dissolving pepsin in PBS buffer of pH 7.0) was tested and it was found that in case of the denatured enzyme the absorbance at 280 nm was same (0.21) as that of the blank. This indicated that though the enzyme activity was inhibited to a large extent, the enzyme was not completely denatured after the synthesis of Au nanoparticles by the enzyme.

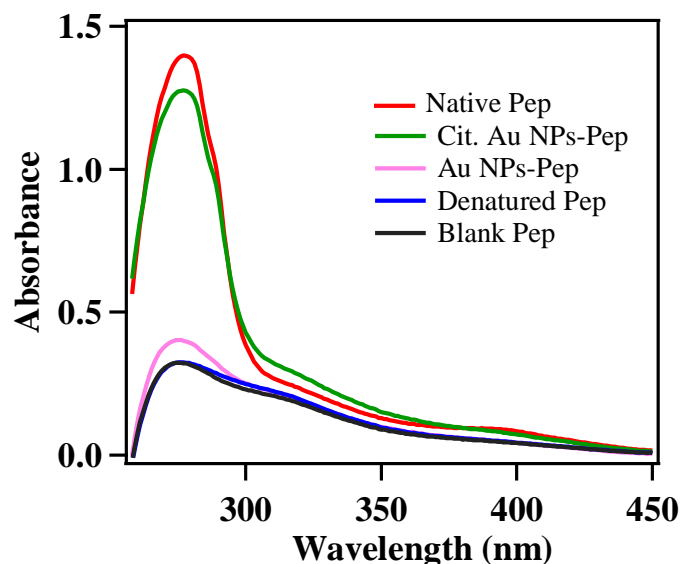


**Figure 4.3.** UV-visible spectrum showing the action of native pepsin, citrate capped Au nanoparticles-pepsin composite, pepsin reduced Au NP-pepsin composite and denatured pepsin on hemoglobin.

### 4.2.3 Conformational changes in the structure of pepsin after the synthesis of Au nanostructures

The decrease in the activity of the enzyme could be attributed to the conformational changes that the enzyme had undergone during the synthesis of Au nanoparticles. The conformational change in pepsin after the synthesis of Au nanoparticles was established by means of circular dichroism (CD), fluorescence spectroscopy and FTIR studies. CD studies of native pepsin and Au NP-pepsin composite were performed in both the far UV and near UV region to get an insight into the conformational changes in the secondary and tertiary structure of the enzyme after the synthesis of Au nanoparticles. As shown in figure 4.4a, the far UV CD spectrum of native pepsin showed a single minimum at 213 nm, which is typical for proteins highly

rich in  $\beta$  sheet components. However, after the synthesis of Au nanoparticles by pepsin, this minimum was shifted to 210 nm along with a decrease in intensity, which was qualitatively consistent with a loss of the  $\beta$  sheet structure in favor of random coil structure.<sup>[39]</sup> The results indicate changes in the secondary structure of the enzyme after the synthesis of Au nanoparticles. In the near UV CD spectrum (figure 4.4b) of the native pepsin, CD bands at 291, 281 and 255-274 nm were observed due to the aromatic amino acid residues.<sup>[40]</sup> However after the synthesis of Au nanoparticles, in addition to these bands, several other bands were observed, which suggested perturbation in the tertiary structure of the enzyme as well.

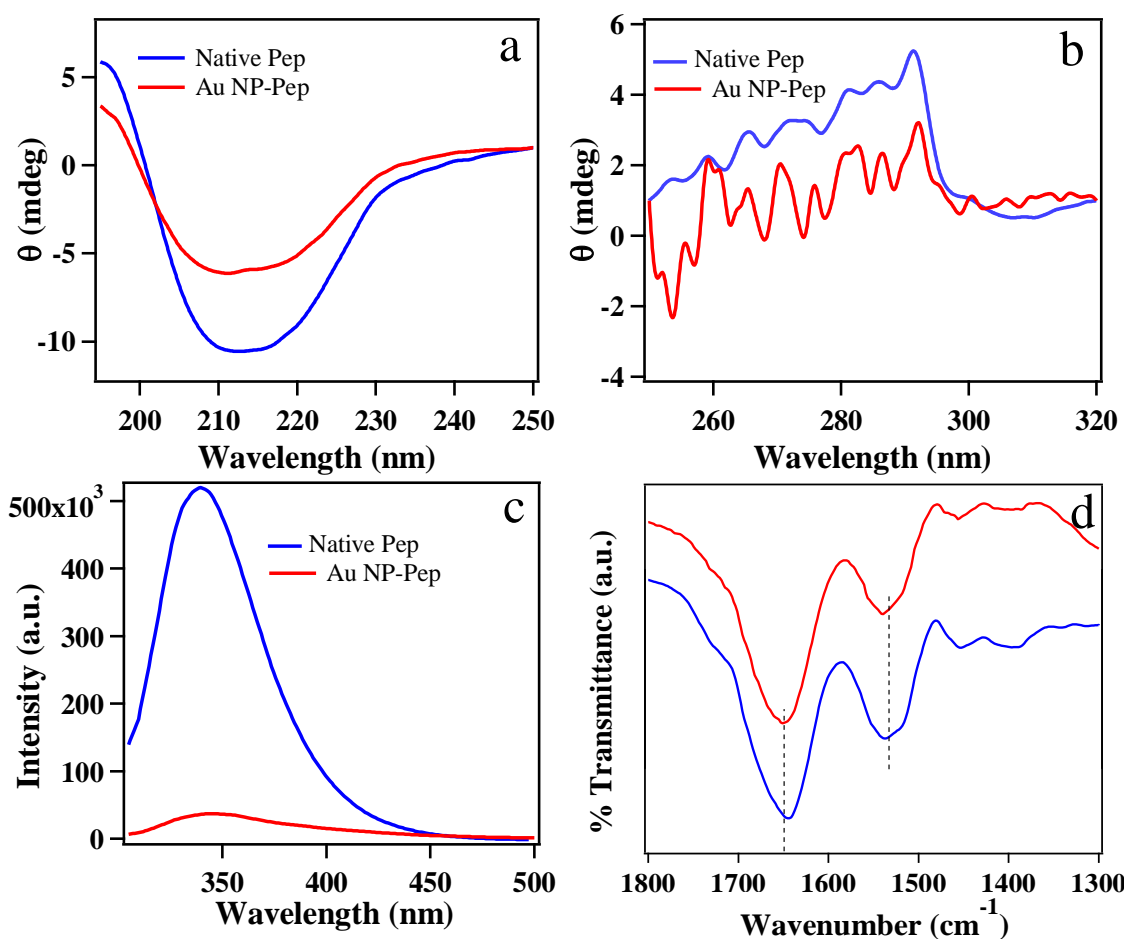


**Figure 4.4.** Circular dichroism spectrum of native pepsin and Au NP-pepsin composite in (a) near UV region and (b) far UV region. (c) Emission spectrum of native pepsin and Au NP-pepsin composite ( $\lambda_{ex}=295$  nm) and (d) FTIR spectrum of native pepsin (blue) and Au NP-pepsin composite (red). Dashed lines in the figure indicate the shift in the amide I and amide II bands in native pepsin and the Au NP-pepsin composite.

The emission of tryptophan residues in pepsin was further used to study the conformational changes in it. The fluorescence emission spectrum of native pepsin upon excitation at 295 nm showed a maximum at 340 nm (figure 4.4c). However, when the Au NP-pepsin composite was excited at the same wavelength, the emission maxima was red shifted by 5 nm, with a drastic decrease in the fluorescence intensity, clearly suggesting a change in the conformation of the enzyme, whereby the tryptophan residues which were in the hydrophobic pockets of pepsin were exposed to hydrophilic environment<sup>[41]</sup> after the synthesis of Au nanoparticles.

FTIR spectroscopy was also employed to study the changes in the secondary structure of pepsin after the synthesis of Au nanoparticles. Small shifts in the position of the amide I and amide II bands indicate conformational changes in the enzyme structure. It was observed that the characteristic amide I and amide II bands in native pepsin shifted from 1645 cm<sup>-1</sup> and 1537 cm<sup>-1</sup> to 1649 cm<sup>-1</sup> and 1540 cm<sup>-1</sup> respectively in Au nanoparticle-pepsin composite (Figure 4.4d). Thus from the fluorescence, circular dichroism and FTIR studies it was quite evident that there were substantial conformational changes in the secondary and tertiary structure of the enzyme after the synthesis of Au nanoparticles that led to a loss in its activity.

#### **4.2.4 Synthesis and characterization of red emitting Au nanoclusters**

Since the natural activity of pepsin was lost due to conformational changes in the structure of pepsin after the synthesis of Au nanostructures even at acidic pH, so the aim of development of nanocomposites with high functionalities that could couple the reduction ability of pepsin with its natural activity could not be accomplished. Therefore, in the next step the catalytic properties of size and shape selective Au nanoparticles synthesized using pepsin towards reduction reactions as model reactions were evaluated. As all nanoparticle surfaces were coated with pepsin, therefore the catalytic activity of the colloidal Au nanoparticles could be fairly evaluated with respect to the role of ligands and the influence of their concentration on the intrinsic activity of the Au nanoparticles. Since, even at acidic pH, the enzyme was denatured when used for the synthesis of Au nanoparticles, so for a better comparison of the catalytic activity, ultrasmall fluorescent Au nanoclusters using pepsin as the reducing and stabilizing

agent at pH 12.0 were synthesized. Metal nanoclusters, comprising of a few hundred of atoms of the metal or less represent an intermediate state of matter between isolated molecules and large nanoparticles, typically with core diameters greater than 2 nm. Aromatic amino acids such as tyrosine or tryptophan present in an enzyme can efficiently reduce Au (III) ions above their pKa at alkaline pH<sup>[29,30]</sup> to form the fluorescent metal nanoclusters. Since pepsin has a rich content of aromatic amino acid residues, it was used for the synthesis of Au nanoclusters. The simple room temperature stirring of pepsin solution (7.5 mg/mL) with HAuCl<sub>4</sub> (1.2 x 10<sup>-3</sup> M) at pH of 12.0 resulted in a change of color from nearly colorless to brown indicating the formation of Au nanoclusters.<sup>[31]</sup> The Au nanoclusters were highly fluorescent and exhibited their emission maximum at 694 nm upon excitation at 370 nm (figure 4.5a). The TEM images showed small spherical particles with an average dimension of 2 nm (figure 4.5b). The red emission of Au particles (inset Figure 4.5a) was indicative of the formation of Au<sub>25</sub> nanocluster.<sup>[29-31,37]</sup> Hence using pepsin as a reducing agent under various pH conditions, size and shape selective Au nanoparticles could be developed that were coated with same stabilizing agent.

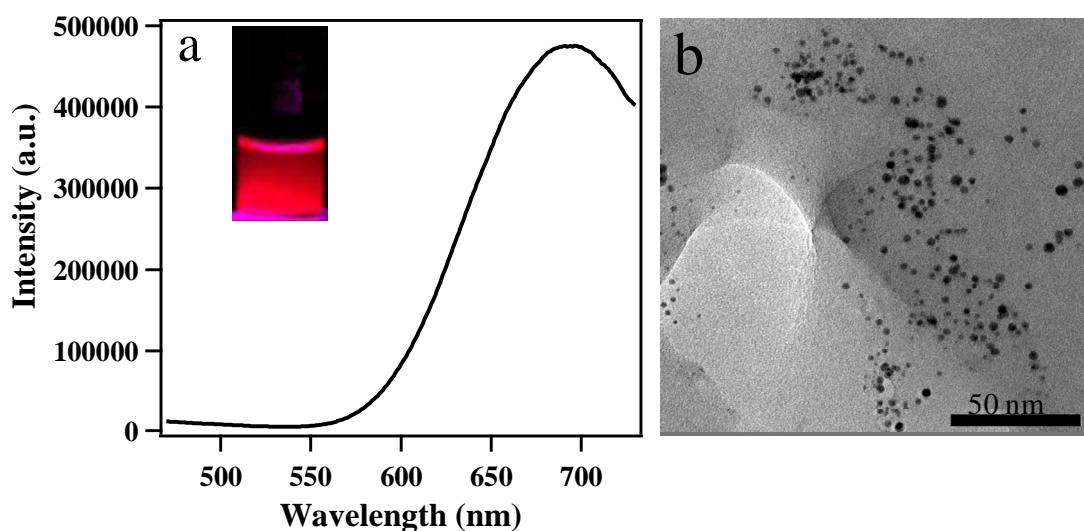


**Figure 4.5.** (a) Emission spectrum of Au nanoclusters synthesized at pH 12.0 by pepsin ( $\lambda_{ex}=370$  nm). Inset: Digital image of Au nanocluster solution under UV lamp and (b) TEM image of the Au nanoclusters synthesized using pepsin.

### 4.2.5 Effect of size of Au nanostructures on the reduction of *p*-nitrophenol

It is well known that size of the nanoparticles play a critical role in deciding the catalytic efficiency of the nanoparticles as a heterogeneous catalyst. As catalysis by nanoparticles involves surface catalyzed reactions, hence nanoparticles with larger surface area to volume ratio are expected to perform better as a catalyst. Based on this principle, nanoparticles with smaller sizes have demonstrated excellent catalysis in various reactions.<sup>[42,43]</sup> For example, the catalytic reduction of *p*-nitroaniline by NaBH<sub>4</sub> with Au nanoparticles of sizes  $6.7 \pm 0.9$  nm was much faster than the reaction catalyzed by Au nanoparticles of size  $13.8 \pm 0.8$  nm, which in turn was faster for the same reaction catalyzed by Au nanoparticles having an average size of  $22.0 \pm 1.2$  nm.<sup>[44]</sup> A similar trend was also observed for the chemoselective hydrogenation of nitroaromatics by oxide supported Au nanoparticles, where Au nanoparticles of size 2.5 nm supported on Al<sub>2</sub>O<sub>3</sub> gave better selectivity for the chemoselective reduction of 4-nitrostyrene to 4-aminostyrene compared to the Au nanoparticles of size 6 nm with the same support material.<sup>[45]</sup> Therefore, to realize the correlation of sizes with the catalytic activity, the reduction of *p*-nitrophenol to *p*-aminophenol by NaBH<sub>4</sub> was performed using various Au nanostructures synthesized by pepsin as catalysts. The reaction is a surface catalyzed reaction and takes place on the surface of the nanoparticles, following a Langmuir-Hinshelwood mechanism.<sup>[9,46-50]</sup> First, the borohydride ions adsorb on the surface of Au nanoparticles and transfer a surface hydrogen species to the surface of the nanoparticles. Concomitantly, *p*-nitrophenol molecules are adsorbed on the surface of the nanoparticles. Both these steps are reversible and can be modeled in terms of Langmuir isotherm. Moreover, the adsorption/desorption equilibriums and diffusion of reactants to the nanoparticles are considered to be fast. The reduction of *p*-nitrophenol, which is the rate-determining step, occurs due to the reaction of adsorbed *p*-nitrophenol with the nanoparticles surface-bound hydrogen atoms. Finally, the product *p*-aminophenol desorbs, leaving free metal surface such that catalytic cycle can begin again.

Since, the reduction of *p*-nitrophenol by NaBH<sub>4</sub> catalyzed by Au nanoparticles is a surface catalyzed reaction, so the influence of the size on the catalytic performance of

Au nanostructures would clearly be reflected by the changes in the reaction rate. With the addition of  $\text{NaBH}_4$  to a solution of *p*-nitrophenol in water, the color of the solution changed from light yellow to intense yellow due to the formation of *p*-nitrophenolate ions. In a controlled experiment in the absence of Au nanostructures, it was observed that the reduction of *p*-nitrophenolate ions did not occur even after two days (figure 4.6b). However, in presence of Au nanostructures as catalysts, the UV-visible spectrum showed an immediate decrease in the intensity of the peak at 400 nm along with the formation of a new peak at 300 nm, indicating the gradual conversion of *p*-nitrophenol to *p*-aminophenol. It was observed that the ultrasmall fluorescent Au nanoclusters prepared at pH 12.0 was the most effective catalyst as the reduction reaction was completed in just 4 minutes (figure 4.6c). On the other hand the reduction reaction reached completion in around 9 minutes in case of larger Au nanoparticles synthesized at pH 5.4 as catalyst (spherical nanoparticles with an average diameter of  $\sim 8$  nm) (figure 4.6d). From these results, it could be concluded that Au nanoclusters with smaller diameter could function as a better catalyst for the reduction of nitrophenols compared to larger spherical nanoparticles that could be correlated to larger surface area to volume ratio.

#### **4.2.6 Effect of shape of Au nanostructures on the reduction of *p*-nitrophenol**

In addition to the size, the shape of the nanoparticles is another important parameter in controlling the catalytic activity of the nanoparticles.<sup>[51]</sup> In general, due to the large surface area to volume ratio, spherical nanoparticles offer enhanced catalytic activities as compared to shape selective nanostructures such as rods, prisms, triangles etc.<sup>[52]</sup> However in case of non-spherical nanoparticles, the growth takes place along a particular crystallographic plane, hence different selectivities and reactivities on distinct facets of the nanoparticles are expected.<sup>[53]</sup> For instance, for the oxidation of styrene Ag nanocubes with {100} facets were found to be 14 times more active than Ag nanoplates and 4 times more active than the spherical nanoparticles.<sup>[54]</sup> Similarly, polygonal gold nanoparticles with {111} facets were found to be much better catalysts than their spherical counterparts for the borohydride reduction of nitrophenols and aerobic

oxidation of different D-hexoses.<sup>[55]</sup> In the present case, since pepsin could be used to generate spherical as well as shape selective anisotropic nanoparticles just by the simple tuning of reaction pH, so the effect of shape of the nanoparticles on their catalytic activity could be fairly evaluated (since stabilizing agent in all the cases was pepsin). It was observed that the reduction of *p*-nitrophenol to *p*-aminophenol was slowest with the Au nanostructures synthesized at pH 4.0 (mixture of anisotropic structures) as evidenced by the longer duration of time (19 minutes) required for the completion of the reaction (figure 4.6e).

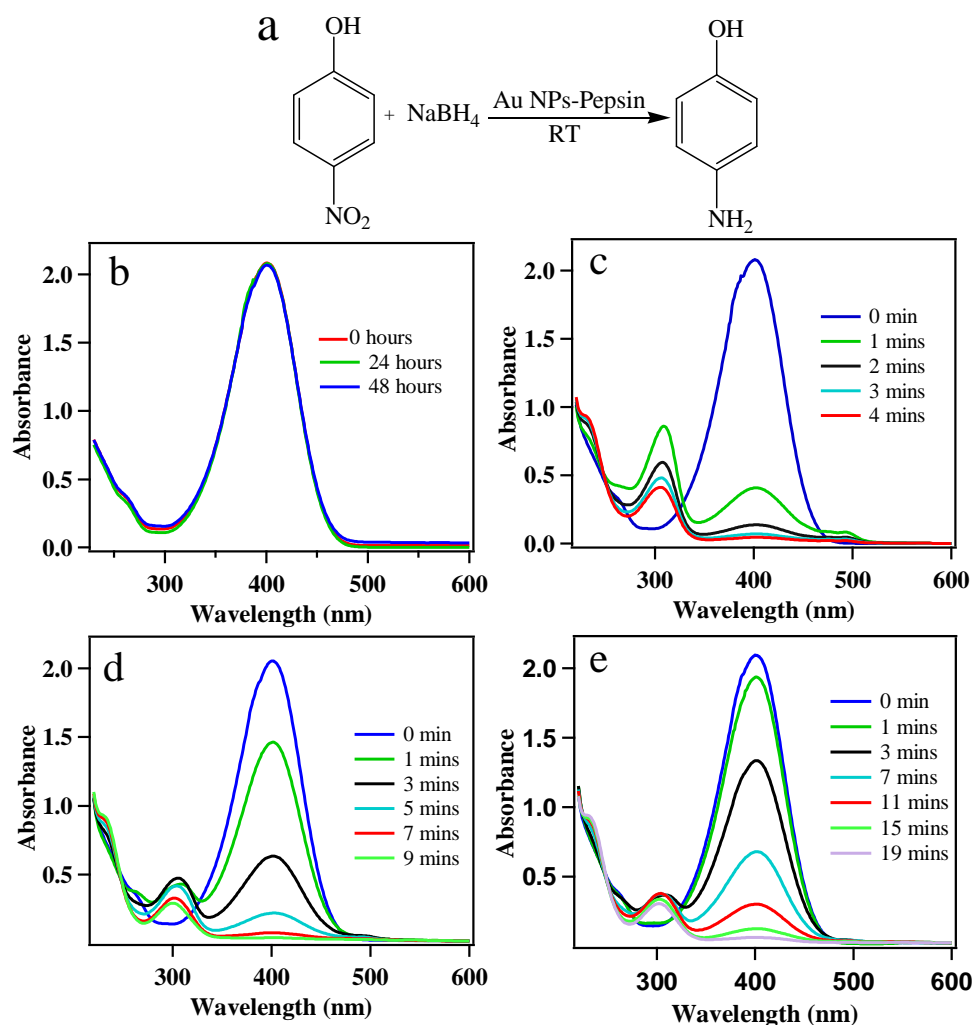


**Figure 4.6.** (a) Scheme for the reduction of *p*-nitrophenol to *p*-aminophenol by NaBH<sub>4</sub> catalyzed by various Au nanostructures synthesized using pepsin. (b) Controlled experiment for the reduction of *p*-nitrophenol to *p*-aminophenol by NaBH<sub>4</sub> in absence of any Au nanostructure. (c), (d) and (e) Time dependent UV-visible spectrum for the reduction of *p*-nitrophenol to *p*-aminophenol by NaBH<sub>4</sub> catalyzed by Au nanostructures synthesized at pH 12.0, pH 5.4 and pH 4.0 respectively.

The difference in activity of the catalyst can be ascribed to their shapes. In case of spherical nanoparticles the growth of the particles is along all the planes, whereas the anisotropic particles grow along a particular plane with higher concentration of the metal along that particular plane. If the catalytic reaction takes place at a plane other than the plane of growth, the anisotropic particles would show lower catalytic activity. The present trend in the catalytic activities for the reduction of *p*-nitrophenol was due to a combined effect of size and shape of the nanostructures. The Au nanoclusters synthesized at pH 12 were spherical and quite small (2 nm), hence provided a larger surface area, accounting for the highest activity of the catalyst. The Au nanoparticles synthesized at pH 5.4 were spherical but with somewhat larger diameter (~8 nm) resulting in a lower activity than the Au nanoclusters. On the other hand, the particles synthesized at pH 4.0 consisted of larger anisotropic particles such as plates, rods, triangles and hexagons, and the slowest catalytic activity of these nanostructures for the conversion of *p*-nitrophenol to *p*-aminophenol was observed.

#### **4.2.7 Rate constants for the reduction of *p*-nitrophenol by different Au nanostructures and role of pepsin in the reduction reaction**

The reduction of *p*-nitrophenol catalyzed by various pepsin reduced Au nanostructures was carried out using a large excess of NaBH<sub>4</sub> such that its concentration remained constant throughout the reaction. So the rate of the reaction could be evaluated with respect to the rate of consumption of *p*-nitrophenol. A linear relationship between the plot of ln (absorbance) of *p*-nitrophenol at 400 nm and time in all the three cases was observed which was indicative of a pseudo first order kinetics (figure 4.7a). The apparent rate constant, *k*, as calculated from the plot of ln *A* versus time was found to be  $15.3 \times 10^{-3} \text{ s}^{-1}$  for the fluorescent Au nanoclusters, while for the Au nanoparticles synthesized at pH 5.4 and 4.0, the apparent rate constants were calculated to be  $7.53 \times 10^{-3} \text{ s}^{-1}$  and  $3.13 \times 10^{-3} \text{ s}^{-1}$  respectively. It is worth mentioning that any isobestic point was not observed during the time dependent reaction studies for the reduction of *p*-nitrophenol which might be due to the scattering caused by H<sub>2</sub> generated during the reduction by NaBH<sub>4</sub>, as have been previously reported.<sup>[56]</sup> It is important to mention here that pepsin alone could not catalyze the reduction reaction (figure 4.7b). Further,

the excess or non-conjugated pepsin was removed from the solution in a cycle of centrifugation and redispersion in appropriate buffer. It was observed that there were no changes in the rate of the reduction reaction, confirming that the excess pepsin in the solution did not play any role in the activation of the reaction and Au NPs alone acted as the catalyst.

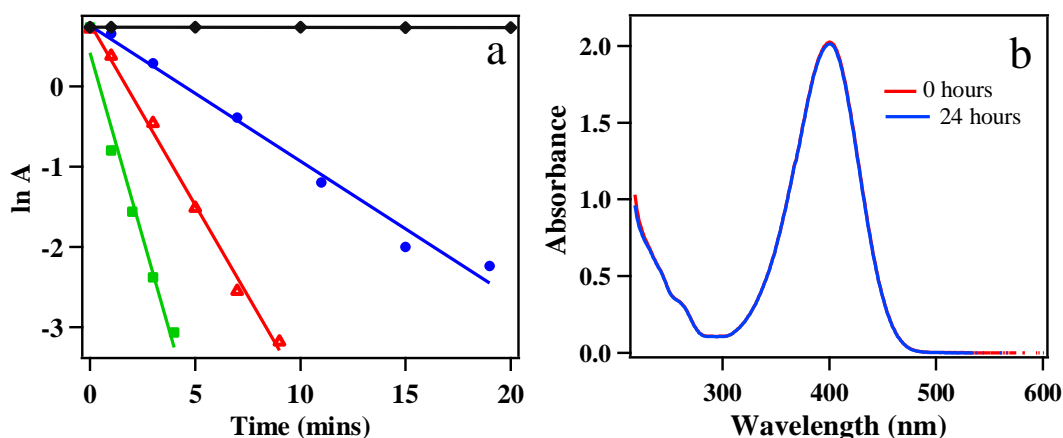
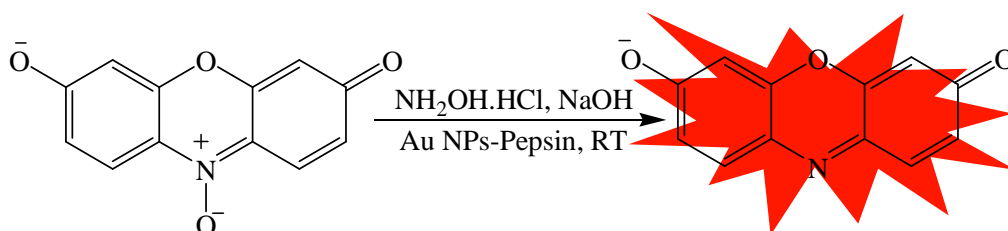


**Figure 4.7.** (a) plot of  $\ln A$  vs  $T$  for the reduction of *p*-nitrophenol to *p*-aminophenol by  $\text{NaBH}_4$  in absence of Au nanoparticles (black) and in presence of Au nanostructures synthesized at pH 4.0 (blue), pH 5.4 (red) and pH 12.0 (green). (b) Controlled experiment for the reduction of *p*-nitrophenol to *p*-aminophenol by  $\text{NaBH}_4$  in presence of pepsin alone.

#### 4.2.8 Catalytic activity of different sized and shaped Au nanostructures towards reduction of resazurin to resorufin

To further extend the scope of catalysis and to confirm the effect of size and shape of the pepsin reduced Au nanostructures on the catalytic activity, the reduction of resazurin to resorufin by  $\text{NH}_2\text{OH}\cdot\text{HCl}$  was performed.



**Scheme 4.1.** Scheme for the reduction of weakly fluorescent resazurin to the highly fluorescent resorufin by  $\text{NH}_2\text{OH}\cdot\text{HCl}$  catalyzed by various Au nanostructures synthesized using pepsin.

Resazurin which is blue in color and absorbs at 599 nm is only weakly fluorescent, whereas its reduced form resorufin is pink in color (figure 4.8a), absorbs at 570 nm and is highly fluorescent.<sup>[57,58]</sup> So the progress of the reaction can be followed easily by UV-visible and fluorescence studies. Control experiment revealed that in the absence of Au nanoparticles, the reaction did not occur even after 24 hours (figure 4.8b). However, the addition of pepsin reduced Au nanoparticles to the reaction medium led to the immediate onset of the reaction as reflected by the decrease in the intensity of the peak at 599 nm due to resazurin in the absorption spectrum. For all the three Au nanoparticle catalytic systems, the UV-visible absorption spectrum (figure 4.8c, d and e) showed a time-dependent decrease in the intensity of the peak at 599 nm (resazurin) and an increase in the intensity of the peak at 570 nm (resorufin). An isosbestic point at 580 nm was observed in the absorption spectrum, which quite clearly indicated the quantitative conversion of resazurin to resorufin. For the catalytic reduction of resazurin to resorufin, a similar trend in the catalytic activity of the various pepsin reduced nanostructures as for the reduction of *p*-nitrophenol to *p*-aminophenol was expected. However, as evident from the UV-visible spectrum, the fluorescent Au nanoclusters (2.0 nm) in this case were found to be the least active, whereas the Au nanoparticles synthesized at pH 5.4 (~ 8.0 nm) catalyzed the reaction most effectively followed by the Au nanostructures of pH 4.0.

Similar to the reduction of *p*-nitrophenol to *p*-aminophenol, the reduction of resazurin was also carried out using a large excess of the reducing agent (NH<sub>2</sub>OH.HCl), so it was quite reasonable to consider its concentration constant throughout the reaction.<sup>[57]</sup> Hence the kinetics of the reduction reaction was evaluated with respect to the rate of resazurin consumption. A plot of ln (absorbance) at 599 nm against time resulted in a straight line, indicative of a pseudo first order kinetics with respect to the rate of resazurin consumption (figure 4.8f). The apparent rate constant as calculated from the plot of ln A vs T were  $4.6 \times 10^{-5} \text{ s}^{-1}$ ,  $3.18 \times 10^{-4} \text{ s}^{-1}$  and  $1.13 \times 10^{-4} \text{ s}^{-1}$  for the reactions catalyzed using Au nanoparticles of pH 12.0 (2 nm), pH 5.4 (~8 nm) and pH 4.0 (anisotropic) respectively.

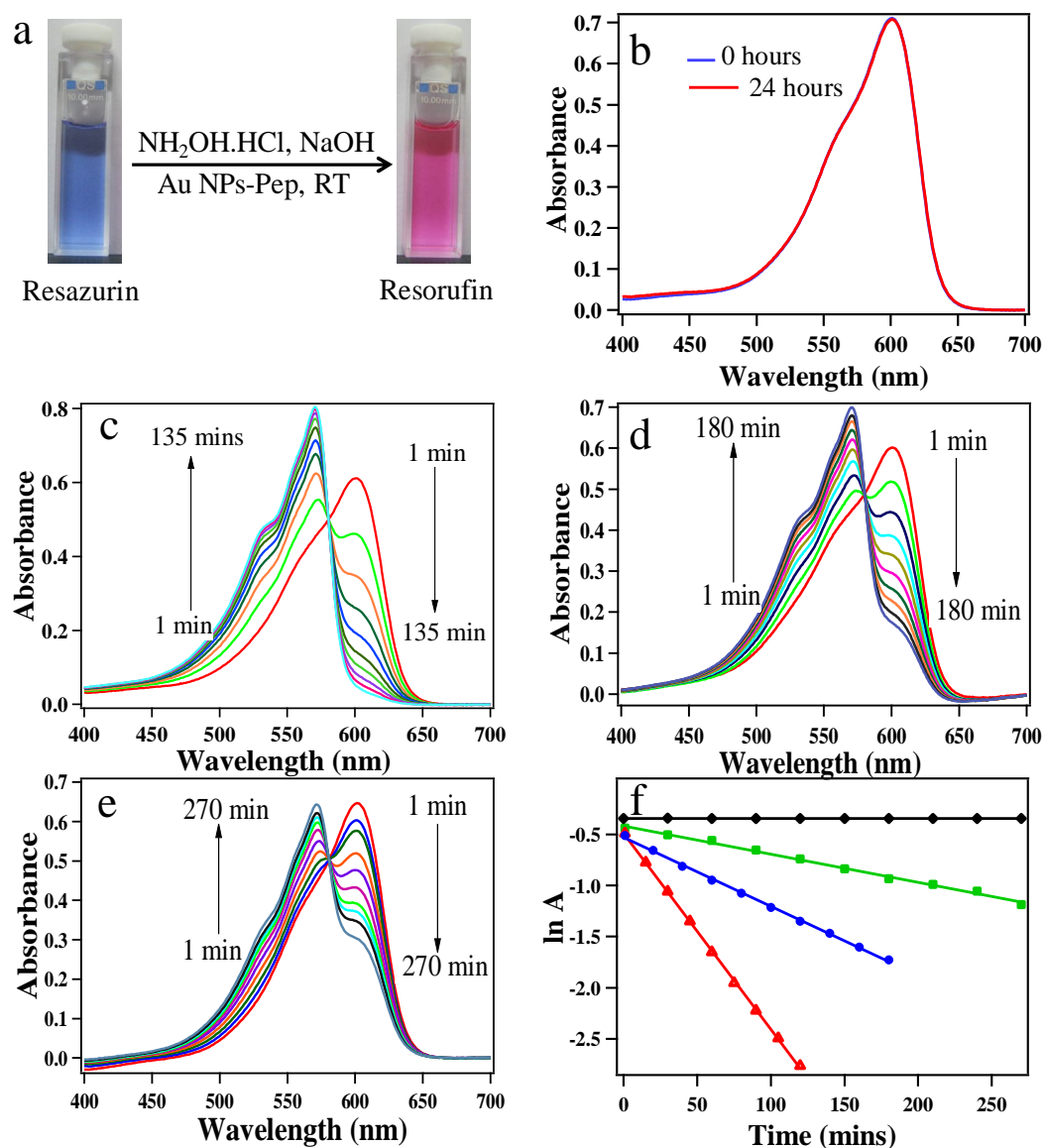


**Figure 4.8.** (a) Digital image of resazurin and resorufin solutions. (b) UV-visible spectrum for the reduction of resazurin to resorufin by  $\text{NH}_2\text{OH}\cdot\text{HCl}$  in the absence of pepsin reduced Au nanostructures. (c), (d) and (e) Time dependent UV-visible spectrum for the reduction of resazurin to resorufin by  $\text{NH}_2\text{OH}\cdot\text{HCl}$  catalyzed by Au nanostructures synthesized at pH 5.4, pH 4.0 and pH 12.0 respectively, and (f) plot of  $\ln A$  vs  $T$  for the reduction of resazurin to resorufin by  $\text{NH}_2\text{OH}\cdot\text{HCl}$  in absence of Au nanostructures (black) and in presence of Au nanostructures synthesized at pH 12.0 (green), pH 4.0 (blue) and pH 5.4 (red).

Since resazurin is only weakly fluorescent, whereas the reduced product resorufin is highly fluorescent, so the progress of the reduction of resazurin was also monitored using fluorescence spectroscopy (figure 4.9). As can be seen from the figure,

the intensity of the emission peak at 582 nm, signifying the formation of resorufin, increased with time and the reaction was found to be quite fast with the Au nanoparticles synthesized at pH 5.4, followed by the Au nanoparticles of pH 4.0. The reaction was slowest with the ultrasmall red emitting Au nanoclusters synthesized at pH 12.0, indicating that the smallest nanostructures were the least effective of the three catalysts for this reduction reaction, which was in accordance with the UV-visible results.

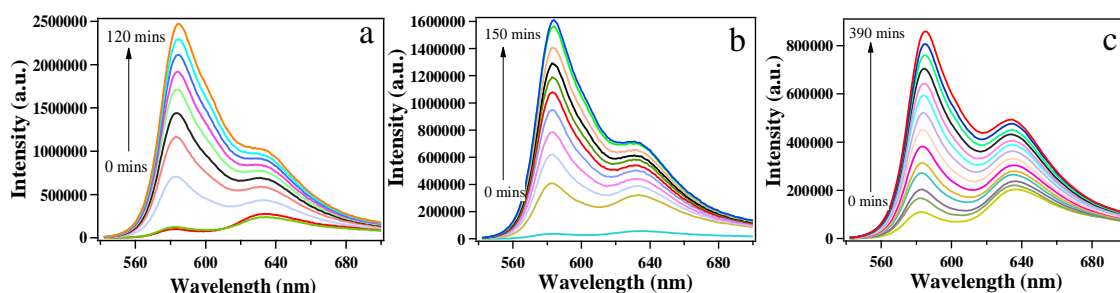


**Figure 4.9.** Time dependent fluorescence spectrum for the reduction of resazurin to resorufin by  $\text{NH}_2\text{OH}\cdot\text{HCl}$  catalyzed by pepsin reduced Au nanostructures of (a) pH 5.4, (b) pH 4.0 and (c) ultra small Au NCs synthesized at pH 12.0.

#### 4.2.9 Effect of surface stabilizing agent (pepsin) on the catalytic activity of Au nanostructures

From the kinetics of the two reduction reactions involving Au nanostructures as catalysts, it was evident that surface stabilizing layer of pepsin also played a decisive role in controlling the catalytic behavior along with size and shape. Although it was expected that smaller Au nanoclusters will demonstrate the most efficient catalysis in both the reduction reactions due to their higher surface area to volume ratio, in case of reduction of resazurin it showed the opposite trend.

It is worth mentioning that a much higher concentration of pepsin was used during the synthesis of ultrasmall fluorescent Au nanoclusters. Probably, pepsin formed a much denser coating on the Au nanoclusters compared to the other bigger nanostructures (lower concentration of pepsin was used for those synthesized at pH 4.0 and 5.4). Therefore it is believed that a smaller molecule such as *p*-nitrophenol could approach the Au surface efficiently during their reduction, whereas relatively larger resazurin molecules could not penetrate the dense pepsin monolayers efficiently in case

of small Au nanoclusters, thus showing a variable trend in the catalytic activity. In order to establish the role of surface stabilizing layers (pepsin) on the catalytic activity of the nanoparticles, spherical Au nanoparticles at pH 5.4 were synthesized by varying the concentration of pepsin (2mg/mL, 4mg/mL and 7.5 mg/mL) while keeping the  $\text{HAuCl}_4$  concentration constant ( $1.2 \times 10^{-3}$  M). In case of the reduction of *p*-nitrophenol to *p*-aminophenol by  $\text{NaBH}_4$ , no significant differences in the reaction rates were observed as indicated by the UV-visible results (figure 4.10). The values of the apparent rate constant were  $7.47 \times 10^{-3} \text{ s}^{-1}$ ,  $7.18 \times 10^{-3} \text{ s}^{-1}$  and  $7.2 \times 10^{-3} \text{ s}^{-1}$  for Au nanoparticles synthesized using pepsin concentration of 2mg/mL, 4mg/mL and 7.5mg/mL respectively, clearly indicating that the concentration of the stabilizing agent (pepsin) had little effect on the catalytic efficiency of the Au nanostructures.

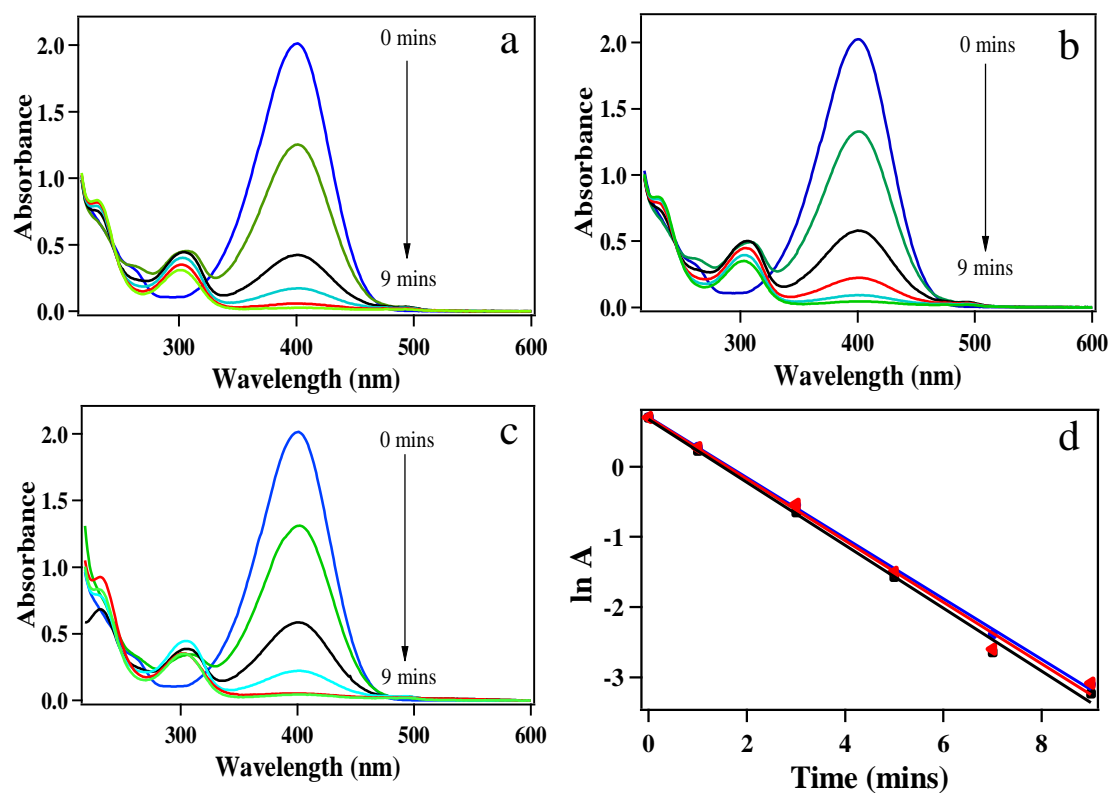


**Figure 4. 10.** Time dependent UV-visible spectrum for the reduction of *p*-nitrophenol to *p*-aminophenol catalyzed by Au nanoparticles synthesized at pH 5.4 with pepsin concentration of (a) 2mg/mL, (b) 4 mg/mL and (c) 7.5mg/mL. (d) plot of  $\ln A$  vs  $T$  for the reduction of *p*-nitrophenol to *p*-aminophenol to resorufin by  $\text{NaBH}_4$  catalyzed by Au nanoparticles synthesized at pH 5.4 with pepsin concentration of 2mg/mL (black), 4 mg/mL (red) and 7.5mg/mL (blue).

However, for the reduction of resazurin to resorufin a significant dependence of rate constant on the thickness of pepsin on Au nanoparticles was observed (figure 4.11). It was observed that for this reaction the Au nanoparticles synthesized with a pepsin concentration of 2 mg/mL was a better catalyst than the Au nanoparticles synthesized with an enzyme concentration of 4 mg/mL followed by the Au nanoparticles synthesized with a pepsin concentration of 7.5 mg/mL. The values of the rate constants as calculated from the plot of  $\ln(\text{absorbance})$  vs time was calculated to be  $2.27 \times 10^{-4} \text{ s}^{-1}$ ,  $8.35 \times 10^{-5} \text{ s}^{-1}$  and  $2.25 \times 10^{-5} \text{ s}^{-1}$  for Au nanoparticles synthesized using pepsin concentration of 2 mg/mL, 4 mg/mL and 7.5 mg/mL respectively.

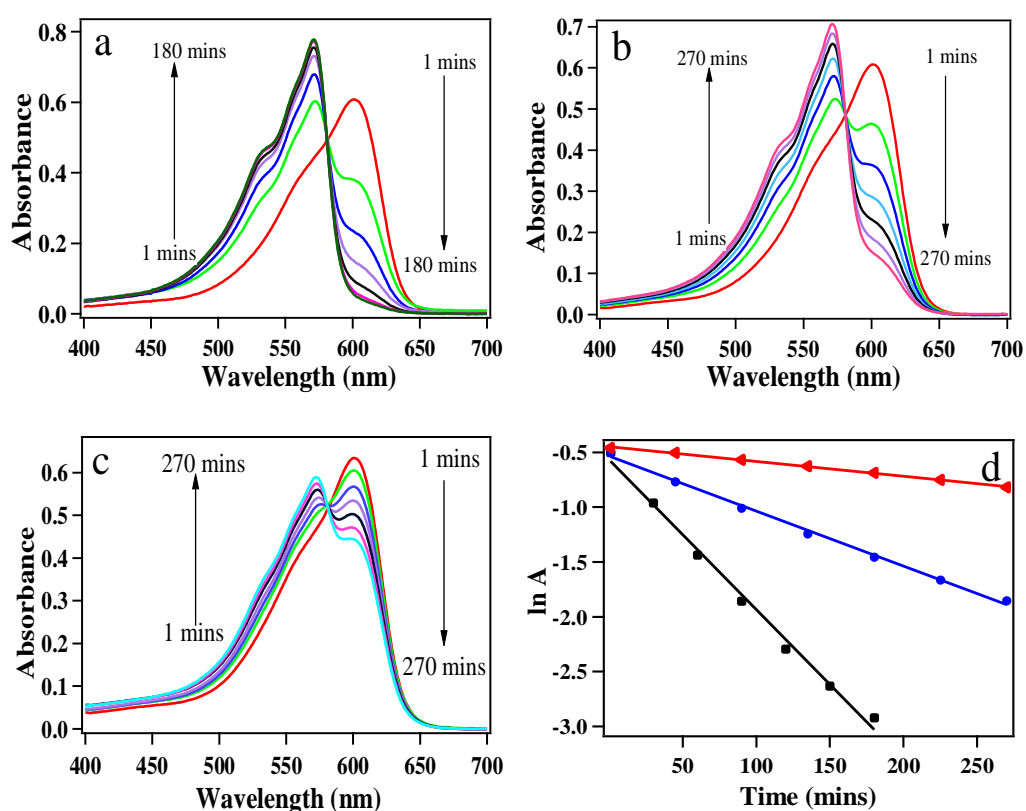


**Figure 4. 11.** Time dependent UV-visible spectrum for the reduction of resazurin to resorufin catalyzed by Au nanoparticles synthesized at pH 5.4 with pepsin concentration of (a) 2mg/mL, (b) 4 mg/mL and (c) 7.5mg/mL. (d) plot of  $\ln A$  vs  $T$  for the reduction of resazurin to resorufin by  $\text{NH}_2\text{OH}\cdot\text{HCl}$  catalyzed by Au nanoparticles synthesized at pH 5.4 with pepsin concentration of 2mg/mL (black), 4 mg/mL (blue) and 7.5mg/mL (red).

These results clearly suggested that the density of pepsin indeed proved to be a barrier for the approach of resazurin onto the surface of Au nanoparticles. Resazurin,

being a large molecule could not effectively penetrate the thick pepsin coating on the surface of the nanoparticles and thus with increasing concentration of pepsin on the Au nanoparticles, the rate of the reaction decreased. On the other hand, *p*-nitrophenol, being a smaller molecule could easily penetrate through the dense pepsin coating and approach the surface of the Au nanoparticles and therefore no significant differences in the rate of the reaction with increasing pepsin concentration was observed.

#### 4.2.10 Recyclability of the catalysts

One of the main advantages of heterogeneous catalysis over homogeneous catalysis is the recyclability of the catalysts. In the present catalytic systems under study, it was observed that the catalysts showed good reusability for both the reduction reactions upto the testing of the fourth cycle without any significant loss in the catalytic activity (figure 4.12). However from the third cycle onwards, slightly longer reaction time was required for the completion of the reactions. This gradual decrease in the reactivity of the catalysts may be ascribed to the poisoning of the surface of Au nanostructures due to the adsorption of the reactants.<sup>[59,60]</sup>

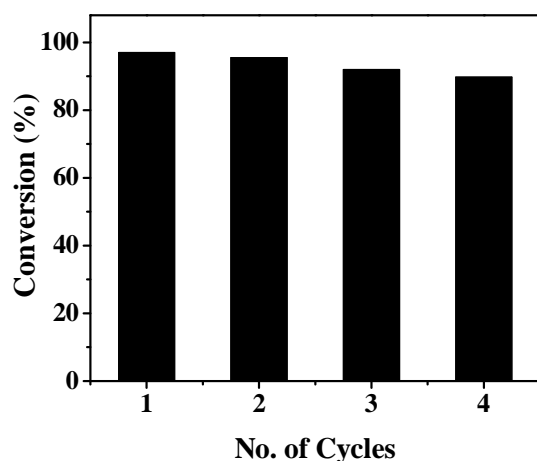


**Figure 4.12.** Reusability of the Au nanostructures synthesized using pepsin for the conversion of *p*-nitrophenol to *p*-aminophenol and resazurin to resorufin in four successive cycles of reaction by various Au nanoparticle-pepsin composites.

### 4.3 Conclusions

In conclusion, a detailed mechanistic investigation into the formation of various Au nanostructures by the enzyme pepsin has been performed. It was found that the

enzyme lost a large fraction of its natural activity after its participation in the reduction of  $\text{Au}^{3+}$  to  $\text{Au}^0$  due to conformational changes in the native structure of the enzyme. Nonetheless, the synthesized nanostructures could be used as effective catalysts for the reduction of *p*-nitrophenol to *p*-aminophenol by  $\text{NaBH}_4$  and resazurin to resorufin by  $\text{NH}_2\text{OH}\cdot\text{HCl}$ . Of the three nanostructures synthesized by varying the pH of the reaction medium, smaller fluorescent  $\text{Au}_{25}$  nanoclusters were found to be the most active, followed by spherical Au nanoparticles synthesized at pH 5.4 in case of reduction of *p*-nitrophenol to *p*-aminophenol. The results showed the usual trend of catalytic activity of surface catalyzed reactions, where nanoparticles with higher surface area to volume ratio demonstrated better efficiency. On the other hand for the reduction of resazurin, spherical Au nanoparticles synthesized at pH 5.4 were the most active followed by the anisotropic Au nanoparticles synthesized at pH 4.0 whereas the ultrasmall fluorescent  $\text{Au}_{25}$  nanoclusters showed the least activity. Therefore the concentration of the surface stabilizing agents also plays an important role on the intrinsic catalytic activity of the nanoparticles. Since for all the three size and shape selective Au nanoparticles, same reducing and stabilizing agent (pepsin) was used, the catalytic activity of the nanostructures could be fairly evaluated and compared with respect to the role of ligands. The use of enzymes such as pepsin will not only provide an environmentally friendly pathway for the generation of size and shape selective nanoparticles, but also provide sufficient stability and support to the nanoparticles for being used as effective catalytic systems for important organic transformations.

## 4.4 Experimental Section

### 4.4.1 Materials

Pepsin from porcine stomach mucosa, Trichloroacetic acid, *p*-nitrophenol, Resazurin and hydroxylamine hydrochloride were purchased from SRL chemicals, India. Hydrogen tetrachloroaurate ( $\text{HAuCl}_4$ ) and Hemoglobin from Bovine blood were purchased from Sigma-Aldrich. Sodium dihydrogen phosphate monohydrate, di-Sodium hydrogen phosphate, Sodium hydroxide and Sodium borohydride were purchased from Merck, India. All the reagents were of analytical grade and were used without any further purification. Milli Q water was used throughout the experiments.

#### **4.4.2 Instrumentation**

UV- visible spectra were recorded on a Varian Cary 100 Bio spectrophotometer. Powder X-ray diffraction spectra (XRD) were recorded on a Rigaku Smartlab, Automated Multipurpose X-ray diffractometer with Cu K $\alpha$  source (wavelength of X-rays was 0.154 nm). The samples for XRD were prepared by drop casting the sample solutions on glass slides and drying them at room temperature. FTIR spectra were recorded in KBr pellet using Bruker Tensor 27 instrument. The transmission electron microscopy (TEM) images were recorded on a JEOL JEM-2100 microscope at an accelerating voltage of 200 kV. The samples for TEM were prepared by drop casting the sample solutions on carbon coated copper grid followed by room temperature drying. Circular Dichroism (CD) experiments were performed using a JASCO J-815 spectropolarimeter. Fluorescence measurement was performed on a fluoromax-4p fluorometer from Horiba (Model: FM-100).

#### **4.4.3 Synthesis of Au nanoparticles at pH 5.4 and 4.0**

To 2 mL of 1 mg/mL enzyme solution in PBS buffer (100 mM) of appropriate pH ( 5.4 and 4.0), 80  $\mu$ L of H<sub>2</sub>AuCl<sub>4</sub> (0.03M) was added such that the final concentration of H<sub>2</sub>AuCl<sub>4</sub> was  $1.2 \times 10^{-3}$  M and the solution was stirred at room temperature for 16 hours.

#### **4.4.4 Synthesis of Au nanoparticles at pH 5.4 for activity assay, fluorescence study and circular dichroism studies**

2 mg of pepsin was dissolved in 2mL of PBS buffer of pH 5.4 (100 mM). To this solution 40  $\mu$ l of 0.03M H<sub>2</sub>AuCl<sub>4</sub> solution was added and the final mixture was stirred at room temperature for 16 hours.

#### **4.4.5 Activity assay of pepsin after the synthesis of Au nanoparticles**

The activity of the native enzyme and Au NP-enzyme composite was tested using a standard procedure based on the action of pepsin on hemoglobin. Au nanoparticles were first synthesized at pH 5.4 as already explained above and native enzyme was also kept under similar conditions (without H<sub>2</sub>AuCl<sub>4</sub>) in the same buffer for 16 hours. After the formation of Au nanoparticles, both the Au NP-enzyme solution as

well as native enzyme solution was diluted with 0.01M HCl such that the concentration of the enzyme in the solution was 0.04 mg/mL. Both these solutions served as the test solutions. Another fresh solution with native pepsin (0.04 mg/mL) was prepared which was used as blank solution. The substrate, hemoglobin solution (2.5%) was prepared by dissolving 2.5g hemoglobin in 100 mL water and was filtered through a glass wool. This solution was then acidified and diluted to 2.0% by adding 20 mL of 0.03M HCl to 80 mL of 2.5% hemoglobin. 5% (w/v) trichloroacetic acid was prepared. Now the following solutions were pipetted out.

	<u>Test (Au NP-pepsin)</u>	<u>Test (pepsin)</u>	<u>Blank (native pepsin)</u>
Hemoglobin 2.0% (w/v)	5.0 mL	5.0 mL	5.0 mL

These solutions were allowed to equilibrate at 37°C for 15 minutes.

Enzyme solution	1.0 mL	1.0 mL	0.0 mL
-----------------	--------	--------	--------

The solutions were properly mixed and kept exactly for another 10 minutes.

Trichloroacetic acid	10.0 mL	10.0 mL	10.0 mL
Enzyme solution	0.0 mL	0.0 mL	1.0 mL

The mixture after incubation at 37°C for another 5 minutes was filtered through a Whatman 42 filter paper and then the absorbance at 280 nm was recorded using a UV-visible spectrophotometer.

In a similar procedure, by treating the citrate capped Au nanoparticles-pepsin composite as test solution, its activity was tested.

#### **4.4.6 Synthesis of red emitting Au nanoclusters**

7.5 mg pepsin was dissolved in 1 mL water. To the enzyme solution 46  $\mu$ L of HAuCl<sub>4</sub> (0.03M) was added and the solution was stirred for 5 minutes after which 150  $\mu$ L of 1M NaOH was added to increase the pH of the solution and the final solution was stirred for 90 minutes at room temperature.

#### 4.4.7 Fluorescence study of pepsin before and after the synthesis of Au nanoparticles

The fluorescence spectrum for both the native pepsin and Au NP-pepsin composite was recorded in PBS buffer (100 mM) at a pH of 5.4 in a cuvette of pathlength 1 cm. The concentration of enzyme in both the solutions was 0.2 mg/mL and the excitation wavelength was 295 nm.

#### 4.4.8 Circular dichroism studies

The Circular Dichroism (CD) measurements were performed at 25 °C with a data pitch of 0.1 nm. The scanning speed was set to 20 nm/ min and the band width was 1nm. The far UV region (190-250 nm) spectra were recorded with an enzyme concentration of 0.2 mg/mL using a quartz cell of 1mm pathlength (Starna Scientific Ltd. Hainault, UK). For the near UV region (250-320 nm) an enzyme concentration of 1.0 mg/mL was used and the measurements were performed in a 1cm pathlength cell (Hellma Analytics). Each spectrum is the result of average of three consecutive scans.

#### 4.4.9 Catalytic reduction of *p*-nitrophenol to *p*-aminophenol

For the catalytic reduction of *p*-nitrophenol to *p*-aminophenol, the Au nanoparticle solutions (with final H<sub>Au</sub>Cl<sub>4</sub> concentration  $1.2 \times 10^{-3}$  M) were first diluted six times, i.e. 50  $\mu$ L of the catalyst was added to 250  $\mu$ L of water.

**Procedure:** To a standard quartz cell of pathlength 1 cm, 2.5 mL of 0.12 mM *p*-nitrophenol, 5 mg NaBH<sub>4</sub> and 25  $\mu$ L of the Au NP-pepsin composite catalyst synthesized at different pH were added and UV-visible spectrum was recorded after appropriate times.

#### 4.4.10 Catalytic reduction of resazurin to resorufin

To 0.83 mL of water taken in a cuvette of pathlength 1cm, 1.67 mL of 0.1M NH<sub>2</sub>OH.HCl was added. To this mixture 150  $\mu$ L of 1M NaOH followed by 50  $\mu$ L of 1mM resazurin was added. Finally 200  $\mu$ L of the as prepared Au nanostructures were added and the UV-visible and fluorescence spectrum were recorded after appropriate times.

---

## 4.5 References

1. Burda C., Chen X., Narayanan R., El-Sayed M. A. (2005), Chemistry and properties of nanocrystals of different shapes, *Chem. Rev.*, 105, 1025-1102 (DOI: 10.1021/cr030063a).
2. Sardar R., Funston M. A., Mulvaney P., Murray R. W. (2009), Gold nanoparticles: Past, present, and future, *Langmuir*, 25, 13840-13851 (DOI: 10.1021/la9019475)
3. Astruc D. (2008), *Nanoparticles and Catalysis*, Wiley-VCH, New York.
4. Ishida T., Haruta M. (2007), Gold catalysts: Towards sustainable chemistry, *Angew. Chem. Int. Ed.*, 46, 7154-7156 (DOI: 10.1002/anie.200701622).
5. Corma A., Garcia H. (2008), Supported gold nanoparticles as catalysts for organic reactions, *Chem. Soc. Rev.*, 37, 2096-2126 (DOI: 10.1039/B707314N).
6. Bawaked S., Dummer N. F., Dimitratos N., Bethell D., He Q., Kiely C. J., Hutchings G. (2009), Solvent free selective epoxidation of cyclooctene using supported gold catalysts, *Green Chem.*, 11, 1037-1044 (DOI: 10.1039/C0GC00550A).
7. Haruta M. (1997), Size-and support-dependency in the catalysis of gold, *Catal Today*, 36, 153-166 (DOI: 10.1016/S0920-5861(96)00208-8).
8. Stratakis M., Garcia H. (2012), Catalysis by supported gold nanoparticles: Beyond aerobic oxidative processes. *Chem. Rev.*, 112, 4469-4506 (DOI: 10.1021/cr3000785).
9. Aditya T., Pal A., Pal T. (2015), Nitroarene reduction: A trusted model reaction to test nanoparticle catalysts, *Chem. Commun.*, 51, 9410-9431 (DOI: 10.1039/C5CC01131K).
10. Wu S., Dzubielia J., Kaiser J., Drechsler M., Guo X., Ballauff M., Lu Y. (2012), Thermosensitive Au-PNIPA yolk-shell nanoparticles with tunable selectivity for catalysis, *Angew. Chem. Int. Ed.*, 51, 2229-2233 (DOI: 10.1002/anie.201106515).
11. Biondi I., Laurenczy G., Dyson P. J. (2011), Synthesis of gold nanoparticle catalysts based on a new water-soluble ionic polymer, *Inorg. Chem.*, 50, 8038-8045 (DOI: 10.1021/ic200334m).

12. Hashmi A. S. K. (2007), Gold-catalyzed organic reactions, *Chem. Rev.*, 107, 3180-3211 (DOI: 10.1021/cr000436x).
13. Bhattacharya T., Sarma T. K., Samanta S. (2012), Self-assembled monolayer coated gold-nanoparticle catalyzed aerobic oxidation of  $\alpha$ -hydroxy ketones in water: An efficient one-pot synthesis of quinoxaline derivatives, *Catal. Sci. Technol.*, 2, 2216-2220 (DOI: 10.1039/C2CY20438J).
14. Mikami Y., Dhaksinamoorthy A., Alvaro M., Garcia H. (2013), Catalytic activity of unsupported gold nanoparticles, *Catal. Sci. Technol.*, 3, 58-69 (DOI: 10.1039/C2CY20068F).
15. Yan W., Mahurin S. M., Pan Z., Overbury S. H., Dai S. (2005), Ultrastable gold nanocatalyst supported on surface-modified TiO<sub>2</sub> nanocrystals, *J. Am. Chem. Soc.*, 127, 10480-10481 (DOI: 10.1021/ja053191k).
16. Tsunoyama H., Sakurai H., Ichikuni N., Negishi Y., Tsutuda T. (2004), Colloidal gold nanoparticles as catalyst for carbon-carbon bond formation: Application to aerobic homocoupling of phenylboronic acid in water, *Langmuir*, 20, 11293-11296 (DOI: 10.1021/la0478189).
17. Coppage R., Slocik J. M., Dakhel H. R., Bedford N. M., Heinz H., Naik R. R., Knecht M. R. (2013), Exploiting localized surface binding effects to enhance the catalytic reactivity of peptide-capped nanoparticles, *J. Am. Chem. Soc.*, 135, 11048-11054 (DOI: 10.1021/ja402215t).
18. Wei Y., Liu J., Zhao Z., Chen Y., Xu C., Duan A., Jiang G., He H. (2011), Highly active catalysts of gold nanoparticles supported on three-dimensionally ordered macroporous LaFeO<sub>3</sub> for soot oxidation, *Angew. Chem. Int. Ed.*, 50, 2326-2329 (DOI: 10.1002/anie.201006014).
19. Zheng N., Stucky G. D. (2006), A general synthetic strategy for oxide-supported metal nanoparticle catalysts, *J. Am. Chem. Soc.*, 128, 14278-14280 (DOI: 10.1021/ja0659929).
20. Liu H., Liu Y., Li Y., Tang Z., Jiang H. (2010), Metal-Organic framework supported gold nanoparticles as a highly active heterogeneous catalyst for aerobic oxidation of alcohols, *J. Phys. Chem. C*, 114, 13362-13369 (DOI: 10.1021/jp105666f).

21. Dai H., Cao N., Yang L., Su J., Luo W., Cheng G. (2014), AgPd nanoparticles supported on MIL-101 as high performance catalysts for catalytic dehydrogenation of formic acid, *J. Mater. Chem. A*, 2, 11060-11064 (DOI: 10.1039/C4TA02066A).
22. Zhang N., Qiu H., Liu Y., Wang W., Li Y., Wang X., Gao J. (2011), Fabrication of gold nanoparticle/graphene oxide nanocomposites and their excellent catalytic performance, *J. Mater. Chem.*, 21, 11080-11083 (DOI: 10.1039/C1JM12539G).
23. Tan X., Deng W., Liu M., Zhang Q., Wang Y. (2009), Carbon nanotube supported gold nanoparticles as efficient catalyst for selective oxidation of cellobiose into gluconic acid in aqueous medium, *Chem. Commun.*, 7179-7181 (DOI: 10.1039/B917224F).
24. Wan X. X., Tan Z. H., Zeng M., Wang J. N. (2014), Carbon nanocages: A new support material for Pt catalyst with remarkably high durability, *Sci. Rep.*, 4, 4437 (DOI:10.1038/srep04437).
25. Rangnekar A., Sarma T. K., Singh A. K., Deka J., Ramesh A., Chattopadhyay A. (2007), Retention of enzymatic activity of  $\alpha$ -Amylase in the reductive synthesis of gold nanoparticles, *Langmuir*, 23, 5700-5706 (DOI: 10.1021/la062749e).
26. Sharma B., Mandani S., Sarma T. K. (2013), Biogenic growth of alloys and core-shell nanostructures using urease as a nanoreactor at ambient conditions, *Sci. Rep.*, 3, 2601, (DOI: 10.1038/srep02601).
27. Sharma B., Mandani S., Sarma T. K. (2014), Enzymes as bionanoreactors: Glucose oxidase for the synthesis of catalytic Au nanoparticles and Au nanoparticle–polyaniline nanocomposites, *J. Mater. Chem. B*, 2, 4072-4079 (DOI: 10.1039/C4TB00218K).
28. Au L., Lim B., Colletti P., Jun Y. -S., Xia Y. (2010), Synthesis of Gold microplates using bovine serum albumin as a reductant and a stabilizer, *Chem Asian J.*, 5, 123-129 (DOI: 10.1002/asia.200900468).

- 
29. Xu Y., Sherwood J., Qin Y., Crowley D., Bonizzoni M., Bao Y. (2014), The role of protein characteristics in the formation and fluorescence of Au nanoclusters, *Nanoscale*, 6, 1515-1524 (DOI: 10.1039/C3NR06040C).
  30. Kawasaki H., Hamaguchi K., Osaka I., Arakawa R. (2011), pH-dependent synthesis of pepsin-mediated gold nanoclusters with blue, green and red fluorescent emission, *Adv. Funct. Mater.*, 21, 3508-3515 (DOI: 10.1002/adfm.201100886).
  31. Xie J., Zhang Y., Ying J. Y., (2009), Protein-Directed Synthesis of Highly Fluorescent Gold Nanoclusters, *J. Am. Chem. Soc.*, 131, 888-889 (DOI: 10.1021/ja806804u).
  32. Zayats M., Baron R., Popov I., Willner I. (2005), Biocatalytic growth of Au nanoparticles: From mechanistic aspects to biosensors design, *Nano Lett.*, 5, 21-25 (DOI: 10.1021/nl048547p).
  33. Scott D., Toney M., Muzikar M. (2008), Harnessing the mechanism of glutathione reductase for synthesis of active site bound metallic nanoparticles and electrical connection to electrodes, *J. Am. Chem. Soc.*, 130, 865-874 (DOI: 10.1021/ja074660g).
  34. Virkutyte J., Varma R. S. (2011), Green synthesis of metal nanoparticles: Biodegradable polymers and enzymes in stabilization and surface functionalization, *Chem. Sci.*, 2, 837-846 (DOI: 10.1039/C0SC00338G).
  35. Deka J., Paul A., Chattopadhyay A. (2012), Modulating enzymatic activity in the presence of gold nanoparticles, *RSC Adv.*, 2, 4736-4745 (DOI: 10.1039/C2RA20056B).
  36. Tang J., Sepulveda P., Marcinişzyn J. Jr., Chen K. C. S., Huang W. -Y., Tao N., Liu D., Lanier J. P. (1973), Amino-acid sequence of porcine pepsin, *Proc. Nat. Acad. Sci. USA*, 70, 3437-3439.
  37. Goswami N., Zheng K., Xie J. (2014), Bio-NCs – the marriage of ultrasmall metal nanoclusters with biomolecules, *Nanoscale*, 6, 13328-13347 (DOI: 10.1039/C4NR04561K).
  38. Anson M. L. (1938), The estimation of pepsin, trypsin, papain and cathepsin with haemoglobin, *J. Gen. Physiol.*, 22, 79-89 (DOI: 10.1085/jgp.22.1.79).
-

- 
39. Dee D., Pencer J., Nieh M. -P., Krueger S., Katsaras J., Yada R. Y. (2006), Comparison of solution structures and stabilities of native, partially unfolded and partially refolded pepsin, *Biochemistry*, 45, 13982-13992 (DOI: 10.1021/bi061270i).
  40. Campos L. A., Sancho J. (2003), The active site of pepsin is formed in the intermediate conformation dominant at mildly acidic pH, *FEBS Lett.*, 538, 89-95 (DOI: 10.1016/S0014-5793(03)00152-2).
  41. Lakowicz J. R. (2006), *Principles of Fluorescence Spectroscopy*, Springer, New York.
  42. Cuenya B. R. (2010), Synthesis and catalytic properties of metal nanoparticles: Size, shape, support, composition, and oxidation state effects, *Thin Solid Films*, 518, 3127-3150 (DOI: 10.1016/j.tsf.2010.01.018).
  43. Panigrahi S., Basu S., Praharaj S., Pande S., Jana S., Pal A., Ghosh S. K., Pal T. (2007), Synthesis and size-selective catalysis by supported gold nanoparticles: Study on heterogeneous and homogeneous catalytic process, *J. Phys. Chem. C*, 111, 4596-4705 (DOI: 10.1021/jp067554u).
  44. Kundu S., Lau S., Liang H. (2009), Shape-controlled catalysis by cetyltrimethylammonium bromide terminated gold nanospheres, nanorods, and nanoprisms, *J. Phys. Chem. C*, 113, 5150-5156 (DOI: 10.1021/jp811331z).
  45. Shimizu K. -I., Miyamoto Y., Kawasaki T., Tanji T., Tai Y., Satsuma A. (2009), Chemoselective hydrogenation of nitroaromatics by supported gold catalysts: Mechanistic reasons of size- and support- dependent activity and selectivity, *J. Phys. Chem. C*, 113, 17803-17810 (DOI: 10.1021/jp906044t).
  46. Wunder S., Polzer F., Lu Y., Mei Y., Ballauff M. (2010), Kinetic analysis of catalytic reduction of 4-nitrophenol by metallic nanoparticles immobilized in spherical polyelectrolyte polymer brushes, *J. Phys. Chem. C*, 114, 8814-8820 (DOI: 10.1021/jp101125j).
  47. Baruah B., Gabriel G. J., Akbashev M. J., Booher M. E. (2013), Facile synthesis of silver nanoparticles catalyzed by cationic polynorbornenes and their catalytic activity in the reduction of 4-nitrophenol, *Langmuir*, 29, 4225-4234 (DOI: 10.1021/la305068p).

- 
48. Ciganda R., Li N., Deraedt C., Gatard S., Zhao P., Salmon L., Hernández R., Ruiz J., Astruc D. (2014), Gold nanoparticles as electron reservoir redox catalysts for 4-nitrophenol reduction: a strong stereoelectronic ligand influence, *Chem. Commun.*, 50, 10126-10129 (DOI: 10.1039/C4CC04454A).
  49. Fu H., Yang X., Jiang X., Yu A. (2013), Bimetallic Ag-Au nanowires: Synthesis, growth mechanism, and catalytic properties, *Langmuir*, 29, 7134-7142 (DOI: 10.1021/la400753q).
  50. Xia B., Fang H., Li L. (2013), Preparation of bimetallic nanoparticles using a facile green synthesis method and their application, *Langmuir*, 29, 4901-4907 (DOI: 10.1021/la400355u).
  51. Narayanan R., El- Sayed M. A. (2005), Catalysis with transition metal nanoparticles in colloidal solution: nanoparticle shape dependence and stability, *J. Phys. Chem. B*, 109, 12663-12676 (DOI: 10.1021/jp051066p).
  52. Kundu S., Wang K., Liang H. (2009), Size-selective synthesis and catalytic application of polyelectrolyte encapsulated gold nanoparticles using microwave irradiation, *J. Phys. Chem. C*, 113, 5157-5163 (DOI: 10.1021/jp9003104).
  53. Cuenya B. R. (2013), Metal nanoparticle catalysts beginning to shape up, *Acc. Chem. Res.*, 46, 1682-1691 (DOI: 10.1021/ar300226p).
  54. Xu R., Wang D., Zhang J., Li Y. (2006), Shape-dependent catalytic activity of silver nanoparticles for the oxidation of styrene, *Chem-Asian J.*, 1, 888-893 (DOI: 10.1002/asia.200600260).
  55. Rashid M. H., Mandal T. K. (2008), Templateless synthesis of polygonal gold nanoparticles: An unsupported and reusable catalyst with superior activity, *Adv. Funct. Mater.*, 18, 2261-2271 (DOI: 10.1002/adfm.200800085).
  56. Li Y., Tang Z., Prasad P. N., Knecht M. R., Swihart M. T. (2014), Peptide-mediated synthesis of gold nanoparticles: effects of peptide sequence and nature of binding on physicochemical properties, *Nanoscale*, 6, 3165-3172 (DOI: 10.1039/C3NR06201E).
  57. Xu W., Kong J. S., Yeh, Y.-T. E., Chen P. (2008), Single-molecule nanocatalysis reveals heterogeneous reaction pathways and catalytic dynamics, *Nat. Mater.*, 7, 992-996 (DOI: 10.1038/nmat2319).

58. Zhou X., Xu W., Liu G., Panda D., Chen P. (2010), Size dependent catalytic activity and dynamics of gold nanoparticles at the single-molecule level, *J. Am. Chem. Soc.*, 132, 138-146 (DOI: 10.1021/ja904307n).
59. Yu T., Xeng J., Lim B., Xia Y. (2010), Aqueous-phase synthesis of Pt-CeO<sub>2</sub> hybrid nanostructures and their catalytic properties, *Adv. Mater.*, 22, 5188-5192 (DOI: 10.1002/adma.201002763).
60. Liang M., Wang L., Liu X., Qi W., Su R., Huang R., Yu Y., He Z. (2013), Cross-linked lysozyme crystal template synthesis of Au nanoparticles as high-performance recyclable catalysts, *Nanotechnology*, 24, 245601 (DOI: 10.1088/0957-4484/24/24/245601).



## Chapter 5

# Ag(I) Ion Mediated Self-Assembly of Nucleobases Towards the Generation of Coordination Polymer Hydrogels

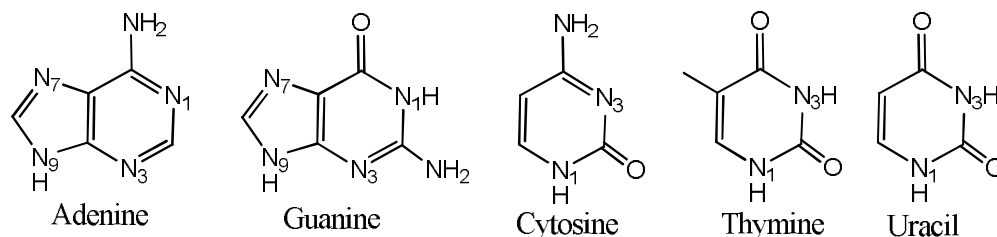
### 5.1 Introduction

The self assembly of small molecules triggered by metal ions into ordered nanostructures such as spheres, rods, tapes, fibers etc. has progressed as a magnificent strategy for the fabrication of materials with tunable physico-chemical properties.<sup>[1-13]</sup> The formation of metallogels, an important class of soft materials, represent one of the most elegant bottom-up approaches towards generation of these functional materials, where discrete metal coordination complexes of low-molecular-weight ligands or well defined coordination polymers enable entangled coordination networks that can immobilize large volume of solvents and guest molecules by different mechanisms.<sup>[14-19]</sup> These integrative self-assembled structures with metallic elements incorporated into the viscoelastic gel matrix harness catalytic, magnetic, stimuli-responsive properties etc. that are crucial for various technological applications including catalysis,<sup>[20-22]</sup> sensing<sup>[23,24]</sup> and optics.<sup>[25,26]</sup> However, mostly due to their toxicity, such materials cannot be employed in several important biological applications such as drug delivery as well as bioimaging because these applications require that the materials be constructed from benign building blocks that are both environmentally and biologically compatible.<sup>[11,27]</sup> Nature has excelled at utilizing supramolecular chemistry to store, transmit and replicate information in a challenging environment with a limited number of structural units. In a biomimetic approach, biomolecules such as amino acids,<sup>[16,18]</sup> peptides<sup>[28,29]</sup> and saccharides<sup>[30]</sup> have gained enough significance for the construction of such materials.

Nucleobase-metal coordination chemistry have been extensively pursued for understanding the role of metal ions in biological systems such as interaction of metals

with DNA, mode of action of numerous metal containing drugs (e.g. *cis*-platin) and genetic information transfer etc.<sup>[31-35]</sup> The accessible nitrogen and oxygen lone pairs in both purine and pyrimidine nucleobases open up possibility of nucleobase-metal interactions as supramolecular motifs resulting in both discrete and infinite supramolecules such as porous BioMOFs.<sup>[36-38]</sup> Several porous coordination polymers involving substituted nucleobases and metal ions have been reported.<sup>[39-41]</sup> Studies involving interaction of Ag<sup>I</sup> with nucleotides or DNA has been extensively pursued due to (i) higher affinity of binding of Ag<sup>I</sup> towards the nucleobases than for the phosphates and (ii) malleable Ag<sup>I</sup> offers a much greater variety of coordination geometries. The extraordinary self-assembly of guanosine and their derivatives into G-quadruplex and subsequent hydrogel formation have been exploited in supramolecular chemistry and nanotechnology.<sup>[42-45]</sup> Supramolecular hydrogels derived from silver ion mediated self-assembly of 5'-guanosine monophosphate also has been reported.<sup>[46]</sup> However, metallohydrogels involving pure nucleobases as ligands have not been realized.

In this chapter, we report our serendipitous discovery of silver ion induced self-assembly of pure nucleobases into hydrogels. Simple addition of Ag<sup>+</sup> ions to an alkaline solution of adenine, cytosine, thymine or uracil resulted in the formation of self-standing hydrogels. The formation of hydrogels was spontaneous and did not require any external stimuli such as heating/cooling or sonication for its formation. A detailed investigation has been carried out using spectroscopic and microscopic as well as theoretical studies in order to have an insight into the properties and structural enticement of the formed hydrogels. Further, under the present conditions, cytosine, thymine and uracil acted as reducing agents for the formation of Ag nanoparticles that were decorated along the fibers of the hydrogel. The antimicrobial activity of the hydrogels has been studied for both gram-positive and gram negative microbes.



**Scheme 5.1.** Chemical structures of the five nucleobases found in DNA and RNA.

## 5.2 Results and Discussion

### 5.2.1 Synthesis and characterization of Ag-adenine hydrogels

Crystal engineering through the interaction of nucleobases, especially substituted adenine, with  $\text{Ag}^{\text{I}}$  has been studied extensively leading to the formation of triads, tetrads, metallaquartets, hexads etc.<sup>[39-41, 47-49]</sup> However, when  $\text{AgNO}_3$  was added to a deprotonated adenine in aqueous medium, maintaining a metal:adenine molar ratio of 1:0.8, spontaneous formation of opaque metallogel was observed. The self-assembled formation of the metallogels ensued spontaneously within one minute at room temperature and did not require the involvement of external stimuli such as heating/cooling or ultrasonication, often required for several other reported metallogels.<sup>[50,51]</sup> It is well known that for enhanced solubility of the nucleobases in aqueous medium, protonation or deprotonation of the nucleobases is essential, which is usually done by the addition of acid or base. The solution became turbid when a very dilute solution of  $\text{AgNO}_3$  (10 mM) was added to the deprotonated adenine solution in aqueous medium (at metal to adenine molar ratio of 1:0.8) signifying the formation of the fibrous gel structures even at very low concentration. However in order to trap all the solvent molecules, higher concentration of  $\text{Ag}^+$  salt (100 mM) and adenine (80 mM) was required. The deprotonation of adenine was carried out by adding NaOH to a final pH of 10.8. In contrast, adenine cannot gelate water under protonated condition (in acidic medium) due to protonation of nitrogen atoms in adenine, clearly indicating that only under alkaline medium, adenine coordinated to  $\text{Ag}^+$  ions to form hydrogel. Further, the hydrogels of adenine with  $\text{Ag}^+$  was highly pH responsive and the hydrogels were dissolved to form a clear solution under acidic conditions. Upon adjusting the pH from acidic to basic the recovery of the hydrogels did not occur, instead a white precipitate was obtained due to the formation of  $\text{AgOH}$ . The gel nature and the mechanical robustness of the formed material were confirmed physically by observing the absence of flow upon the inversion of the tube. In order to ascertain the role of variable concentrations of the metal and ligand component on the gel formation, we varied the metal:ligand ratio and observed the gel formation physically. Increasing the  $\text{Ag}^+$ :adenine molar ratio upto 2:1 resulted in gel formation. On the other hand, when  $\text{Ag}^+$  molar concentration was less than adenine, fibrous network formation was

observed resulting in partial formation of gels. However, the gels were unable to trap all the water molecules as observed by the inversion of tube method. The results suggested that for stable gel formation, the concentration of  $\text{Ag}^+$  had to be higher than that of adenine. From all the studies, the most stable gels were obtained at a metal:adenine ratio of 1:0.8 (Table 5.1). In order to estimate the role of counter ions in gel formation,<sup>[52,53]</sup> we used  $\text{AgClO}_4$  or  $\text{CH}_3\text{COOAg}$  for complexation with deprotonated adenine solution. The gel formation occurred spontaneously, signifying that counterions with hard base characteristics did not significantly influence the gel formation.

$\text{Ag}^+$	Adenine	Result
1	0.8	Gel
1	1	Gel with some water
2	1	Gel
0.25	1	Partial gel formation, with the gel floating in the excess nucleobase solution

**Table 5.1.** Table for the interaction of  $\text{Ag}^+$  ions and adenine at various  $\text{Ag}^+$ :adenine molar ratio.

The effect of solvent on the formation of gels was studied by mixing a deprotonated adenine solution in aqueous medium with  $\text{AgNO}_3$  dissolved in various solvents such as methanol, DMF and acetonitrile under the standard reaction conditions. The formation of gel was studied in polar solvents due to insolubility of adenine in common non-polar solvents. Spontaneous formation of gels was observed in all cases in these mixed-solvent systems having water as a component. On the other hand, only precipitation was observed in methanol, DMF or DMF-methanol mixture. The observations clearly suggested that the presence of water molecules was crucial for the formation of hydrogels. The strong hydrogen bonding ability of water propagated the extensive hydrogen bonded network by binding with the available nitrogen of the parent molecular assembly resulting in the formation of the hydrogels. Further, when adenosine, *i.e.* adenine attached to a ribose sugar moiety via a  $\beta$ -N<sub>9</sub>-glycosidic bond, was mixed with  $\text{AgNO}_3$  under our reaction conditions, only precipitation occurred, suggesting that any substitution at the N9 position was detrimental towards hydrogel formation. In order to confirm this we performed the hydrogelation experiment by mixing deprotonated N9-methyladenine with  $\text{AgNO}_3$  in water. We observed

spontaneous precipitation of the coordination complex and no hydrogel formation even at elevated temperature or using ultrasonication could be observed. The results show the importance of the N9 position and its probable involvement in coordination to metal ion or extensive hydrogen bonding of water molecules with the Ag-adenine moiety that directs the hydrogel formation.

In order to access the morphological features of the gel forming network, electron microscopy of the hydrogel was performed. The transmission electron microscopy images of the Ag-adenine gel revealed the formation of very homogeneous short individual nanofibers (figure 5.1a). The thickness of the fibers, as calculated from the TEM images varied between 20 to 35 nm and several micrometer in length. Field emission scanning electron microscopy (FESEM) studies confirmed the highly entangled nanofibrillar morphology of the Ag-adenine hydrogel (figure 5.1b). Probably the fibers observed in the SEM image consist of bundles of gelator aggregates. The water molecules are understandably immobilized within such a microfibrillar network.

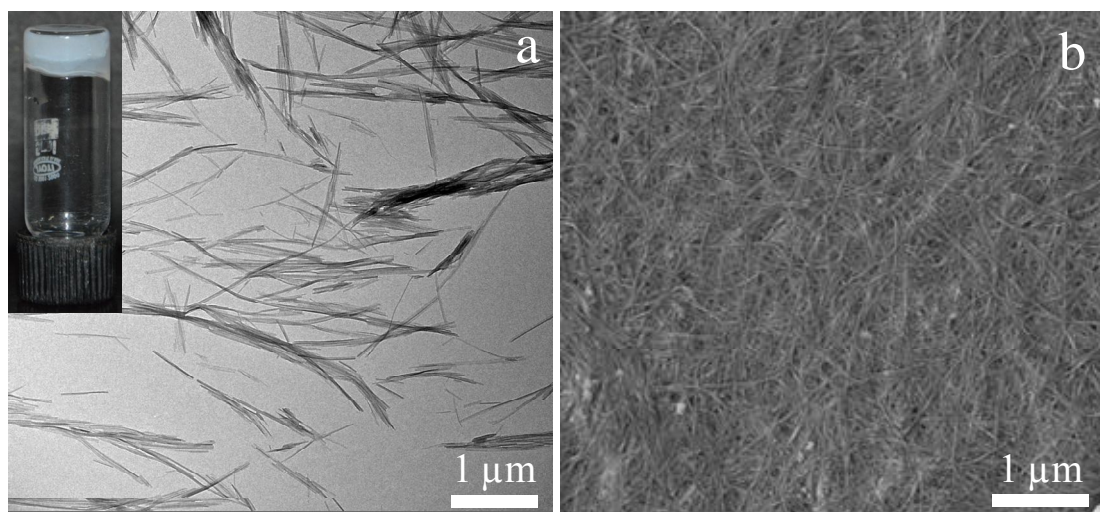


**Figure 5.1.** (a) TEM image and (b) FESEM image of the Ag-adenine hydrogel. Inset in (a) is the digital image of the Ag-adenine hydrogel.

In order to get an insight into the structural composition of these self-assembled hydrogels, growth of single crystals suitable for crystallographic analysis would have been ideal, however we could not obtain single crystals after several attempts under the processing conditions of the gel matrix. Therefore, the crystallinity of the Ag-adenine

hydrogels was evaluated by powder X-ray diffraction. The wide angle X-ray diffraction pattern (figure 5.2a) of the dried hydrogels deposited on a glass plate are all characterized by a group of well-resolved reflections, suggesting that the hydrogel was highly crystalline in nature. Major diffraction peaks at  $2\theta = 7.1^\circ$ ,  $14.1^\circ$ ,  $21.2^\circ$ ,  $27.5^\circ$ ,  $33.8^\circ$ ,  $42.1^\circ$ ,  $47.2^\circ$  and  $56.2^\circ$  with corresponding d-values of 12.5 Å, 6.3 Å, 4.2 Å, 3.2 Å, 2.1 Å, 1.7 Å, 1.5 Å and 1.3 Å respectively, which followed a ratio of 1: 1/2: 1/3: 1/4: 1/5: 1/6: 1/7: 1/8, suggesting that the hydrogels were mainly assembled in a layered structure and the interlayer distance was 12.5 Å. This value is quite close to the value of the length of two adenine units connected through hydrogen bonding with water (12.7 Å). Thermogravimetric analysis of the freeze dried gel was performed to have an idea about the thermal stability of the Ag-adenine gel. The TGA plot (figure 5.2b) showed an initial weight loss of approx. 10% at a temperature of 102 °C, which is assumed to be due to the loss of water molecules in the hydrogel matrix. No significant weight loss was observed thereafter upto a temperature of 340 °C. Further, two weight losses at 340 °C and 450 °C were observed which can be attributed to the decomposition of the ligand (adenine).

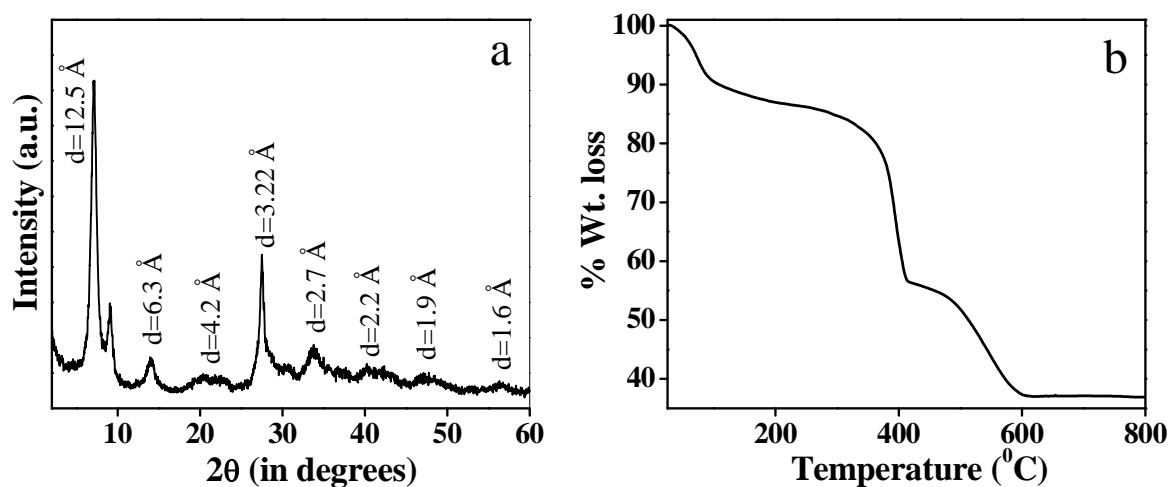


**Figure 5.2.** (a) Powder X-ray diffraction spectrum and (b) Thermogravimetric plot of freeze dried Ag-adenine gel.

One of the most important characteristic properties of gels which reflect their mechanical properties is their viscoelastic nature. The mechanical strength of a gel is measured by elastic storage modulus ( $G'$ ) and loss modulus ( $G''$ ). If the value of  $G'$  is

higher than  $G''$  then the sample behaves as an elastic material. Therefore, to have an idea about the elastic nature of the Ag-adenine gel, dynamic strain sweep and frequency sweep experiment were performed (figure 5.3). From the strain sweep experiment, it was observed that initially  $G'$  was significantly higher than  $G''$  and maintained the difference over a large range of strain. However, at higher values of strain the difference between the modulus began decreasing, and at a strain of 51%,  $G''$  became greater than  $G'$ , indicating the transformation of the hydrogel from gel to sol state. To further establish the elastic nature of the Ag-adenine hydrogel, frequency sweep rheological measurement was performed. The figure clearly depicts that in the frequency range of 0.1 to 100  $s^{-1}$ ,  $G'$  is always greater than  $G''$  by several factors, which demonstrated that the elastic behavior of the hydrogel dominated over its viscous nature. This kind of mechanical behavior is a characteristic feature of soft materials such as gels.

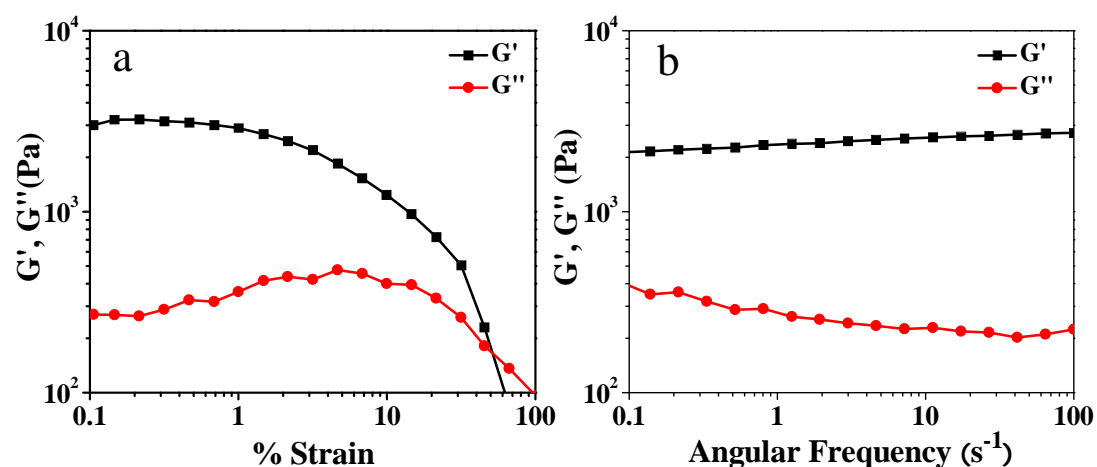


**Figure 5.3.** (a) Amplitude sweep measurement of the Ag-adenine hydrogel at a constant frequency of 10  $rad\ s^{-1}$  and (b) Frequency sweep measurement at a fixed strain of 1%, showing the elastic gel like behavior of the Ag-adenine gel.

Fourier transform infra-red spectroscopy (FTIR) is a major tool in studies related to changes in the functional groups of the ligand upon metallation. Therefore to have an idea on the changes in the functional groups present in adenine upon complexation with  $Ag^+$  ions, FTIR studies of pure adenine and the freeze dried Ag-adenine gel were performed (figure 5.4). From the FTIR spectrum, it was observed that the peaks at  $3310\ cm^{-1}$  and  $3110\ cm^{-1}$  due to  $NH_2$  stretching disappeared and a new

broad peak at  $3440\text{ cm}^{-1}$  was observed due to O-H stretching vibrations, which might have arisen due to the trapped water molecules. Further the peak at  $2790\text{ cm}^{-1}$  due to N-H stretching disappeared in the complex, suggesting the probable involvement of N9 of adenine in metal coordination. Again, the peak at  $1670\text{ cm}^{-1}$  in pure adenine, which is observed due to  $\text{NH}_2$  scissoring, shifted to  $1642\text{ cm}^{-1}$  in the Ag-adenine complex, indicating the probable involvement of  $\text{NH}_2$  in binding to silver ions or in H-bonding. The peak at  $1259\text{ cm}^{-1}$  due to N-H bending in adenine disappeared in the complex, again indicating the involvement of N9 in coordination to  $\text{Ag}^+$  ions.

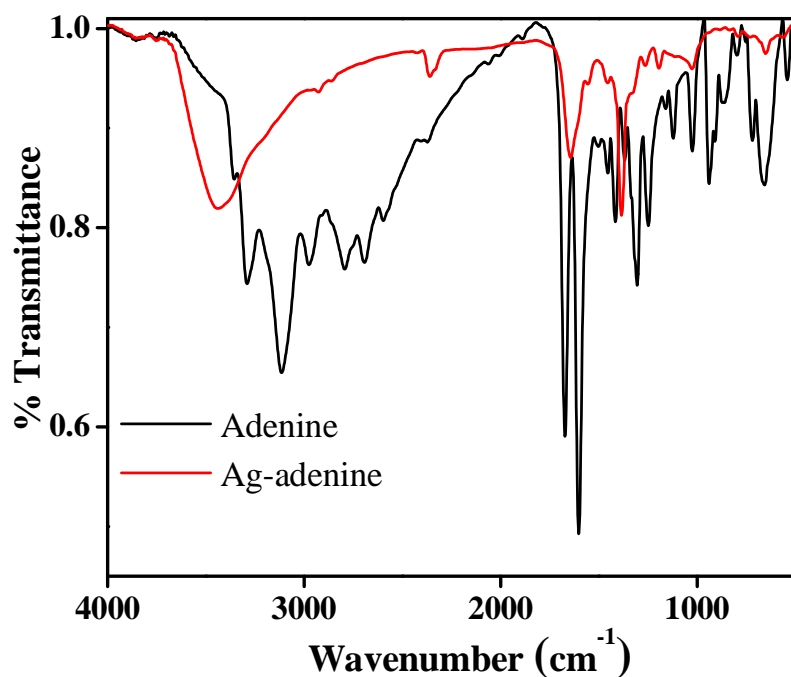


*Figure 5.4. FTIR spectrum of pure adenine and Ag-adenine, showing the changes in adenine upon complexation with Ag.*

### 5.2.2 Synthesis and characterization of Ag-cytosine, Ag-thymine and Ag-uracil hydrogels

Inspired by the successful formation of Ag-adenine hydrogel, we extended the same methodology for the generation of coordination polymer hydrogels with other nucleobases as well. It was observed that similar to the Ag-adenine hydrogel, the simple addition of an aqueous solution of  $\text{Ag}^+$  ions to a basic solution of either of cytosine (C), thymine (T) or uracil (U) resulted in the formation of stable self-standing opaque hydrogel. All the four hydrogels, when diluted in water and observed under electron

microscopes (figure 5.5) revealed the formation of dense entangled three dimensional networks of nanofibers, which were capable of trapping a large volume of water, resulting in the formation of hydrogels.

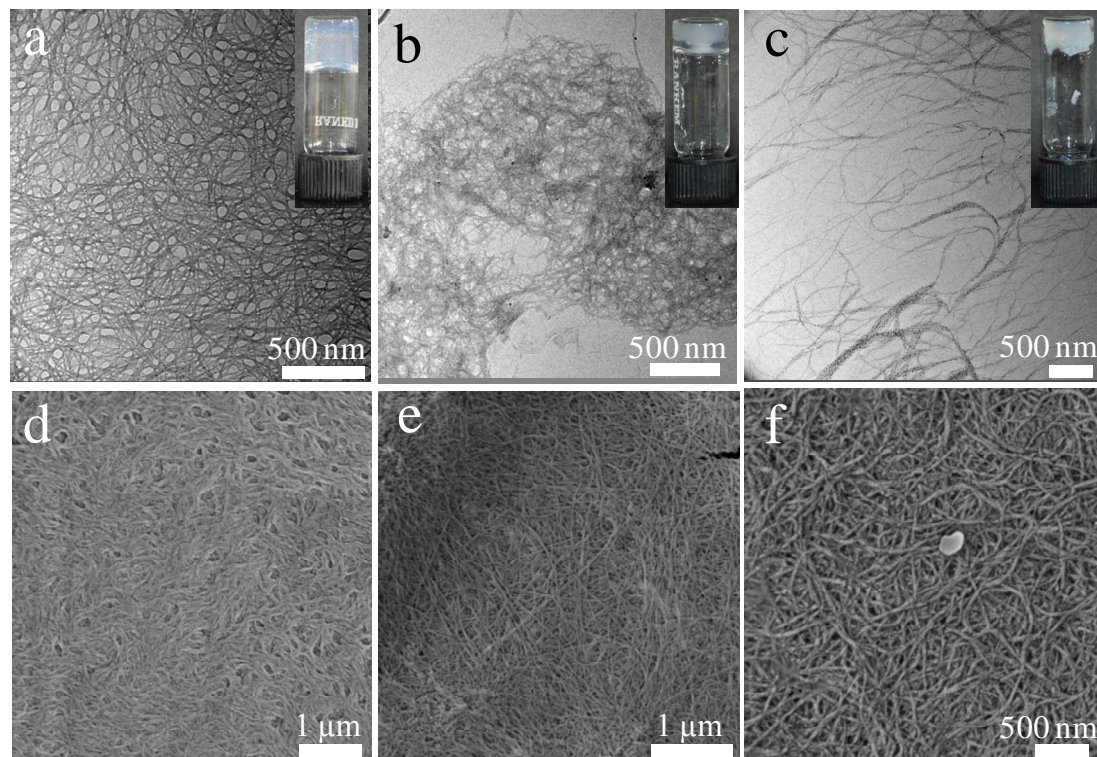


**Figure 5.5.** TEM images of (a) Ag-cytosine, (b) Ag-thymine and (c) Ag-uracil hydrogels; Inset: Digital images of the respective hydrogels. (d), (e) and (f) are the SEM images of the Ag-C, Ag-T and Ag-U metallogels respectively.

The crystalline nature of the nanofibers formed in the three hydrogels was confirmed from the powder XRD studies, which showed several peaks in the  $2\theta$  range of 1-60 degrees (figure 5.6a). For the Ag-T and Ag-U gels well-resolved diffraction peaks with a reflection ratio of 1: 1/2: 1/3: 1/4: 1/5, similar to the Ag-adenine gel were observed, which suggested that the hydrogels were arranged in a layered structure with an interlayer separation of 13.8 Å and 15.4 Å respectively. On the other hand, for the Ag-C hydrogel, although well-resolved diffraction peaks could be seen, such periodic reflections were not observed. Thermal stability of the three xerogels was studied by thermogravimetric analysis. TGA performed on the three freeze dried gels (figure 5.6b) indicated that for the Ag-cytosine and the Ag-thymine gel two weight losses at nearly

240 °C and 330 °C were observed due to the decomposition of the ligands in the complex. On the other hand, for the Ag-uracil gel an initial mass loss of 2.7% in the temperature range of 25 °C to 190 °C was observed, which might be due to the loss of water molecules in the complex. Again two weight losses at 220 °C and 330 °C were observed for the Ag-uracil gel, which might be due to the decomposition of the organic components from the complex.

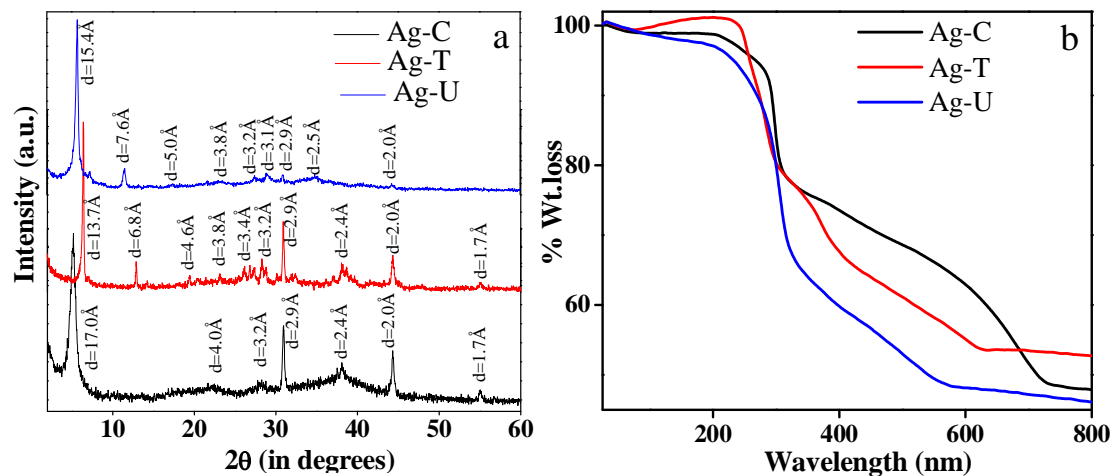


Figure 5.6. (a) Powder XRD pattern and (b) TGA plots of the freeze dried Ag-C, Ag-T and Ag-U gels.

FTIR studies were performed in order to have an idea about the binding of  $\text{Ag}^+$  ions to the nucleobases. In the FTIR spectrum of pure cytosine and the Ag-cytosine complex (figure 5.7a), it was observed that the peaks at  $3380\text{ cm}^{-1}$  and  $3160\text{ cm}^{-1}$  due to  $\text{NH}_2$  stretching vibrations decreased in intensity in the complex, probably due to their involvement in H-bonding. Again the weak peak at  $2780\text{ cm}^{-1}$  due to N-H stretching was absent in the complex, suggesting the involvement of the N1 nitrogen of cytosine in bonding to the  $\text{Ag}^+$  ions. The binding of N1 to silver was further supported by the loss of the peak at  $1270\text{ cm}^{-1}$  due to N-H bending vibrations in the complex.

For the Ag-thymine gel (figure 5.7b), the weak peak at  $2805\text{ cm}^{-1}$  due to N-H stretching in thymine disappeared, suggesting the engagement of the N1 or N3 sites in metal binding. Further, it was observed that the peak at  $1730\text{ cm}^{-1}$  due to C=O stretching vibrations shifted to  $1660\text{ cm}^{-1}$ , suggesting that the oxygen atoms are also involved in binding to  $\text{Ag}^+$  ions or in H-bonding. Again the disappearance of the peak at

1250  $\text{cm}^{-1}$  due to N-H bending was a signature of the binding of  $\text{Ag}^+$  ions to either N1 or N3 position of thymine.

Similarly, for the Ag-uracil gel (figure 5.7c), the peak at 2815  $\text{cm}^{-1}$  in the pure uracil due to N-H stretching disappeared in complex, signifying the binding of metal to either the N1 or N3 site. Also the peak at 1720  $\text{cm}^{-1}$  due to C=O stretching was shifted to 1640  $\text{cm}^{-1}$ , suggesting its probable involvement in binding to  $\text{Ag}^+$  ions. Further, the peak at 1240  $\text{cm}^{-1}$  in pure uracil due to N-H bending was absent in the complex, thus confirming the binding of  $\text{Ag}^+$  ions to the N1 or N3 site of uracil.

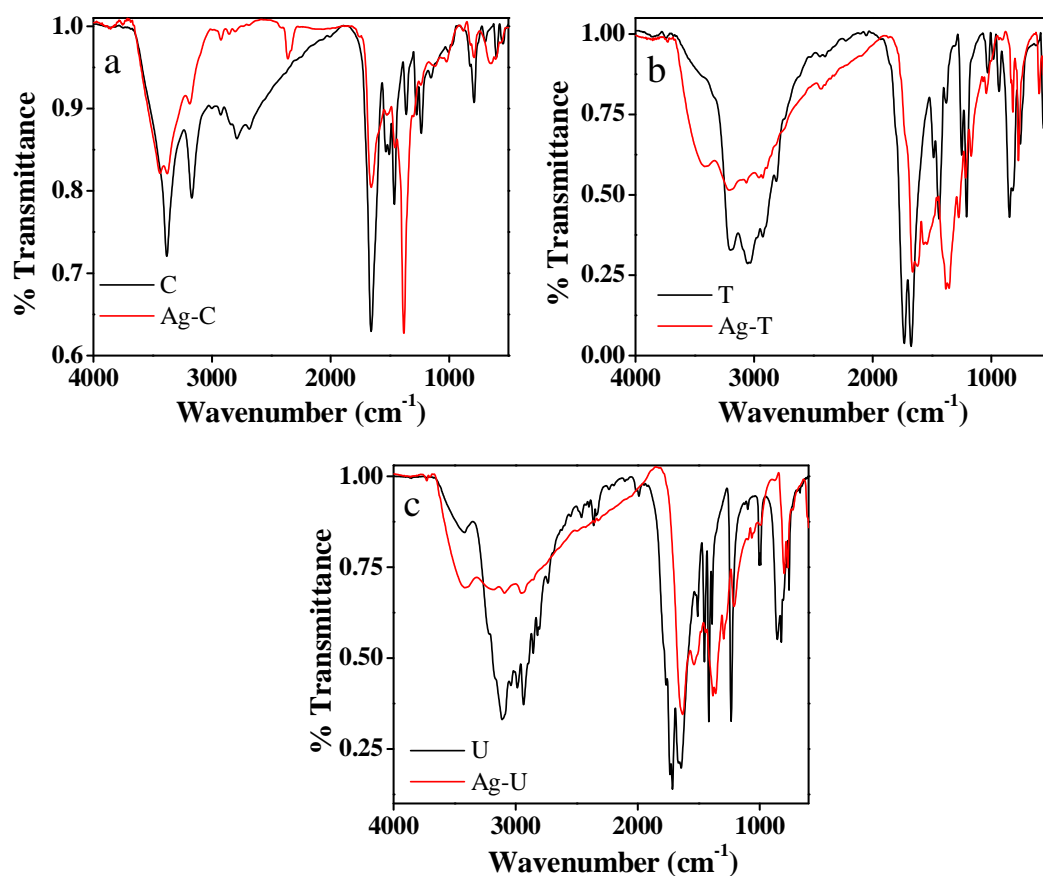


**Figure 5.7.** FTIR spectrum of (a) C and Ag-C, (b) T and Ag-T and (c) U and Ag-U gels respectively.

Rheological investigation performed on the three hydrogels suggested that each of the three materials had solid like elastic properties. Both the strain sweep and the frequency sweep experiments were performed and as shown in figure 5.8, for the Ag-C and Ag-T gel, the value of the elastic storage modulus ( $G'$ ) was greater than the loss modulus ( $G''$ ) by several factors in both the experiments, indicating the elastic behavior

of both the gels. However, in case of Ag-U gel, in the strain sweep experiment, it was observed that  $G'$  dominated over  $G''$  upto a strain of 41%, beyond which the material behaved as a viscous sol, as indicated by the higher values of  $G''$  than that of  $G'$ .

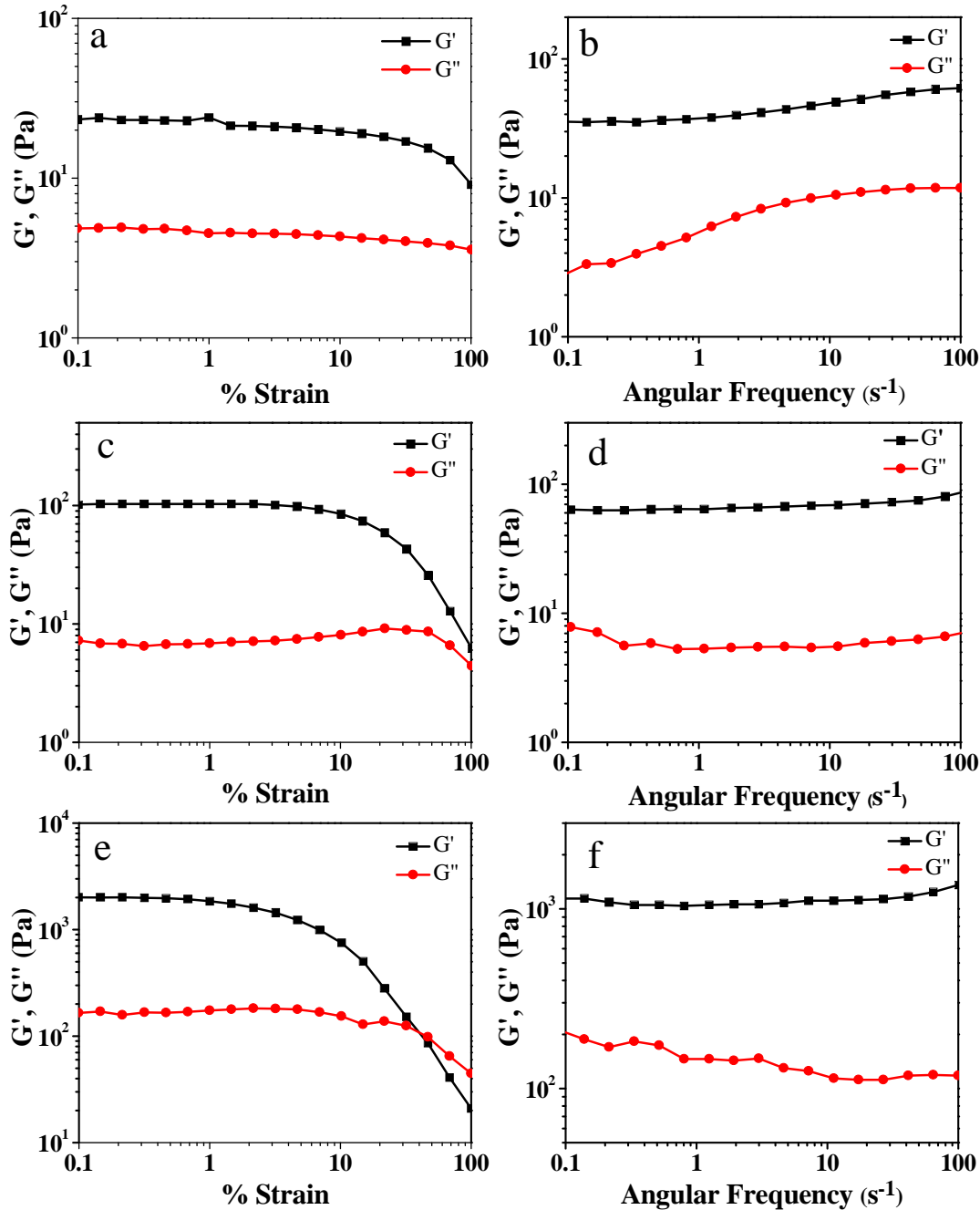


**Figure 5.8.** (a), (c) and (e) Amplitude sweep measurement for the Ag-C, Ag-T and Ag-U gels respectively and (b), (d) and (f) frequency sweep measurement (at a constant strain of 1%) for the Ag-C, Ag-T and Ag-U gels respectively.

### 5.2.3 Interaction of AgNO<sub>3</sub> with guanine in alkaline conditions

The interaction of the four nucleobases adenine, cytosine, thymine and uracil with Ag<sup>+</sup> ions resulted in the formation of hydrogels in alkaline medium. However, under similar conditions, the addition of AgNO<sub>3</sub> to deprotonated solution of guanine (at pH 10.9) resulted in the formation of a white precipitate (Ag-G) and no gel formation was observed. The flow of water from the complex during inverted tube experiment confirmed our observation (figure 5.9a). This result was quite unexpected, because guanine derivatives are known to self-assemble in presence of metal ions forming G-quadruplex and there are several reports of hydrogel formation taking advantage of this incredible self-assembled behavior of guanine using a variety of guanine derivatives.<sup>[42-46]</sup>

The morphology of the precipitate was studied by scanning electron microscope, which revealed the formation of fibrous aggregates that assembled to give a large flower like morphology (figure 5.9b & c). However, the formation of entangled fibrous network primarily responsible for entrapping solvent molecules in hydrogels, were not observed in case of Ag-G composite. Powder X-ray diffraction of the dried Ag-G gel showed crystallinity of the composite with major peaks arising at  $2\theta = 6.0^\circ, 8.2^\circ, 10.4^\circ, 15.2^\circ, 27.7^\circ$  and  $34.1^\circ$  along with several sharp peaks originating from NaNO<sub>3</sub> (figure 5.9d). The most intense peak at  $2\theta = 27.7^\circ$  corresponds to  $d$ -value of  $3.2 \text{ \AA}$ , which is very close to that of  $\pi$ - $\pi$  stacking interactions in guanine based hydrogels.<sup>[43]</sup> From the FTIR spectrum (figure 5.9e), it was observed that the medium intensity, sharp peak at  $2695 \text{ cm}^{-1}$  in case of pure guanine disappeared after addition of Ag<sup>+</sup> ions suggesting the probable involvement of N9 or N1 of guanine in binding to Ag<sup>+</sup>. Again the shoulder peak at  $2990 \text{ cm}^{-1}$  in pure guanine arising due to N-H stretching of amide was absent in the complex, indicating that the N1 position of guanine was engaged in binding to Ag<sup>+</sup>. Further, the peak at  $1698 \text{ cm}^{-1}$  in case of pure guanine due to C=O stretching vibrations shifted to  $1691 \text{ cm}^{-1}$  in the complex, suggesting the probable involvement of oxygen in H-bonding. The involvement of N1 or N9 positions in binding to Ag<sup>+</sup> ions was further supported by the absence of the peak at  $1259 \text{ cm}^{-1}$  due to N-H bending vibrations in the Ag-G complex.

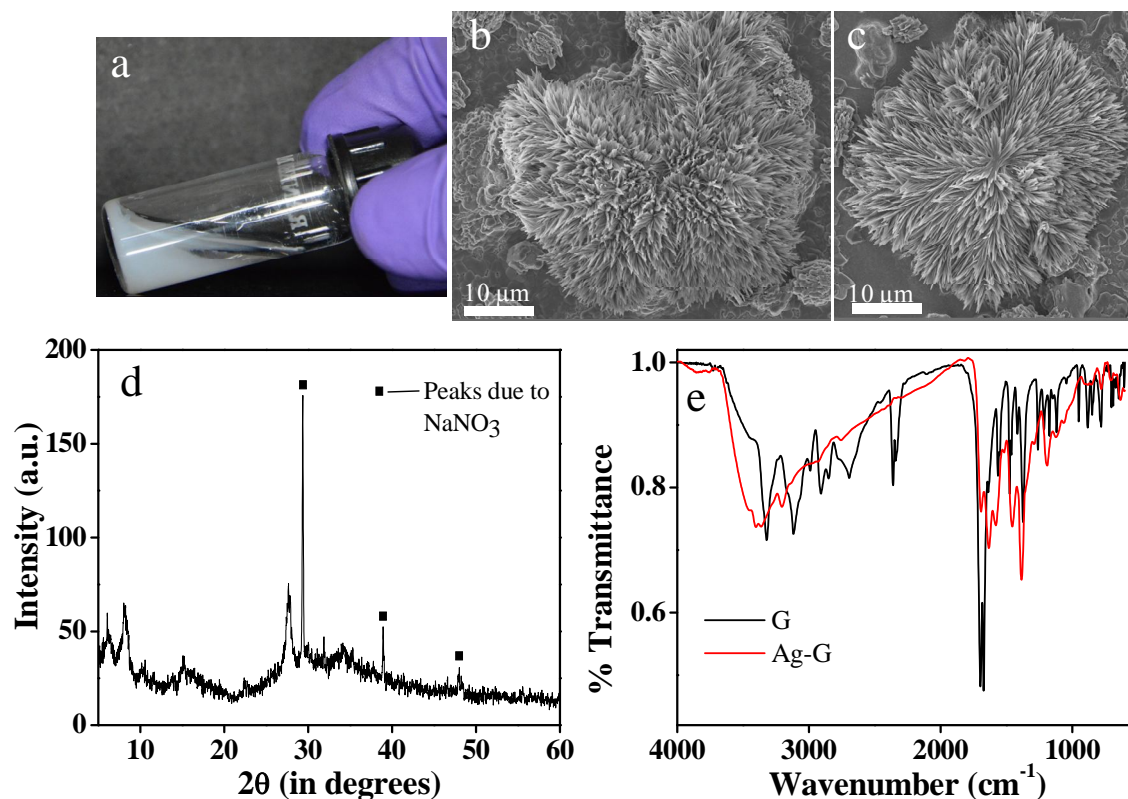


**Figure 5.9.** (a) Digital image, (b) and (c) FESEM images, (d) Powder XRD spectrum of the precipitate formed upon addition of silver ions to alkaline guanine. (e) FTIR spectrum of pure guanine and Ag-guanine precipitate.

#### 5.2.4 Gel formation in a mixture of two or three nucleobases

After our success in the bi-component hydrogel formation through coordination between deprotonated nucleobases (A, C, T, U) as small molecule hydrogelator and Ag<sup>+</sup> as metallic counterpart, the formation of hydrogels in a tri- or tetra-component system was studied involving two or three nucleobases coordination with Ag<sup>+</sup> ions in aqueous alkaline medium. We observed spontaneous hydrogelation in all combinations, except for when guanine was present. The presence of G in a mixture of nucleobases, when mixed with Ag<sup>+</sup>, led to precipitation of the crystalline composite. The formation of hydrogels in all these cases was confirmed by the inverted tube method as well as microscopic studies. The SEM images as shown in figure 5.10 revealed the formation of entangled fibrous network capable of trapping large volume of water, responsible for the formation of gels.

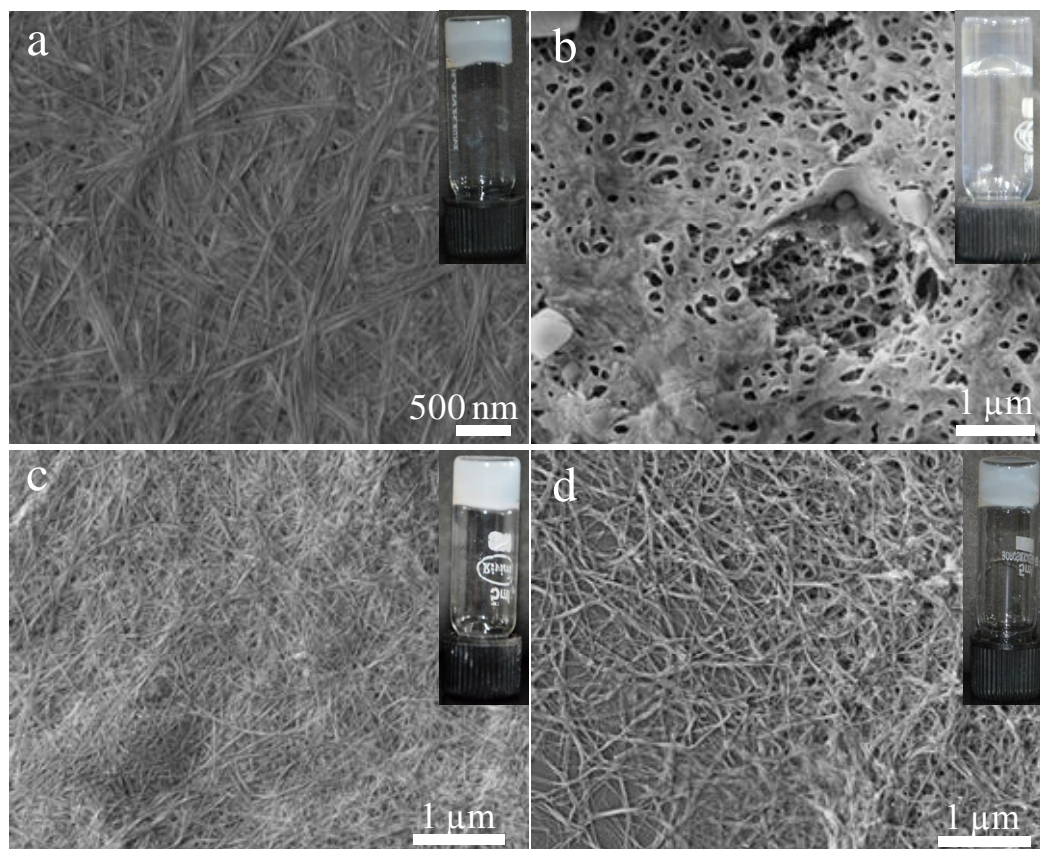


**Figure 5.10.** FESEM images of hydrogels formed by the addition of  $\text{Ag}^+$  ions to a mixture of nucleobases, (a) Ag-adenine-cytosine, (b) Ag-cytosine-thymine, (c) Ag-adenine-cytosine-uracil, (d) Ag-adenine-thymine-uracil.

Rheological studies were performed in order to have an idea of the mechanical stability of the gels formed using mixtures of the nucleobases and  $\text{Ag}^+$  ions. The rheological studies of the hydrogels indicated that the materials had elastic solid like properties. The amplitude sweep measurements for the gels formed from a mixture of two or three nucleobases (figures 5.11a, c & e) suggested an elastic behavior, as indicated by the dominance of the storage modulus  $G'$  over the loss modulus  $G''$  in the entire range of strain from 0.05% to 100%. To further confirm the elastic nature of these hydrogels, frequency sweep experiments were performed. As shown in figures 5.11b, d & f, the value of  $G'$  was significantly higher than that of  $G''$  in the complete frequency range of 0.05-100  $\text{s}^{-1}$  which clearly demonstrated the supremacy of their elastic behavior over the viscous nature.

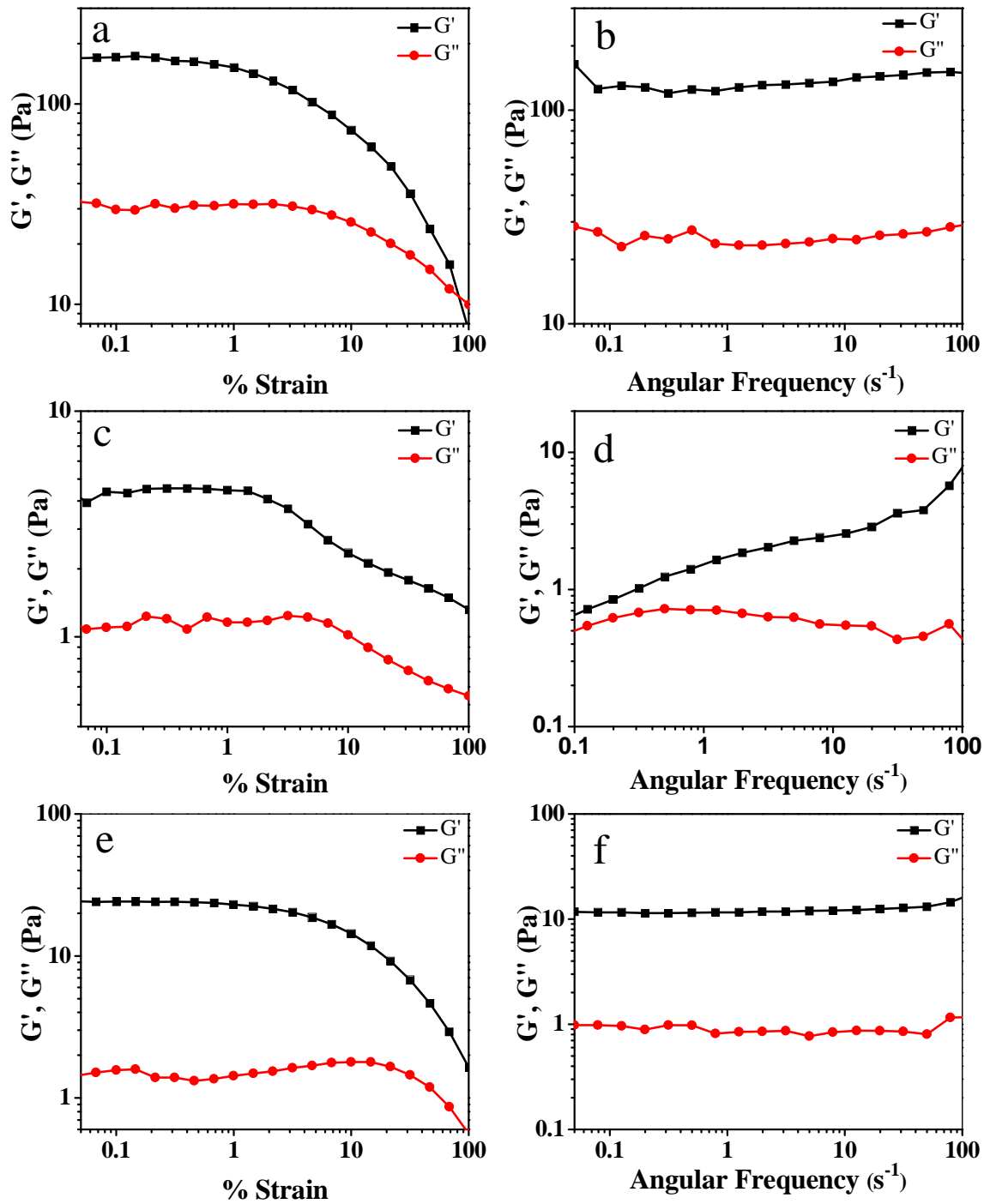


**Figure 5.11.** (a), (c) and (e) Strain sweep rheological experiment of Ag-adenine-cytosine, Ag-cytosine-thymine, and Ag-adenine-thymine-uracil gels respectively and (b), (d) and (f) are the frequency sweep experiment at a constant strain of 1% for Ag-adenine-cytosine, Ag-cytosine-thymine, and Ag-adenine-thymine-uracil gels respectively.

### 5.2.5 Formation of Ag nanoparticles within the gels

The synthesis or incorporation of colloidal metal nanoparticles in a gel matrix has recently gained significance because generating such a system is an attempt to integrate nanoparticles into unconventional environments, with the aim of producing hybrid materials. The coupling of metal nanoparticles with gel matrix is important as such a hybrid system can be used for several technological applications such as sensing, catalysis, biological labeling, antimicrobial agents and drug delivery, to name a few.<sup>[54-58]</sup> The main advantage of using hydrogels as templates for the growth of nanoparticles is that in the swollen stage, the hydrogels provide free space between the networks, which can serve for the nucleation and growth of the nanoparticles.<sup>[59]</sup>

Although the reducing property of nucleobases to convert metal salts into metal nanoparticles have not been reported, it was found that  $\text{Ag}^+$  ions involved in the formation of hydrogels were *in situ* reduced to Ag nanoparticles in Ag-C, Ag-T and Ag-U hydrogels under alkaline conditions. On standing, the formation of Ag nanoparticles was observed within 24 hours (figure 5.12a). Interestingly, the gels were not disrupted during the formation of Ag nanoparticles, which suggested that probably the excess  $\text{Ag}^+$  ions present in the hydrogel matrix were reduced, without disturbing the fibrous network. The formed nanoparticles exhibited their characteristic surface plasmon resonance band, with the peak maxima at 460 nm in case of Ag-T and Ag-U hydrogels and 484 nm in Ag-C, as observed from the solid state UV-visible studies (figure 5.12b). The powder XRD spectrum of the hydrogels shown in figure 5.6a exhibited peaks at  $2\theta$  values of  $38.2^\circ$  and  $44.4^\circ$  corresponding to the (111) and (200) planes of Ag in addition to the other peaks signifying the presence of Ag nanoparticles in the matrix. Transmission electron microscopy was employed to have an idea on the size and shape of the nanoparticles. From the TEM images, small and nearly spherical Ag nanoparticles having an average size of  $4 \pm 1.2$  nm, decorated along the fibers of the hydrogels were observed for all the three cases (figure 5.12c, d & e). Under similar conditions, no nanoparticles were observed in the Ag-adenine gel, as indicated from both the UV-visible studies as well as TEM analysis, which suggested the involvement of carbonyl groups in cytosine, thymine or uracil in the reduction of the metal salt to metal nanoparticles.

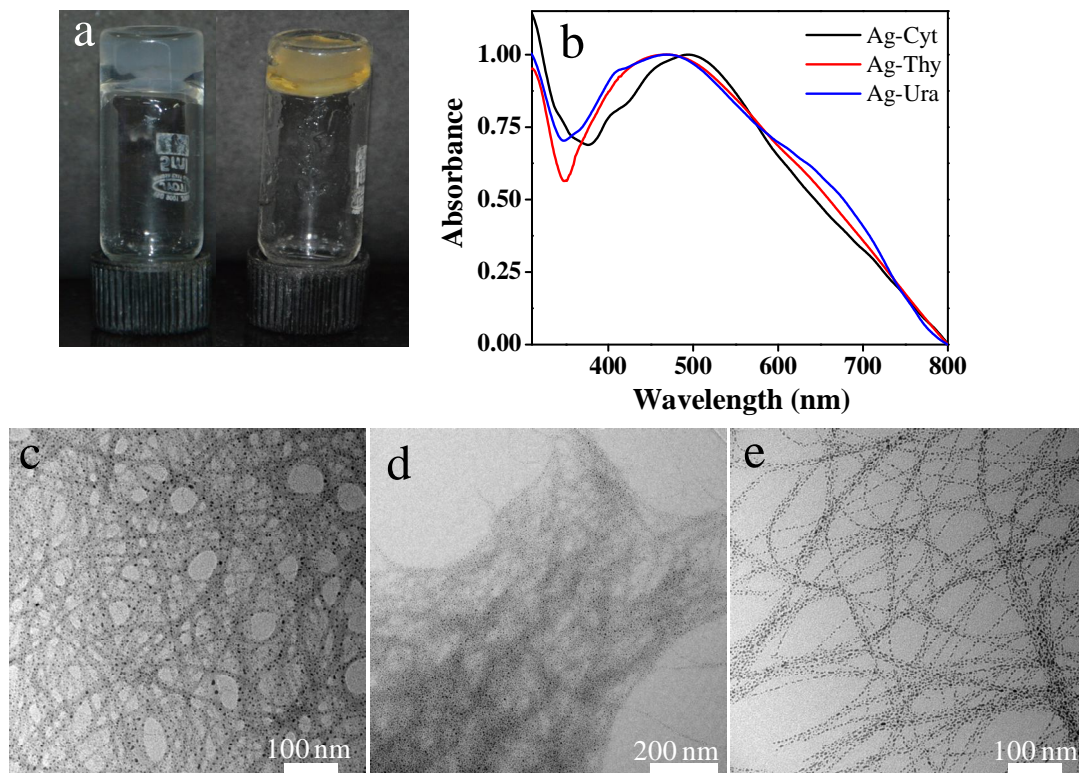
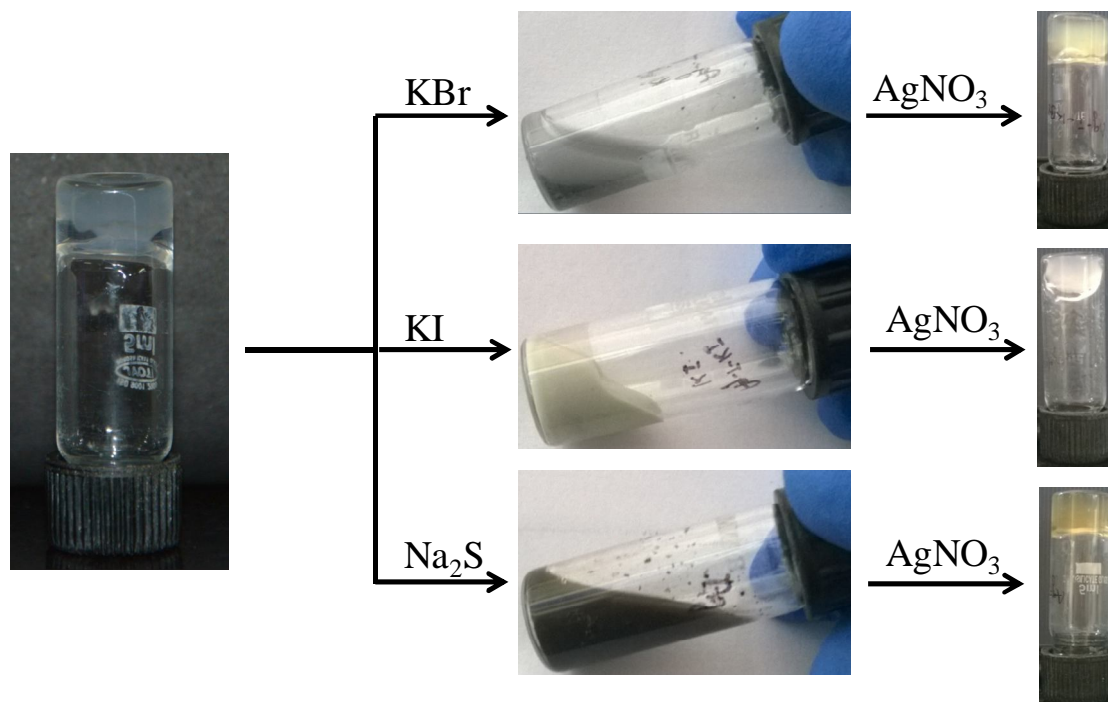


**Figure 5.12.** (a) Digital images of Ag-thymine gel 30 minutes after preparation (white) and 7 days after preparation (yellow), suggesting the formation of Ag nanoparticles in the gel. (b) Solid state UV-visible spectrum of the three hydrogels, showing the SPR band of Ag nanoparticles and (c), (d) and (e) TEM images of the Ag nanoparticles decorated along the fibres of Ag-cytosine, Ag-thymine and Ag-uracil gels respectively.

### 5.2.6 Chemical response of the gels

The physical properties of gels can easily be tuned by using external stimuli such as pH, temperature, mechanically or chemically.<sup>[60-62]</sup> So we tested the anion responsiveness of the four Ag-nucleobase hydrogels. It is well-known that the labile Ag(I) based compounds can be easily manipulated by anions.<sup>[60]</sup> In case of Ag-nucleobase hydrogels, anion tuning could be performed easily and quick chemical response to several anions was observed leading to sol-gel transformations, due to the breaking of the bond of silver with the nucleobases. For example, the addition of aqueous solutions of KBr, KI or Na<sub>2</sub>S to the Ag-thymine gel resulted in the formation of precipitates, in the form of AgBr, AgI or Ag<sub>2</sub>S (scheme 5.2). This implies the breaking of Ag-T coordination bond in presence of halides or sulfides. However, the chemical

reversibility was observed, as removing the precipitates by filtration and addition of  $\text{AgNO}_3$  resulted in the return of the gel state. The higher affinity of silver ions towards these anions resulted in the formation of the precipitates and this led to a decrease in the concentration of silver ions for complexation with nucleobases, which resulted in the ligand being free for coordination. After the filtration of the precipitate, the nucleobase (ligand) can easily coordinate again to the silver ions to form the hydrogels.



**Scheme 5.2.** Schematic illustration of the chemical response of the Ag- nucleobase gels towards different chemicals. All these examples are shown with the Ag-thymine gel.

### 5.2.7 Antimicrobial activity of the hydrogels

Since the ancient times, silver ion has been known to be quite effective against a variety of microorganisms<sup>[63-65]</sup> and has been used to treat a variety of infections such as burn wounds, arthroplasty as well as to prevent bacterial colonization on prostheses, catheters, dental materials etc.<sup>[63]</sup> Recently, a silver containing hydrogel was reported to act as an effective antibacterial material against microorganisms such as *Staphylococcus epidermidis*, *E. Coli*, *Pseudomonas aeruginosa* etc.<sup>[28]</sup> Due to the presence of silver we anticipated our hydrogels to function as efficient antimicrobial agents. The antimicrobial activity of the hydrogels was tested against the gram negative, rod shape

bacteria *Escherichia Coli* (*E. Coli*) and the gram positive bacterium, *Staphylococcus*, using the cylinder-plate or cup-plate method. It was observed that for all the microbes, the hydrogels showed excellent antimicrobial activity that prevented their growth in a particular region, known as zone of inhibition (figure 5.13). As observed from the diameter of the zone of inhibition it was found that the Ag-U gel was the most effective of the four hydrogels, whereas the Ag-adenine hydrogel was the least effective. The average diameter of the zone of inhibition for *E. coli* was about 12, 14, 15 and 18 mm, respectively for the Ag-A, Ag-C, Ag-T and Ag-U gels, when 80  $\mu$ L of the gel was used. On the other hand, the zone of inhibition for *Staphylococcus* was 13, 17, 18 and 21 mm, for the Ag-A, Ag-C, Ag-T and Ag-U gels respectively, when the same amount of gel was used (80  $\mu$ L). The poor activity of the Ag-A gels as compared to the other three gels may be ascribed to the presence of Ag nanoparticles in the other gels, which makes them more effective against these microorganisms.

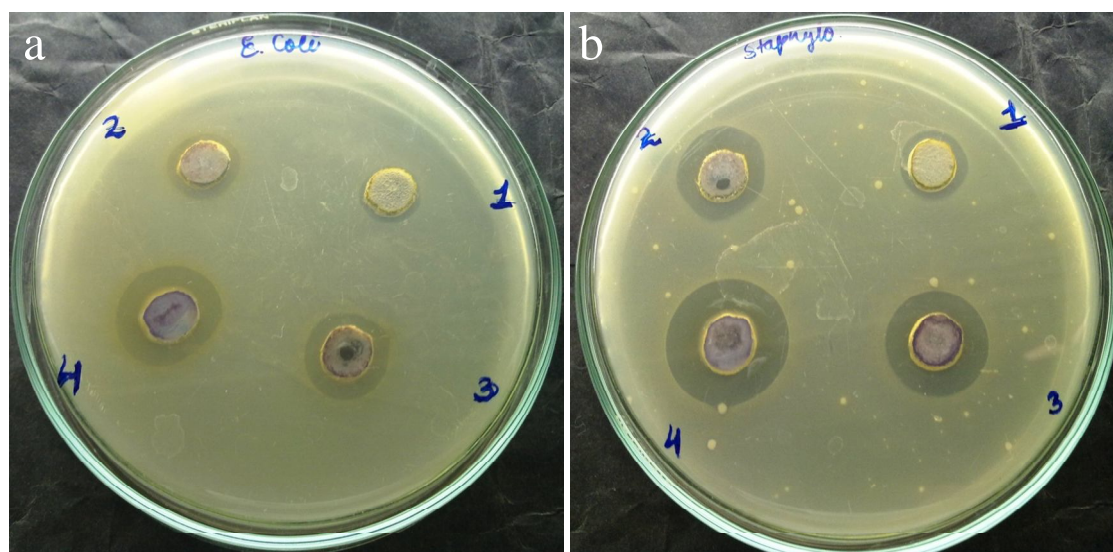


**Figure 5.13.** Antimicrobial activity of the four hydrogels against (a) *E. Coli* and (b) *staphylococcus*; 1- Ag-adenine gel, 2- Ag-cytosine gel, 3-Ag-thymine gel and 4- Ag-uracil gel.

### 5.2.8 Interaction of $\text{Ag}^+$ ions with nucleobases under acidic conditions

The pure nucleobases can be dissolved in aqueous medium not only under basic conditions, but also under acidic conditions. All the five nucleobases were protonated and solubilized by the addition of nitric acid and an aqueous solution of  $\text{AgNO}_3$  was

added. The results were quite interesting and were exactly opposite to that observed under basic conditions. Under acidic conditions the addition of  $\text{Ag}^+$  ions to a solution of adenine resulted in the formation of a white precipitate, whereas with the three pyrimidine bases (cytosine, thymine and uracil), clear solutions were obtained. On the other hand, the addition of silver ions to an acidic solution of guanine resulted in the formation of a self-standing gel.

Initial confirmation on the formation of gels was obtained by inverting the tube containing the material, which did not result in the flow of solution, indicating the formation of a gel like material (inset; figure 5.14a). The morphology of the gel was studied using FESEM. The FESEM images of the gel suggested the formation of hybrid cubic particles having a size of around 200 nm (figures 5.14a & b). It is interesting to note that the coordination of Ag and protonated G did not lead to any fibrous structures, as is commonly observed in gel networks. The rheological studies confirmed the gel like elastic nature of the material. From the strain sweep experiment, it was observed that  $G'$  dominated  $G''$  upto a strain of 68 % (figure 5.14c), indicating that the material behaved as an elastic solid upto a strain of 68 %. Beyond this value of strain, the value of  $G''$  was higher than  $G'$  due to transformation of the material from gel to sol and the material behaved as a viscous sol. The elastic nature of the gel was further established by the frequency sweep experiments, which showed the dominance of  $G'$  over  $G''$  in the complete frequency range (figure 5.14d). The powder XRD spectrum of the lyophilized gel showed a complex pattern of peaks, suggesting the crystalline nature of the particles formed in the gel (figure 5.14e). From the powder XRD spectrum, major intense peaks at  $2\theta = 7.1^\circ$ ,  $14.4^\circ$ ,  $28.3^\circ$ ,  $35.5^\circ$  and  $43.5^\circ$  corresponding to  $d$ - spacing of 12.5 Å, 6.1 Å, 4.1 Å, 3.2 Å and 2.1 Å respectively were observed in addition to several other sharp peaks. These peaks followed a ratio of 1: 1/2: 1/3: 1/4: 1/5, suggesting that the hydrogels were mainly assembled in a layered structure and the interlayer distance was 12.5 Å. Along with these peaks, a broad peak at  $2\theta = 26.7^\circ$  was observed, which corresponded to a  $d$ - value of 3.3 Å, which could be related to the  $\pi$ - $\pi$  stacking interactions between two adjacent guanine molecules.<sup>[43]</sup> Thermogravimetric analysis of the lyophilized gel was performed to study the thermal stability of the gel. From the TGA plot, two weight losses with a total mass loss of 66% in the temperature range of

180-500 °C was observed (figure 5.14f), which could be attributed to the decomposition of the ligands (guanine) in the Ag-G complex.

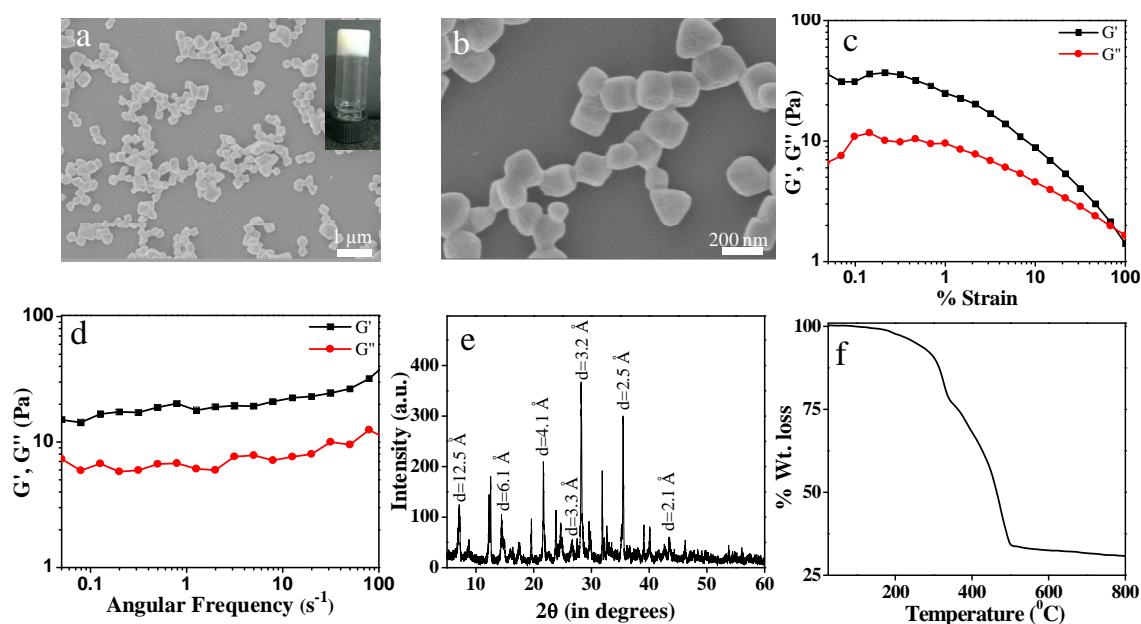


**Figure 5.14.** (a) FESEM image; inset: Digital image, (b) magnified FESEM image, (c) Strain sweep rheological experiment, (d) Frequency sweep rheological experiment, (e) powder XRD pattern and (f) TGA plot for the Ag-guanine gel formed in acidic medium.

### 5.2.9 Density functional theory (DFT) studies

Since the single crystals of the Ag-nucleobase gels could not be obtained and also due to their poor solubility in commonly available solvents, the exact nature of bonding of silver in these materials could not be established. Therefore, to have an idea on the nature of bonding in these materials, density functional theory (DFT) studies were carried out. From the studies, it was concluded that under basic medium, the most acidic hydrogen (with lowest pKa) is abstracted from the nucleobases, as already reported<sup>[66]</sup>. Accordingly, N9-H, N1-H, N1-H, N3-H and N3-H (scheme 5.1) are the most acidic hydrogen for abstraction in basic medium from adenine, guanine, cytosine, uracil and thymine respectively. It is well known that counter anions play a vital role in the formation of polymeric networks such as metallogels. Therefore, we have calculated the binding energy between the silver and nitrate in its pure form and upon binding to nucleobases. It is clear from Table 5.2 that binding energy of silver with nucleobase is

not affected much, when it binds to the nucleobases along with nitrate, indicating that nitrate ions have a negligible influence on the binding of silver to the nucleobases. So, it must be the binding of silver ions to the nucleobases and the hydrogen bonding, which is responsible for the formation of the hydrogels.

System	Adenine		Cytosine		Thymine		Uracil		Guanine	
	Basic	Acidic								
NO <sub>3</sub> Ag---- Nucleo	- 22.45	-15.34	- 24.06	-9.85	- 25.32	-	- 24.99	-	- 23.45	-20.80
Ag--- Nucleo	- 21.47	-	- 23.59	-	- 24.23	-	- 24.66	-	- 24.33	-
NucleoAg-- --NO <sub>3</sub>	- 15.21	-16.53	- 14.74	-15.47	- 14.87	-	- 14.87	-	- 13.35	-14.78
Ag----NO <sub>3</sub> (pure)	-14.19									

**Table 5.2.** Binding energy of (1) silver with nucleobases (first two rows) with and without nitrate, (2) silver with nitrate (last two rows) when bound to nucleobases and the binding energy of pure AgNO<sub>3</sub>.

Based on our DFT calculations, the most stable nucleobase-silver monomeric unit of all the five nucleobases in alkaline medium are shown in figure 5.15. It is evident from the figure that Ag<sup>+</sup> ions binds to adenine, cytosine, thymine and uracil through their most preferred N-atoms (N9 of adenine, N1 of cytosine and N3 of thymine and uracil). The second nitrogen atom of the nucleobases is therefore free to bind to another silver atom, which helps in the formation of polymeric network of the nucleobases. Again, N3, O2, O4 and O4 sites of adenine, cytosine, uracil and thymine respectively remain free for H-bonding with water which further assists in the formation of hydrogel. In contrast, silver is most stable when it is in the bridged position between N7 and O6 sites of guanine. Therefore, second nucleobase unit can bind to the silver only through the bridge position which prevents the formation of polymeric network beyond a dimer, due to the unavailability of any stable binding site of guanine with silver. Again, since the O6 is also involved in bonding to silver ions, so the formation of polymeric network via H-bonding is also not feasible in this case.

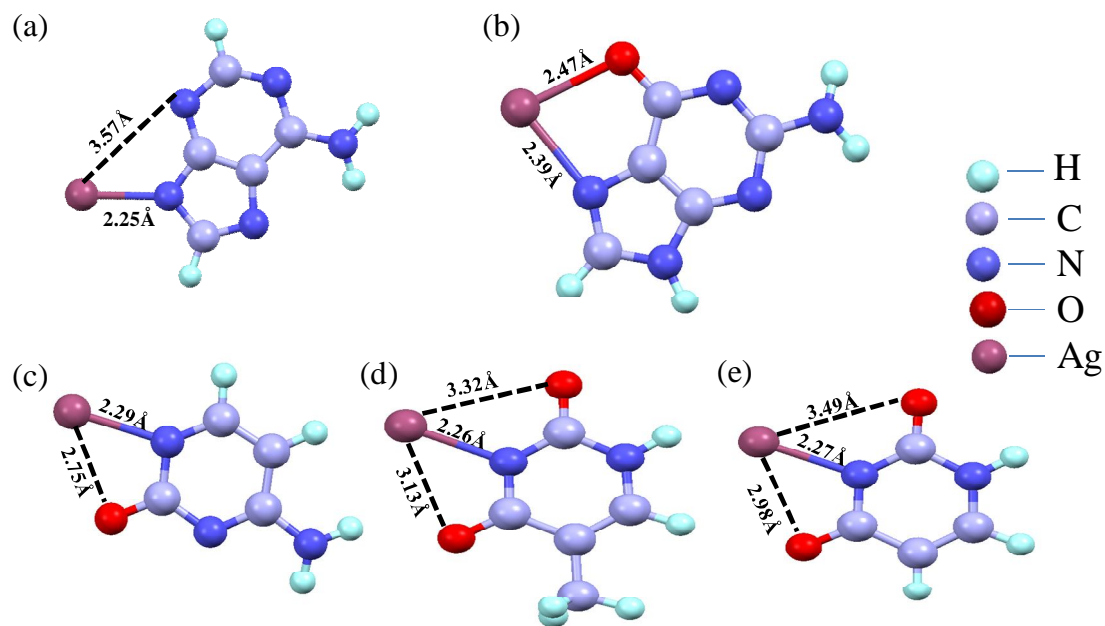


**Figure 5.15.** Optimized structure of silver-nucleobase monomeric unit in basic medium. [(a) Ag-adenine, (b) Ag-guanine (c) Ag-cytosine, (d) Ag-thymine and (e) Ag-uracil hydrogels].

To explore the polymeric nature of these silver-nucleobase units, we have considered two metal-nucleobase units. Different binding sites and different orientations of the second nucleobase-silver unit are considered to bind with the previous unit and the most energetically stable structure is considered as the nucleobase-silver dimeric unit. The most preferred nucleobase-silver dimeric unit for all the nucleobases is shown in figure 5.16. As clearly indicated in the figure, the Ag-guanine complex cannot extend beyond a dimeric unit. On the other hand, all the other four Ag-nucleobase complexes (Ag-A, Ag-C, Ag-T and Ag-U) can be extended further to give polymeric chains and this results in the formation of hydrogels when adenine, cytosine, thymine and uracil are used as ligands and with guanine, the addition of silver ions can only result in the formation of a precipitate. The theoretical calculations were also supported by some experimental evidences. For example, When  $\text{Ag}^+$  ions were added to the nucleoside solutions (in which the N9 of adenine and N1 of cytosine were blocked by the sugar units) under similar conditions, it could not result in the formation of hydrogels, (only precipitate was obtained) clearly suggesting, the importance of these N-atoms for

coordination to  $\text{Ag}^+$  ions leading to the formation of hydrogels. The results were further supported by the FTIR studies.

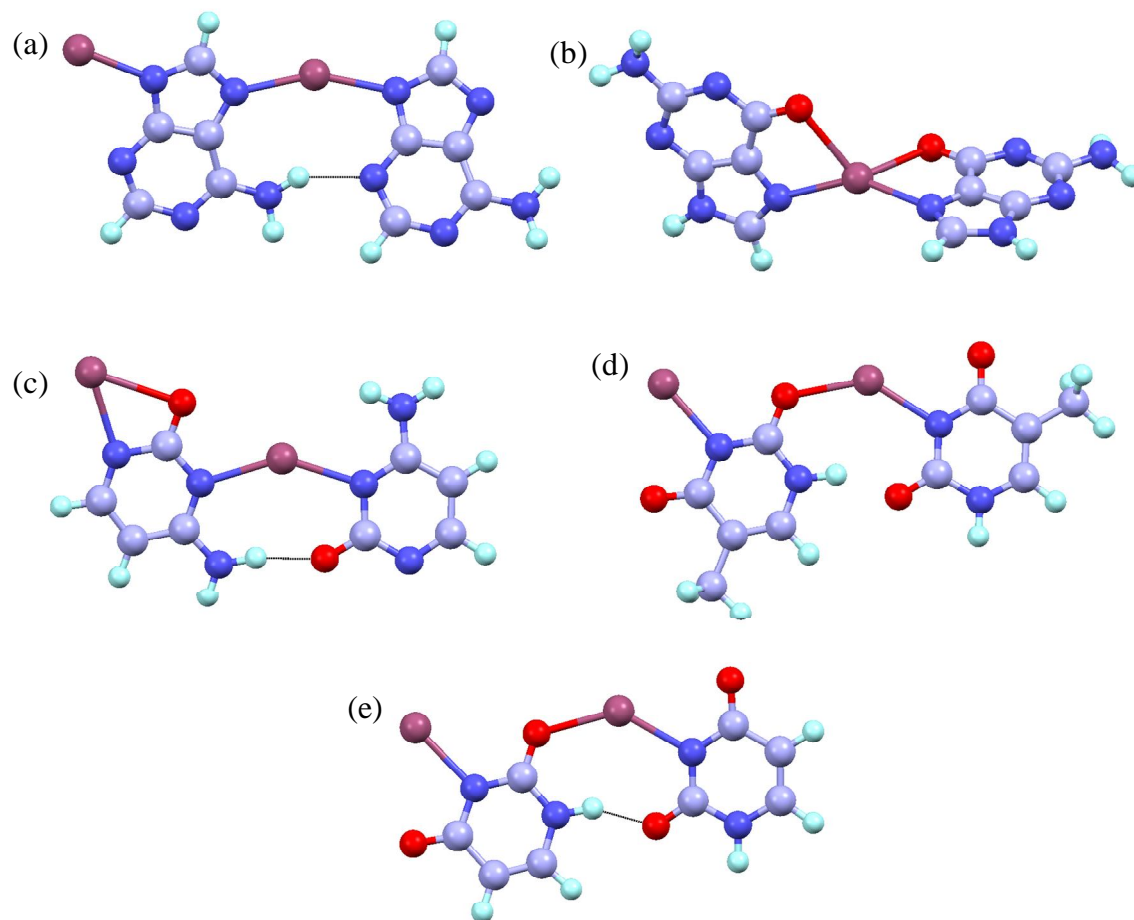


**Figure 5.16.** Optimized structure of silver-nucleobase dimeric unit in basic medium. [(a) Ag-adenine, (b) Ag-guanine (c) Ag-cytosine, (d) Ag-thymine and (e) Ag-uracil hydrogels].

Based on the DFT calculations and experimental studies such as powder XRD and FTIR, we propose the following structure for the Ag-A hydrogel under alkaline conditions (figure 5.17). The polymer chain is extended by the coordination of  $\text{Ag}^+$  ions to adenine units at the N9 and N7 positions. The N1 position of each adenine unit is hydrogen bonded with water molecules. The structure is further stabilized through intermolecular hydrogen bonding between hydrogen of the  $\text{NH}_2$  group in one adenine unit with N3 of another adenine.

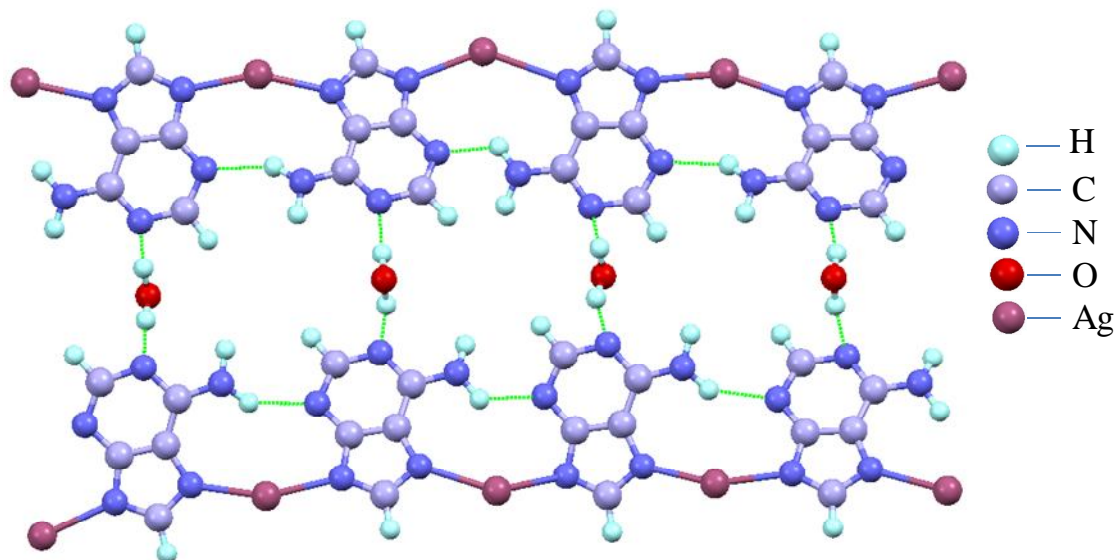


**Figure 5.17.** Proposed structure of the complex formed upon the interaction of  $\text{Ag}^+$  ions to adenine under alkaline conditions.

Under acidic conditions, protonation occurs at that specific site of the nucleobase which shows highest pKa values among all possible sites. Accordingly, N1, N3 and N9 are the most preferred sites for protonation of adenine, guanine and cytosine respectively. Uracil and thymine have extremely low pKa values, suggesting their reluctance to protonation. Literature reports have shown that at acidic pH, the metal counter ions largely facilitate the formation of a crystal upon the interaction of the metal salts with the nucleobases.<sup>[67,68]</sup> The calculated binding energies (Table 5.2) show that nitrate ions bind strongly to the silver when silver is bonded to nucleobase unit which implies that binding of nitrate to the silver atom is the main driving force for the silver-nucleobase bonding. In case of adenine, binding of silver and nitrate is very strong (-16.53 kcal/mol) which suggest that positive charge of silver is compensated by nitrate. This prevents silver to bind to another nucleobase unit for the formation of polymeric chain, resulting in the precipitation of monomeric silver-nucleobase unit. In contrast, binding of silver with guanine is very (-20.80 kcal/mol) strong than the binding of silver and nitrate (-14.78 kcal/mol) in case of guanine. It implies that Ag-guanine binding is more favorable than Ag- $\text{NO}_3$  binding, which helps in the formation of polymeric chain. Besides, O-sites are free for hydrogen bonding with water, helping to the formation of hydrogel. In case of cytosine, silver-nucleobase binding (-9.85 kcal/mol) is not

favorable, since silver-nitrate binding is relatively strong (-15.47 kcal/mol), suggesting its tendency to remain as  $\text{AgNO}_3$ . The theoretical prediction agrees well with experimental results where a clear solution was obtained in case of cytosine which might be due to the  $\text{AgNO}_3$  solution. Due to the significantly lower binding energy of silver and cytosine, thymine or uracil, silver nitrate remained as such, resulting in a clear solution. The optimized structures of silver-nucleobase monomeric units under acidic conditions are shown in figure 5.18.

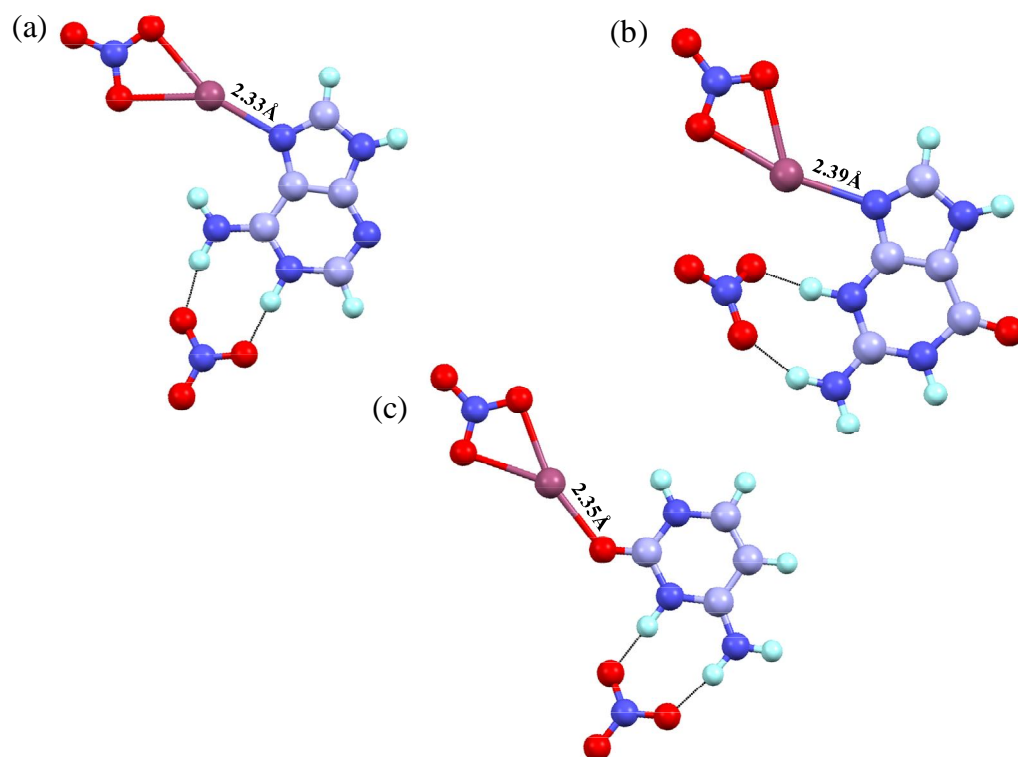


**Figure 5.18.** Optimized structure of silver-nucleobase monomeric unit in acidic medium. [(a) Ag-adenine, (b) Ag-guanine and (c) Ag-cytosine].

To explore the polymeric nature of these silver-nucleobase units in acidic medium, we have considered two metal-nucleobase units. Different binding sites and different orientations of the second nucleobase-silver unit are considered to bind with the previous unit and the energetically most stable structure is considered as the nucleobase-silver dimeric unit. The most preferred nucleobase-silver dimeric unit for the three nucleobases, based on the DFT studies is shown in the figure 5.19.

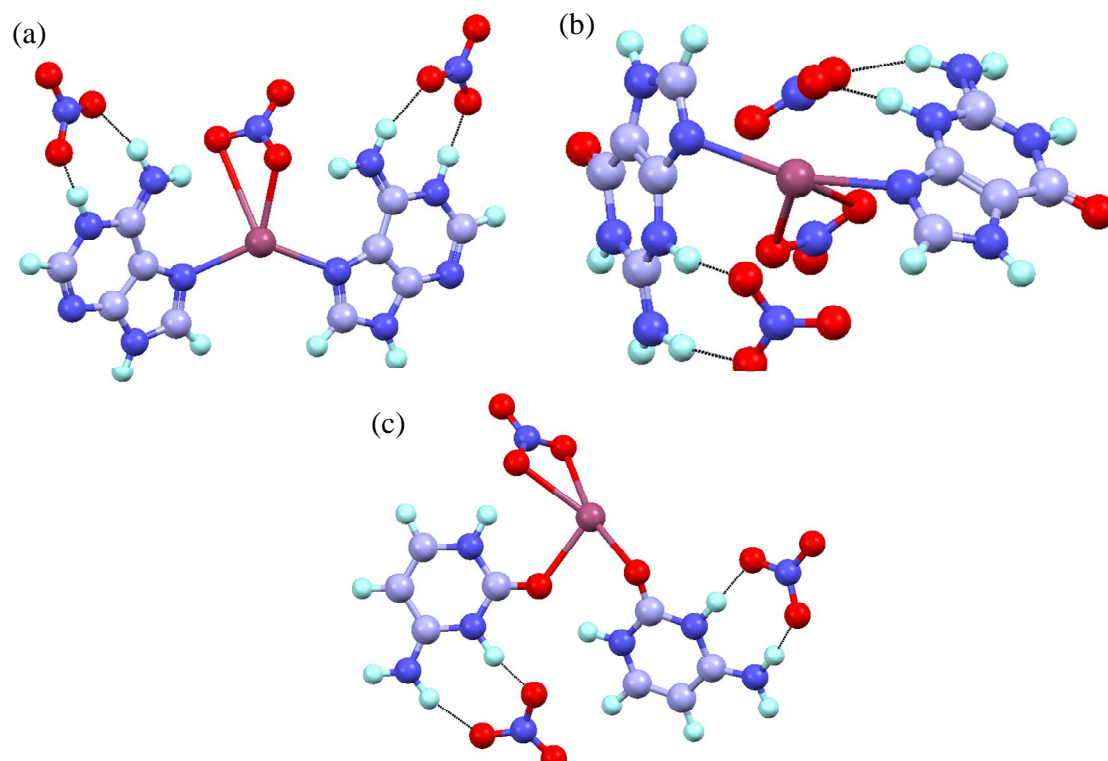


**Figure 5.19.** Optimized structure of silver-nucleobase dimeric unit in acidic medium. [(a) Ag-adenine, (b) Ag-guanine and (c) Ag-cytosine].

### 5.3 Conclusion

In conclusion, we have developed the synthesis of functional metallogels based on the combination of two commercially available and relatively inexpensive components: a silver salt and nucleobase. Our study is the first to establish the ability of pure unsubstituted nucleobases, to act as ligands that can complex with  $\text{Ag}^+$  ions for the generation of functional biocoordination hydrogels. The gelation process takes place rapidly (within a minute) and at room temperature, without the aid of external stimuli such as sonication, heating/cooling. All the nucleobases except guanine, formed stable hydrogels with  $\text{Ag}^+$  ions. The key novelties of our investigation include: (i) the first demonstration of the use of pure nucleobases for the generation of biocoordination polymer hydrogel, (ii) the exploration of nucleobases forming the gel (except adenine) as reducing agents for the synthesis of Ag nanoparticles decorated along the fibers of the gels, (iii) the investigation of gelation ability of two or three nucleobases (mixed ligand) with silver ions, (iv) the demonstration of the antimicrobial activity of these

metallogels against different microbes and (v) the investigation of guanine to form a metallogel with  $\text{Ag}^+$  ions under highly acidic pH, which under alkaline pH forms precipitate with  $\text{Ag}^+$  ions. The results open up newer avenues for the bottom up design of hybrid functional materials utilizing the nucleobases as ligands.

## **5.4 Experimental Section**

### **5.4.1 Materials**

Adenine, guanine, cytosine, thymine, uracil and silver perchlorate were purchased from Aldrich chemicals. Silver nitrate was purchased from S. D. Fine chemicals, India. Silver acetate, sodium hydroxide, potassium bromide, potassium iodide, sodium sulfide and nitric acid were purchased from Merck, India. All the chemicals were of analytical grade and were used without any purification. Milli Q water was used throughout the experiments.

### **5.4.2 Instrumentation**

Transmission electron microscopy (TEM) images were recorded with a Technai G<sup>2</sup> 20 Ultra-Twin microscope at an accelerating voltage of 200 kV. Field emission scanning electron microscopy images were recorded on a Carl Zeiss Supra 55 instrument after coating with gold. Rheological measurements were performed using an Anton Paar Physica MCR 301 rheometer with parallel plate geometry (diameter 50 mm). Powder X-ray diffraction patterns (XRD) of the freeze dried gels were recorded on a Rigaku Smartlab, Automated Multipurpose X-ray diffractometer with Cu K $\alpha$  source (wavelength of X-rays was 0.154 nm). FTIR spectra were recorded in KBr pellet using Bruker Tensor 27 instrument. Thermogravimetric analysis was done using a Mettler Toledo instrument. Solid state UV-visible spectra were recorded on a Perkin Elmer lambda Instrument.

### **5.4.3 Synthesis of Ag-nucleobase hydrogels in basic medium**

Stock solutions of both the nucleobases and  $\text{AgNO}_3$  were first prepared. A stock solution of each nucleobases (0.1 M) was prepared by the addition of solid NaOH to it in small parts under sonication, until the nucleobase was completely

dissolved and a clear solution was obtained. Similarly,  $\text{AgNO}_3$  solution (0.1 M) was prepared by simple dissolution of the metal salt in water.

In a typical synthesis, 0.8 mL of the as prepared nucleobase solution was taken in a tube and to it 1 mL of the  $\text{AgNO}_3$  solution was added, which resulted in the formation of self standing hydrogels.

#### **5.4.4 Synthesis of Ag-guanine gel in acidic medium**

Initially stock solution of guanine (0.1M) was prepared by dissolving the required amount of guanine in water- $\text{HNO}_3$  mixture. In a typical synthesis, 1.0 mL of  $\text{AgNO}_3$  was added to the acidic guanine solution, which resulted in the formation of a hydrogel within a few minutes.

#### **5.4.5 Electron microscopy studies**

The samples for both TEM and FESEM were prepared by diluting the gel samples in water. A small amount of the gel was taken in an eppendorf tube and after addition of water the gel was crushed using a micropestle and was drop casted on a carbon coated copper grid (for TEM) and glass slides (for FESEM), followed by room temperature drying.

#### **5.4.6 Rheological studies**

Rheological investigations were performed using parallel plate geometry of diameter 50 mm. For the measurements, both the hydrogels were first prepared, and then a piece of the gel was placed on the plate of the rheometer using a microspatula. The temperature was maintained at 25 °C using an integrated temperature controller from Julabo. Dynamic strain sweep experiments were performed using a constant frequency of 10  $\text{rad s}^{-1}$ . The dynamic frequency sweep of the hydrogels was measured as function of frequency in the range of 0.05-100  $\text{rad s}^{-1}$  with constant strain value 1%.

#### **5.4.7 Study of response of gels towards different anions**

The chemical response of the Ag-nucleobase hydrogels was studied by using the Ag-thymine gel as the model gel. The gel was first prepared by adding

0.75 mL of AgNO<sub>3</sub> (0.2 M) to 0.6 mL of alkaline thymine (0.2 M). To the gels taken in different tubes, 0.15 mL of 1.0 M KBr, KI and Na<sub>2</sub>S was added and allowed to stand for 12 hours, upon which the gel was converted to sol with precipitates. The precipitate was then removed by centrifugation and to the supernatant 0.75 mL of AgNO<sub>3</sub> (0.1 M) was again added, which resulted in the reformation of the gel.

#### 5.4.8 Antimicrobial studies

The antimicrobial activity of the hydrogels was studied using the cup plate method. Initially, both the gram negative *E. Coli* and the gram positive staphylococcus were cultured in the nutrient broth by incubation at 37 °C for 24 hours. Then nutrient media was prepared and inoculated with 1 ml of suitable suspension of the bacteria which was then poured in a petri dish and allowed to cool to room temperature, upon which the agar solidified. Four holes were cut in the agar by means of a 10 mm cork borer in which the gels to be tested were filled. The petri dish was then incubated at 37 °C for 24 hours, and the zone of inhibition was measured.

#### 5.4.9 DFT Calculations

DFT calculations were performed using M06-2X level of theory as implemented in Gaussian 09 program. This functional is considered for our calculations as the dispersion interaction is more accurately defined for non-bonded interactions. We have used 6-311++G\*\* basis set for the main group atoms and DGDZVP for the silver atom. The effects of the water hydration on the structures and relative energy of complexes were taken into account by means of the polarizable continuum model (PCM). The gas phase structures were reoptimized within the PCM. Binding energies are calculated as the difference between the electronic energy of the complexes and the respective monomers, i.e.

$$\Delta E = E_{N-Ag} - (E_N + E_{Ag}),$$

Where  $E_{N-Ag}$  is the total energy of the nucleobase-silver complex,  $E_N$  and  $E_{Ag}$  are the energies of the nucleobases and silver ion respectively.

---

## 5.5 References

1. Oh M., Mirkin C. A. (2005), Chemically tailorable colloidal particles from infinite coordination polymers, *Nature*, 438, 651-654 (DOI: 10.1038/nature04191).
2. Sun X., Dong S., Wang E. (2005), Coordination-induced formation of submicrometer-scale, monodisperse, spherical colloids of organic–inorganic hybrid materials at room temperature, *J. Am. Chem. Soc.*, 127, 13102-13103 (DOI: 10.1021/ja0534809)
3. Spokoyny K. M., Kim D., Sumrein A., Mirkin C. A. (2009), Infinite coordination polymer nano- and microparticle structures, *Chem. Soc. Rev.*, 38, 1218-1227 (DOI: 10.1039/B807085G).
4. Carnaé A., Carbonell C., Imaz I., MasPOCH D. (2011), Nanoscale metal–organic materials, *Chem. Soc. Rev.*, 40, 291-305 (DOI: 10.1039/C0CS00042).
5. Oh M., Mirkin C. A. (2006), Ion exchange as a way of controlling the chemical compositions of nano- and microparticles made from infinite coordination polymers, *Angew. Chem. Int. Ed.*, 45, 5492-5494 (DOI: 10.1002/anie.200601918).
6. Taylor K. M. L., Rieter W. J., Lin W. (2008), Manganese-Based Nanoscale Metal-Organic Frameworks for Magnetic resonance imaging, *J. Am. Chem. Soc.*, 130, 14358-14359 (DOI: 10.1021/ja803777x).
7. Wei H., Li B., Du Y., Dong S., Wang E. (2007), Nucleobase–metal hybrid materials: Preparation of submicrometer- scale, spherical colloidal particles of adenine–gold(III) via a supramolecular hierarchical self-assembly approach, *Chem. Mater.*, 19, 2987-2993 (DOI: 10.1021/cm070028a).
8. Jung S., Oh M. (2008), Monitoring shape transformation from nanowires to nanocubes and size-controlled formation of coordination polymer particles, *Angew. Chem. Int. Ed.*, 47, 2049-2051 (DOI: 10.1002/anie.200704209).

9. He C., Liu D., Lin W. (2015), Nanomedicine applications of hybrid nanomaterials built from metal–ligand coordination bonds: Nanoscale metal–organic frameworks and nanoscale coordination polymers, *Chem. Rev.*, 115,11079-11108 (DOI: 10.1021/acs.chemrev.5b00125).
10. Rieter W. J., Taylor K. M. L., Lin W. (2007), Surface modification and functionalization of nanoscale metal-organic frameworks for controlled release and luminescence sensing, *J. Am. Chem. Soc.*, 129, 9852-9852 (DOI: 10.1021/ja073506r).
11. Imaz I., Rubio-Martínez M., Garcia-Fernández L., Garcia F., Ruiz-Molina D., Hernando J., Puentes V., Maspoch D. (2010), Coordination polymer particles as potential drug delivery systems, *Chem. Commun.*, 46, 4737-4739 (DOI: 10.1039/C003084H).
12. Lee H. J., We J., Kim J. O., Kim D., Cha W., Lee E., Sohn J., Oh M. (2015), Morphological and structural evolutions of metal–organic framework particles from amorphous spheres to crystalline hexagonal rods, *Angew. Chem. Int. Ed.*, 54, 10564-10568 (DOI: 10.1002/anie.201504873).
13. Cho W., Lee H. J., Oh M. (2008), Growth-controlled formation of porous coordination polymer particles, *J. Am. Chem. Soc.*, 130, 16943-16946 (DOI: 10.1021/ja8039794).
14. Tam A. Y. –Y., Yam W. –W. (2013), Recent advances in metallogels, *Chem. Soc. Rev.*, 42, 1540-1567 (DOI: 10.1039/C2CS35354G).
15. Saha S., Schön E. –M. Cativiela C., Díaz Díaz D., Banerjee R. (2013), Proton-conducting supramolecular metallogels from the lowest molecular weight assembler ligand: A quote for simplicity, *Chem. Eur. J.*, 19, 9562-9568 (DOI: 10.1002/chem.201204542).
16. Imaz I., Rubio-Martínez M., Saletta W. J., Amabilino D. B., Maspoch D. (2009), Amino acid based metal-organic nanofibers, *J. Am. Chem. Soc.*, 131, 18222-18223 (DOI: 10.1021/ja908721t).
17. Bairi P., Roy B., Nandi A. K. (2011), pH and anion sensitive silver(I) coordinated melamine hydrogel with dye absorbing properties:

- metastability at low melamine concentration, *J. Mater. Chem.*, 21, 11747-11749 (DOI: 10.1039/c1jm11994j).
18. Shen J. -S., Mao G. -J., Zhou Y. -H., Jiang Y. -B., Zhang H. -W. (2010), A ligand-chirality controlled supramolecular hydrogel, *Dalton Trans.*, 39, 7054-7058 (DOI: 10.1039/c0dt00364f).
19. Banerjee S., Kandanelli R., Bhowmick S., Maitra U. (2011), Self-organization of multiple components in a steroidal hydrogel matrix: Design, construction and studies on novel tunable luminescent gels and xerogels, *Soft. Matter.*, 7, 8207-8215 (DOI: 10.1039/c1sm05672g).
20. Seo J. S., Whang D., Lee H., Jun S. I., Oh J., Jeon Y. J., Kim K. (2000), A homochiral metal-organic porous material for enantioselective separation and catalysis, *Nature*, 404, 982-986 (DOI: 10.1038/35010088).
21. Liu Y. -R., He L., Zhang J., Wang X., Su S. -Y. (2009), Evolution of spherical assemblies to fibrous networked Pd(II) metallogels from a pyridine-based Tripodal ligand and their catalytic property, *Chem. Mater.*, 21, 557-563 (DOI: 10.1021/cm802841r).
22. Xing B., Choi M. -F., Xu B. (2002), Design of coordination polymer gels as stable catalytic systems, *Chem. Eur. J.*, 8, 5028-5032 (DOI: 10.1002/1521-3765(20021104)8:21<5028::AID-CHEM5028>3.0.CO;2-1).
23. Bhattacharya S., Sengupta S., Bala S., Goswami A., Ganguli S., Mondal R. (2014), Pyrazole-based metallogels showing an unprecedented colorimetric ammonia gas sensing through gel-to-gel transformation with a rare event of time-dependent morphology transformation, *Cryst. Growth. Des.*, 14, 2366-2374 (DOI: 10.1021/cg5000827).
24. Sarkar S., Dutta S., Chakraborti S., Bairi P., Pal T. (2014), Redox-switchable copper(I) metallogel: a metal-organic material for selective and naked-eye sensing of picric acid, *ACS Appl. Mater. Interfaces.*, 14, 6308-6316 (DOI: 10.1021/am501491u).

- 
25. Evans O. R., Lin W. (2002), Crystal engineering of NLO materials based on metal-organic coordination networks, *Acc. Chem. Res.*, 35, 511-522 (DOI: 10.1021/ar0001012).
  26. Chen P., Li Q., Grindy S., Andersen N. –H. (2015), White-light-emitting lanthanide metallogels with tunable luminescence and reversible stimuli-responsive properties, *J. Am. Chem. Soc.*, 137, 11590-11593 (DOI: 10.1021/jacs.5b07394).
  27. Imaz I., Rubio-Martínez M., An J., Solé-Font I., Rosi N. L., Maspoch D. (2011), Metal–biomolecule frameworks (MBioFs), *Chem Commun.* 47, 7287-7302 (DOI: 10.1039/c1cc11202c).
  28. Liu Y., Ma W., Liu W., Li C., Liu Y., Xiang X., Tang Z. (2011), Silver(I)–glutathione biocoordination polymer hydrogel: effective antibacterial activity and improved cytocompatibility, *J. Mater. Chem.*, 21, 19214-19218 (DOI: 10.1039/c1jm13693c).
  29. Manton A., Massüger L., Rabu P., Palivan C., McCusker L. B., Taubert A. (2008), Metal-peptide frameworks (MPFs): “Bioinspired” metal organic frameworks, *J. Am. Chem. Soc.*, 130, 2517-2526 (DOI: 10.1021/ja0762588).
  30. Joshi S. A., Kulkarni N. D. (2009), A new trinuclear Cu(II) complex of inositol as a hydrogelator, *Chem. Commun.*, 2341-2343 (DOI: 10.1039/b821283j).
  31. Sigel H. (1993), Interactions of metal ions with nucleotides and nucleic acids and their constituents, *Chem. Soc. Rev.*, 22, 255-267 (DOI: 10.1039/CS9932200255).
  32. Chifotides H. T., Dunbar K. R. (2005), Interactions of metal–metal-bonded antitumor active complexes with DNA fragments and DNA, *Acc. Chem. Res.*, 38, 146-156 (DOI: 10.1021/ar0302078).
  33. Pizarro A. M., Sadler P. J. (2009), Unusual DNA binding modes for metal anticancer complexes, *Biochimie*, 98, 1191-1211 (DOI: 10.1016/j.biochi.2009.03.017).

- 
34. Bruijninx P. C. A., Sadler P. J. (2008), New trends for metal complexes with anticancer activity, *Curr. Opin. Chem. Biol.*, 12, 197-206 (DOI: 10.1016/j.cbpa.2007.11.013).
  35. Sivakova S., Rowan S. J. (2005), Nucleobases as supramolecular motifs, *Chem. Soc. Rev.*, 34, 9-21 (DOI: 10.1039/B304608G).
  36. An J., Shade C. M., Changelis-Czegán D. A., Petoud S., Rosi N. L. (2011), Zinc-adeninate metal–organic framework for aqueous encapsulation and sensitization of near-infrared and visible emitting lanthanide cations, *J. Am. Chem. Soc.*, 133, 1220-1223 (DOI: 10.1021/ja109103t).
  37. An J., Farha O. K., Hupp J. T., Pohl E., Yeh J. I. Rosi N. L. (2012), Metal-adeninate vertices for the construction of an exceptionally porous metal-organic framework. *Nat. Commun.* 3:604 (DOI: 10.1038/ncomms1618).
  38. An J., Geib S. J., Rosi N. L. (2010), High and selective CO<sub>2</sub> uptake in a cobalt adeninate metal–organic framework exhibiting pyrimidine- and amino-decorated pores, *J. Am. Chem. Soc.*, 132, 38-39 (DOI: 10.1021/ja909169x).
  39. Verma S., Mishra A. K., Kumar J. (2010), The many facets of adenine: Coordination, crystal patterns, and catalysis, *Acc. Chem. Res.*, 43, 79-91 (DOI: 10.1021/ar9001334).
  40. Purohit C. S., Verma S. (2006), A luminescent silver–adenine metallamacrocyclic quartet, *J. Am. Chem. Soc.*, 128, 400-401 (DOI: 10.1021/ja056452z).
  41. Purohit C. S., Verma S. (2007), Patterned deposition of a mixed-coordination adenine–silver helicate, containing a  $\pi$ -stacked metallacycle, on a graphite surface, *J. Am. Chem. Soc.*, 129, 3488-3489 (DOI: 10.1021/ja068892b).
  42. Sreenivasachary N., Lehn J. –M. (2005), Gelation-driven component selection in the generation of constitutional dynamic hydrogels based on guanine-quartet formation, *Proc. Natl. Acad. Sci. USA*, 102, 5938-5943 (DOI: 10.1073/pnas.0501663102).

- 
43. Das R. N., Kumar Y. P., Pagoti S., Patil A. J., Dash J. (2012), Diffusion and birefringence of bioactive dyes in a supramolecular guanosine hydrogel, *Chem. Eur. J.*, 18, 6008-6014 (DOI: 10.1002/chem.201103814).
44. Davis J. T. (2004), G-quartets 40 years later: From 5'-GMP to molecular biology and supramolecular chemistry, *Angew. Chem. Int. Ed.*, 43, 668-698 (DOI: 10.1002/anie.200300589).
45. Li Z., Buerkle L. E., Orseno M. R., Streletzky K. A., Seifert S., Jamieson A. M., Rowan S. J. (2010), Structure and gelation mechanism of tunable guanosine-based supramolecular hydrogels, *Langmuir*, 26, 10093-10101 (DOI: 10.1021/la100211y).
46. Dash J., Patil A. J., Das R. N., Dowdall F. N., Mann S. (2011), Supramolecular hydrogels derived from silver ion-mediated self-assembly of 5'-guanosine monophosphate, *Soft Matter*, 7, 8120-8126 (DOI: 10.1039/C1SM05839H).
47. Amo-Ochoa P., Miguel P. J. S., Lax P., Alonso I., Roitzsch M., Zamora F., Lippert B. (2005), Models of putative (AH)G(AH)G nucleobase quartets, *Angew. Chem, Int. Ed.*, 44, 5670-5674 (DOI: 10.1002/anie.200500896).
48. Knobloch B., Siegel R. K. O., Lippert B., Sigel H. (2004), Two metal ions coordinated to a purine residue tolerate each other well, *Angew. Chem, Int. Ed.*, 43, 3793-3795 (DOI: 10.1002/anie.200453987).
49. Shen W. -J., Lippert B. (2008), Cyclic, trinuclear Pd<sup>II</sup> complex of cytidine with pronounced double cone structure, *J. Inorg. Biochem.*, 102, 1134-1140 (DOI: 10.1016/j.jinorgbio.2007.12.024).
50. Zhong J. -L., Xia X. -J., Liu H. -J., Luo X. -Z., Hong S. -G., Zhang N., Huang J. -B. (2016), Self-assembled metallo gels formed from *N,N',N''*-tris(4-pyridyl)trimesic amide in aqueous solution induced by Fe(III)/Fe(II) ions, *Soft Matter.*, 12,191-199 (DOI 10.1039/C5SM01513H).
51. Liu Z. -X., Feng Y., Zhao Z. -Y., Yan Z. -C., He Y. -M., Luo X. -J., Liu C. -Y., Fan Q. -H. (2014), A new class of dendritic metallo gels with multiple stimuli-responsiveness and as templates for the in situ synthesis
-

- of silver nanoparticles, *Chem. Eur. J.*, 20, 533-541 (DOI: 10.1002/chem.201302780).
52. Pipenbrock M. –O. M., Clarke N., Steed J. W. (2009), Metal ion and anion-based “tuning” of a supramolecular metallogel, *Langmuir*, 25, 8451-8456 (DOI: 10.1021/la900145n).
53. Amacher A. M. *et al.* (2006), Coordination-directed self-assembly of a simple benzothiadiazole-fused tetrathiafulvalene to low-bandgap metallogels, *Chem. Commun.*, 51, 15063-15066 (DOI: 10.1039/C5CC06819C).
54. Thoniyot P., Tan M. J., Karim A. A., Young D. J., Loh X. J. (2015), Nanoparticle–hydrogel composites: Concept, design, and applications of these promising, multi-functional materials, *Adv. Sci.*, 1430010, (DOI: 10.1002/advs.201400010).
55. Satarkar N. S., Biswal D., Hilt J. Z. (2010), Hydrogel nanocomposites: A review of applications as remote controlled biomaterials, *Soft Matter*, 6, 2364-2371 (DOI: 10.1039/B925218P).
56. Cametti M., Džolić Z. (2014), New frontiers in hybrid materials: noble metal nanoparticles – supramolecular gel systems, *Chem. Commun.*, 50, 8273-8286 (DOI: 10.1039/C4CC00903G).
57. Mandal S. K., Brahmachari S., Das P. K. (2014), In situ synthesized silver nanoparticle-infused l-lysine-based injectable hydrogel: development of a biocompatible, antibacterial, soft nanocomposite, *ChemPlusChem*, 79, 1733-1746 (DOI: 10.1002/cplu.201402269).
58. Han M., Gao X., Su J. Z., Nie S. (2001), Quantum-dot-tagged microbeads for multiplexed optical coding of biomolecules, *Nat. Biotechnol.*, 19, 631-635 (DOI: 10.1038/90228).
59. Mohan Y. M., Premkumar T., Lee K., Geckeler K. E. (2006), Fabrication of silver nanoparticles in hydrogel networks, *Macromol. Rapid Commun.*, 27, 1346-1354 (DOI: 10.1002/marc.200600297).
60. Lloyd G. O., Steed J. W. (2009), Anion-tuning of supramolecular gel properties, *Nat. Chem.*, 1, 437-442 (DOI: 10.1038/nchem.283).

- 
61. Steed J. W. (2010), Anion-tuned supramolecular gels: A natural evolution from urea supramolecular chemistry, *Chem. Soc. Rev.*, 39, 3686-3699 (DOI: 10.1039/b926219a).
62. Liu Q., Wang Y., Li W., Wu L. (2010), Structural characterization and chemical response of a Ag-coordinated supramolecular gel, *Langmuir*, 23, 8217-8223 (DOI: 10.1021/la700364t).
63. Jung W. K., Koo H. C., Kim K. W., Shin S., Kim S. H., Park Y. H. (2008), Antibacterial activity and mechanism of action of the silver ion in *Staphylococcus aureus* and *Escherichia coli*, *Appl. Environ. Microbiol.*, 74, 2171-2178 (DOI: 10.1128/AEM.02001-07).
64. Lossaso C. *et al.* (2014), Antibacterial activity of silver nanoparticles: sensitivity of different *Salmonella* serovars, *Front. Microbiol.*, 5, 227 (DOI: 10.3389/fmicb.2014.00227).
65. Chakraborty I., Udayabhaskararao T., Deepesh G. K., Pradeep T. (2013), Sunlight mediated synthesis and antibacterial properties of monolayer protected silver clusters, *J. Mater. Chem. B*, 1, 4059-4064 (DOI: 10.1039/c3tb20603c).
66. Verdolino V., Cammi R., Munk H., Schlegel H. B. (2008), Calculation of  $pK_a$  values of nucleobases and the guanine oxidation products guanidinohydantoin and spiroiminodihydantoin using density functional theory and a polarizable continuum model, *J. Phys. Chem. B*, 112, 16860-16873 (DOI: 10.1021/jp8068877).
67. Purohit C. S., Mishra A. K., Verma S. (2007), Four-stranded coordination helices containing silver-adenine (purine) metallaquartets, *Inorg. Chem.*, 6, 8493-8495 (DOI: 10.1021/ic701465d).
68. Klika K. D., Kivelä H., Ovkarenko V. V., Nieminen V., Sillanpää R., Arpalahti J. (2007), Synthesis and NMR characterization of the *cis* and *trans* isomers of  $[Pt^{II}(N^9\text{-adeH})_2(pz)_2]$  and X-ray crystallography of the *trans* isomer, *Dalton Trans.*, 3966-3970 (DOI: 10.1039/B709697F).



## Chapter 6

# Zn<sup>2+</sup>-Nucleobase Coordination Polymer Particles: Synthesis and Photocatalytic Activity

### 6.1 Introduction

The research on micro and nanosized coordination polymer particles has grown significantly in the recent years owing to their potential use in a myriad of applications such as catalysis, sensing, optics as well as medical diagnostics.<sup>[1-8]</sup> The properties and applications of such coordination particles largely depends not only on the composition of these particles, but also on their structures and morphologies.<sup>[9]</sup> Therefore, realizing the changes in the morphology and structure of particles with changes in the composition is crucial for the controlled formation of particles. Recently, the use of biological ligands such as amino acids,<sup>[10-12]</sup> peptides<sup>[13]</sup> as well as nucleotides<sup>[14,15]</sup> has progressed as an attractive strategy for the fabrication of such nanoscale coordination particles, with an aim to generate biocompatible and less toxic particles that can be employed for biomedical applications.<sup>[16]</sup> These particles synthesized using biological ligands are often termed as ‘biocoordination polymer particles’.

Metallogels, formed by the combination of one or more organic ligand and inorganic metal ions, represent an important class of hybrid organic-inorganic materials.<sup>[17]</sup> Metallogels are formed as a result of interaction of metal ions and organic ligands,<sup>[17]</sup> leading to the formation of ordered micro- or nanostructures such as fibers, tapes or spheres which can trap a large volume of water. As such, formation of metallogels has been regarded as the generation of coordination polymer particles. Again highly branched structures with flower like morphology have attracted special attention due to their applications in various fields ranging from magnetic materials, optoelectronic devices, solar cells to medicine.<sup>[18-22]</sup> Recently, Zare and co-workers reported the formation of hybrid flower like structures upon the interaction of Cu<sup>2+</sup> with various proteins in phosphate buffered saline.<sup>[23]</sup> Similarly, there have been reports on the formation of flower shaped pure organic supramolecules generated by the self-

assembly of pyrimido[4,5-d]pyrimidine nucleosides.<sup>[24]</sup> Although nucleobase-metal coordination chemistry has been studied for a long time, the ability of pure nucleobases to form coordination polymer particles has only recently been realized.<sup>[25]</sup>

Semiconductor photocatalysis, inspired by natural photosynthesis of green plants and other micro-organisms, is considered to be the most promising solution to address the environmental and energy problems in a carbon neutral fashion. Most popular among the photocatalysts are the semiconducting materials such as TiO<sub>2</sub> and ZnO and engineering of these materials in various nanostructures have been actively pursued for photocatalytic water splitting<sup>[26-28]</sup> as well as disinfection of water and oxidation of organic contaminants.<sup>[29-31]</sup> Several other types of materials such as metal-doped zeolites and metal complexes have been explored and studied for light induced redox processes and organosynthesis to advance artificial photosynthesis.<sup>[32-34]</sup> On the other hand, the development of nano or microscale coordination polymer particles and metallogels for photocatalytic activities is almost negligible.

In this chapter, we report our studies on the interaction of Zn<sup>2+</sup> ions with two nucleobases, namely cytosine and guanine that leads to the formation of stable metallogels. Further, the addition of zinc ions to a combination of mixed ligands under appropriate reaction conditions resulted in the formation of gelatinous precipitate composed of flower shaped coordination polymer microparticles. Both the metallogels as well as microflowers have been used as catalyst for the photocatalytic degradation of organic pollutant dyes such as methyl orange and methylene blue.

## **6.2 Results and Discussion**

### **6.2.1 Synthesis and characterization of Zn-nucleobase hydrogels**

The formation of Zn based metallogels using two nucleobases, namely cytosine (C) and guanine (G) was afforded by the simple addition of an aqueous solution of Zn(NO<sub>3</sub>)<sub>2</sub> to an alkaline solution of C or G at room temperature. Within a few minutes, the mixture turned into a self-standing opaque gel like material, which was affirmed by the inverted tube method that did not allow the mass to follow under gravity. Similar to the Ag-nucleobase gels, the effect of metal counterions on the gelation ability of the nucleobases was tested. Change of metal counterion from nitrate to chloride or acetate

did not affect the gel formation (although a slightly longer time was required for the formation of gel using cytosine and  $\text{Zn}(\text{CH}_3\text{COO})_2$ ), indicating that the gel formation was independent of the nature of metal counterions. Further, the formation of these Zn-nucleobase hydrogels did not require any external force such as heating/cooling or sonication and the gels readily formed at room temperature.

Electron microscopy was employed to investigate the morphology of the metallogels. The TEM images shown in figure 6.1a and b, clearly demonstrated that both the metallogels consisted of individual nanofibers, which were capable of trapping a large volume of water, leading to the formation of hydrogels. The diameter of the Zn-cytosine nanofibers, as calculated from the TEM image varied from 15 to 28 nm. On the other hand, the Zn-guanine nanofibers were somewhat thicker and their diameter varied from 34 to 52 nm. The SEM studies (figure 6.1c and d) performed on the samples confirmed their fibrous morphology and were in good agreement with the TEM studies.

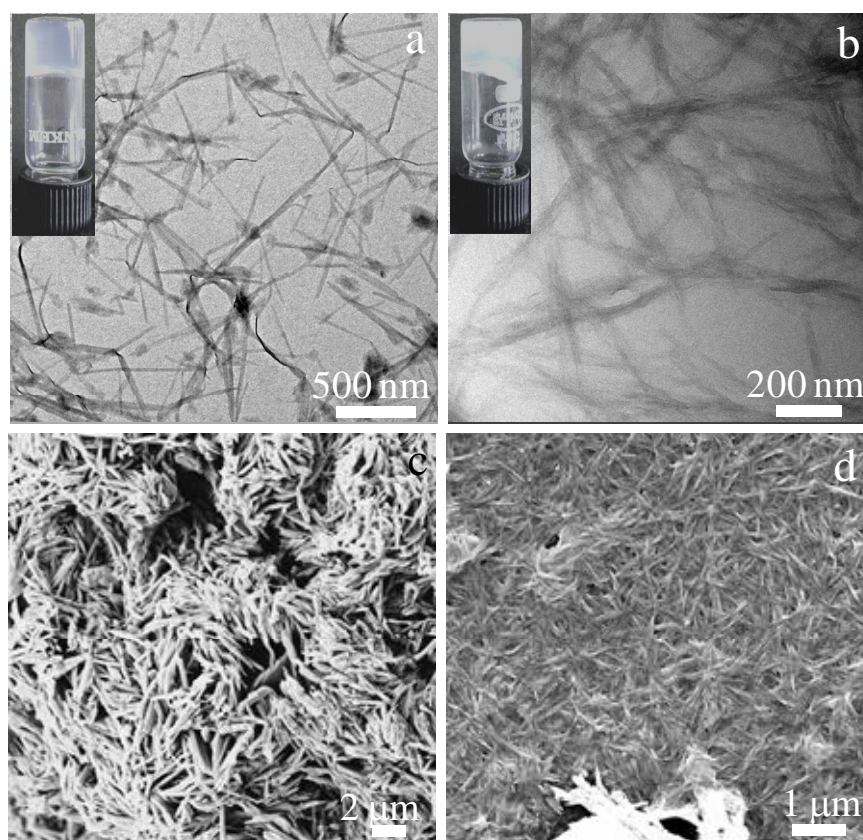


**Figure 6.1.** (a, c) TEM and SEM images of Zn-C metallogel and (b, d) TEM and SEM images of Zn-G metallogels. Inset in (a) and (b) are the digital images of Zn-C and Zn-G metallogels respectively.

The mechanical robustness of the hydrogels was studied by rheological investigations. Strain sweep and frequency sweep rheological measurements were performed on the hydrogel samples to establish the dominance of elastic behavior over the viscous behavior as shown in figure 6.2. During the strain sweep experiments, the value of the elastic storage modulus ( $G'$ ) was significantly higher than the loss modulus ( $G''$ ) over the complete range of strain for the Zn-C hydrogel. On the other hand for the Zn-G hydrogel, the value of  $G'$  dominated the value of  $G''$  over a long range of strain, but merged together at a strain of 100%, indicating the dominance of the viscous nature over the elastic nature beyond a strain of 100%. The supremacy of the elastic solid like behavior of both the gels was further ascertained from the frequency sweep measurements, which clearly depicted that in the frequency range  $0.05$  to  $100\text{ s}^{-1}$ ,  $G'$  is always greater than  $G''$  by several factors, thus confirming the dominance of elastic behavior over the viscous nature of the material.

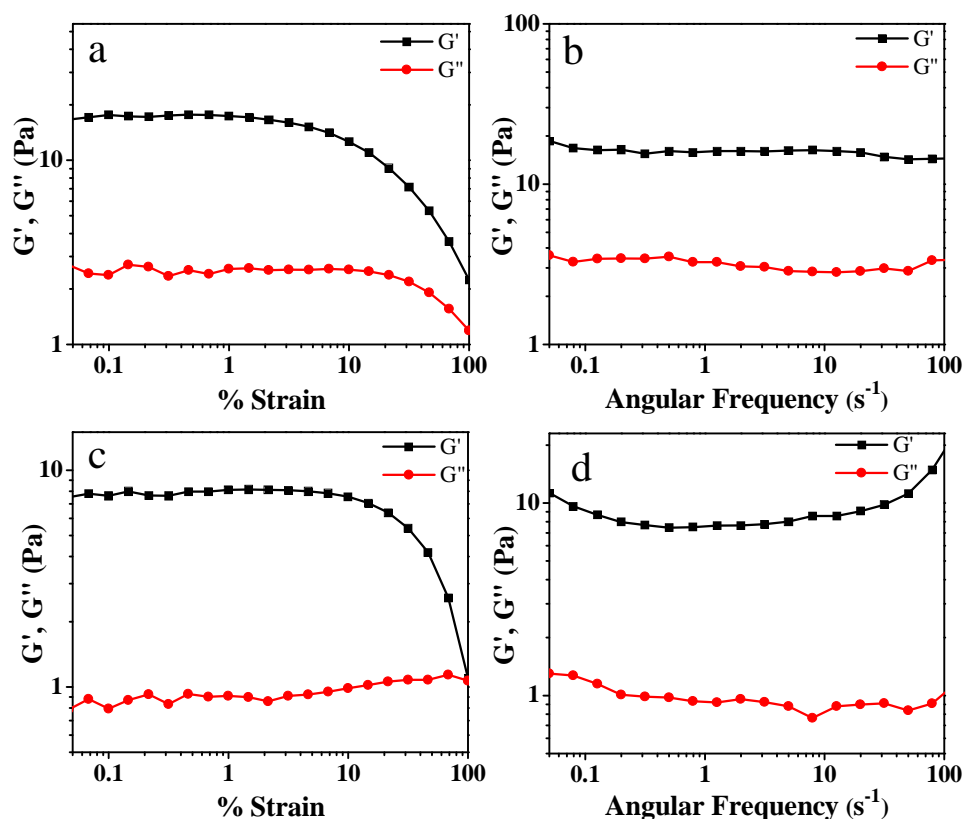


**Figure 6.2.** (a) and (c) Dynamic strain sweep experiment of the Zn-cytosine and Zn-guanine hydrogel respectively. (b) and (d) Dynamic frequency sweep experiments of the Zn-cytosine and Zn-guanine hydrogel respectively at a constant strain of 1%.

Due to the nanometer dimension of the fibers repeated attempts to crystallize the materials were unsuccessful. Therefore to have an idea on whether the synthesized materials were crystalline or amorphous, powder X-ray diffraction studies of the lyophilized hydrogels was performed. The powder XRD spectrum for both the materials (figure 6.3a) showed a complex pattern of peaks at  $2\theta$  values between 1 to 60 degrees which indicated that the materials were crystalline in nature. For the Zn-C gel, peaks at  $2\theta$  values of 5.7, 11.4, 18.0, 22.6, 28.6, 35.4, 42.5 and 48.4 degrees corresponding to  $d$ -values of 15.5 Å, 7.7 Å, 4.9 Å, 3.9 Å, 3.1 Å, 2.5 Å, 2.1 Å and 1.8 Å were observed in addition to several other sharp peaks. These  $d$ -values followed a ratio of 1: 1/2: 1/3: 1/4: 1/5: 1/6: 1/7: 1/8, suggesting that the hydrogels were mainly assembled in a layered structure with an interlayer separation of 15.5 Å. For the Zn-G gel, such periodic reflections were however not observed. A low intensity peak at  $2\theta = 27.6^\circ$ , corresponding to a  $d$ -value of 3.2 Å was observed, which is very close to that of  $\pi$ - $\pi$  stacking interactions in guanine based hydrogels, suggesting that  $\pi$ - $\pi$  stacking interactions play an important role in the formation of Zn-G gel. The thermal stability of both the xerogels was studied by thermo gravimetric analysis (figure 6.3b). For the Zn-C xerogel, continuous weight loss from 85 °C to 600 °C was observed, which suggested the loss of organic ligands in this range. Again for the Zn-G xerogel, an initial weight loss of 9.5 % in the range of 25 °C to 125 °C was observed, probably due to the loss of water molecules in the complex. Another weight loss of approximately 55% was observed in the temperature range of 300°C to 640 °C, indicating the decomposition of the guanine molecules from the complex.

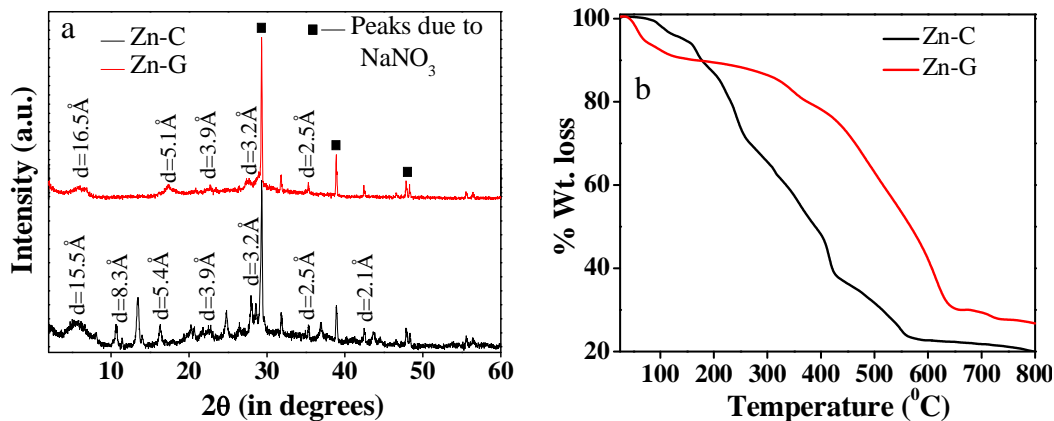


Figure 6. 3. (a) Powder XRD spectrum and (b) TGA plot of the Zn-C and Zn-G xerogels respectively.

The change in the environment around different functional groups in cytosine and guanine upon complexation with  $\text{Zn}^{2+}$  ions to form hydrogel was studied using FTIR spectroscopy. From the FTIR spectrum of cytosine and Zn-cytosine (figure 6.4a) it was observed that the peak at  $3380\text{ cm}^{-1}$  and  $3160\text{ cm}^{-1}$  due to the  $\text{NH}_2$  stretching vibrations in cytosine was absent in the metallogel and a new broad peak at  $3430\text{ cm}^{-1}$  was observed, indicating the presence of water molecules and extensive hydrogen bonding. Also, the peak at  $2780\text{ cm}^{-1}$  due to N-H stretching was absent in the complex, suggesting the involvement of the N1 nitrogen of cytosine in bonding to the  $\text{Zn}^{2+}$  ions. Further, the peak at  $1657\text{ cm}^{-1}$ , which is a combination of both  $-\text{NH}_2$  bending and  $\text{C}=\text{O}$  stretching splitted into two weak bands at  $1674\text{ cm}^{-1}$  and  $1636\text{ cm}^{-1}$ , suggesting the probable involvement of  $\text{NH}_2$  and  $\text{C}=\text{O}$  in hydrogen bonding. Again, the loss of peak at  $1272\text{ cm}^{-1}$  due to N-H bending again suggested the involvement of N1 of cytosine in binding to  $\text{Zn}^{2+}$  ions. Similarly, the FTIR spectrum of guanine and Zn-guanine (figure 6.4b) suggested the involvement of  $\text{NH}_2$  in hydrogen bonding. The peak at  $1697\text{ cm}^{-1}$  due to the  $\text{C}=\text{O}$  stretching shifted to  $1650\text{ cm}^{-1}$  in the complex, suggesting its probable involvement in metal binding and the peak at  $1672\text{ cm}^{-1}$  due to  $\text{NH}_2$  stretching vibrations in pure guanine shifted to  $1622\text{ cm}^{-1}$ , suggesting its involvement in either hydrogen bonding or metal binding.

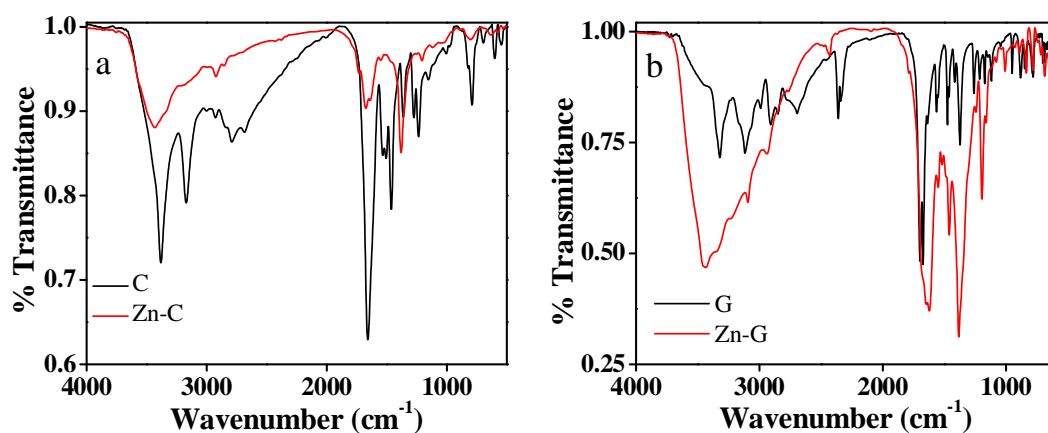
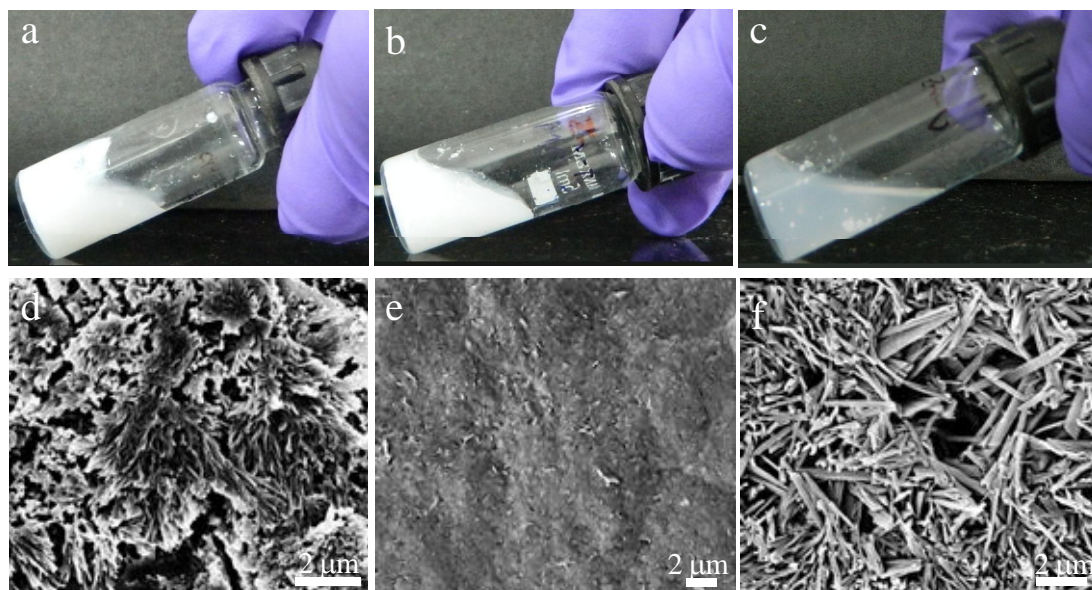


Figure 6.4. (a) FTIR spectrum of pure C and Zn-C and (b) FTIR spectrum of pure G and Zn-G.

### 6.2.2 Interaction of $\text{Zn}^{2+}$ ions with adenine, thymine or uracil

Unlike cytosine and guanine, the addition of  $\text{Zn}^{2+}$  ions to an alkaline solution of adenine (A), thymine (T) or uracil (U) resulted in the formation of a gelatinous white

precipitate, rather than a gel. The formation of precipitates in all the three cases was ascertained by the inverted tube method, which showed a flow of the material (fig 6.5a, b and c). SEM studies of the precipitates revealed the formation of large fibrous aggregates in case of the Zn-A precipitate (figure 6.5d), while in case of Zn-T, no defined structure could be observed (figure 6.5e). On the other hand for the Zn-U complex, rod shaped coordination polymer particles ranging from hundreds of nanometer to several micrometers in length were observed (figure 6.5f).



**Figure 6.5.** Digital images of (a) Zn-A precipitate, (b) Zn-T precipitate and (c) Zn-U precipitate. (d), (e) and (f) FESEM images of Zn-A precipitate, Zn-T precipitate and Zn-U precipitate respectively.

### 6.2.3 Interaction of $\text{Zn}^{2+}$ ions with a mixture of cytosine and guanine

Functional coordination polymers having two or more metal ions or organic linkers are expected to possess extraordinary properties as the structure and morphology of these materials strongly depend on their composition.<sup>[9]</sup> Therefore, after the successful formation of metallogels with C and G, we explored the possibility of formation of a complex of zinc with a combination of these two ligands which individually formed metallogels with  $\text{Zn}^{2+}$ . The addition of  $\text{Zn}(\text{NO}_3)_2$  to a mixture of C and G, quite surprisingly resulted in the formation of a gelatinous precipitate, rather than gel. The morphology of the precipitate was studied using electron microscopy.

From the SEM images, beautiful flower shaped particles having a diameter of about 4.2  $\mu\text{m}$  were observed (figure 6.6a and b). The formation of coordination polymer particles with flower like morphology was further confirmed from TEM studies (figure 6.6c).

The crystalline nature of the precipitate could be established from the powder XRD studies which showed multiple peaks in  $2\theta$  range between 1 to 60 degrees (figure 6.6e). Periodic reflections at  $2\theta$  values of 5.3, 8.0, 16.1, 19.8, 28.1 and 31.8 degrees, corresponding to  $d$ -values of 16.5  $\text{\AA}$ , 11.0  $\text{\AA}$ , 5.5  $\text{\AA}$ , 4.5  $\text{\AA}$ , 3.2  $\text{\AA}$ , and 2.8  $\text{\AA}$  respectively were observed, which followed a ratio of 1: 1/2: 1/3: 1/4: 1/5: 1/6, which indicated that a self assembly led to the formation of layered structure. Such a pattern is common for hydrogels, however in the present case hydrogels could not be obtained, probably due to the H-bonding between G and C which prevented the binding of  $\text{Zn}^{2+}$  ions to the preferred nitrogen in the nucleobases. The thermal stability of the microflowers was studied by thermogravimetric analysis, which initially showed a loss of 7.5% at 115  $^{\circ}\text{C}$  corresponding to the loss of water molecules. Then another weight loss upto 600  $^{\circ}\text{C}$  was observed, which can be attributed to the decomposition of the ligands in the complex.

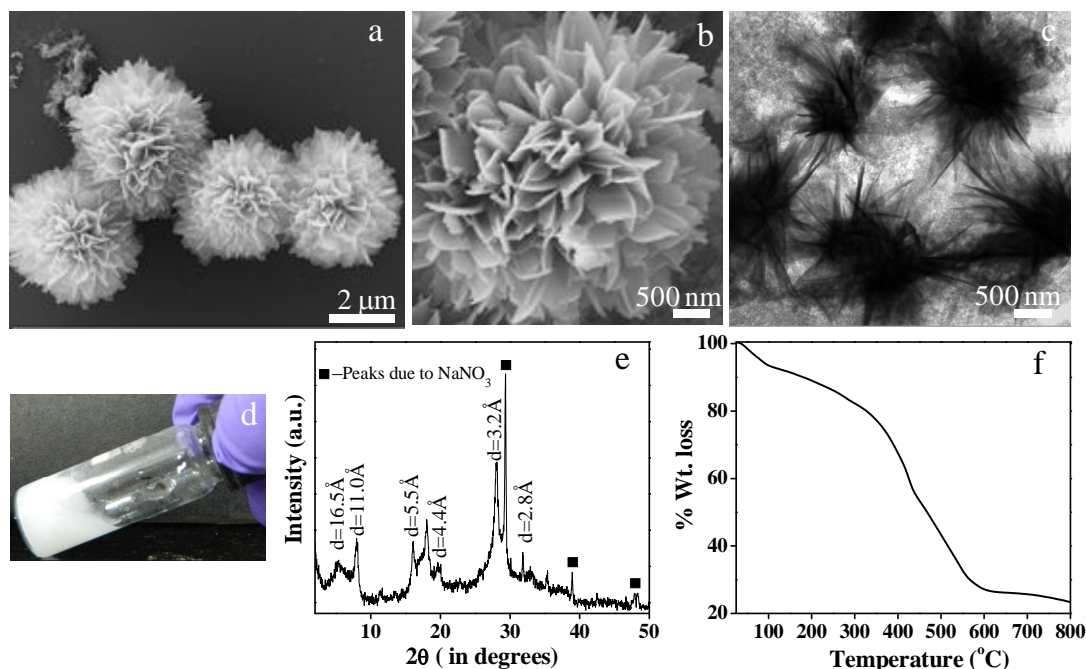


**Figure 6.6.** (a) and (b) FESEM images of the microflowers formed by the interaction of  $\text{Zn}^{2+}$  and mixture of C and G, (c) TEM image of the microflowers, (d) Digital image, (e) Powder XRD spectrum and (f) TGA plot of the precipitate containing microflowers upon addition of  $\text{Zn}^{2+}$  to a mixture of C and G.

To have an idea on the formation of microflowers, time dependent SEM studies were performed (figure 6.7). From the time dependent studies, it was observed that at the initial stages, small fibrous aggregates were formed within 5 minutes after the addition of  $Zn^{2+}$  ions to the mixture of cytosine and guanine. After 30 minutes these small aggregates fused together to form larger aggregates and within 6 hours, these larger aggregates self assembled into flower like structures. Within 12 hours petal formation of the flowers was clearly evident and after 24 hours, the structures self assembled into beautiful individual flowers.

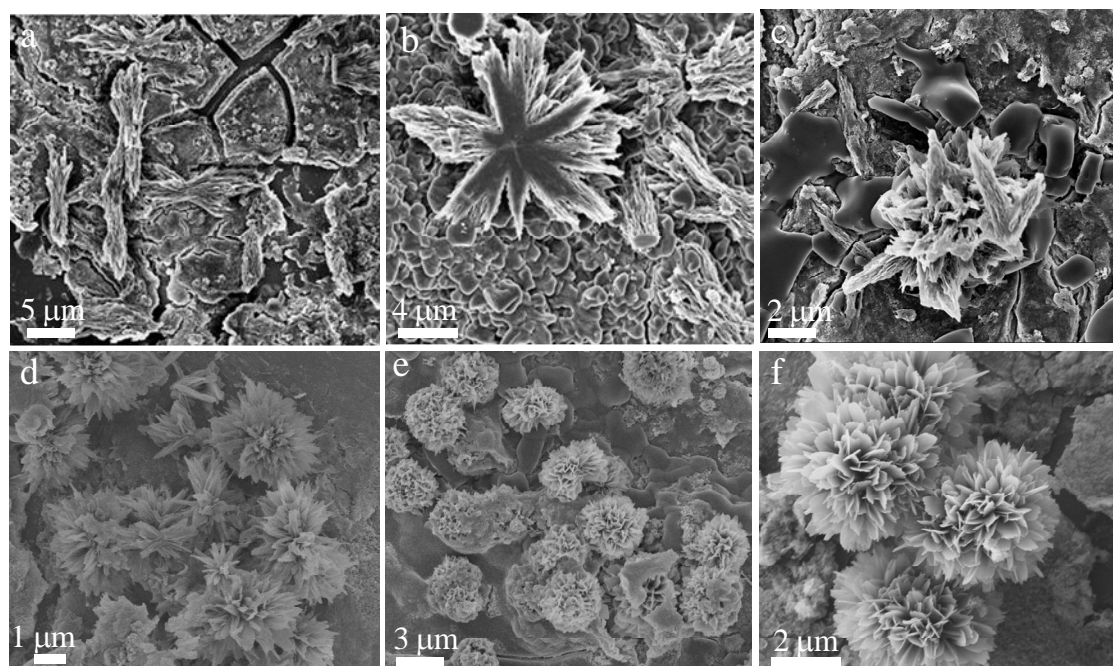


**Figure 6.7.** Time dependent FESEM images for the growth of Zn-cytosine-guanine microflowers. FESEM recorded at various time intervals after addition of  $Zn^{2+}$  to a mixture of C and G, (a) 5 mins, (b) 30 mins, (c) 6 hours, (d) 12 hours, (e) 24 hours and (f) 72 hours.

#### 6.2.4 Photocatalytic activity of the three zinc based materials

Zinc based materials are known to function as efficient photocatalysts due to their semiconducting nature. Therefore to have an idea about the band gap of the three materials and their efficiency to function as photocatalysts, solid state UV-visible absorption studies were performed. From the solid state UV-visible studies (figure 6.8), the band gap was calculated to be 3.06 eV and 3.01 eV respectively for the Zn-cytosine and Zn-guanine hydrogels. On the other hand the band gap energy for the Zn-cytosine-

guanine precipitate was calculated to be 3.23 eV, which suggested that any light source with energy higher than 3.23 eV could be used to excite these materials and these materials could function as photocatalysts.

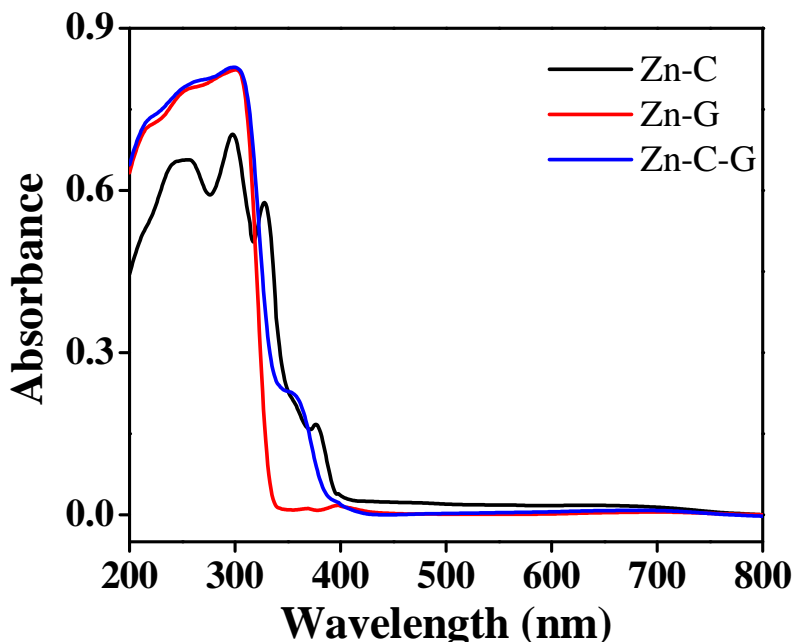


**Figure 6.8.** Solid state UV-visible spectrum for the calculation of the band gap of the three Zn based materials

The photocatalytic activity of the three materials was tested for the degradation of two organic dyes, methylene blue and methyl orange. Since both methylene blue and methyl orange absorb in the visible region, therefore the degradation of both methylene blue and methyl orange could easily be studied by observing the changes in the UV-visible spectrum at 664 nm and 464 nm respectively.<sup>[34]</sup> Controlled experiment performed in the absence of light suggested that the degradation of the dyes did not occur at all as indicated by the little change in the UV-visible spectrum and color of the solution even after 4 hours. However, when the dye solution containing the catalysts was illuminated with a 365 nm UV lamp, changes in the UV-visible spectrum were quite evident. Figure 6.9 shows the degradation of methylene blue using the three synthesized materials as catalysts. It was observed that the intensity of the absorption band of methylene blue at 664 nm began to decrease gradually as a function of increasing reaction time, clearly suggesting the degradation of methylene blue. As can

be seen from figure 6.9d, while 90% the dye was degraded when Zn-C was used as a catalyst, the use of Zn-G nanofibers and Zn-C-G microparticles as photocatalyst led to the degradation of methylene blue by 94% and 48% respectively. Controlled experiments were performed in the absence of catalysts, but in the presence of UV light to establish the superior catalytic activity of the materials, and it was observed that even in the absence of catalysts, 36% of methylene blue was decomposed, which was consistent with the previous literature reports.<sup>[33,34]</sup>

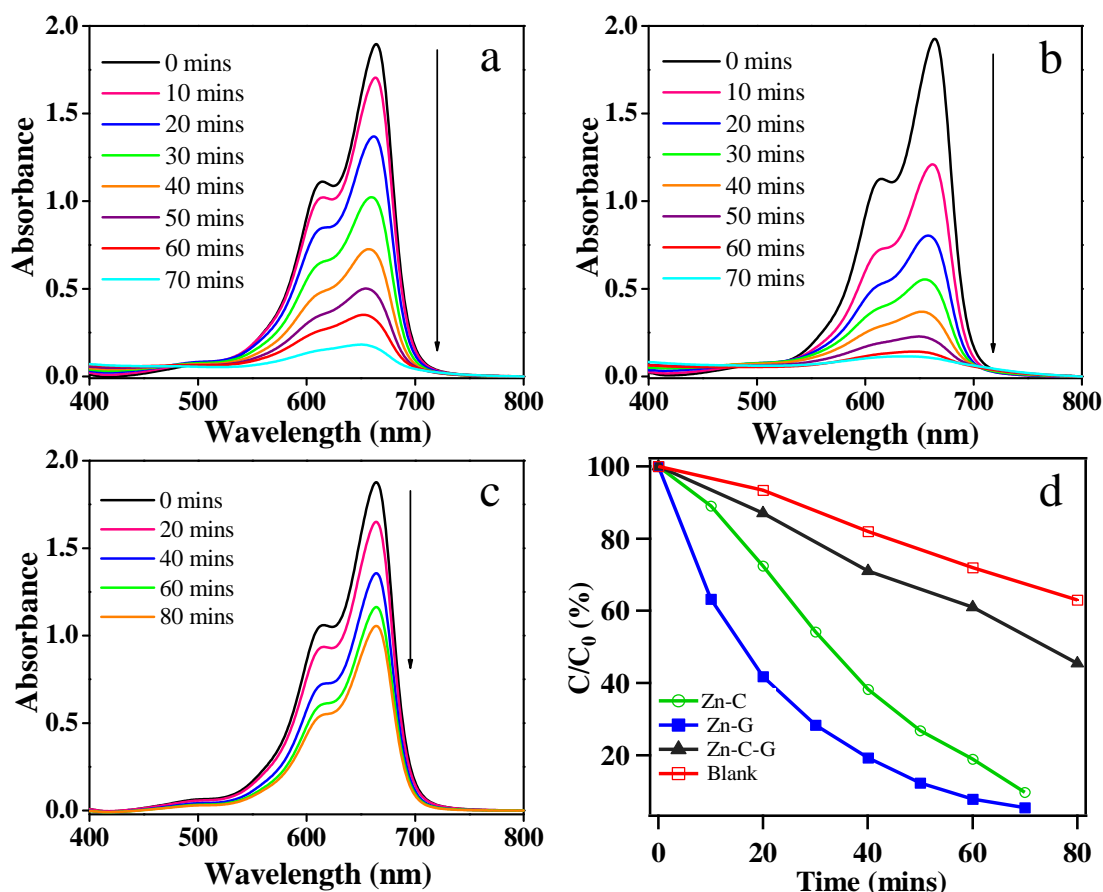


**Figure 6.9.** Time dependent UV-visible studies for the degradation of methylene blue by UV lamp of wavelength 365 nm, using (a) Zn-C, (b) Zn-G and (c) Zn-C-G as photocatalysts. (d) Plots of absorbance of the methylene blue solutions at different time intervals ( $C_0$  is the initial concentration of the dye and  $C$  is the concentration of the dye at any given time).

In a similar manner, the photocatalytic activities of the three catalysts were tested for the photocatalytic decomposition of methyl orange. The effect of the three catalysts on the absorption spectrum of methyl orange is shown in figure 6.10. From the

UV-visible studies it was clear that whereas the Zn-cytosine nanofibers degraded 84% of the methyl orange in 90 minutes, the use of Zn-guanine nanofibers as catalyst afforded the degradation of methyl orange by 86% under similar duration of time. On the other hand, the flower shaped coordination polymer particles formed by the interaction of zinc ions with a mixture of cytosine and guanine degraded the dye only by 41%. Similar to methylene blue, controlled experiments were performed with MO in the absence of catalysts and it was observed that 31% of the dye degraded under similar duration of time which was consistent with previous results.<sup>[34]</sup>

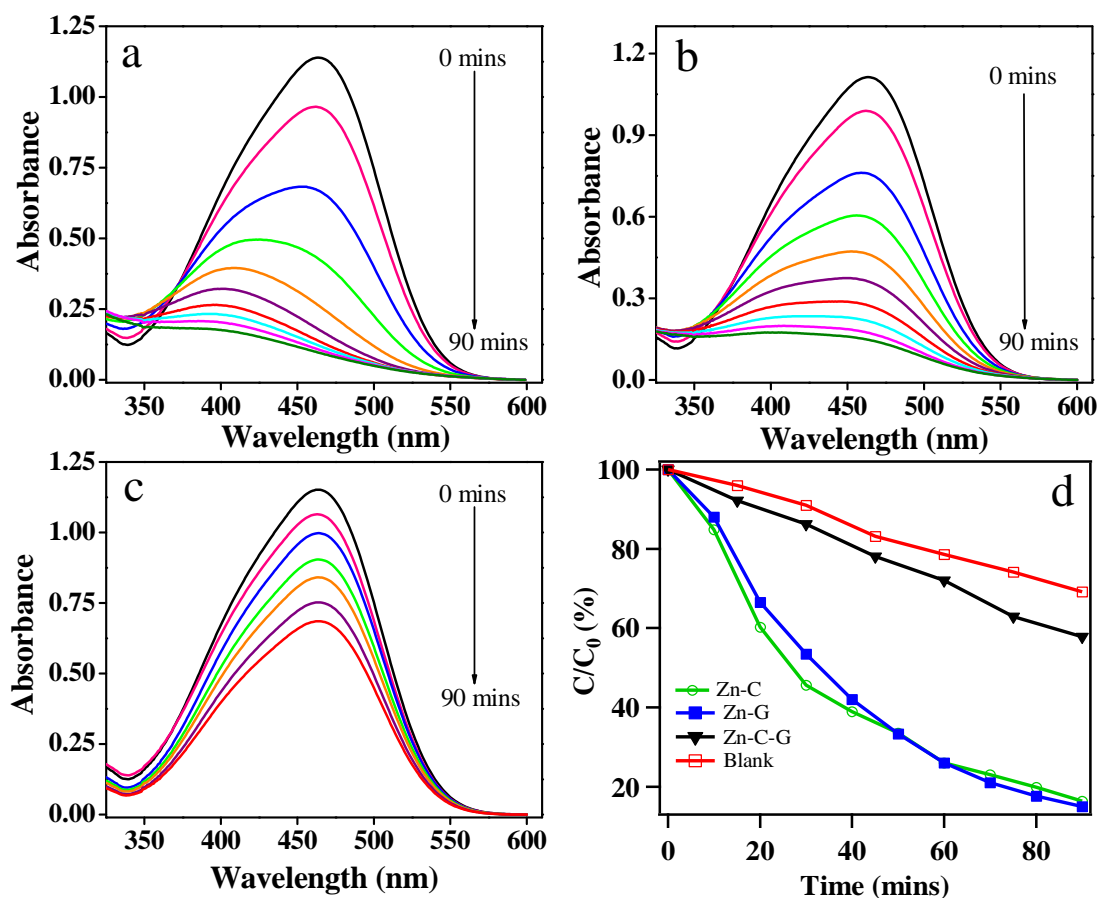


**Figure 6.10.** Time dependent UV-visible studies for the degradation of methyl orange by UV lamp of wavelength 365 nm, using (a) Zn-C, (b) Zn-G and (c) Zn-C-G as photocatalysts. (d) Plots of absorbance of the methyl orange solutions at different time intervals ( $C_0$  is the initial concentration of the dye and  $C$  is the concentration of the dye at any given time).

From the photocatalytic degradation studies of the two dyes, it was evident that the nanofibers formed from the interaction of  $Zn^{2+}$  and G were the most effective

photocatalysts followed by the nanofibers of Zn-C, and the flower shaped coordination polymer particles were the least effective catalyst. This behavior in the catalytic activity of the three catalysts was quite expected as the band gap energies for the three catalysts are in the opposite order. Since the band gap energy for the Zn-G complex is the least, therefore it showed the best catalytic activity, whereas for the flower shaped particles, the band gap energy is maximum resulting in their lower catalytic activity.

The plausible mechanism for the photocatalytic degradation of the organic dyes may be proposed as follows:<sup>[35-37]</sup> After the absorption of energy equal to or more than the band gap energies, the electrons ( $e^-$ ) from the valence band get excited to the conduction band, leaving behind holes ( $h^+$ ) in the valence band. The electrons then reduce the  $O_2$  into  $\cdot O_2^-$ , which finally transforms into hydroxyl radicals  $\cdot OH$ . Again the holes oxidize the  $H_2O$  to generate  $\cdot OH$  radicals, which can effectively decompose the organic dyes.<sup>[38,39]</sup>

### 6.3 Conclusions

In conclusion, we have used the pure nucleobases cytosine and guanine for the generation of coordination polymer hydrogels (consisting of nanofibers), upon their interaction with  $Zn^{2+}$  ions in alkaline medium. The gels showed quite good elastic behavior as indicated by the rheological investigation. On the other hand, the addition of  $Zn^{2+}$  ions to an aqueous alkaline solution of the other three nucleobases resulted in the formation of a precipitate. Further, coordination polymer particles with flower shaped morphology could be generated upon the addition of  $Zn^{2+}$  ions to an aqueous solution containing a mixture of both cytosine and guanine. The photocatalytic activity of the three materials was tested towards the reduction of organic pollutant dyes such as methylene blue and methyl orange. For both the reactions, the Zn-guanine nanofibers were the most effective catalyst, followed by the Zn-cytosine nanofibers and the Zn-cytosine-guanine microflowers were the least effective, which was exactly as expected based on the band gap values of the three photocatalysts. The coordination polymer microflowers hold promise for being used as a mimick for several zinc containing biological molecules such as carbonic anhydrase and carboxypeptidase, although detailed studies would be required in this regard.

## 6.4 Experimental Section

### 6.4.1 Materials

Adenine, guanine, cytosine, thymine, uracil and zinc nitrate hexahydrate were purchased from Aldrich chemicals. Zinc chloride, zinc acetate dihydrate and sodium hydroxide were purchased from Merck, India. Methylene blue was purchased from Alfa Aesar and methyl orange was purchased from SRL, India. All the chemicals were of analytical grade and were used without any purification. Milli Q water was used throughout the experiments.

### 6.4.2 Instrumentation

Transmission electron microscopy (TEM) images were recorded with a Technai G<sup>2</sup> 20 Ultra-Twin microscope at an accelerating voltage of 200 kV. Field emission scanning electron microscopy images were recorded on a Carl Zeiss Supra 55 instrument after coating with gold. Rheological measurements were performed using an Anton Paar Physica MCR 301 rheometer with parallel plate geometry (diameter 50 mm). Powder X-ray diffraction spectra (XRD) of the freeze dried gels and microflowers were recorded on a Rigaku Smartlab, Automated Multipurpose X-ray diffractometer with Cu K $\alpha$  source (wavelength of X-rays was 0.154 nm). FTIR spectra were recorded in KBr pellet using Bruker Tensor 27 instrument. Thermogravimetric analysis was done using a Mettler Toledo instrument. Solution state UV-visible spectra were recorded on a Varian Cary 100 Bio spectrophotometer. Solid state UV-visible spectra were recorded on a Perkin Elmer lambda Instrument. Photocatalytic studies were performed using a photocatalytic reactor from SAIC instruments, with a 365 nm lamp of power 125 watt.

### 6.4.3 Synthesis of Zn-cytosine and Zn-guanine hydrogels

A stock solution of each nucleobase (0.2 M) was prepared by the addition of solid NaOH to it in small parts under sonication, until the nucleobase dissolved and a clear solution was obtained. Similarly, a solution of Zn(NO<sub>3</sub>)<sub>2</sub>·6H<sub>2</sub>O (0.2 M) was prepared by simple dissolution of the metal salt in water.

In a typical synthesis, to 1.0 mL of the nucleobase solution, 1.0 mL of Zn(NO<sub>3</sub>)<sub>2</sub>·6H<sub>2</sub>O solution was added which resulted in the formation of hydrogels.

#### **6.4.4 Electron microscopy studies**

The samples for both TEM and FESEM were prepared by diluting the gel samples in water. A small amount of the gel was taken in an eppendorf tube and after addition of water the gel was crushed using a micropestle and was drop casted on a carbon coated copper grid (for TEM) and glass slides (for FESEM), followed by room temperature drying.

#### **6.4.5 Rheological studies**

Rheological investigations were performed using parallel plate geometry of diameter 50 mm. For the measurements, both the hydrogels were first prepared, and then a piece of the gel was placed on the plate of the rheometer using a microspatula. The temperature was maintained at 25 °C using an integrated temperature controller from Julabo. Dynamic strain sweep experiments were performed using a constant frequency of 10 rad s<sup>-1</sup>. The dynamic frequency sweep of both the hydrogels was measured as function of frequency in the range of 0.05-100 rad s<sup>-1</sup> with constant strain value 1%.

#### **6.4.6 Synthesis of Zinc-cytosine-guanine microflowers**

In a typical synthesis, first the two solutions of C and G (0.2 M) were mixed together (0.5 mL each). To this mixed nucleobase solution 1 mL Zn(NO<sub>3</sub>)<sub>2</sub>.6H<sub>2</sub>O (0.2 M) was added, resulting in the formation of a gelatinous precipitate.

#### **6.4.7 Photocatalytic studies**

Photocatalytic studies were performed using a methylene blue concentration of 10 mg/L and methyl orange concentration of 15 mg/L. A 1L solution of both the dyes was taken in the photocatalytic reactor and 40 mg of the catalysts was added to the dye solutions and this mixture was stirred at room temperature in the dark for 60 minutes to establish the adsorption-desorption equilibrium. Then the UV lamp was turned on and reaction mixtures were withdrawn from the reactor after suitable intervals of time and monitored using UV-visible spectrophotometer.

---

## 6.5 References

1. Spokoyny K. M., Kim D., Sumrein A., Mirkin C. A. (2009), Infinite coordination polymer nano- and microparticle structures, *Chem. Soc. Rev.*, 38, 1218-1227 (DOI: 10.1039/B807085G).
2. Carnaé A., Carbonell C., Imaz I., MasPOCH D. (2011), Nanoscale metal-organic materials, *Chem. Soc. Rev.*, 40, 291-305 (DOI: 10.1039/C0CS00042).
3. Park K. H., Jang K., Son S. U., Sweigart D. A. (2006), Self-supported organometallic rhodium quinonoid nanocatalysts for stereoselective polymerization of phenylacetylene, *J. Am. Chem. Soc.*, 128, 8740-8741 (DOI: 10.1021/ja062907o).
4. He C., Liu D., Lin W. (2015), Nanomedicine applications of hybrid nanomaterials built from metal-ligand coordination bonds: Nanoscale metal-organic frameworks and nanoscale coordination polymers, *Chem. Rev.*, 115, 11079-11108 (DOI: 10.1021/acs.chemrev.5b00125).
5. Fleischhaker F., Arsenault A. C., Kitaev V., Peiris F. C., Freymann G. V., Manners I., Zentel U., Ozin G. A. (2005), Photochemically and thermally tunable planar defects in colloidal photonic crystals, *J. Am. Chem. Soc.*, 127, 9318-9319 (DOI: 10.1021/ja0521573).
6. Rieter W. J., Taylor K. M. L., Lin W. (2007), Surface modification and functionalization of nanoscale metal-organic frameworks for controlled release and luminescence sensing, *J. Am. Chem. Soc.*, 129, 9852-9852 (DOI: 10.1021/ja073506r).
7. Oh M., Mirkin C. A. (2006), Ion exchange as a way of controlling the chemical compositions of nano- and microparticles made from infinite coordination polymers, *Angew. Chem. Int. Ed.*, 45, 5492-5494 (DOI: 10.1002/anie.200601918).
8. Imaz I, Rubio-Martínez M., Garcia-Fernández L., Garcia F., Ruiz-Molina D., Hernando J., Puentes V., MasPOCH D. (2010), Coordination polymer particles as potential drug delivery systems, *Chem. Commun.*, 46, 4737-4739 (DOI: 10.1039/C003084H).

- 
9. Lee H. J., We J., Kim J. O., Kim D., Cha W., Lee E., Sohn J., Oh M. (2015), Morphological and structural evolutions of metal–organic framework particles from amorphous spheres to crystalline hexagonal rods, *Angew. Chem. Int. Ed.*, 54, 10564-10568 (DOI: 10.1002/anie.201504873).
  10. Imaz I, Rubio-Martínez M., Saletta W. J., Amabilino D. B., MasPOCH D. (2009), Amino acid based metal-organic nanofibers, *J. Am. Chem. Soc.*, 131, 18222-18223 (DOI: 10.1021/ja908721t).
  11. Wu H., Tian C., Zhang Y., Yang C., Zhang S., Jiang Z. (2015), Stereoselective assembly of amino acid-based metal–biomolecule nanofibers, *Chem. Commun.*, 51, 6329-6332 (DOI: 10.1039/C5CC00446B).
  12. Chao L., Deng K., Tang Z., Jiang L. (2010), Twisted metal-amino acid nanobelts: Chirality transcription from molecules to frameworks, *J. Am. Chem. Soc.*, 132, 8202-8209 (DOI: 10.1021/ja102827f).
  13. Manton A., Massüger L., Rabu P., Palivan C., McCusker L. B., Taubert A. (2008), Metal-peptide frameworks (MPFs): “Bioinspired” metal organic frameworks, *J. Am. Chem. Soc.*, 130, 2517-2526 (DOI: 10.1021/ja0762588).
  14. Nishiyabu R. *et al.* (2009), Nanoparticles of adaptive supramolecular networks self-assembled from nucleotides and lanthanide ions, *J. Am. Chem. Soc.*, 131, 2151-2158 (DOI: 10.1021/cm070028a).
  15. Aimé C., Nishiyabu R., Gondo R., Kaneko K., Kimizuka N. (2008), Controlled self-assembly of nucleotide–lanthanide complexes: specific formation of nanofibers from dimeric guanine nucleotides, *Chem. Commun.*, 6534-6536 (DOI: 10.1039/B815779K).
  16. Imaz I, Rubio-Martínez M., An J., Solé-Font I., Rosi N. L., MasPOCH D. (2011), Metal–biomolecule frameworks (MBioFs), *Chem Commun.*, 47, 7287-7302 (DOI: 10.1039/c1cc11202c).
  17. Tam A. Y. –Y., Yam W. –W. (2013), Recent advances in metallogels, *Chem. Soc. Rev.*, 42, 1540-1567 (DOI: 10.1039/C2CS35354G).

18. Tian Q. *et al.* (2011), Hydrophilic flower-like CuS superstructures as an efficient 980 nm laser-driven photothermal agent for ablation of cancer cells, *Adv. Mater.*, 23, 3542-3542 (DOI: 10.1002/adma.201101295).
19. Rafique M. Y., Pan L., Khan W. S., Iqbal M. Z., Qiu H., Farooq M. H., Ellahi M., Guo Z. (2013), Controlled synthesis, phase formation, growth mechanism, and magnetic properties of 3-D CoNi alloy microstructures composed of nanorods, *CrystEngComm*, 15, 5314-5325 (DOI: 10.1039/C3CE40385H).
20. Yin J., Wang J., Li M., Jin C., Zhang T. (2012), Iodine ions mediated formation of monomorphic single-crystalline platinum nanoflowers, *Chem. Mater.*, 24, 2645-2654 (DOI: 10.1021/cm300056h).
21. Hsieh T. -L., Chen H. -W., Kung C. -W., Wang C. -C., Vittal R., Ho K. -C. (2012), A highly efficient dye-sensitized solar cell with a platinum nanoflowers counter electrode, *J. Mater. Chem.*, 22, 5550-5559 (DOI: 10.1039/C2JM14623A).
22. Kharisov B. I. (2008), A review for synthesis of nanoflowers, *Recent Pat. Nanotechnol.*, 2, 190-200.
23. Ge J., Lei J., Zare R. N. (2012), Protein-inorganic hybrid nanoflowers, *Nat. Nanotechnol.*, 7, 428-432 (DOI: 10.1038/NNANO.2012.80).
24. Zhao H. *et al.* (2014), Complex self-assembly of pyrimido[4,5-d]pyrimidine nucleoside supramolecular structures, *Nat. Commun.*, 5: 3108 (DOI: 10.1038/ncomms4108).
25. Sharma B., Mahata A., Mandani S., Pathak B., Sarma T. K. (2015), Manuscript submitted for publication.
26. Liu J. *et al.* (2015), Metal-free efficient photocatalyst for stable visible water splitting via a two-electron pathway, *Science*, 347, 970-974 (DOI: 10.1126/science.aaa3145)
27. Liao L. *et al.* (2014), Efficient solar water-splitting using a nanocrystalline CoO photocatalyst, *Nat. Nanotechnol.*, 9, 69-73 (DOI: 10.1038/nnano.2013.272).

- 
28. Maeda K., Domen K. (2010), Photocatalytic water splitting: Recent progress and future challenges, *J. Phys. Chem. Lett.*, 1, 2655-2661 (DOI: 10.1021/jz1007966).
29. Hisika A., Papaconstantinou E. (1992), Photocatalytic oxidation of organic compounds by polyoxometalates of molybdenum and tungsten. Catalyst regeneration by dioxygen, *Inorg. Chem.*, 31, 163-167 (DOI: 10.1021/ic00028a007).
30. Ohzu S., Ishizuka T., Hirai Y., Fukuzumi S., Kozima T. (2012), Photocatalytic oxidation of organic compounds in water by using ruthenium(II)-pyridylamine complexes as catalysts with high efficiency and selectivity, *Chem. Eur. J.*, 19, 1563-1567 (DOI: 10.1002/chem.201203430).
31. Zhou X., Li F., Li X., Li H., Wang Y., Sun L. (2015), Photocatalytic oxidation of organic compounds in a hybrid system composed of a molecular catalyst and visible light-absorbing semiconductor, *Dalton. Trans.*, 44, 475-479 (DOI: 10.1039/C4DT02945C).
32. Zhang Z., Zhang J., Xu T., Bu X., Feng P. (2008), Three-dimensional open framework built from Cu-S icosahedral clusters and its photocatalytic property, *J. Am. Chem. Soc.*, 130, 15238-15239 (DOI: 10.1021/ja805449p).
33. Li M., Liu L., Zhang L., Lv X., Ding J., Hou H., Fan Y. (2014), Novel coordination polymers of Zn(II) and Cd(II) tuned by different aromatic polycarboxylates: synthesis, structures and photocatalytic properties, *CrystEngComm*, 16, 6408-6416 (DOI: 10.1039/C4CE00093E).
34. Dai M., Su X. -R., Wang X., Wu B., Ren Z. -G., Zhou X., Lang J. -P. (2014), Three zinc(II) coordination polymers based on tetrakis(4-pyridyl)cyclobutane and naphthalenedicarboxylate linkers: Solvothermal syntheses, structures, and photocatalytic properties, *Cryst. Growth. Des.*, 14, 240-248 (DOI: 10.1021/cg4014416).

35. Wen T., Zhang D. -X., Zhang J. (2013), Two-dimensional copper(I) coordination polymer materials as photocatalysts for the degradation of organic dyes, *Inorg. Chem.*, 52, 12-14 (DOI: 10.1021/ic302273h).
36. Das M. C. *et al.* (2011), A Zn<sub>4</sub>O-containing doubly interpenetrated porous metal-organic framework for photocatalytic decomposition of methyl orange, *Chem. Commun.*, 47, 11715-11717 (DOI: 10.1039/c1cc12802g).
37. Shi Y., Zhou K., Wang B., Jiang S., Qiang S., Gui Z., Yuan R. K. K., Hu Y. (2014), Ternary graphene-CoFe<sub>2</sub>O<sub>4</sub>/CdS nanohybrids: Preparation and application as recyclable photocatalysts, *J. Mater. Chem. A*, 2, 535-544 (DOI: 10.1039/c3ta13409a).
38. Joseph J. M., Destailats H., Hung H. -M., Hoffmann M. R. (2000), The sonochemical degradation of azobenzene and related azo dyes: Rate enhancements via fenton's reactions, *J. Phys. Chem. A*, 104, 301-307 (DOI: 10.1021/jp992354m).
39. Yang H., Liu T., Cao M., Li H., Gao S., Cao R. (2010), A water-insoluble and visible light induced polyoxometalate-based photocatalyst, *Chem. Commun.*, 46, 2429-2431 (DOI: 10.1039/B919868G).

## Chapter 7

# Cd(II)-Nucleobase Coordination Polymer Hydrogels for the Generation of CdS Quantum Dots

### 7.1 Introduction

Supramolecular self-assembly of small molecules has emerged as a splendid strategy for the generation of newer materials, such as supramolecular gels with several functional properties.<sup>[1-6]</sup> Various non covalent interactions such as hydrophobic,  $\pi$ - $\pi$  stacking, van der waals and hydrogen bonding play a key role in self assembling low molecular weight organic gelators (LMOGs) to form three dimensional networks capable of capturing solvents.<sup>[7-9]</sup> Such supramolecular gels have been used for various applications such as optical devices, drug delivery, cosmetics, waste water treatment etc.<sup>[10-14]</sup> Metallogels represent one important subclass of these functional materials, where physico-chemical characteristics of both the hydrogel and metallic constituents can be harnessed towards multifunctionality. Metallogels are formed by the interaction of metal ions with organic ligands, leading to the formation of coordination polymers, which eventually develop into metallogels, through multiple non-covalent interactions and incorporation of solvent molecules in the matrix.<sup>[8]</sup> Metallogels are widely studied due to their important properties and wide applicability in catalysis, sensing, proton conductivity and in situ generation of inorganic nanoparticles.<sup>[15-23, 8]</sup>

The fabrication of hybrid gel systems comprised of inorganic nanoparticles (metallic and semiconductor) has received considerable interest in recent times due to their interesting properties and applications.<sup>[8,23-25]</sup> The combination may result in a synergistic property enhancement of each component, for example the mechanical stiffness as well as bioactivity of the hydrogels are remarkably enhanced in a nanoparticle-hydrogel hybrid compared to hydrogel without nanoparticles.<sup>[26,27]</sup> Several approaches have been adopted towards forming these hybrid systems: 1) hydrogel

formation in a nanoparticle suspension, 2) physically embedding the nanoparticles into hydrogel matrix after gelation, 3) reactive nanoparticle formation within a performed gel, 4) cross-linking using nanoparticles to form hydrogels and 5) gel formation using nanoparticles, polymers and distinct gelator molecules.<sup>[25]</sup> The in-situ generation of nanoparticles in hydrogel matrix holds promise as this method leads to generation of uniformly distributed nanoparticles in the gel matrix. Semiconducting nanoparticles have shown potential in various applications, therefore development of semiconducting nanoparticle-hydrogel hybrid systems may find importance for opto-electronics, bio-sensing and cell-labelling studies. Taking into account the inherent cytotoxicity associated with the semiconducting nanoparticles, development of hybrid systems using commonly available biomolecules as hydrogelators might be influential in enhancing biocompatibility of the composite system. Therefore, there has been a huge surge on the development of metal organic hybrid systems involving biological molecules as ligands<sup>[28-34]</sup> and are generally termed as metal-biomolecule frameworks.<sup>[28,33]</sup>

In this chapter, we report our study on the generation of coordination polymer hydrogels of the nucleobases thymine (T) and uracil (U) upon their interaction with  $\text{Cd}^{2+}$  ions. The self-standing metallogels are formed at room temperature, without the aid of any other external stimuli. Further, the addition of  $\text{Cd}^{2+}$  ions to a mixture of thymine or uracil also resulted in the formation of hydrogel. Again, quantum dot such as CdS, decorated along the fibers of the hydrogels could be synthesized *in situ* by simple addition of a sulfide precursor ( $\text{Na}_2\text{S}$ ) to the nucleobase solution followed by the addition of  $\text{Cd}^{2+}$  ions. It is also imperative to mention that under acidic medium, the addition of  $\text{Cd}(\text{NO}_3)_2$  to any of the five nucleobases resulted in clear solutions.



**Scheme 7.1.** Schematic for the generation of coordination polymer hydrogel using T and U as ligands and  $\text{Cd}(\text{NO}_3)_2$  as metal salt.

## 7.2 Results and Discussion

### 7.2.1 Synthesis and characterization of Cd-nucleobase hydrogels

The simple addition of an aqueous solution containing  $\text{Cd}^{2+}$  ions to an alkaline solution of T or U resulted in the spontaneous formation of self-standing opaque hydrogels. The formation of the hydrogels was initially confirmed by tube inversion method, which did not allow the mass to flow under gravity (inset figure 7.1a and b). Further, the change of metal counterions from nitrate to chloride or acetate also led to the spontaneous formation of hydrogels, clearly indicating that the metal counterions do not play any significant role in the formation of Cd-nucleobase hydrogels.

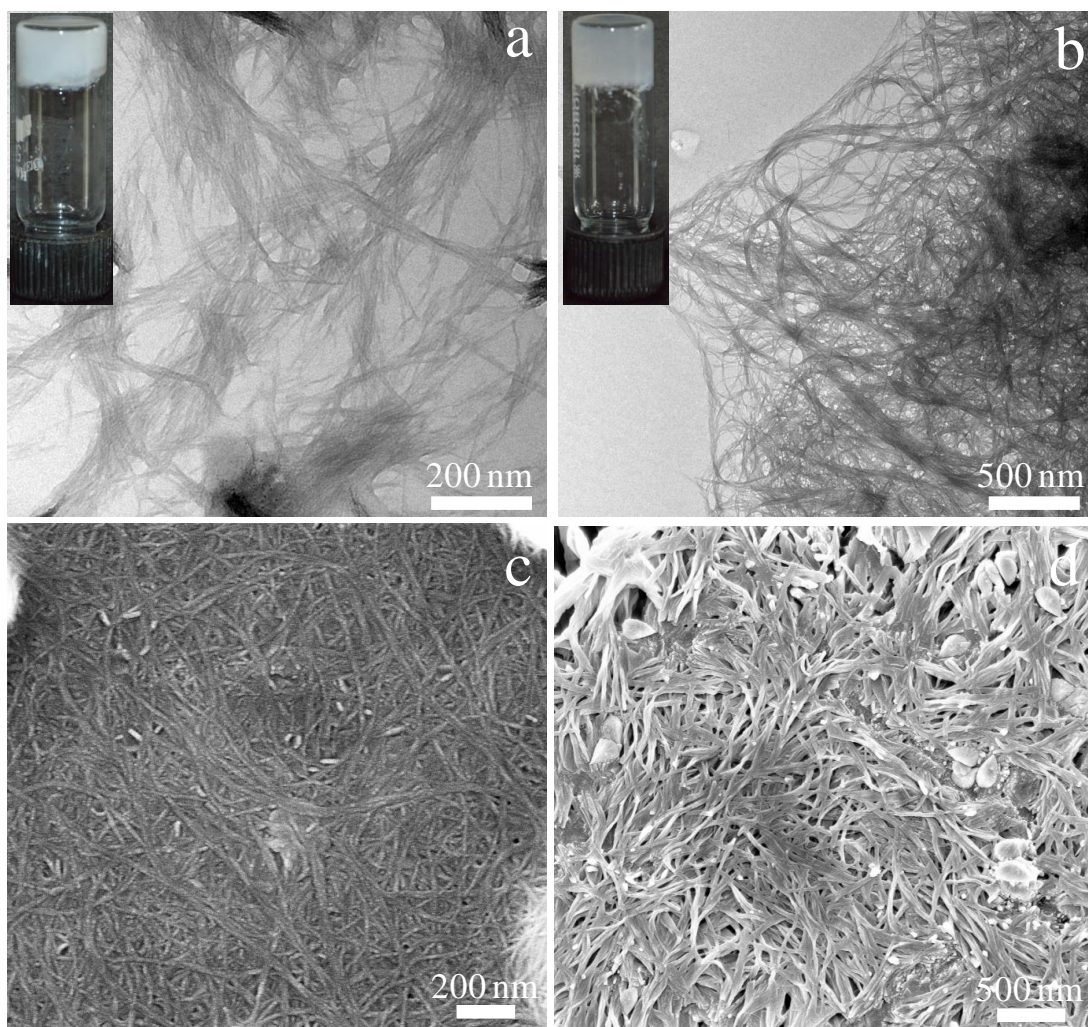


**Figure 7.1.** (a) and (c) TEM and SEM images of the Cd-T hydrogel respectively and (b) and (d) TEM and SEM images of the Cd-U hydrogel respectively.

Electron microscopy was employed to have an idea on the morphology of the hydrogels (figure 7.1). The transmission electron microscopy images of the hydrogels showed the formation of very homogeneous entwined three dimensional nanofibers capable of trapping large volume of water, resulting in the formation of the hydrogels. The Cd-T nanofibers were several hundreds of nanometers in length, while their thickness varied from 7-23 nm. For the Cd-U gel, the length of the nanofibers ranged from several hundreds of nanometer to micrometer, whereas the thickness of the fibers varied from 15-30 nm. The scanning electron microscopy images of both the hydrogels further confirmed the 3D entangled nanofibrillar morphology and were in good agreement to the TEM images.

Several attempts were made to obtain single crystals suitable for powder X-ray diffraction. However, due to the nanometer dimension of the fibers, any of such attempts could not result in the generation of single crystals of the hydrogels. Nonetheless, the crystalline nature of the nanofibers could be confirmed using powder X-ray diffraction studies, which showed a complex pattern of several peaks in the XRD spectrum at  $2\theta$  values between 1-50 degrees for both the hydrogels (figure 7.2a). The powder XRD spectrum of Cd-T gel, showed a periodic pattern of reflections, with the major reflections observed at  $2\theta = 7.0^\circ, 14.2^\circ, 21.4^\circ, 28.4^\circ, 35.4^\circ$  and  $43.4^\circ$ , corresponding to  $d$ -spacing of 12.6 Å, 6.3 Å, 4.2 Å, 3.1 Å, 2.5 Å and 2.1 Å respectively. These  $d$ -spacing follow a pattern of 1: 1/2: 1/3: 1/4: 1/5: 1/6, indicating that the hydrogel are organized in a layered pattern, with an inter layer separation of 12.6 Å. For the Cd-U gel, in addition to several peaks, major diffraction peaks at  $2\theta$  values of 12.6, 25.5, and 40.3 degrees corresponding to a  $d$ -spacing of 7.0 Å, 3.5 Å and 2.2 Å respectively were observed and followed a ratio of 1: 1/2: 1/3, suggesting that the hydrogels were arranged in a layered pattern. The thermal stability of the freeze dried hydrogels was studied by thermogravimetric analysis (figure 7.2b). From the TGA plots it was observed that the freeze dried Cd-T hydrogels showed an initial weight loss of about 20% in the temperature range of 25-240 °C, which might be due to the loss of water molecules in the complex. Two other weight losses were observed in the range of 240-600 °C. Both these weight losses could be attributed to the decomposition of ligand

molecules. Similarly for the Cd-U gel, an initial weight loss of 5.5% at 123 °C due to the probable loss of water molecules was observed. Two other weight losses in the range of 135-405 °C and 410-600 °C corresponding to the decomposition of the ligands were observed.

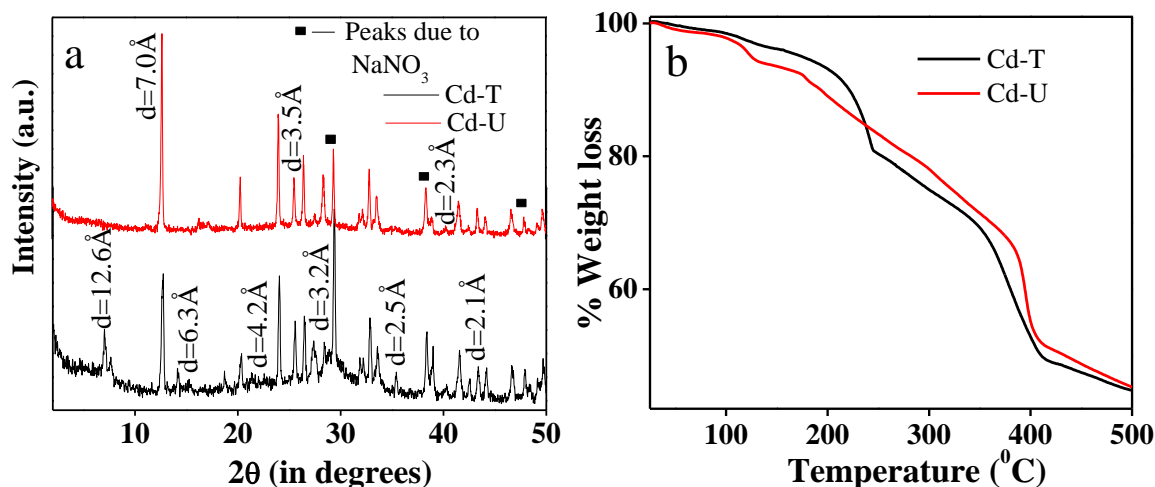


**Figure 7.2.** (a) Powder XRD spectrum and (b) TGA plots of the freeze-dried Cd-T and Cd-U gels.

The elastic nature and the mechanical robustness of the two hydrogels were ascertained from the rheological experiments. The strain sweep experiment for the Cd-T gel is shown in figure 7.3a. It is clear from the figure that the storage modulus ( $G'$ ) dominated over the loss modulus ( $G''$ ) almost in the complete range of strain, signifying the elastic of the gel. However at values of strain close to 100%, the two modulus merged together, signifying the gel to sol transformation beyond this range of strain. The elastic nature of the Cd-T hydrogel was further ascertained from the frequency sweep experiments (figure 7.3b), which showed the supremacy of  $G'$  over  $G''$  in the complete range of frequency, clearly proving that the material behaved as an elastic solid. Similarly, for the Cd-U gel, the higher values of  $G'$  over  $G''$  in the complete range of strain suggested the dominance of elastic behavior of the material over the viscous nature (figure 7.3c). The results obtained from the strain sweep experiments were further supported by the frequency sweep experiments (figure 7.3d), which suggested that the Cd-U gel behaved as an elastic solid. This type of solid like behavior is characteristic of supramolecular gel systems.

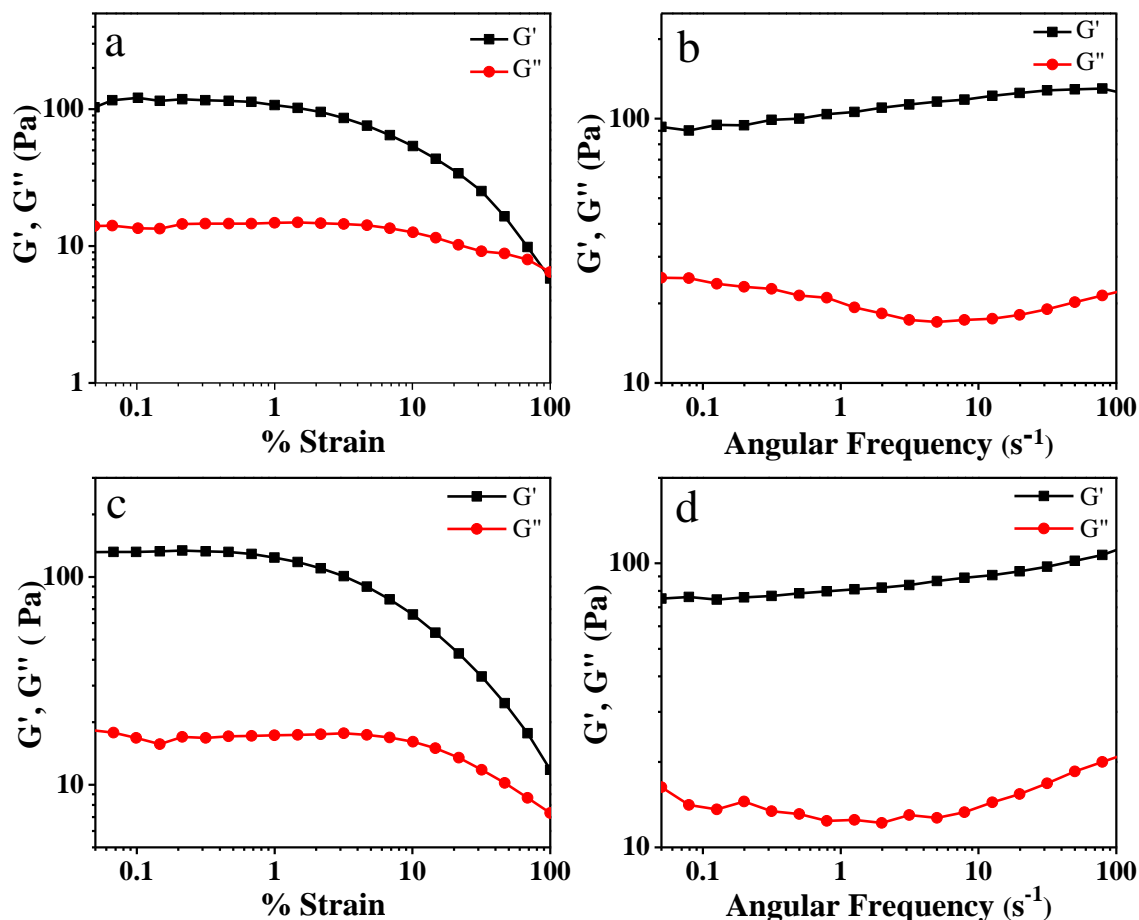


**Figure 7.3.** (a) Dynamic amplitude sweep experiment and (b) Frequency sweep experiment for the Cd-T gel. (c) Strain sweep experiment and (d) frequency sweep experiment for the Cd-U hydrogel respectively.

The changes in the environment of different functional groups in the nucleobases upon the binding of  $Cd^{2+}$  ions were studied by FTIR spectroscopy. From the FTIR spectrum of pure T and freeze dried Cd-T gel (figure 7.4a), it was observed that a broad peak at  $3445\text{ cm}^{-1}$ , characteristic of O-H stretching was observed in the complex, which might have arisen as a result of the trapped water molecule. Again, the peak at  $2805\text{ cm}^{-1}$  due to N-H stretching drastically decreased in intensity in the complex, suggesting the involvement of at least one of the N1 or N3 nitrogen atoms in binding to  $Cd^{2+}$ . Similarly from the FTIR spectrum of pure U and Cd-U, it was evident that either N1 or N3 nitrogen atoms of uracil were involved in bonding to the cadmium ions. Also the appearance of a broad peak at  $3505\text{ cm}^{-1}$  clearly indicated the presence of water molecules in the complex.

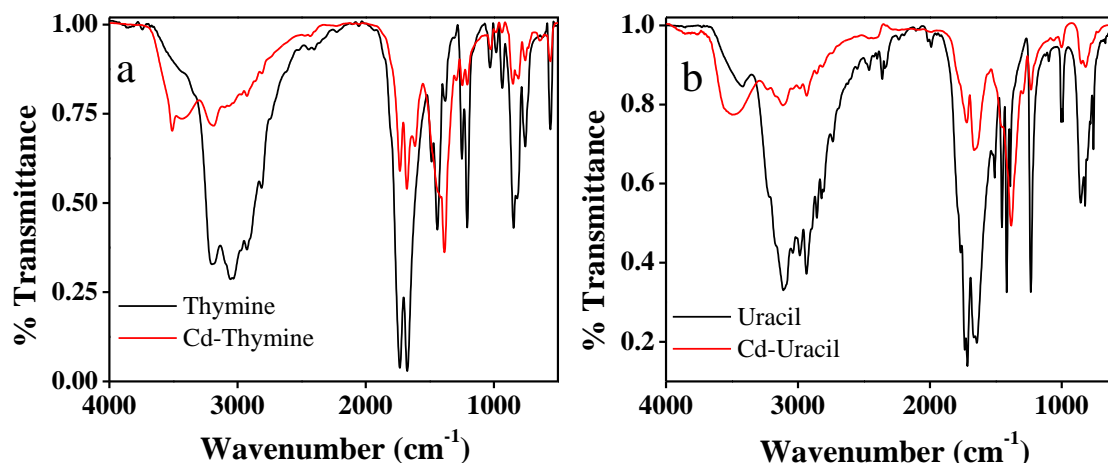


**Figure 7.4.** (a) FTIR spectrum of (a) T and Cd-T gel and (b) pure U and Cd-U gel.

### 7.2.2 Interaction of $\text{Cd}^{2+}$ ions with adenine, guanine and cytosine

The interaction of  $\text{Cd}^{2+}$  ions with nucleobases resulting in the formation of hydrogels was specific for thymine and uracil. The other three nucleobases namely, adenine (A), guanine (G) and cytosine (C) under identical conditions showed different results upon addition of  $\text{Cd}^{2+}$  ions. While A and G resulted in the formation of a white gelatinous precipitate (figure 7.5a and b), the addition of  $\text{Cd}^{2+}$  ions to an alkaline solution of cytosine resulted in the formation of a precipitate, which within a moment of seconds disappeared and a clear solution was obtained (figure 7.5c). The precipitate could not be transformed to gel even upon incubation at room temperature for several days, or by using external forces such as ultrasonication or heating/cooling.



**Figure 7.5.** Digital images of (a) Cd-A precipitate, (b) Cd-G precipitate and (c) Cd-C clear solution respectively.

The morphology of the products formed upon the addition of  $\text{Cd}(\text{NO}_3)_2$  to the nucleobases A, G and C was studied using scanning electron microscopy. From the SEM images it was observed that whereas the Cd-A precipitate consisted of a cluster of

small rod like particles (figure 7.6a), the precipitate obtained from the interaction of  $\text{Cd}^{2+}$  and G was composed of fibrous aggregates having dimensions in the micrometer range (figure 7.6b). On the other hand, the solution obtained by the addition of  $\text{Cd}(\text{NO}_3)_2$  to alkaline solution of C, when observed under a SEM, showed the formation of individual rod like particles as well as a cluster of rod like particles giving rise to a larger spherical particles, consisting of several rod like individual particles (figures 7.6c and d). Although, the interaction of  $\text{Cd}^{2+}$  ions with G and C led to the formation of coordination polymer particles with fibrous or rod like morphology, these formed structures (fibers and rods) were unable to trap water, and therefore could not lead to the formation of hydrogels

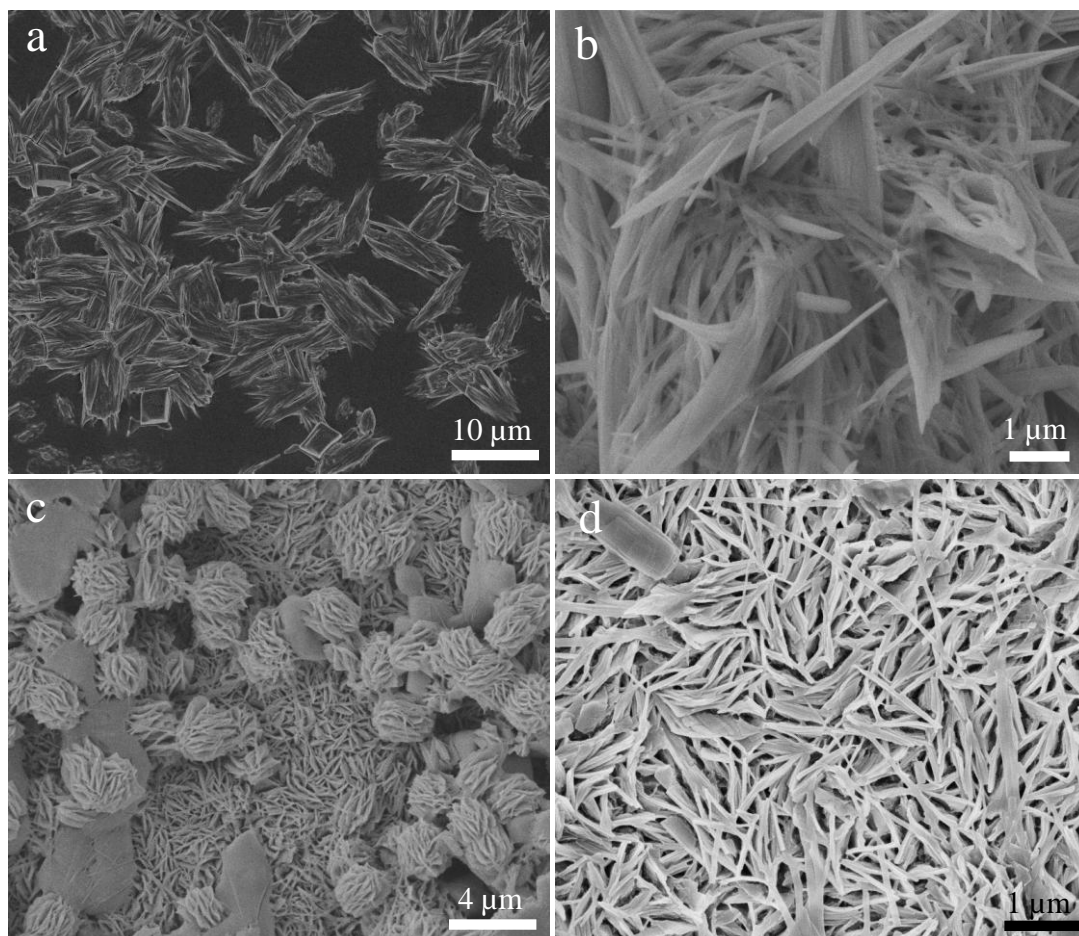


**Figure 7.6.** FESEM images of precipitates obtained upon the addition of  $\text{Cd}(\text{NO}_3)_2$  to an alkaline solution of (a) A and (b) G. (c) FESEM image of the clear solution containing Cd-C complex and (d) magnified SEM image of the rod like particles formed in the clear solution of Cd-C.

### 7.2.3 Gel formation in a mixture of thymine and uracil

It is well known that the structure and morphology of functional coordination materials are strongly dependent on their composition.<sup>[35]</sup> Therefore, functional coordination polymer materials with more than one metal ion or ligand are expected to show different properties as well as morphology. So, we studied the interaction of  $\text{Cd}^{2+}$  ions with a mixture of two ligands, T and U, which individually upon complexation to  $\text{Cd}^{2+}$  ions led to the formation of hydrogels. Unlike the formation of a precipitate, composed of microflowers, as in the case of Zn-cytosine-guanine, the addition of  $\text{Cd}^{2+}$  ions to a mixture of T and U resulted in the formation of hydrogel.

The formation of the hydrogel was confirmed from the tube inversion method, which did not allow the mass to flow under gravity. SEM images of the gel revealed the formation of very thin entangled network of fibers in the nanometer regime, responsible for the capturing of water, leading to the formation of hydrogel (figure 7.7a and b).

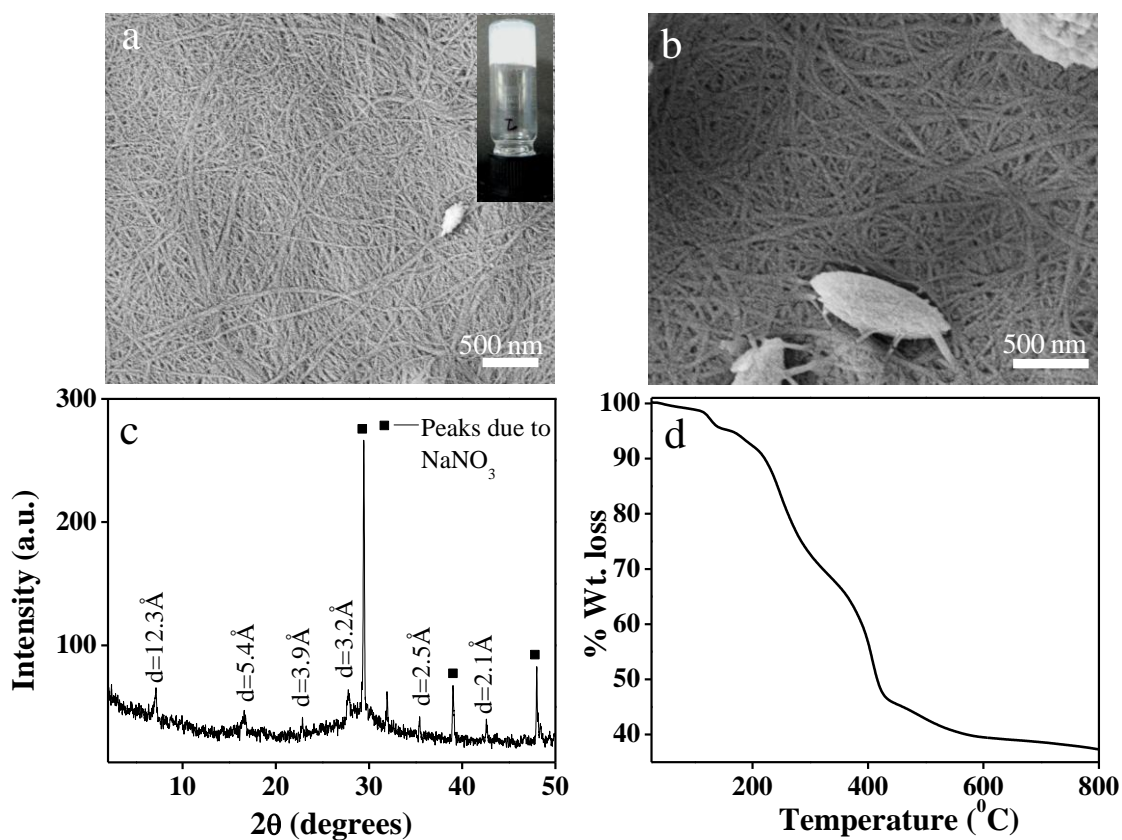


**Figure 7.7.** (a) and (b) FESEM images of the Cd-T-U hydrogel, (c) powder XRD spectrum and (d) TGA plot of the Cd-T-U hydrogel respectively; inset in (a); digital image of the Cd-T-U hydrogel.

The powder XRD analysis confirmed that the nanofibers were crystalline in nature (figure 7.7c). Major diffraction peaks at  $2\theta = 7.2^\circ$ ,  $16.6^\circ$ ,  $22.9^\circ$ ,  $27.8^\circ$ ,  $35.4^\circ$  and  $42.6^\circ$  corresponding to  $d$ -values of 12.3 Å, 5.3 Å, 3.9 Å, 3.2 Å, 2.5 Å and 2.1 Å, which followed a ratio of 1: 1/2: 1/3: 1/4: 1/5: 1/6 were observed. This pattern suggested that the hydrogel was mainly assembled in a layered structure with an interlayer separation of 12.3 Å. Further, the thermal stability of the freeze dried gel was studied using thermogravimetric analysis (figure 7.7b). The TGA plot of the gel showed an initial weight loss of 4.7% in the temperature range of 25-140 °C due to the loss of the trapped water molecules. Further, two other weight losses in the temperature range of 140-580 °C were observed which could be assigned to the thermal decomposition of the ligand molecules from the complex.

Rheological investigation of the gel formed upon the addition of  $\text{Cd}(\text{NO}_3)_2$  to a mixture of T and U suggested that the material had elastic solid like properties. The amplitude sweep experiment (figure 7.8a) showed that the value of the storage modulus  $G'$  was higher than the loss modulus  $G''$  by several factors in the entire range of strain from 0.05% to 100%, indicating that the material behaved as an elastic solid, rather than a viscous sol.

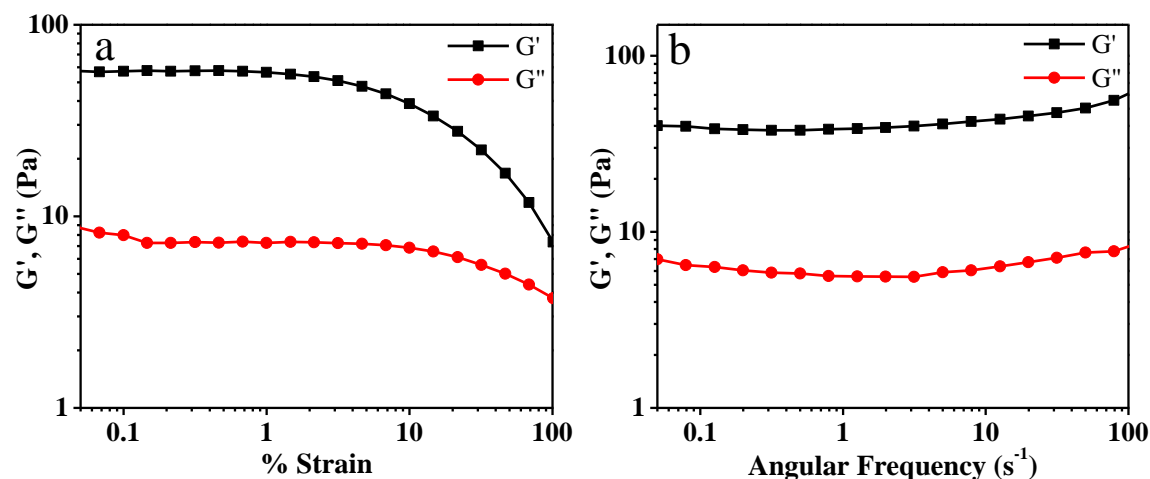


**Figure 7.8.** (a) Amplitude sweep experiment and (b) frequency sweep experiment at a constant strain of 1% for the Cd-T-U gel.

The elastic nature of the Cd-T-U hydrogel was further established by frequency sweep experiment. From the frequency sweep experiment performed at a constant strain

of 1%, it was evident that the value of  $G'$  was significantly higher than that of  $G''$  by a factor of eight in the complete frequency range of 0.05-100  $s^{-1}$ , clearly demonstrating the supremacy of elastic behavior over the viscous nature.

### 7.2.4 Formation of CdS quantum dots within the gels

The synthesis or incorporation of inorganic nanoparticles, such as metallic or semiconductor nanoparticles in a gel matrix has recently gained interest and inspired researchers, mainly because generating such a system is an attempt to organize the nanoparticles in the 3D gelator matrix, so that the properties of such nanoparticles can be tuned.<sup>[23]</sup> Further, the integration of nano-objects such as nanoparticles within microenvironments, such as those provided by hydrogels could eventually generate materials of macro dimensions whose properties might open new perspectives from both technological as well as applicative aspects.<sup>[24]</sup>

Since the nucleobases, thymine and uracil can result in the *in situ* formation of Ag nanoparticles within the Ag-nucleobase hydrogels,<sup>[36]</sup> so we attempted to synthesize CdS quantum dots within the Cd-T and Cd-U gels. It was observed that the simple addition of a sulfide precursor ( $Na_2S$ ) to the alkaline solution of T or U, followed by the addition of  $Cd(NO_3)_2$  immediately resulted in the formation of slightly yellow colored gel, suggesting the formation of CdS quantum dots.

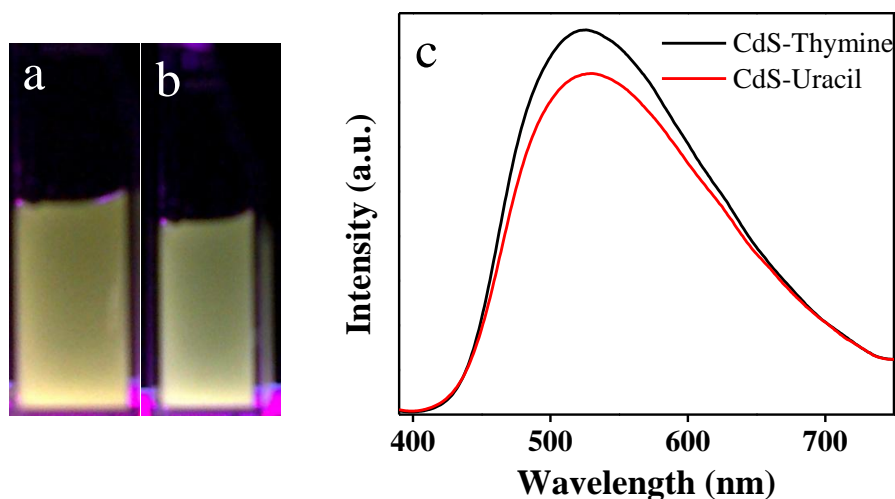


**Figure 7.9.** Digital images of *in situ* formed CdS quantum dots in (a) Cd-T gel and (b) Cd-U gel, when observed under UV light of wavelength 365 nm. (c) Fluorescence emission spectrum of CdS quantum dots formed within the Cd-T and Cd-U gels ( $\lambda_{ex}=380$  nm).

The gels when observed under UV lamp of wavelength 365 nm showed yellow emission (figure 7.9a and b), again indicating the formation of CdS quantum dots within the gel. The fluorescence emission spectrum of Cd-T and Cd-U hydrogels showed fluorescence with emission maxima of 526 nm and 530 nm respectively (figure 7.9c), confirming the formation of yellow fluorescent CdS quantum dots within the gel.

TEM was used to understand the size and shape of CdS quantum dots formed within the gels. From the TEM images, it was evident that spherical nanoparticles having an average size of  $6.1 \pm 1.1$  nm were formed within the Cd-T hydrogel (figure 7.10a). The HRTEM image of the CdS nanoparticles in the Cd-T gel showed a lattice separation of 0.29 nm (figure 7.10b) attributed to the (200) plane of cubic CdS structure.<sup>[37]</sup> The CdS nanoparticles formed within Cd-uracil gel were also found to be spherical in shape (figure 7.10c) and had an average diameter of  $7.0 \pm 1.1$  nm. The HRTEM image (figure 7.10d) exhibited clearly resolved lattice fringes having an interplanar spacing of 0.33 nm assigned to the (111) plane of the cubic CdS structure.<sup>[38]</sup>

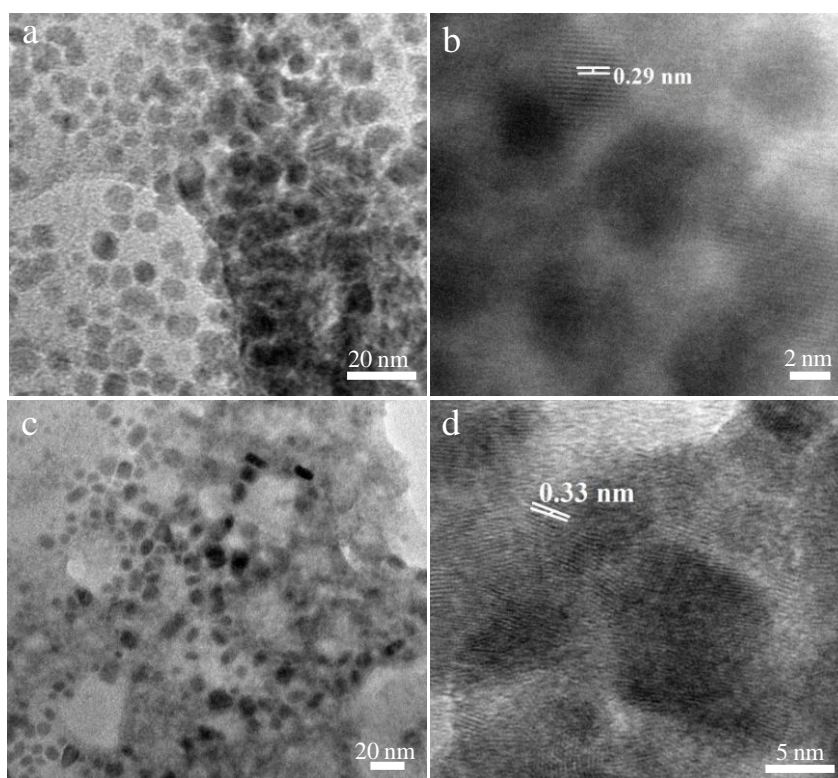


**Figure 7.10.** (a) and (b) TEM and HRTEM images of CdS NPs formed in the Cd-T gel respectively. (c) and (d) TEM and HRTEM images of CdS NPs formed in the Cd-U gel respectively.

The CdS quantum dots were however not very stable, as indicated by the intensity of the color of the gels observed under UV-light. The instability of the CdS quantum dots was further confirmed from the time dependent fluorescence studies (figure 7.11). As can be seen from figure 7.11, the emission intensity of the CdS nanoparticles in both the gels decreased with time, together with a slight red shift in emission maximum.

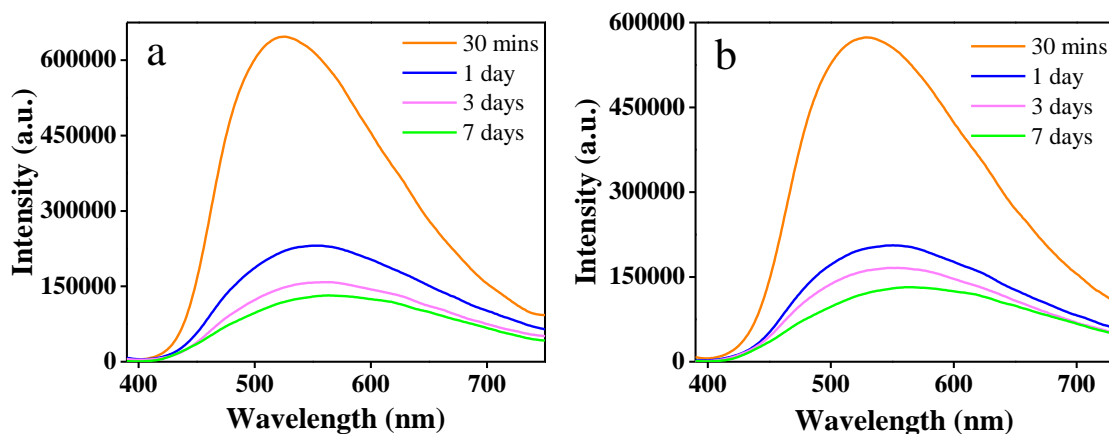


**Figure 7.11.** Time dependent fluorescence emission spectrum of CdS nanoparticles formed within (a) Cd-T gel and (b) Cd-U gel.

To understand the mechanism of the decrease in emission intensity of CdS quantum dots within the gels, time dependent TEM studies were performed. From the TEM studies, it was very evident that with time, the initially formed quantum dots agglomerated to give larger particles. For the Cd-T gel, it was observed that initially tiny nanoparticles having an average size of  $0.9 \pm 0.2$  nm (figure 7.12a) were observed (at 30 mins). Within 24 hours, these molecules aggregated to form larger particles having an average diameter of  $3.3 \pm 0.7$  nm (figure 7.12b). The TEM image recorded after three days (figure 7.12c) showed even larger particles having an average size of  $6.0 \pm 1.0$  nm. Similar increase in the sizes of the CdS nanoparticles with time was observed in case of Cd-U hydrogel (figures 7.12d, e and f). This agglomeration of the particles leading to the formation of larger aggregates might be the reason for the decrease in the emission intensity of the nanoparticles together with a slight shift towards the red region.

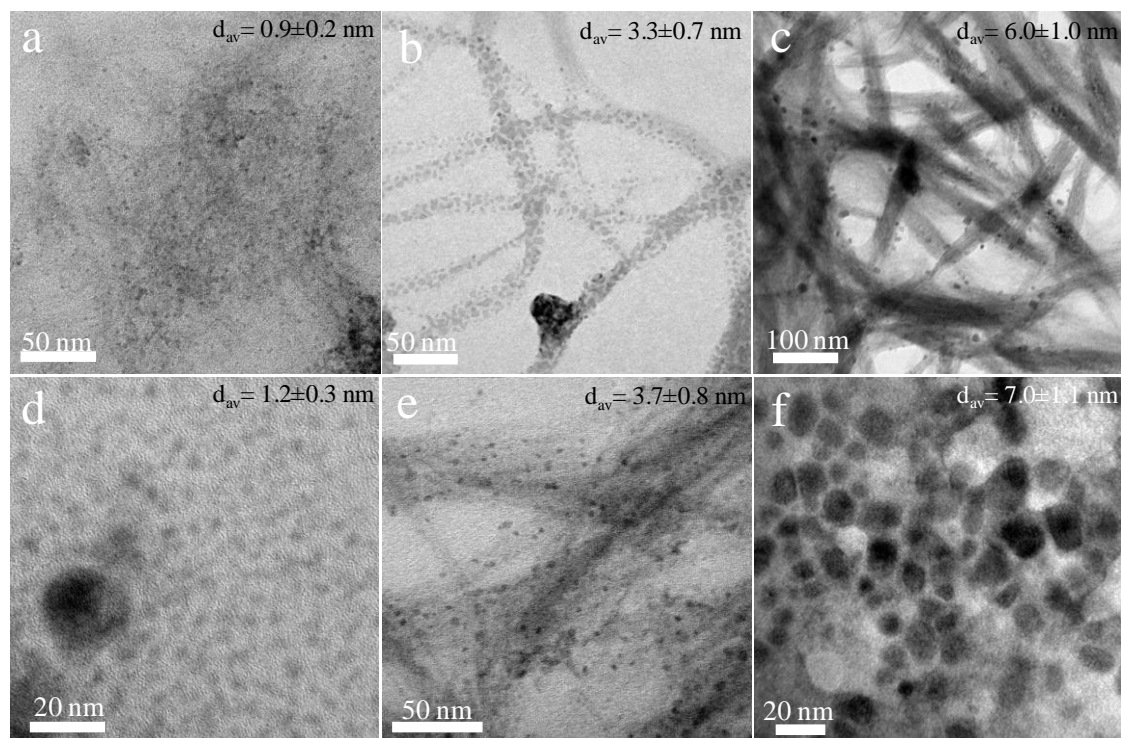


**Figure 7.12.** Time dependent TEM studies for the growth of CdS nanoparticles within (a, b, c) Cd-T gel and (d, e, f) Cd-U gel. (a, d) after 30 minutes, (b, e) after 1 day and (c, f) after 3 days.

### 7.3 Conclusions

In conclusion, the coordination capability of two nucleobases, thymine and uracil have been exploited for the generation of coordination polymer hydrogels upon their interaction with  $\text{Cd}^{2+}$  ions under basic conditions. The gels consisted of crystalline nanofibers and showed good elastic behavior. The gelation process is rapid and takes place without the aid of external forces such as heating/cooling or sonication. The formation of cadmium based metallogel has also been observed for a mixture of thymine and cytosine. Further, the nucleobases have been used as nanoreactors for the growth of CdS quantum dots. The formation of the quantum dots takes place within the gel and does not require any external capping agent. However, the quantum dots are not very stable and tend to agglomerate with time. Studies are being performed to optimize the reaction conditions, such that the growth of the quantum dots within the gel can be controlled. Such a quantum dot incorporated gel holds promise for use as visible light photocatalysts for various important reactions such as photocatalytic water splitting.

This method can be extended towards the development of other semiconducting nanoparticle (CdSe, CdTe etc.) hydrogel composite, by using appropriate metal salts. Further, the coordination of toxic metals such as cadmium to biologically important molecules such as nucleobases can largely reduce the toxicity of the metal ions in the hybrid materials, although detailed studies are required in this field.

## **7.4 Experimental Section**

### **7.4.1 Materials**

Adenine, guanine, cytosine, thymine, uracil were purchased from Aldrich chemicals. Cadmium nitrate tetrahydrate, cadmium chloride, cadmium acetate, sodium hydroxide, sodium sulfide and nitric acid were purchased from Merck, India. All the chemicals were of analytical grade and were used without any purification. Milli Q water was used throughout the experiments.

### **7.4.2 Instrumentation**

Transmission electron microscopy (TEM) images were recorded with a Technai G<sup>2</sup> 20 Ultra-Twin microscope and Jeol JEM 2100 microscope at an accelerating voltage of 200 kV. Field emission scanning electron microscopy images were recorded on a Carl Zeiss Supra 55 instrument after gold coating. Rheological measurements were performed using an Anton Paar Physica MCR 301 rheometer with parallel plate geometry (diameter 50 mm). Powder X-ray diffraction spectra (XRD) of the freeze dried gels were recorded on a Rigaku Smartlab, Automated Multipurpose X-ray diffractometer with Cu K $\alpha$  source (wavelength of X-rays was 0.154 nm). FTIR spectra were recorded in KBr pellet using Bruker Tensor 27 instrument. Thermogravimetric analysis was done using a Mettler Toledo instrument. Emission spectra were recorded using a fluoromax-4p fluorometer from Horiba (Model: FM-100).

### **7.4.3 Synthesis of Cd-thymine and Cd-uracil hydrogels**

A stock solution of the two nucleobases (0.2 M) was first prepared by addition of solid NaOH in parts under sonication, until a clear solution was obtained. Another stock solution of Cd(NO<sub>3</sub>)<sub>2</sub> (0.2 M) was prepared by dissolving the metal salt in water.

In a typical synthesis, to 1.0 mL of the as prepared nucleobase solution taken in a tube, 1.0 mL of the  $\text{Cd}(\text{NO}_3)_2$  solution was added, which resulted in the immediate formation of opaque, self-standing hydrogels.

#### **7.4.4 Electron microscopy studies**

The samples for both TEM and FESEM were prepared by diluting the gel samples in water. A small amount of the gel was taken in an eppendorf tube and after addition of water the gel was crushed using a micropestle and was drop casted on a carbon coated copper grid (for TEM) and glass slides (for FESEM), followed by room temperature drying.

#### **7.4.5 Rheological studies**

Rheological investigations were performed using parallel plate geometry of diameter 50 mm. For the measurements, both the hydrogels were first prepared, and then a piece of the gel was placed on the plate of the rheometer using a microspatula. The temperature was maintained at 25 °C using an integrated temperature controller from Julabo. Dynamic strain sweep experiments were performed using a constant frequency of 10  $\text{rad s}^{-1}$ . The dynamic frequency sweep of both the hydrogels was measured as function of frequency in the range of 0.05-100  $\text{rad s}^{-1}$  with constant strain value 1%.

#### **7.4.6 Formation of gel in the mixture of thymine and uracil**

In a tube 0.5 mL of both thymine and uracil (0.2 M each) were taken and mixed properly by vortexing. To this mixed solution, 1.0 mL of the  $\text{Cd}(\text{NO}_3)_2$  was added which resulted in the immediate formation of an opaque gel.

#### **7.4.7 Synthesis of CdS quantum dots within the gel**

In a typical synthesis, to 1.0 mL of thymine or uracil (0.2 M) taken in a tube, 0.1 mL of  $\text{Na}_2\text{S}$  (0.1 M) was added, followed by the addition of 1.0 mL of  $\text{Cd}(\text{NO}_3)_2$ , which immediately led to the formation of a yellow colored gel.

---

## 7.5 References

1. Sangeetha N. M., Maitra U. (2005), Supramolecular gels: Functions and uses, *Chem. Soc. Rev.*, 34, 821-836 (DOI: 10.1039/b417081b).
2. Yang Z., Liang G., Xu B. (2008), Enzymatic hydrogelation of small molecules, *Acc. Chem. Res.*, 41, 315-326 (DOI: 10.1021/ar7001914).
3. Estroff L. A., Hamilton A. D. (2004), Water gelation by small organic molecules, *Chem. Rev.*, 104, 1201-1218 (DOI: 10.1021/cr0302049).
4. Terech P., Weiss R. G. (1997), Low molecular mass gelators of organic liquids and the properties of their gels, *Chem. Rev.*, 97, 3133-3160 (DOI: 10.1021/cr9700282).
5. Skilling K. J., Citossi F., Bradshaw T. D., Ashford M., Kellam B., Marlow M. (2014), Insights into low molecular mass organic gelators: A focus on drug delivery and tissue engineering applications, *Soft Matter.*, 10, 237-256 (DOI: 10.1039/c3sm52244j).
6. Das D., Kar T., Das P. K. (2012), Gel-nanocomposites: Materials with promising applications, *Soft Matter*, 8, 2348-2365 (DOI: 10.1039/c1sm06639k)
7. Díaz Díaz D., Kühbeck D., Koopmans R. J. (2011), Stimuli-responsive gels as reaction vessels and reusable catalysts, *Chem. Soc. Rev.*, 40, 427-448 (DOI: 10.1039/c005401c).
8. Bhattacharjee S., Samanta S. K., Moitra P., Pramoda K., Kumar R., Bhattacharya S., Rao C. N. R. (2015), Nanocomposite made of an oligo(p-phenylenevinylene)-based trihybrid thixotropic metallo(organo) gel comprising nanoscale metal-organic particles, carbon nanohorns, and silver nanoparticles, *Chem. Eur. J.*, 21, 5467-5476 (DOI: 10.1002/chem.201405522).
9. Zhao Z., Lam J. W. Y., Tang B. Z. (2013), Self-assembly of organic luminophores with gelation-enhanced emission characteristics, *Soft Matter.*, 9, 4564-4579 (DOI: 10.1039/C3SM27969C).
10. Hirst A. R., Escuder B., Miravet J. F., Smith D. K. (2008), High-tech applications of self-assembling supramolecular nanostructured gel-phase

- materials: From regenerative medicine to electronic devices, *Angew. Chem. Int. Ed.*, 47, 8002-8018 (DOI: 10.1002/anie.200800022).
11. Praveen V. K., Ranjith C., Bandini E., Ajayaghosh A., Armaroli N. (2014), Oligo(phenylenevinylene) hybrids and self-assemblies: versatile materials for excitation energy transfer, *Chem. Soc. Rev.*, 43, 4222-4242 (DOI: 10.1039/C3CS60406C).
  12. Babu S. S., Praveen V. K., Ajayaghosh A. (2014), Functional  $\pi$ -gelators and their applications, *Chem. Rev.*, 114, 1973-2129 (DOI: 10.1021/cr400195e).
  13. Cheng N., Hu Q., Guo Y., Wang Y., Yu L. (2015), Efficient and selective removal of dyes using imidazolium-based supramolecular gels, *ACS Appl. Mater. Interfaces*, 7, 10258-10265 (DOI: 10.1021/acsami.5b00814).
  14. Ajayaghosh A., Praveen V. K., Vijayakumar C. (2008), Organogels as scaffolds for excitation energy transfer and light harvesting, *Chem. Soc. Rev.*, 37, 109-122 (DOI: 10.1039/B704456A).
  15. Jung J. H., Lee J. H., Silverman J. R., John G. (2013), Coordination polymer gels with important environmental and biological applications, *Chem. Soc. Rev.*, 42, 924-936 (DOI: 10.1039/c2cs35407a).
  16. Tam A. Y. -Y., Yam W. -W. (2013), Recent advances in metallogels, *Chem. Soc. Rev.*, 42, 1540-1567 (DOI: 10.1039/C2CS35354G).
  17. Xing B., Choi M. -F., Xu B. (2002), Design of coordination polymer gels as stable catalytic systems, *Chem. Eur. J.*, 8, 5028-5032 (DOI: 10.1002/1521-3765(20021104)8:21<5028::AID-CHEM5028>3.0.CO;2-1).
  18. Lanigan N., Wang X. (2013), Supramolecular chemistry of metal complexes in solution, *Chem. Commun.*, 49, 8133-8144 (DOI: 10.1039/C3CC44350G).
  19. Zhang J., Su C. -Y. (2013), Metal-organic gels: From discrete metallogelators to coordination polymers, *Coord. Chem. Rev.*, 257, 1373-1408 (DOI: 10.1016/j.ccr.2013.01.005).

- 
20. Aiyappa H. B., Saha S., Wadge P., Banerjee R., Kurungot S. (2014), Fe(III) phytate metallogel as a prototype anhydrous, intermediate temperature proton conductor, *Chem. Sci.*, 6, 603-607 (DOI: 10.1039/c4sc02294g).
  21. Saha S., Schön E. –M. Cativiela C., Díaz Díaz D., Banerjee R. (2013), Proton-conducting supramolecular metallogels from the lowest molecular weight assembler ligand: A quote for simplicity, *Chem. Eur. J.*, 19, 9562-9568 (DOI: 10.1002/chem.201204542).
  22. Bairi P., Roy B., Nandi A. K. (2011), pH and anion sensitive silver(I) coordinated melamine hydrogel with dye absorbing properties: Metastability at low melamine concentration, *J. Mater. Chem.*, 21, 11747-11749 (DOI: 10.1039/c1jm11994j).
  23. Saha S., Das G., Thote J., Banerjee R. (2014), Photocatalytic metal-organic framework from CdS quantum dot incubated luminescent metallohydrogel, *J. Am. Chem. Soc.*, 136, 14845-14851 (DOI: 10.1021/ja509019k).
  24. Cametti M., Džolić Z. (2014), New frontiers in hybrid materials: noble metal nanoparticles – supramolecular gel systems, *Chem. Commun.*, 50, 8273-8286 (DOI: 10.1039/C4CC00903G).
  25. Thoniyot P., Tan M. J., Karim A. A., Young D. J., Loh X. J. (2015), Nanoparticle–hydrogel composites: Concept, design, and applications of these promising, multi-functional materials, *Adv. Sci.*, 1430010, (DOI: 10.1002/advs.201400010).
  26. Liu Y., Meng H., Konst S., Sarmiento R., Rajachar R., Lee B. P. (2014), Injectable dopamine-modified poly(ethylene glycol) nanocomposite hydrogel with enhanced adhesive property and bioactivity, *ACS Appl. Mater. Interfaces*, 6, 16982-16992 (DOI: 10.1021/am504566v).
  27. Skelton S., Bostwick M., O'Connor K., Konst S., Casey S., Lee B. P. (2013), Biomimetic adhesive containing nanocomposite hydrogel with enhanced materials properties, *Soft Matter*, 2013, 9, 3825-3833 (DOI: 10.1039/C3SM27352K).

- 
28. Imaz I., Rubio-Martínez M., An J., Solé-Font I., Rosi N. L., Maspoch D. (2011), Metal–biomolecule frameworks (MBioFs), *Chem Commun.* 47, 7287-7302 (DOI: 10.1039/c1cc11202c).
  29. Imaz I., Rubio-Martínez M., Saletta W. J., Amabilino D. B., Maspoch D. (2009), Amino acid based metal-organic nanofibers, *J. Am. Chem. Soc.*, 131, 18222-18223 (DOI: 10.1021/ja908721t).
  30. Wei H., Li B., Du Y., Dong S., Wang E. (2007), Nucleobase–metal hybrid materials: Preparation of submicrometer- scale, spherical colloidal particles of adenine–gold(III) via a supramolecular hierarchical self-assembly approach, *Chem. Mater.*, 19, 2987-2993 (DOI: 10.1021/cm070028a).
  31. Liu Y., Ma W., Liu W., Li C., Liu Y., Xiang X., Tang Z. (2011), Silver(I)–glutathione biocoordination polymer hydrogel: effective antibacterial activity and improved cytocompatibility, *J. Mater. Chem.*, 21, 19214-19218 (DOI: 10.1039/c1jm13693c).
  32. Manton A., Massüger L., Rabu P., Palivan C., McCusker L. B., Taubert A. (2008), *J. Am. Chem. Soc.*, Metal-peptide frameworks (MPFs): “Bioinspired” metal organic frameworks, 130, 2517-2526 (DOI: 10.1021/ja0762588).
  33. An J., Geib S. J., Rosi N. L. (2009), Cation-triggered drug release from a porous zinc–adeninate metal–organic framework, *J. Am. Chem. Soc.*, 131, 8376-8377 (DOI: 10.1021/ja902972w).
  34. Kumar A., Kumar V. (2014), Biotemplated inorganic nanostructures: Supramolecular directed nanosystems of semiconductor(s)/metal(s) mediated by nucleic acids and their properties, *Chem. Rev.*, 114, 7044-7078 (DOI: 10.1021/cr4007285).
  35. Lee H. J., We J., Kim J. O., Kim D., Cha W., Lee E., Sohn J., Oh M. (2015), Morphological and structural evolutions of metal–organic framework particles from amorphous spheres to crystalline hexagonal rods, *Angew. Chem. Int. Ed.*, 54, 10564-10568 (DOI: 10.1002/anie.201504873).
-

36. Sharma B., Mahata A., Mandani S., Pathak B., Sarma T. K. (2015), Manuscript submitted for publication.
37. Tak Y., Hong S. J., Lee J. S., Yong K. (2009), Fabrication of ZnO/CdS core/shell nanowire arrays for efficient solar energy conversion, *J. Mater. Chem.*, 19, 5945-5951 (DOI: 10.1039/b904993b).
38. Qi L., Cölfen H., Antonietti M. (2001), Synthesis and characterization of CdS nanoparticles stabilized by double-hydrophilic block copolymers, *Nano Lett.*, 1, 61-65 (DOI: 10.1021/nl0055052).



## Chapter 8

### Conclusions and Scope for Future Works

#### 8.1 Conclusions

Development of Hybrid organic-inorganic functional nanoscale materials has been an research area with tremendous focus as the synergy of inorganic and organic components leads to enhanced stability as well as desirable physico-chemical properties for wide range of applications ranging from catalysis, opto-electronic devices, biomedical applications, tissue engineering and so on. One important parameter that controls the properties and applications of functional materials is their size and shape. Therefore, the synthesis of functional materials with precise size and controlled morphology has gained immense significance. Of the various available pathways for the generation of hybrid functional materials with defined size and shape, the biomolecule assisted pathway has gained significant interest because biomolecules can not only provide a green and benign pathway for the generation of these functional materials, but can also direct the final structure of the resulting materials due to their intrinsic self-assembling properties.

In this thesis, we have demonstrated the ability of biomolecules for the generation of two classes of hybrid functional nanoscale materials, (i) metallic nanoparticles and (ii) coordination polymer hydrogels. A detailed mechanistic insight into the formation of metallic nanoparticles by enzymes has been provided. Additionally, the natural activity alone or the natural activity of the enzyme has been coupled together with its reduction capability for the generation of functional hybrid materials such as Au nanoparticle-conducting polymer nanocomposite and Au nanoparticle-ZnO core-shell nanostructures. Further, the several available coordination sites of nucleobases (chief component of DNA and RNA) have been taken advantage of for the generation of functional coordination polymer hydrogels by coordination to transition metal ions, with a potential to act as effective antimicrobial agents and photocatalysts.

In chapter 2 the ability of glucose oxidase, a flavo protein to function as both reducing as well as stabilizing agent for the synthesis of Au nanoparticles under physiological conditions has been demonstrated. The synthesized Au nanoparticles could be used as effective catalyst for the reduction of *p*-nitrophenol. However, the involvement of glucose oxidase in the reduction of the metal salt led to conformational changes in the structure of the enzyme, resulting in the loss of activity of the enzyme. Nevertheless, the natural activity of the native enzyme could then be taken advantage of for the room temperature generation of technologically relevant Au nanoparticle-polyaniline conducting nanocomposite at room temperature.

In chapter 3, the reducing ability of another enzyme, urease for the generation of monometallic as well as alloy nanoparticles have been established. The activity of the enzyme after the synthesis of nanoparticles was partially inhibited due to conformational changes in the native structure of the enzyme. Nevertheless, the reducing ability of urease could be coupled with its natural activity (partially inhibited) for the room temperature generation of hybrid materials such as Au@ZnO core-shell nanostructures.

In chapter 4, it has been demonstrated that the thickness of stabilizing layer on the nanoparticles plays a crucial role in deciding the catalytic activity of the nanoparticles, in addition to their size and shape. Simple variation in the pH of the reaction medium or the concentration of the enzyme using pepsin as a reducing and stabilizing agent led to the synthesis of nanoparticles with different sizes and shapes. These nanostructures could be used as catalysts for the reduction reactions. The reduction of smaller substrates such as *p*-nitrophenol was independent of the concentration of the enzyme used and was solely dependent on the size and shape of the nanoparticles. However, the reduction of relatively larger substrates such as resazurin was controlled by the concentration of the stabilizing layer (pepsin) on the nanoparticles, and nanoparticles having a denser layer of pepsin were found to be the weakest catalyst.

In chapter 5, the numerous binding sites offered by the five nucleobases for the generation of coordination polymer hydrogels under different conditions upon their interaction with Ag<sup>+</sup> ions have been exploited for the first time. While under basic

conditions adenine, cytosine, thymine and uracil interacted with  $\text{Ag}^+$  ions at physiological conditions to yield stable hydrogels, guanine resulted in the formation of a precipitate. On the other hand, under acidic conditions the addition of  $\text{Ag}^+$  ions to guanine resulted in the formation of hydrogel, whereas with adenine a precipitate was observed and the other three nucleobases resulted in clear solutions. Again under basic conditions the nucleobases cytosine, thymine and uracil could reduce  $\text{Ag}^+$  ions for the *in situ* generation of Ag nanoparticles decorated along the fibers of the hydrogels, leading to the formation of hybrid metal nanoparticle-hydrogel composite. Further, the Ag-nucleobase hydrogels could be used as effective antimicrobial agents against both gram positive as well as gram negative microbes.

In chapter 6, the self assembly of cytosine and guanine under the influence of  $\text{Zn}^{2+}$  ions, leading to the formation of metallo gels at room temperature has been reported. Additionally, the changes on the morphology and structure of materials upon the changes in the composition have been shown. The use of a mixture of cytosine and guanine as ligands afforded coordination polymer particles with flower like morphology. All these three materials, due to their semiconducting nature could be used as photocatalysts for the degradation of organic pollutant dyes such as methyl orange and methylene blue.

Chapter 7 is an attempt to synthesize semiconducting nanoparticles such as CdS within the gel matrix such that the nanoparticles are decorated along the fibers of the hydrogel. The ability of thymine and uracil for the generation of metallo gels using  $\text{Cd}^{2+}$  ions as metal ions was first exploited. The addition of  $\text{Na}_2\text{S}$  to the nucleobase solution followed by the addition of  $\text{Cd}^{2+}$  ions resulted in the formation of CdS incorporated hydrogels. The CdS nanoparticles, however tend to agglomerate as observed from the time dependent fluorescence and TEM studies.

## 8.2 Scope for future works

The use of biological molecules for the generation of hybrid functional materials such as metallic nanoparticles and coordination polymer hydrogels is important because biomolecules feature rich functional group chemistry due to which metal ions can easily be reduced or can bind to the biomolecules. Further, biomolecules provide a green and

environmentally benign pathway for the fabrication of functional materials, thus considerably reducing the energy requirements involved in manufacturing processes. The use of enzymes as reducing as well as stabilizing agents for the synthesis of metallic nanoparticles is important to understand the effect of covalent attachment of enzymes onto the nanoparticle surface on the natural activity of the former. Also the reducing ability of the enzyme could be coupled with its natural activity to generate technologically relevant hybrid materials in a greener pathway alternative to the current environmentally harsh and energy exhaustive processes. Further, the use of enzymes for the synthesis of metallic nanoparticles will give a mechanistic intimation towards the capability of microorganisms such as fungus, virus and bacteria in synthesizing nanoparticles. Also, the immobilization and growth of these nanoparticle-enzyme composites on various substrates will afford opportunities for the development of technologically pertinent systems. Additionally, the possibility of formation of coordination polymer hydrogels generated from the interaction of metal ions with low molecular weight biomolecules such as nucleobases are expected to offer a new pathway towards the generation of spontaneous, low-cost and highly efficient systems for various applications. Although we have demonstrated only a very few applications of these hydrogels such as antibacterial, photocatalytic and in situ generation of semiconducting nanoparticles, the application potential can be exploited to several areas of research including organocatalysis, drug and gene delivery, bio-sensing, bio-labelling and tissue engineering applications. It is well-reported that immobilizing functional biomolecules such as proteins, enzymes and DNA inside such coordination polymer matrices enhances the robustness as well as their functionality for their uses in chemical processing, pharmaceuticals and biostorage. These coordination polymer hydrogels might give rise to new possibilities of exploitation of biomacromolecules through rapid, low-cost biomimetic mineralization process. The development of these dynamic hybrid systems taking advantage of the metal ion's coordination, the orientation and functionality of the polydentate biomolecules and directed self-assembly are expected to induce rational design of practical systems for various applications.